Dublin City University
School of Physical Sciences

Surface and interface characterisation of high-κ dielectric materials on silicon and III-V semiconductor substrates

Barry Brennan B.Sc.
Doctor of Philosophy

December 2009

Supervised by Professor Greg Hughes

Dedications and Acknowledgements

I would like to express my gratitude to my supervisor, Greg Hughes who has been a constant source of inspiration and motivation to me throughout this work. His enthusiasm, dedication and ability to surprise with information and ideas is something I can only hope to aspire to. I can't think him enough for giving me the opportunity to work alongside him and for always being there with advice and guidance throughout.

To everyone in the Surface and Interfaces Research Group that have come and gone over the years; Stephen, Oisin, Patrick, Ian, Justin, Robert, Kumar, for help and input throughout, and more importantly for the necessary distractions which helped the time to pass so quickly. They were always friends first and colleagues second. Many thanks also to Paul Hurley and everyone I collaborated with in the Tyndall Institute in Cork and to Bob Wallace in the University of Texas in Dallas for inviting me to join his group and work in his research lab. It was an amazing experience that gave me the opportunity to grow as a researcher and also to learn a lot about myself. A special mention goes to Adam, Chris, Servando, Marko, Manori and Andy for making me feel welcome and at home during my time with them there.

Thanks to Tom and Rob for putting up with me and providing great company over the years in Lanesborough, as well as all my friends from Donegal and Dublin for helping me to maintain a level of sanity over the years.

Most importantly, many thanks go to all my family, Colin and Kevan and especially my parents, Mary and Tommy. Words can't do justice to the debt of gratitude I owe to them for everything they have given me. Their belief and insistence that I do what I enjoy, what ever that may be, has led me here and made me who I am today; Mum with her constant support and always being there with encouragement and Dad, instilling a desire for perfection in my work and a curiosity into the hows and whys of everything from a young age.

Finally I would like to acknowledge the Irish Research Council for Science Engineering and Technology for the financial support of this work.

Declaration

I hereby certify that this material, which I now submit for assessment on the program of study leading to the award of doctor of Philosophy is entirely my own work and has not been taken from the work of others save and to the extent that such work has been cited and acknowledged within the text of my work.

Signed:______________________________(Candidate)

ID No.: 51008129

Date:________________________

Abstract

Interface formation between high-κ dielectric oxide materials and semiconductor surfaces is of critical importance to the development of the next generation of high speed semiconductor devices. This thesis investigates the deposition and characterisation of a range of candidate high-κ materials on both silicon and III-V (InGaAs and InP) semiconductor substrates, with the focus on interface formation. The primary characterisation techniques used to study the interface chemistry were x-ray photoelectron spectroscopy (XPS) and synchrotron radiation based photoemission, while atomic force microscopy (AFM) was used in some experiments for surface roughness measurements. The first part of the study evaluates a range of surface preparation methods prior to dielectric deposition aimed at removing the native oxides and passivating the surfaces while keeping surface roughness to a minimum. Methods investigated for silicon surface preparation included flash cleaning, hydrofluoric acid (HF) etching and the growth of self limiting ultra-thin oxides. For InGaAs the optimisation of the ammonium sulphide $(NH_4)_2S$ and hydrogen sulphide (H_2S) passivation treatments was investigated and an in-depth study of atomic hydrogen cleaning was undertaken. For InP surfaces, an $(NH_4)_2S$ based treatment was compared to an alternative acid based etch. The dielectric/substrate systems investigated included the reactive deposition of magnesium oxide (MgO) on Si studied by XPS and synchrotron radiation photoemission and aluminium oxide (Al_2O_3) deposited by atomic layer deposition (ALD) on indium gallium arsenide (InGaAs) also studied by XPS. Electron beam deposition studies of HfO_2 were also carried out on InP after various surface treatments, followed by XPS and electrical characterisation to determine the effect of the surface treatments in terms of native oxide and defect generation.

Publications arising from this work

Photoemission studies of the initial interface formation of ultrathin MgO dielectric layers on the Si(111) surface

Barry Brennan, Stephen McDonnell, Greg Hughes

Thin Solid Films, In Press, (available online Aug. 2009)

High resolution photoemission study of SiO_x/Si(111) interface disruption following in situ HfO_2 deposition

Stephen McDonnell, Barry Brennan, and Greg Hughes

Appl. Phys. Lett. 95, 072903 (2009)

Half-cycle atomic layer deposition reaction study using O_3 and H_2O oxidation of Al_2O_3 on $In_{0.53}Ga_{0.47}As$

B. Brennan, M. Milojevic, H. C. Kim, P. K. Hurley, J. Kim, G. Hughes, and R. M. Wallace.

Electrochem. Solid-State Lett., Volume 12, Issue 6, pp. H205-H207 (2009)

Photoemission studies of the interface formation of ultrathin MgO dielectric layers on the oxidised Si(111) surface

B Brennan, S McDonnell and G Hughes

J. Phys.: Conf. Ser**.** 100 042047 (4pp), (2008)

Detection of Ga suboxides and their impact on III-V passivation and Fermi-level pinning

C. L. Hinkle, M. Milojevic, B. Brennan, A. M. Sonnet, F. S. Aguirre-Tostado, G. J. Hughes, E. M. Vogel, and R. M. Wallace.

Appl. Phys. Lett. 94, 162101 (2009)

In situ H_2S passivation of $In_{0.53}Ga_{0.47}As$/InP metal-oxide-semiconductor capacitors with atomic-layer deposited HfO_2 gate dielectric

E. O'Connor, R. D. Long, K. Cherkaoui, K. K. Thomas, F. Chalvet, I. M. Povey, M. E. Pemble, B. Brennan, G. Hughes, S. B. Newcomb and P. K. Hurley

Appl. Phys. Lett., 92, 022902-1-3 (2008)

Growth, ambient stability and electrical characterisation of MgO thin films on silicon surfaces

P. Casey, E. O'Connor, R. Long, B. Brennan, S.A. Krasnikov, D. O'Connell, P.K. Hurley and G. Hughes

Microelectronic Engineering, 86, 1711-1714, (2009)

Table of Contents

Figure Captions

1. Introduction

1.1 Introduction

This introduction will discuss the reasons and justification for this research in terms of the challenges associated with it. The formation of an atomically clean surface and creation of a high quality interface between two materials is a non trivial matter and a number of material considerations have to be taken into account. It will also discuss the properties that make a material suitable for use as a gate oxide, especially in terms of its dielectric constant value and the role it plays in semiconductor devices.

1.2 Semiconductor device parameters

In traditional silicon based semiconductor device technology, the gate oxide dielectric material of choice is silicon dioxide due to its relative ease of production and high quality interface with silicon as it can be grown directly on top of an atomically clean Si surface by thermally controlled oxidation[1]. With the continued drive for faster computer chips and devices, there has been a huge amount of research carried out to produce the optimal device and increase the drive current of the devices to allow for high speed operation[2].

The equation describing drive current at saturation I_{ds} is:

$$I_{ds} = K\frac{W}{L}\left(\frac{(V_{gs} - V_t)^2}{2}\right)$$

where

$$K = \frac{\varepsilon_{ins}\,\varepsilon_0\,\mu}{d} \quad = \mu C_{ox}$$

Here W is the channel width, L is the channel length, V_{gs} is the voltage applied at the gate, V_t is the threshold voltage to invert the channel region, μ is the electron/hole mobility which in turn is given by the velocity of the charge carrier in the channel region divided by the applied electric field, ε_{ins} or k is the relative permittivity or dielectric constant, ε_0 is the relative permittivity of free space, d is the dielectric thickness and C_{ox} is the capacitance per unit area of the oxide.

As a result of this, there are a few possible options to increase the drive current:

1. Reduce the channel length L
2. Reduce the threshold voltage V_t
3. Increase the channel width W
4. Increase the gate oxide dielectric constant ε_{ins}
5. Reduce the thickness of the gate oxide t_{ox} (*d*)
6. Increase the supply voltage V_{gs}

With an increased emphasis on the reduction of power consumption in devices, increasing the supply voltage is not particularly viable and the increased electric field it produces reduces reliability. Increasing the channel width will increase the overall capacitance of the device but it will also use up valuable die space on a semiconductor wafer. Reducing the threshold voltage by lowering the doping concentration of the substrate increases the likelihood of electron punch through between the source and drain,[3] especially if coupled with a reduction in the gate length. This leaves reducing the gate oxide thickness and consequently having to increase the gate oxide dielectric constant.

Currently, the nitrided SiO_2 dielectric layer used in leading edge semiconductor devices is approaching 1 nm in physical thickness. At this dimensional scale, quantum mechanical tunnelling starts to have a significant effect as in n-channel metal oxide semiconductor (n-MOS) devices, electrons tunnel from the channel region to the gate creating a leakage current. This reduced thickness can also lead to a reduced dielectric breakdown voltage and increases the susceptibility to defects and pinholes occurring in the oxide. Because of these effects, SiO_2 based dielectric technology is reaching its physical limits for further incorporation as the sole dielectric material in devices[4]. A reduction in power consumption is a major goal for the semiconductor device industry and at present, it is of greater urgency than the demand to increase processor speed, especially with the increasing emphasis on mobile technology.

1.3 Dielectric constant and alternative high-κ dielectric materials

Increasing the gate oxide dielectric constant above that of SiO_2 (3.9) has the effect of reducing the leakage current and therefore has a direct impact on power consumption.

What this would mean is that for a similar I_{ds}, a thicker dielectric layer could be used which would have an equivalent oxide thickness (EOT) to SiO_2 based on the equation:

$$t_{highk} = \frac{k_{highk}}{k_{ox}} EOT = \frac{k_{highk}}{3.9} EOT$$

where k is the dielectric constant. For a material of a k value of roughly 20, a 5nm layer would have the same dielectric properties as 1nm of SiO_2 and would significantly reduce any leakage current.

Replacing SiO_2 is not a trivial matter however and the following criteria have to be addressed before a suitable candidate can be chosen;

1. Thermodynamic stability
2. CMOS process and material compatibility
3. Morphology
4. Interface quality
5. Reliability
6. Permittivity, band gap and band alignment to silicon or other semiconducting materials.

Due to constraints of the semiconductor device fabrication process whereby samples are annealed up to 1000 °C, the dielectric material ideally would be stable at these temperatures and avoid any chemical interaction with the substrate material. It also has to be compatible with other materials that are used in the process, from gate materials (which is one of the reason metal gates are being investigated) to interconnects and the various gases and etching steps that are used along the device processing line. The morphology of the film can impact as for polycrystalline layers the presence of grain boundaries can act as large current leakage paths, so amorphous or fully crystalline layers are desirable[5].

The fact that SiO_2 is grown straight from the silicon substrate by thermal oxidation means the interface can be made to a high quality and strategies to reduce the interface state densities are well developed[6]. With high-k materials in general, deposition processes have to be found that can recreate this near perfect interface with comparable concentrations of interface defects to that of SiO_2 on Si. A layer by layer growth like atomic layer deposition (ALD)[7] is probably the most promising candidate to carry this out but it is not without its problems with the potential introduction of impurities from the various carrier gases. Physical vapour deposited layers have been shown to produce the highest quality films however, these processes can potentially roughen the surfaces so work is still needed to identify the best way forward.

Silicon dioxide has been shown to have a working life time as a dielectric of roughly 10 years before failure so a similar level of reliability would be expected of any replacement dielectric material. The fact that silicon based devices have been used and studied for so long and still there are many questions left to be answered regarding many of its characteristics makes it all the more critical that research is carried out on III-V semiconductors and alternative dielectrics to determine their performance characteristics over extended lifetimes.

Essentially, the dielectric constant of any new dielectric material has to be larger than that of SiO_2 and to be electrically compatible with the semiconductor substrate. This study has investigated the properties of three different dielectrics, hafnium dioxide (HfO_2), aluminium oxide (Al_2O_3) and magnesium oxide (MgO). HfO_2 was chosen because it has a good mix of relatively large band gap, ~5.7eV and dielectric constant of 25 which compare favourably to the SiO_2 values of 8.9eV and 3.9 respectively. [8] MgO has a band gap of ~7.5eV and a dielectric constant of 8.9. Although the κ value is only twice that of SiO_2, MgO is chemically very stable so it is possible that it could be used as part of a dielectric stack acting as a buffer layer with a material of higher dielectric constant on top. Al_2O_3 was used due to its well understood atomic layer deposition characteristics as well as having a dielectric constant of ~12. [9]

1.4 Semiconductor materials and properties

Another method of increasing the I_{ds} of semiconductor devices not mentioned above is to increase the mobility of the electrons in the channel region. Since this is an intrinsic parameter of the semiconductor, the only way to do this is to change the semiconductor material being used. Table 1.1 lists the band gap E_g, electron mobility μ_e and saturation velocity υ_{sat} of electrons in the channel region for some common semiconducting materials.

Table 1.1 Band gap, mobility and electron saturation velocity for a selection of semiconductor materials.[10]

	Si	**GaAs**	**$In_{0.53}Ga_{0.47}As$**	**InP**
E_g (eV)	1.12	1.42	0.75	1.35
μ_e (cm^2/V-s)	800	4000	7000	3200
υ_{sat} (cm/s)	8×10^6	8×10^6	7×10^6	1.5×10^7

As can be seen from the table $In_{0.53}Ga_{0.47}As$ (which is lattice matched to InP) has a significantly higher electron mobility than Si and while InP has not got as high a value, this is compensated for with an increase in carrier saturation velocity in the channel. InP also has a larger band gap than silicon and InGaAs which allows for a larger voltage modulation between accumulation and depletion if the Fermi level is mid gap. The native oxides on InGaAs and InP are known to have poor electrical characteristics[11] and have poor insulating properties so the search for other suitable dielectric materials is also a necessary step if they are to be used for future semiconductor device applications.

1.5 Roll of the gate oxide and permittivity

The ability of a material to resist the flow of electrons in the presence of an electric field is predominantly due to the formation of dipoles along the field lines in the dielectric material, a measure of which is its permittivity.[12] Taking for example the description of the metal oxide semiconductor field effect transistor (MOSFET), when a voltage is applied to the gate in order to form a conduction channel region at the semiconductor/oxide interface, the electric field this creates is described by the equation,

$$E = {V_g}/{t_{ox}}$$

where V_g is the voltage applied to the gate and t_{ox} is the oxide thickness between the gate and the semiconductor.

However, the gate voltage is not the same as the voltage on the gate oxide (V_{ox}) due to the difference in work functions between that of the gate material (ϕ_{ms}) and the semiconductor material such that

$$V_{ox} = V_g - \phi_{ms} - \varphi_s$$

where φ_s is the surface potential and is related to substrate surface band bending as shown in figure 1.1.

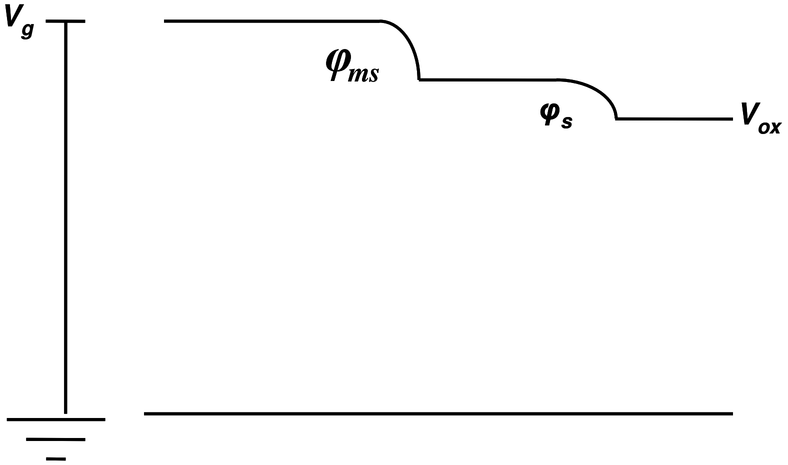

Figure 1.1 Actual voltage across the gate oxide as a result of the gate workfunction (φ_{ms}) and band bending at the substrate surface (φ_s)

This also explains why a lot of work is going into engineering suitable metallic gates[13] which would have a work function matched to that of the substrate and hence reducing the discrepancy between the applied gate voltage and actual voltage across the oxide.

This gives the electric field across the oxide as:

$$E_{ox} = V_{ox}/t_{ox}$$

In a similar way to carriers being attracted to the dielectric/channel interface to oppose the charge on the gate of a transistor, the electrons on atoms in the oxide region also effectively move to oppose the electric field. In this case however they are still bound in their atomic configurations, as opposed to the behaviour of free carriers in the channel region. If we think of the electron configuration in an atom as a cloud of electrons, in the presence of the electron field, the net electron distribution changes from a random distribution around the nucleus, to a situation where there is a shift in charge distribution which forms a dipole. We can then take the total number of atoms in the oxide as a collection of dipoles uniformly lined up with their net dipole moment set up in opposition to the direction of the applied electric field. [14]

Taking for example the description of the MOSFET; when a voltage is applied to the gate, the electric field this creates in order to form a channel region at the semiconductor/oxide interface acts across the entirety of the oxide region. In the presence of this electric field, the electrons in the atoms shift their position to oppose the electric field. What this effectively does is to rearrange the charge so that a dipole moment is formed in each atom with the net displacement between the positive nucleus and the negative electrons given as *D* and the degree of polarisation this causes in the oxide region is given by *P*. It is the interaction between the dipole moment and the electric field that defines the performance of the dielectric such that

$$D = \varepsilon_o E_{ox} + P$$

The value given to the degree that a medium is affected by an electric field is called permittivity with units of Farads per meter (F/m) and is given the symbol ε.

In an isotropic material, i.e. a material showing good crystal structure, D and E are parallel vectors and ε is a scalar describing their interaction where typically ε can be expressed as

$$\varepsilon = \frac{1}{\mu v^2}$$

where μ is the magnetic permeability in the medium and v is the phase velocity or frequency of oscillation of the electric field.

When this is applied to a vacuum, it gives the term ε_o, which describes the permittivity of free space and can be calculated as:

$$\varepsilon_o = \frac{1}{c^2 \mu_0}$$

where c is the speed of light in a vacuum and μ_0 is the magnetic constant or permeability of free space which describes the magnetic field in a vacuum in terms of the magnetic flux density. This gives a value for ε_o of 8.854 F/m (or $A^2s^4kg^{-1}m^{-3}$)

The degree of polarisation P of a material can then be described as:

$$P = \varepsilon_o \chi_e E_{ox}$$

where χ_e is the electron susceptibility and describes how easy it is to polarise a material in an electric field. The electron susceptibility of a vacuum is 0. This can be modified to express the relative permittivity of a given material $\varepsilon_r = 1 + \chi_e$.

To work out the total displacement current induced by the electric field, we must then take into account the vacuum and material contributions

$$D = \varepsilon_o E_{ox} + \varepsilon_o \chi_e E_{ox} \text{ or } D = \varepsilon_o E_{ox}(1 + \chi_e)$$

and since $\varepsilon_r = 1 + \chi_e$ and $\varepsilon = \varepsilon_r \varepsilon_o$, this allows us to describe the displacement current as

$$D = \varepsilon_o \varepsilon_r E_{ox} = \varepsilon E_{ox}$$

This is a simplified description as it does not take into account the frequency dependence of the electric field. As stated earlier $\varepsilon = \frac{1}{\mu v^2}$, so there is an inverse square relationship between permittivity and frequency due to the fact that the material response to the frequency is not instantaneous and this introduces a phase difference in the polarisation. In order to express this, the permittivity can be described by a complex function, such that $\varepsilon \rightarrow \hat{\varepsilon}(v)$ and $D = \varepsilon E$ becomes

$$De^{-ivt} = \hat{\varepsilon}(v) E_{ox} e^{-ivt}$$

where $-vt$ is the change in frequency over time or the phase shift (δ). Separating this equation into its real and imaginary parts so that

$$\hat{\varepsilon}(v) = \frac{D}{E_{ox}}(\cos\delta - i\sin\delta)$$

allows us to associate the real part with the energy stored in the material (since when $\delta = 0$, $\varepsilon = D/E_{ox}$) and the imaginary part as the energy lost within the medium.

At low frequencies as $v \rightarrow 0$, the permittivity begins to act as if it were in a static electric field, giving a relationship for the static permittivity of $\varepsilon_s = \lim_{v \rightarrow 0} \hat{\varepsilon}(v)$ which is the lower limit of the material's permittivity.

At high frequencies, the polarisation response time of the material can become too slow to compensate for the fluctuations in the field and as a result a large phase shift is introduced increasing the energy loss to such an extent that the region can start to act like a metal, causing the high-κ layer to break down due to the increased probability of electron collisions and the generation of free electrons, which in turn can generate more free electrons, inducing an avalanche type effect.[15]

Typically, the frequency of operation for CMOS devices in the $10^8 - 10^{10}$ Hz range as this is a region where very little intrinsic loss in the material is experienced and a range of constant permittivity is seen as the polarisation is able to track the changes in the field. The losses are essentially due to the time dependant response of the material to the electric field above which the material is no longer able to track the fluctuations in the field with the ionic response time typically on the order of 10^{12} Hz as shown in figure 1.2.[16]

The complex permittivity in terms of frequency and relaxation time τ of the material was developed by Debye and states that

$$\hat{\varepsilon}(\nu) = \varepsilon_\infty + \frac{\varepsilon_s - \varepsilon_\infty}{1 + i\nu\tau}$$

where ε_∞ is the permittivity at the high frequency limit.

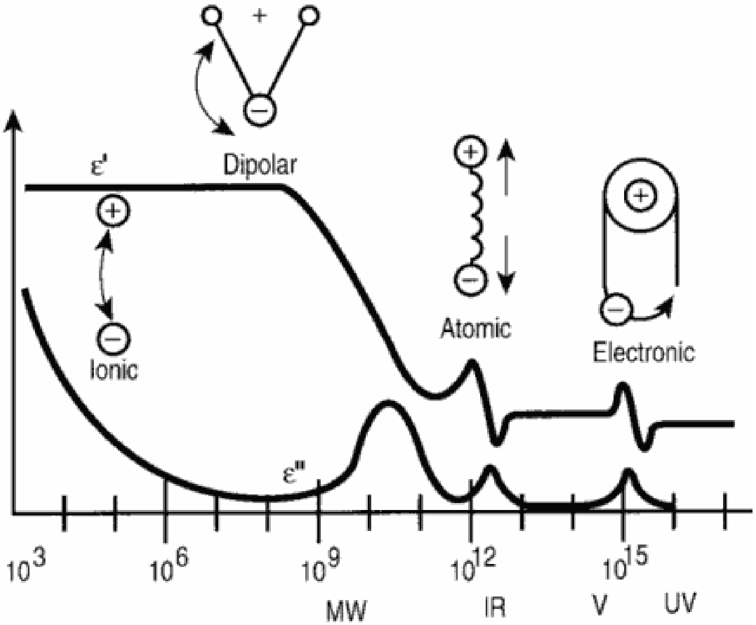

Figure 1.2 Frequency dependence of permittivity highlighting the frequency ranges over which the various atomic properties dictate the permittivity values[16]

In order to determine the amount of energy stored in the electric field, we can apply Gauss's Law, which describes the distribution of electric charge in an electric field, in terms of the displacement current

Gauss's Law in differential form can be written as

$$\nabla \cdot E = \frac{\rho}{\varepsilon_0}$$

where ∇ describes the divergence of the field and ρ is the charge density in C/m^2.

The total potential energy U stored in a material is related to the integral of the charge density with respect to the total volume of the material such that

$$U = \frac{1}{2} \int_{Volume} \rho(r) V(r) d^3 r$$

where $V(r)$ is the voltage at a particular position (r) in the material.

This can be simplified for a given volume to give the expression

$$U = \int_V \frac{1}{2} \varepsilon \left| E_{ox} \right|^2 dV$$

or

$$U = \frac{1}{2} \varepsilon \left| E_{ox} \right|^2 \text{ per unit volume}$$

As long as the threshold voltage V_t needed to form an inversion layer at the semiconductor oxide interface still falls within the "good design rule"[*] of $V_t / V_g \leq 1/5$ to guarantee a good drive current and acceptable noise level, the voltage on the gate can be reduced, thereby reducing the power consumption of the device.

The degree of polarisation of a material is generally seen to scale with atomic number due to the increased dipole strength formed when a large number of electrons move relative to the nucleus in the presence of an electric field in comparison to lighter materials, as long as there are no available states in the conduction band which would allow charge transport directly though the material. [14]

However there are some factors that impact on the value of a material's dielectric constant. For example in the presence of an electric field, the dipole moment does not

---

[*] this ratio is for silicon based devices and so would be expected to scale for III-V devices which can have a higher carrier concentration and mobility and hence a lower V_t

necessarily line up parallel to the electric field vector, which reduces the overall magnitude of the displacement current vector. Also, in ionic materials, the presence of an electric field can cause distortions to the positive and negative planes in the material, creating an ionic dipole that acts in different directions depending on the crystal orientation. The resultant field vector can be added to the vector formed due to the displacement current and can cause a reduction in the permittivity. This also tends to scale with atomic number due to the increased atomic radius and hence plane separation with larger elements. While it is not very significant in most metal oxides, it is the largest contributing factor in perovskite crystals of TiO_3 based oxides where displacement of Ti ions can lead to some of the highest dielectric constant materials currently attainable. [17]

It must also be noted that high-κ materials from higher atomic number elements are not always the most suitable materials for use in semiconductor devices as the increase in atomic number is generally accompanied by a decrease in band gap.[12] Due to the increased number of electron orbitals available for higher atomic number elements, during oxide formation some of the orbitals are left only partially filled, creating electron transition pathways with lower energy than that defined by the conduction band – valence band offset, causing increased leakage currents and effectively rules out the use of TiO_3 based materials with extremely high-κ values. Therefore a trade off is necessary to find a suitable material with a high enough dielectric constant to make it favourable for use in devices but a wide enough band gap to inhibit charge carrier transport.

1.6 Tunnelling Currents

Two distinct types of tunnelling currents take place across the gate oxide dielectric, Fowler Nordheim (F-N) tunnelling and direct current (DC) tunnelling.

F-N tunnelling is caused due to the presence of the electric field and forms the principle for field emission. As mentioned earlier, in the presence of an electric field, electrons can be induced to travel across the barrier region at the semiconductor oxide interface, from the conduction band of the gate material through a triangular barrier dependant on the barrier height to the oxide and from there to the substrate[18] as shown schematically in figure 1.3.

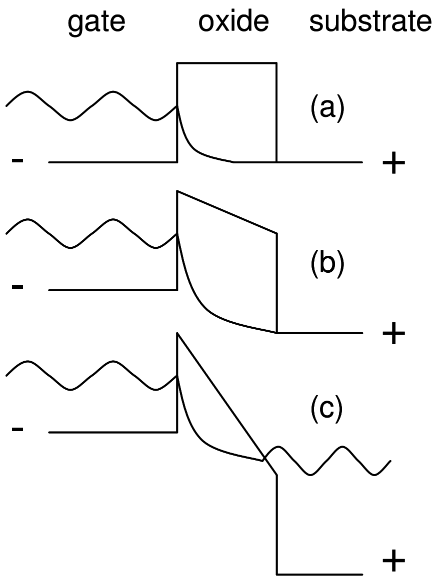

Figure 1.3 With no voltage applied to gate (a) electrons unable to tunnel through oxide, applying a voltage to the gate (b) begins to form a triangular barrier region and with increasing gate voltage (c) onset of F-N tunnelling where electrons are able to tunnel through the narrower triangular barrier region

Direct current tunnelling is a quantum mechanical effect based on the probability of an electron appearing on the opposite side of a barrier region quantified by the Schrödinger Wave Equation. This level of tunnelling is strongly dependant on the thickness of the oxide region, with an exponential decrease in current seen with increased thickness.

The F-N tunnel current density (J_{FN} with units: A/cm^2) can be described by the equation:

$$J_{FN} = \left(\frac{q^3 E_{ox}^2}{8\pi h \phi_B} \right) \exp\left(\frac{-8\pi \left(2m_e^*\right)^{1/2} \phi_B^{3/2}}{3hqE_{ox}} \right)$$

where q is the charge on an electron, m_e^* is the effective mass of an electron in the band gap of the oxide, ϕ_B is the barrier height at the oxide semiconductor interface and *h* is Planks constant.

Rearranging this leads to:

$$\ln\frac{J_{FN}}{E_{ox}^2}=\ln\frac{q^3}{8\pi h\phi_B}-\frac{-8\pi\left(2m_e^*\right)^{1/2}\phi_B^{3/2}}{3hqE_{ox}}$$

which can be used to calculate the barrier height of the material, where the slope, m, of $\frac{J_{FN}}{E_{ox}^2}$ Vs. E_{ox}^{-1} gives:

$$\phi_B^{3/2}=\frac{3hq}{8\pi\left(2m_e^*\right)^{1/2}m}$$

The DC tunnelling current density J_{DT} through the oxide can be expressed as:

$$J_{DT}=\frac{q^2}{2\pi ht_{ox}^2}\Phi\exp\left(\frac{-8\pi}{h}\left(2m_e^+\right)^{1/2}t_{ox}\Phi^{1/2}\right)$$

where m_e^+ is the effective mass of direct tunnelling electrons, t_{ox} is the thickness of the oxide and

$$\Phi=\phi_B-\frac{E_{ox}t_{ox}}{2}$$

which, similar to the slope from J_{FN} can be used to calculate m_e^+, the effective mass of electrons. These equations show the strong dependence on oxide thickness and barrier height at the interface.

Both mechanisms are dependant on the magnitude of the electric field and the barrier height and while both tunnelling regimes are seen to take place concurrently, direct tunnelling is the predominant tunnelling mechanism for SiO_2 oxides below 3 nm in thickness (and this could scale up to 4-5 nm with reduced band gap high-κ materials), where the current induced by the probability of an electron from the gate appearing on the other side of the oxide is greater than that by F-N tunnelling. Above this thickness, F-N begins to dominate, however DC tunnelling is still evident in SiO_2 up to 5 nm. DC tunnelling can be reduced by using materials with larger band gaps, however, this is just another difficulty in replacing SiO_2 as with a band gap of 9 eV, there are very few materials that possess a band gap of this magnitude and also offer good band alignment to the semiconductor.

1.7 References

---

[1] M.M. Atalla , U.S. Patent 2899344, (1959)

[2] R Droopad, K Rajagopalan, J Abrokwah, M Canonico, M Passlack, Solid-State Electron., 50, 1175, (2006)

[3] Y. Gu, J. S. Yuan, Southcon/96. Conference Record (Cat. No.CH35925), p 390-5, 1996

[4] M.A. Alam, B.E. Weir, P.J. Silverman, IEEE Trans. Electron Devices, 49, 232, (2002)

[5] G.D. Wilk, R.M. Wallace, J.M. Anthony, J. Appl. Phys., 89, 5243, (2001)

[6] C.L. Hinkle, M. Milojevic, B. Brennan, A.M. Sonnet, F.S. Aguirre-Tostado, G. Hughes, E.M. Vogel, R.M. Wallace, Appl. Phys. Lett., 94, 162101, (2009)

[7] R. L. Puurunen, J. Appl. Phys., 97, 121301 (2005).

[8] G. D. Wilk, R. M. Wallace, Appl. Phys. Lett. 74, 2854 (1999)

[9] E.-L. Lakomaa, A. Root, T. Suntola, Appl. Surf. Sci. 107, 107, (1996).

[10] A. Erol, Semiconductor properties Dilute III-V Nitride Semiconductors and Material Systems: Physics and Technology, Springer, 2008

[11] J.E. Stannard, T.A. Kennedy, J. Vac. Sci. Tech., 13, 869, (1976)

[12] A.K. Jonscher, Dielectric relaxation in solids, Chelsea Dielectrics Press, (1983)

[13] S. Matsuda, H. Yamakawa, A. Azuma and Y. Toyoshima, 2001 Symposium on VLSI Technology. Digest of Technical Papers, 63, (2001)

[14] J.R. Hook, H.E. Hall, Solid State Physics, Wiley, (1991)

[15] X. Dong, W.M.T Kong,, Y Xiaoping, L. Mohnkern, P. Seekell, L. Mt. Pleasant, K.G. Duh, P.M. Smith, C. Pane-Chane, Electron Device Lett., 30, 793, (2009)

[16] ©Prof. Kenneth A. Mauritz used under a creative commons licence

[17] A. Korkin, E. Gusev, J. K. Labanowski, S. Luryi, Nanotechnology for Electronic Materials and Devices, Springer, (2006)

[18] D.R. Wolters, H.L. Peek, Solid-State Electron., 30, 835, (1987)

2. Principals of experimental techniques

2.1. X-ray Photoelectron Spectroscopy

The principle analytical tool used in this work is X-ray photoemission spectroscopy and in order to detail the development of XPS as a surface analysis technique, we need first to recognise the discoveries and theories that form the basis for it.

2.1.1. History and development

The emission of electric charge upon illumination of a sample with radiation was first noticed by Heinrich Hertz in 1887[1]. In his experiments he had placed a coil to act as a receiver in close proximity to a spark generator and when the apparatus was exposed to UV radiation, the spark generated was significantly longer than when it was covered by glass. He proposed that since the glass blocked UV radiation from impinging on the sample, this was causing the increase in charge, although he was unable to explain how this was happening.

Around this time, George J. Stoney had proposed the concept of a fundamental unit of electrical charge which he termed the electron and in 1897[2], J.J. Thompson through his work with cathode rays was able to conclusively prove the existence of the electron and put forward a reasonable value for the charge to mass ratio[3].

Max Planck, working on a description for how the intensity of the radiation emitted from a blackbody radiator was dependant on the frequency and temperature of the radiation, discovered that in order to fully represent the data, he would have to introduce a constant to describe the emission spectrum. He hypothesised that the radiation emitted originated from a series of harmonic oscillators and that the intensity of the radiated energy at a given frequency (ν) could be described by the equation

$$I = \frac{2h\nu^3}{c^2}\frac{1}{e^{\frac{h\nu}{kT}}-1}$$

where *I* is the radiated energy per time and area, *k* is Boltzman's constant and h is Planck's constant[4].

Planck was not fully aware of the implications of his quantisation of the energy and spent many years trying to rationalise it in terms of classical theory thinking of it as "a purely formal assumption." It was not really until Einstein put forward his theory for the photoelectric effect that the actual quantisation of energy was proposed as a fundamental concept which eventually underpinned the development of quantum mechanics as we know it today.[5]

Einstein predicted the energy itself was quantised and this could be used to explain why in the photoelectron effect, electrons were being emitted once a threshold frequency was reached. In his model, he described light as being made up of discrete quanta of energy called photons, such that the energy was equivalent to the frequency of the electromagnetic radiation multiplied by Planck's constant or:

$$E = h\nu$$

From this he postulated that if the photon interacted with an electron in the material, there was a probability that the photon could be absorbed, transferring its energy to the electron and giving it enough energy to leave the surface of the material, as described by the equation

$$hv = \phi + E_k$$

where Φ is the total work function of the material, or the energy needed to escape from the material and E_k is the kinetic energy of the electron once it escapes. For this Einstein earned the Noble Prize in 1921.[6]

Here the total work function Φ, can be thought of as the sum of two components, the electron binding energy, E_b and the sample work function Φ_s where E_b is the energy from the electron core level to the Fermi level and Φ_s is the energy from the Fermi level to the vacuum level at which point the electron feels no attraction to the sample. The electron binding energy itself can be thought of as a combination of both initial state (before the electron is emitted) and final state (after emission) effects. Final state effects are due to atomic rearrangements of the atom due to the removal of the electron from its orbital, which allows electrons from higher energy states to drop to the lower energy level transferring the excess energy to another electron potentially leading to, for example, Auger electron emission, or the emission of a photon causing X-ray fluorescence.

Thus, the complete description of the electron binding energy is:

$$E_b = -\varepsilon_k - E_r(k) - \delta\varepsilon_{corr} - \delta\varepsilon_{rel}$$

where – ε_k is the negative of the electron orbital energy, $E_r(k)$ is the relaxation energy and $\delta\varepsilon_{corr}$ and $\delta\varepsilon_{rel}$ are differential and relativistic energy corrections respectively however these last two components are very small and are generally ignored. As such, if no final state effects are observed, it is fair to say that the electron binding energy is essentially just the negative of the electron orbital energy in the atom or $E_b = -\varepsilon_\kappa$.
There are a number of final state effects that can take place aside from Auger emission and X-ray fluorescence, due to the interaction of the atom and electron with neighbouring atoms, unpaired electrons in higher orbitals and valance band and surface interactions. These will be gone into in more detail later when describing XPS spectral features.

Einstein did not however carry out any experiments to prove his theory. This came in 1907 when Innes, using a Rontgen tube fitted with a Pt anode (producing Pt X-rays) and two Helmholtz coils generating a magnetic field to velocity select the electrons emitted from a sample due to the incident X-rays.[7] The electrons were then incident on a photographic plate where their presence was detected and therefore able to fully demonstrate the principal.

A group working under Ernest Rutherford in Manchester were the first to really develop the field of photoemission spectroscopy and this led a number of conceptual breakthroughs with regards to understanding atomic structure up to 1913. They had previous experience of using magnetic fields to deduce electron energies due to work with β radiation spectroscopy and so by replacing the β sources with X-ray generators, Rutherford was able to determine the nuclear nature of the atom in 1911 with the nucleus made up of a positive charge surrounded by negative electrons.[8] The significance of the atomic number[9] was discovered by Mosely in 1913 and the quantised nature of the atom with electrons in orbitals around the nucleus[10] was proposed by Neils Bohr, who had spent some time working with Rutherford.

With the outbreak of the World War I, most scientific research was put on hold and it was not really until the end of World War II that interest in X-ray photoemission began to take off again. Up to this point, high energy X-ray sources were being used with broad line widths and coupled with little advance in electron analysis, the spectra that were being produced were essentially just bands of energy, with band edges representing the binding energy of the electrons. While photoelectron spectra for a number of materials were taken, very little practical information was forthcoming from these spectra and advances in alternative techniques like X-ray diffraction (which typically provided the X-ray sources for the photoemission experiments) were much more useful and providing much more interesting results. In the mid 1920's, a breakthrough in the understanding of the spectra did take place with the independent description of the Auger process of radiationless emission of electrons by atomic reconstructions by Leise Meitner[11] and Pierre Auger.[12]

From around 1946-1950, research in the area was revived by Steinhardt and Serfass and they were instrumental in proposing X-ray photoelectron spectroscopy (XPS) as a viable analysis tool by demonstrating the ability for quantitative analysis of elements in a material by comparing the intensities of the features in the photoemission spectrum.[13] They also put forward the idea of using XPS to carry out chemical analysis on the structure of a material. In order to do this however it was recognised by Kai Siegbahn that it would be necessary to design an apparatus that could resolve the spectra[14] with resolution approaching the line width of the atomic levels (~1eV). Apparatus up to this point were still based around using systems designed for β emission studies similar to Rutherford's early work having line widths greater than 3 eV, however Siegbahn had developed an analyser that would for the first time provide resolution approaching 1 eV and when coupled with an 8 keV Cu Kα X-ray source, was able to produce a photoemission spectrum showing sharp peaks representing the core level position of the electrons as distinct from energy bands that had previously been produced, giving an accurate value for the electron binding energies.[15] Around this time also Henke had introduced the hemispherical electron analyser and a dedicated X-ray source for XPS using lower energy X-rays than the commonly used sources borrowed from X-ray diffraction systems, however he was unable to combine these to provide an improvement on overall resolution. This was due to another realisation by Siegbahn that surface contamination had a major effect on the overall spectra necessitating the use of ultra high vacuum (UHV) systems to control the sample conditions.

The next major breakthrough was the introduction of much softer X-ray sources, principally Al and Mg Kα sources, which were able to provide narrow line widths below 1 eV so that the presence of chemical shifts due to chemical state changes, while reported as early as 1920, were able to be unambiguously verified. The publication of this data[16] in 1968 immediately brought XPS (or electron spectroscopy for chemical analysis, ESCA, as Siegbahn termed it) to the attention of the wider scientific community who started to see the implications and benefits it could have on a wide range of fields. This piqued the interest in a number of commercial vacuum system manufacturers who were willing to build dedicated XPS systems, making the technique available to the wider research community and also helped to refine and improve the overall resolution possible. Kai Seighbahn was awarded the Noble prize for physics in 1981 for his contribution to the development of X-ray photoemission spectroscopy.

2.1.2. Apparatus and setup

The basic set up for a standard XPS system is shown in figure 2.1, consisting of the sample under investigation, a source of X-rays, an electron lens, an electron energy analyser and detection system and an external computer system to display the detector output.

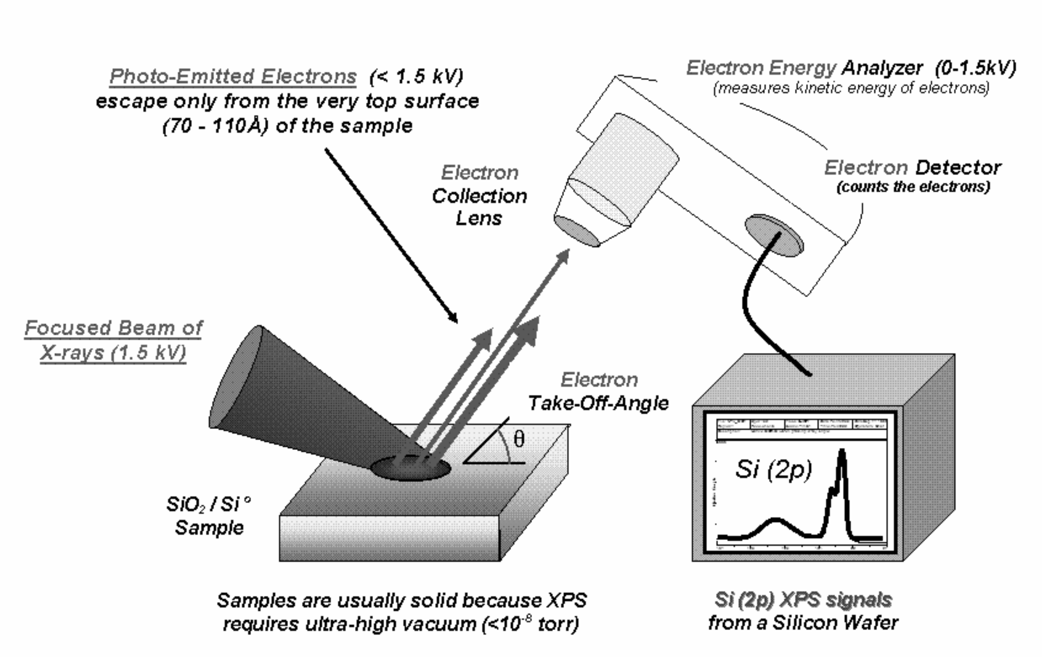

Figure 2.1 Basic configuration and set up of a standard XPS system[17]

The X-ray source in a conventional XPS system, shown schematically in figure 2.2, consists of a copper, water cooled anode target coated with a thin film of aluminium or a combination of aluminium and magnesium that can be selected independently. This is placed in line with a high voltage cathode, typically operating at voltages ranging from 10-15 keV, which bombards the target with high energy electrons. The high electron flux necessitates water cooling of the target due to the high levels of heat generated, which would be enough to evaporate or damage the metal thin films on the surface of the anode.

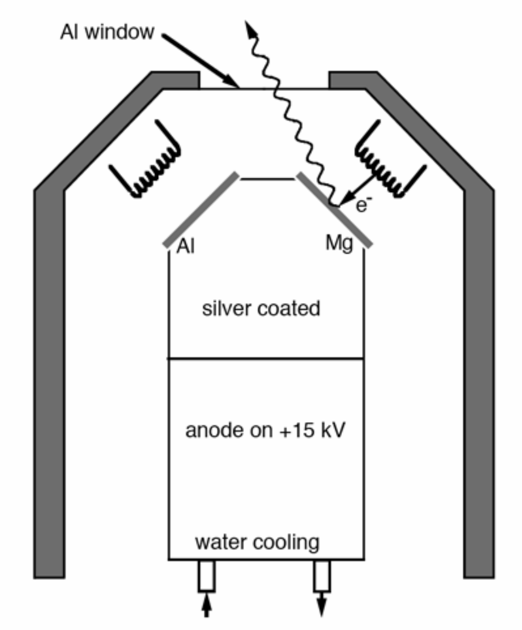

Figure 2.2 Schematic of a twin anode, water cooled X-ray source for XPS

The electron beam generates a continuous Bremsstrahlung energy distribution emission, with a maximum intensity at the Kα transition energy which results from the transition of an electrons from the unresolved Al or Mg 2*p* doublet to the 1*s* core level. For the aluminium target this results in a peak energy of 1486.7 eV with a line width of 0.85 eV and for the Mg target, the value is 1253.6 eV with line width of 0.7 eV. The line width is a reflection of the doublet separation of the 2*p* peak and is a composite of the natural line widths of the $2p_{3/2}$ and $2p_{1/2}$ peaks. For Al 2*p* the doublet separation of the component peaks is 0.43 eV, making it difficult to resolve the individual peak components and so contributes to a broader overall line width. The doublet separation for the Mg 2*p* is significantly smaller than that of the Al 2*p* peak, producing the narrower overall line width. The use of an X-ray monochromator can substantially reduce the X-ray line width for the Al Kα line from 0.85 eV to ~0.3 eV.

Other energy transitions can take place, for example K_β transition from the valence band to the 1*s* levels and transitions from multiply charged atoms, eg. $K\alpha_3$ and $K\alpha_4$ transitions, which can show up as ghost peaks at lower binding energies in the XPS spectra with unmonochromated sources at well known positions relative to the main peak and with intensities ranging from 9.2% to 2% of the principal $K\alpha_1$ emission for the $K\alpha_3$ and K_β transitions, respectively. As mentioned before, there is also a certain amount of Bremsstrahlung radiation generated and in order to filter out most of this, as well as prevent any of the electrons generated in the process from interacting with the sample being analysed, a thin metal foil (Al ~2 μm thick) is placed at the exit of the X-ray source.

Residual Bremsstrahlung radiation which adds to the electron background in the XPS spectra, as well as the satellite peaks can be removed with the use of an X-ray monochromator, which is shown schematically in figure 2.3. Essentially this restricts the range of X-ray wavelengths coming from an Al Kα X-ray source to an energy of 1486.7 eV and a line width of ~0.3 eV. This is done by reflecting the emitted X-rays off an α-quartz crystal orientated in the $10\bar{1}0$ plane with a lattice spacing (d) of 0.425 nm positioned along the Rowland circle of the spectrometer.

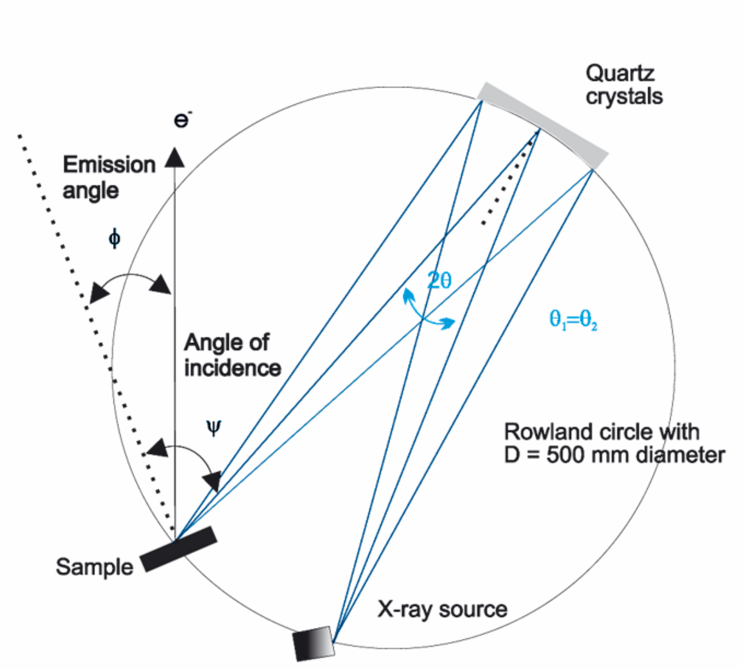

Figure 2.3 X-ray monochromator configuration

The wavelength of the Al Kα line at 1486.7 eV is 0.836 nm calculated from $E = {hc}/{\lambda}$, such that it satisfies the Bragg equation, $n\lambda = 2dSin\theta$ at an angle of 78°. Because this diffraction condition is wavelength specific, the linewidth of the X-rays is no longer determined by the natural linewidth of the transitions from the core levels at the source, but by the small range of wavelengths that are able to satisfy the diffraction equation, resulting in the much reduced line width.The use of a monochromator does reduce the X-ray flux reaching the sample and hence the number of photoemitted electrons, but this can be compensated for with an efficient electron collection lens, energy analyser and multi-channel detection system.

The electrostatic electron lens which is used to collect and focus the electrons coming from the sample into the electron energy analyser is schematically shown in figure 2.4. [18] The acceptance angle of the lens depends on the analyser design and while increasing this angle would increase the overall electron yield it would result in a trade off between the total sampling area with an increased angle taking electrons from a wider surface area. This is especially critical for angular resolved XPS as it would result in electrons with different take off angles being collected creating discrepancies in the apparent electron escape depths. For angle resolved XPS, a small acceptance angle is preferred. The electrostatic lens is designed to generate an electric field which focuses the electrons to a focal point. This is typically carried out twice with the second focal point positioned at the entrance of the electron analyser in order to reduce the spread of the electrons due to the variation in the acceptance angle.

The position of the focal point is determined by the energy of the electrons entering the lens and higher energy electrons will experience a greater interaction with the electric field generated by the lens elements and hence have a different focal point to that of lower energy electrons. In order to overcome this, the electrons first pass through a fine mesh grid, to which a negative potential is applied to retard the electron velocities entering the lens thereby restricting the kinetic energy of the electrons to a range called the pass energy, generally with a value between 5 and 25 eV. As the energy of the electrons to be detected changes, this retardation voltage changes in order keep the pass energy constant right across the spectrum, but this also means that the lens voltages also have to track the changes to the grid voltage carefully in order to maintain a constant focal length as variations in energy of the electrons result in changes to the lens acceptance angle. These issues are generally offset by the benefit reduced pass energy has on the energy resolving power of the XPS analyser as shall be explained shortly.

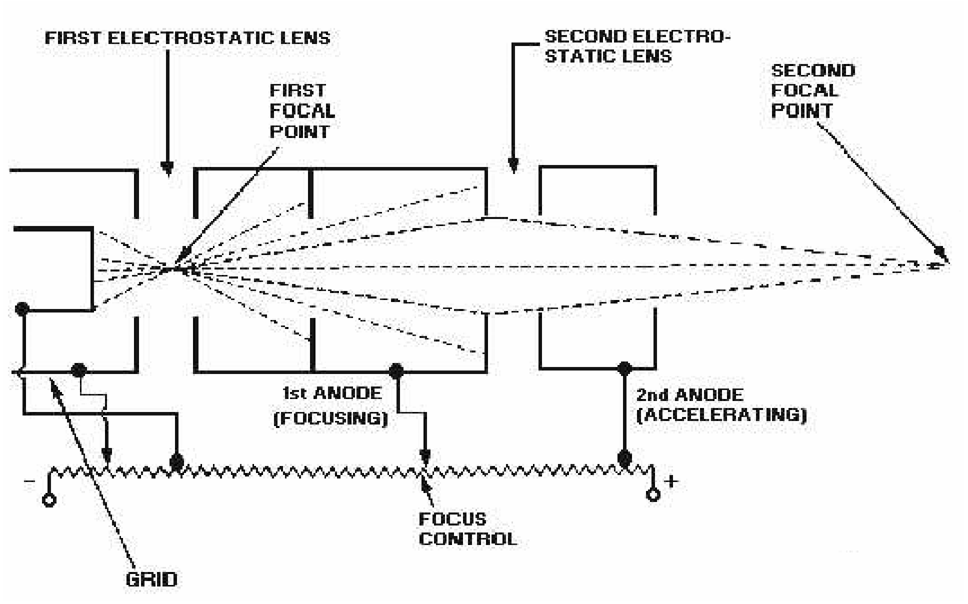

Figure 2.4 Electron lens configuration in a typical electron analyser system

The standard electron analyser is the hemispherical analyser. This basically consists of two concentric hemispherical plates or radius R_1 and R_2 such that the mean radius between the two is R_0 as shown in figure 2.5.

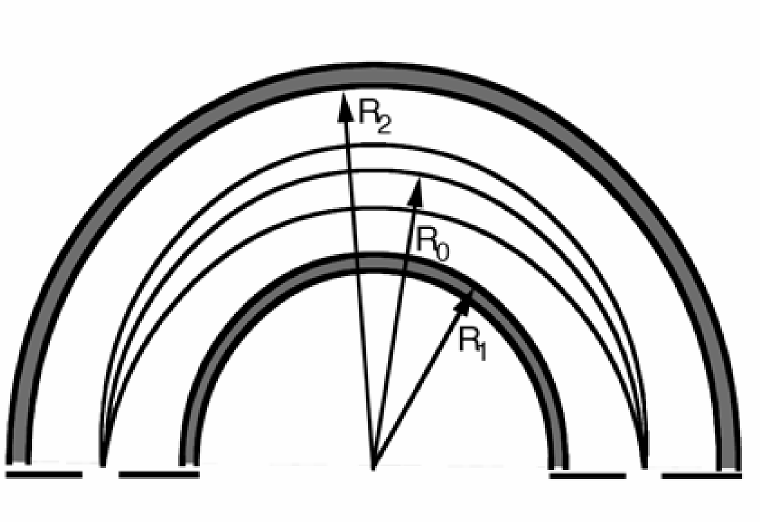

Figure 2.5 Schematic of hemispherical analyser with R_0 the mean distance between R_1 and R_2

As the electrons enter the analyser after being focused by the lens with energy $E_0 = eV_0$, where V_0 is the retardation voltage applied to the grid, the voltage applied to the two hemispheres are adjusted so that only electrons that exactly match the pass energy are allowed to transverse along R_o between the two plates. This is achieved by applying a negative voltage with respect to V_0 to the outer hemisphere (V_2) which repels the electrons and a positive voltage with respect to V_0 to the inner hemisphere (V_1) which attracts the electrons. V_1 and V_2 are related to the radius of the hemispheres by the relationships:

$$V_1 = V_0(3 - 2\frac{R_0}{R_1})$$

$$V_2 = V_0(3 - 2\frac{R_0}{R_2})$$

so that the voltage between the plates is

$$V_2 - V_1 = V_0(\frac{R_2}{R_1} - \frac{R_1}{R_2})$$

and $V_1 = (-1.33)V_0$ and $V_2 = (0.5)V_0$.

As a result the retarded electron velocity is maintained. Electrons with large energy variations from E_0 will be lost to collisions with the hemispheres before they are able to transverse the full distance to the detector.

The remaining electrons are then detected at the end of the analyser by either hitting a channel plate which is able to determine the energy of the electrons depending on where they hit the plate, i.e. the deviation from the expected position for E_0 along the plate, or by the use of a channeltron electron detector which, if there is only one, restricts the energy range around E_0 to a smaller value and hence passes a reduced number of electrons compared to the channel plate as well as a slight decrease in resolution. The channel plate which is essentially made up of series of multipliers orientated in parallel is schematically shown in figure 2.6 as is a single channeltron detector.[19]

The multipliers generally consist of a semiconductor glass tube with a funnel at the entrance to increase the acceptance angle of the electrons coming from the analyser with a length to diameter ratio of roughly 50. A potential difference of 2-4 kV is applied across the channeltron which causes an electron avalanche effect, with each successive collision releasing ever more electrons. In order in increase the number of collisions possible along the length of the tube as well as reduce ionic feedback generated in the collisions, the tube can be curved. The output of the multiplier is then measured as a pulse, providing an electron gain of 10^6 - 10^8 and potential count rates of greater than 10^6 counts per second (c.p.s.). Modern systems come equipped with multi-channel detectors run in series giving significant increases to the count rates and sensitivities possible. The output from the pulse counters is then fed into analysis software that is able to plot the (c.p.s) as a function of the electron binding energy.

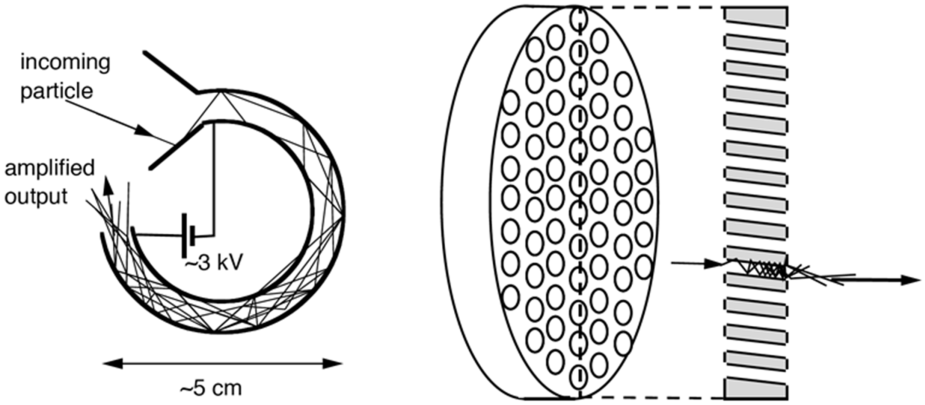

Figure 2.6 Channeltron and channel plate consisting of a series of electron multipliers arranged in parallel

At this point it is worth commenting on the electron binding energy in relation to the XPS system. We know that the Einstein equation ($hv = \phi + E_k$) tells us the kinetic energy an electron will have after it is photoemitted from a sample with workfunction *Φ*. However, once a conducting sample is introduced into the XPS system, we are no longer able to think in terms of the material workfunction. In contact with the spectrometer, the Fermi level of the sample lines up with the Fermi level of the spectrometer by grounding both the sample and the spectrometer. The spectrometer has its own workfunction and this then becomes the potential that the electron has to overcome to reach the electron vacuum level. This means that once the workfunction of the spectrometer (Φ_{sp}) is known, the electron binding energy with respect to the Fermi level can be calculated from the measured kinetic energy of the emitted electrons irrespective of variations in workfunction between different materials based on the equation,

$$E_b = h\nu - E_k - \Phi_{sp}$$

which is represented schematically in figure 2.7.

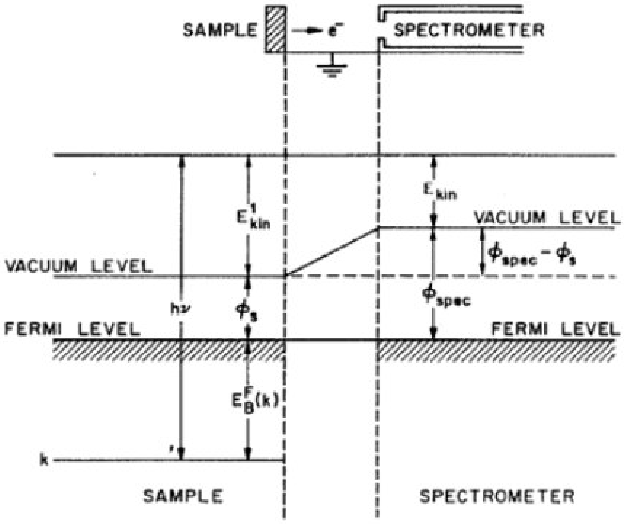

Figure 2.7 Schematic representation of the energy levels of a sample and spectrometer in electrical contact

In the case of insulating materials, where the electrical conductivity of the material is lower than the emitted photocurrent of electrons, the loss of the electrons can cause a change in the charge at the surface, with a net positive charge reducing the kinetic energy of the emitted electrons, resulting in an apparent increase in binding energy in the photoemission spectra. In order to compensate for this, a low energy flux of electrons can be flooded onto the surface, which will not change the overall charge at the surface but will allow the emitted electrons to be easily replaced negating the charging effect. This is mostly seen with monochromated sources as unmonochromated sources, having a larger photon flux and a significant Bremsstrahlung emission which can generate electrons compensating for the charging effects. This is not fully reliable however and generally, photoemission peaks will be charge referenced to a peak with a well known binding energy, for example adventitious carbon, present on most samples introduced from atmospheric conditions with the C 1*s* peak occurring at 284.5 eV. This value is then fixed and the shift in the measured carbon spectra relative to this value is applied to all other peaks.

The energy resolution of the analyser is related to the total energy range over which it operates (E) as well as the ability to resolve peaks with small core level shifts (ΔE), which is termed the absolute resolution. *E/ΔE* is referred to as the resolving power and Δ*E/E* is known as the relative resolution. The factors that ultimately determine these values are R_0 for the analyser, the slit widths entering the analyser (w) and the acceptance angle of the electrons into the analyser (α). These can be written in terms of the relative resolution as:

$$\frac{\Delta E}{E} = \frac{w + R_0 \alpha^2}{2R_0}$$

The typical operation range of the XPS is ~1500 eV with a desired absolute resolution on the order of 0.1 eV for monochromated x-ray sources. Putting these values into the above equation would give an energy resolution of ~ 6.7 x 10^{-5} eV and would require unfeasibly small values for w and α or a very large R_0. This is the reason that the relatively low pass energy of the electrons is necessary for high resolution spectra. If we use a pass energy of 20 eV for the electrons with the same absolute resolution, $\Delta E/E$ comes out at 5 x 10^{-3}, which is readily achievable assuming system parameters of w = 1 mm, R_0 = 0.13 m and an acceptance angle of ~3°.

2.1.3. Systems used

A number of different UHV systems were used throughout the course of these experiments, each with certain benefits over the others in terms of the experimental conditions needed. The first system used shown in figure 2.8, was a dedicated surface science chamber with in-situ thin film deposition techniques and high temperature resistive heating capabilities of the substrate for annealing and surface cleaning purposes. A base pressure of better than 10^{-10} mbar was routinely achieved after a bakeout procedure with pumping carried out by a turbo molecular pump backed by a rotary roughing pump. The chamber could be modified to take either single samples fixed in-situ so that temperatures of >1000 °C could be reached by direct current resistive heating, passing a current through them, or to take samples mounted on sample studs which could be introduced through a load lock allowing for easy introduction of *ex-situ* prepared samples. These samples could also be raised to temperatures of up to 700 °C using modified sample holders. The chamber is equipped with a dual anode X-ray source (Mg and Al) and a VG CLAM electron energy analyser as well as low energy electron diffraction (LEED) optics, a mass spectrometer, e-beam and thermal evaporation sources for thin film deposition and a hydrogen cracker for surface cleaning purposes.

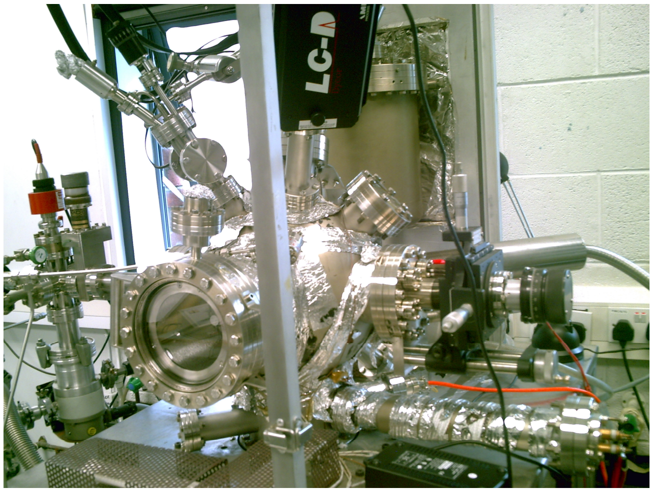

Figure 2.8 UHV surface science chamber equipped with XPS, LEED, mass spec, thermal cracker, e-beam and hot wire deposition systems

The second system in figure 2.9 consists of three chambers (load lock, prep and analysis) to allow for rapid introduction of ex-situ prepared samples to UHV conditions, maintained at 10^{-2} mbar, 10^{-7}mbar and 10^{-10} mbar respectively using diffusion pumps backed by rotary pumps.

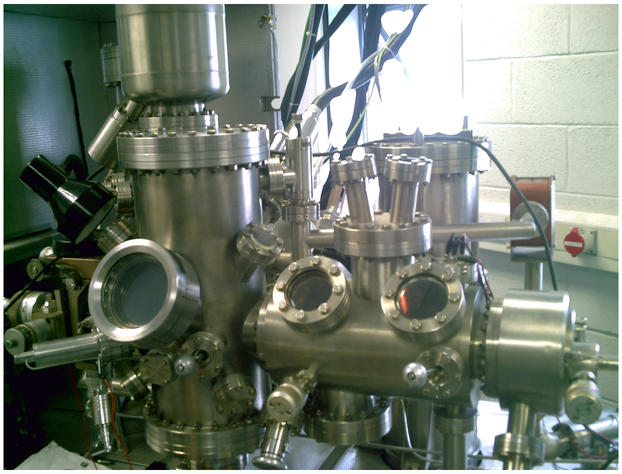

Figure 2.9 Dedicated XPS system with 3 vacuum chambers to allow for rapid sample introduction to UHV

The third system in figure 2.10, located in the National Science and Engineering Research Lab in the University of Texas, Dallas, is a multi-chamber deposition and analysis system equipped with monochromated XPS, UPS, LEED, reflection high energy electron diffraction (RHEED) and ion scattering spectroscopy (ISS) analysis techniques. The deposition techniques include sputter, e-beam, molecular beam epitaxy (MBE), and ALD modules. A UV oxidation facility, hydrogen cracking and annealing capabilities up to 1200 °C were also available for sample preparation. All of these capabilities were *in-situ* at a base pressure of better than 10^{-10} mbar with the system capable of handling samples up to 200mm in diameter.

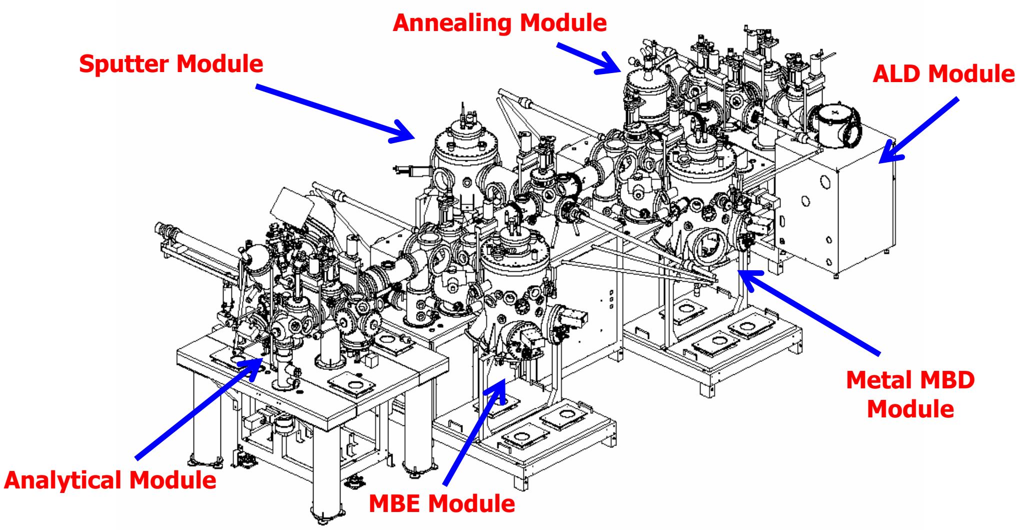

Figure 2.10 Multi chamber analysis and deposition system at the University of Texas as Dallas

2.2. Synchrotron radiation based photoemission

Another method of providing increased resolution and surface sensitivity is by using synchrotron radiation to carry out photoemission studies. This is electromagnetic radiation generated by the acceleration of charged particles, typically electrons, close to the speed of a light in a magnetic field. Synchrotron radiation is characterised by:

- High brightness and high intensity, many orders of magnitude more than with X-rays produced in conventional X-ray tubes

- High brilliance, exceeding other natural and artificial light sources by many orders of magnitude: 3rd generation sources typically have a brilliance larger than 10^{18} photons/s/mm^2/mrad^2/0.1%BW, where 0.1%BW denotes a bandwidth 10^{-3} υ centred around the frequency υ.
- High collimation, i.e. small angular divergence of the beam
- Low emittance, i.e. the product of source cross section and solid angle of emission is small
- Widely tunable in energy/wavelength by monochromatization (sub eV up to the MeV range)
- High level of polarization (linear or elliptical)
- Pulsed light emission (pulse durations at or below one nanosecond)

The machine works by first linearly accelerating electrons and then injecting them into a storage ring which is designed to maintain the electron beam circulating in the ring for many hours at a time. Storage rings are typically made up of a series of straight sections connected in a polygon arrangement. The change in momentum of the electron beam as it negotiates the curved sections results in the concentrated emission of synchrotron radiation at these points. The radiation is extracted through a series of beamlines connected to the ring at these points of centripetal acceleration, bringing the radiation to different user stations where it can be used in a range of different analysis techniques. Broad band radiation is emitted for the accelerated electrons ranging from radio waves all the way up to gamma radiation and through the use of monochromators, specific energy wavelengths can be chosen allowing for the selection of various photon energies for photoemission studies.

At the Astrid synchrotron light source in the University of Aarhus, as schematically shown in figure 2.11 using the SGM1 and SX700 beamlines, photon energies from 30-700 eV can be selected allowing for core level, valence band and workfunction measurements to be taken at a range of surface sensitive energies. Typical flux values are ≥ 10^{10} photons/sec at 130eV which is the optimum surface sensitive photon energy for the silicon 2*p* core level.

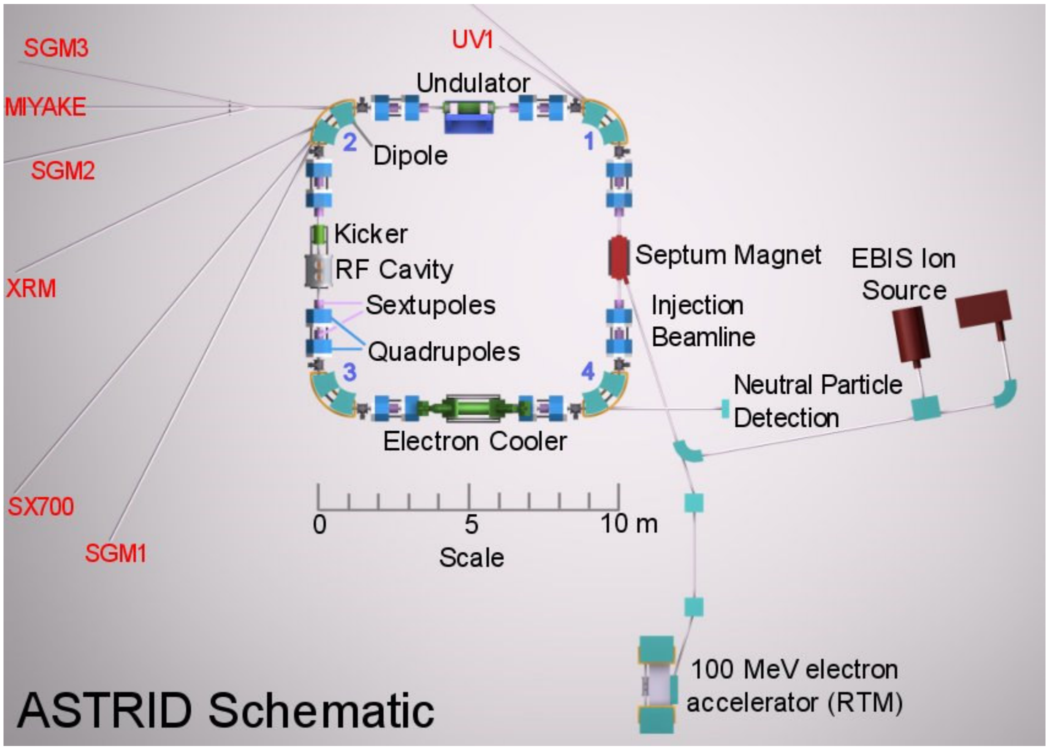

Figure 2.11 Schematic of the ASTRID synchrotron source at the University of Aarhus, Denmark

2.3. Spectral features in Photoemission spectra

2.3.1. Initial State effects

When carrying out XPS analysis of a sample, the first step generally is to undertake a wide energy survey scan from 0 eV to ~1000 eV in binding energy in order to get an idea of the elemental composition of the sample. As described earlier, the photoemission process will cause electrons with specific energies related to the atomic core level binding energies to be emitted. These will show up as intense and narrow peaks in the wide energy scan relative to other spectral features as shown in figure 2.12 for a survey scan from an $In_{0.53}Ga_{0.47}As$ sample. The position of these peaks provide a fingerprint of the chemical make up of the sample as, while some individual peaks might overlap in binding energy position, each element has a unique set of core level binding energies and by comparing a number of these peaks in the survey scan, it is generally possible to identify the overall elemental composition.

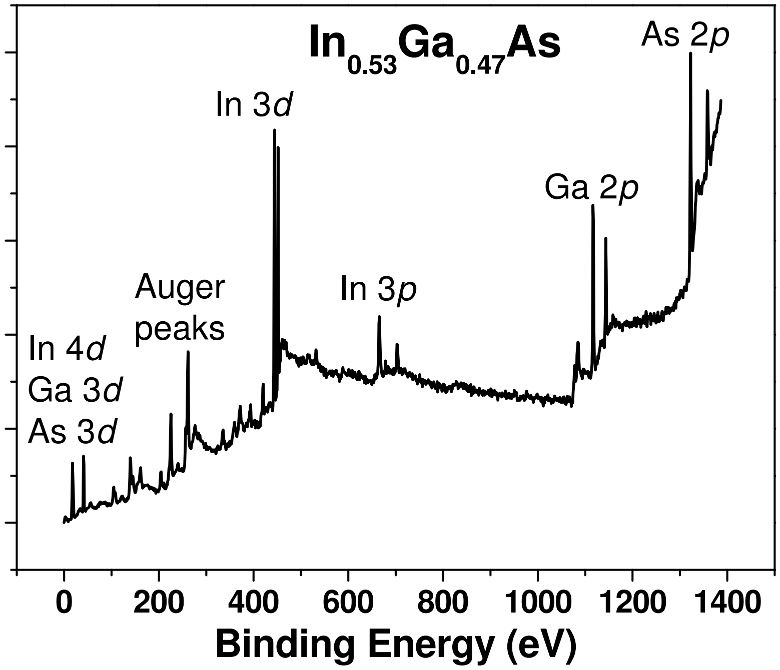

Figure 2.12 XPS survey scan of an $In_{0.53}Ga_{0.47}As$ sample with the principal core level peaks labelled

For most elements, it is also possible to observe Auger electron emission features in the survey scan caused by the transition of a core level electron to deeper lying empty energy level which results in the transfer of energy to another bound electron giving it sufficient kinetic energy to be emitted from the surface. This process is binding energy independent with the energy of the emitted electron only dependant on the energy separation between core levels, so the peaks will always appear at the same kinetic energy position regardless of the incident photon energy making them very useful for element identification. Tables of measured and calculated binding energies for almost all elements are widely available to aid in the identification process.[20, 21, 22]

After identification of the elemental content, narrow scans are carried over smaller energy ranges, typically 10-20 eV, with smaller energy step sizes and larger dwell times in order to better resolve the principle peaks seen in the survey scan for each individual element present. Depending on what material is being analysed, it can be useful to look at different core level peaks from the same element. This is because as the kinetic energy of the photoemitted electrons gets lower, the inelastic mean free path (IMFP) of the electrons in the sample is also reduced. Therefore, the low kinetic energy photoemitted electrons are predominantly coming from the near surface region and provide the highest surface sensitivity. This is highlighted by the curve in figure 2.13 which shows the MFP versus electron kinetic energy for a range of different materials. The increase in MFP below ~50 eV is due to a change in the scattering mechanism at this energy range,[23] predominantly due to surface phonon scattering as opposed to the interaction with conduction electrons at higher energy, such that the highest surface sensitivity is typically achieved for electrons with kinetic energy in the 50-100 eV range.

At a synchrotron source, this can also be achieved by changing the photon energy of the radiation used to generate the photoemitted electrons. Conversely, if more bulk sensitive measurements are needed, peaks with low binding energies are preferable as the higher kinetic energy electrons increase the probability of electrons from deeper in the material being emitted. It is possible to detect the presence of materials with concentration levels of a fraction of a monolayer.

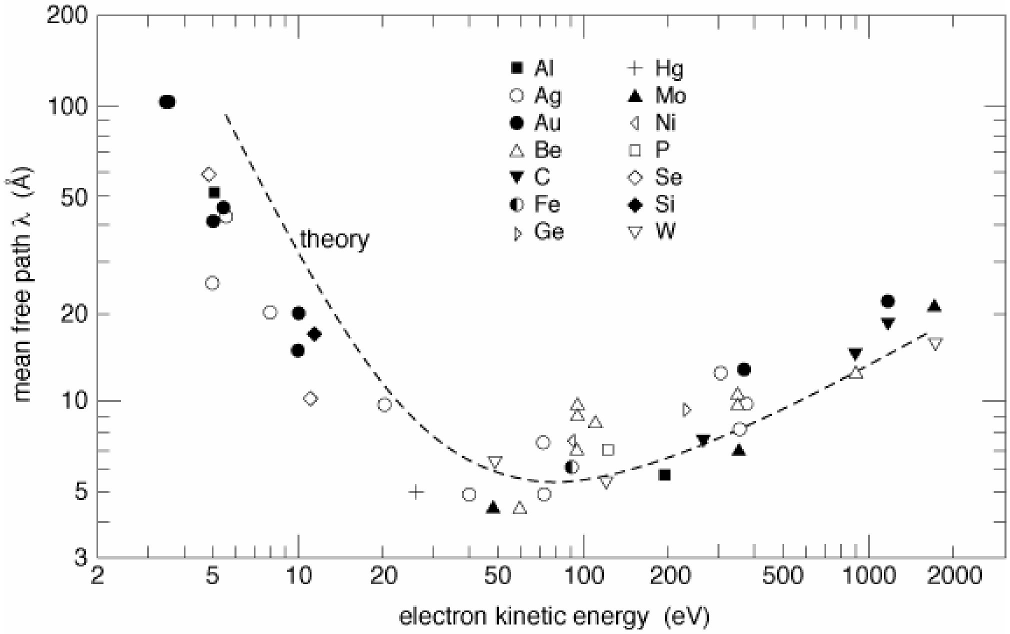

Figure 2.13 Universal curve for MFP for a range of materials showing an increase in MFP with increasing electron kinetic energy (except below ~50 eV)

An important factor to take into account at this point is the spectral peak width. Generally, a photoemission peak will have a peak shape comprising a mixture of Gaussian and Lorentzian components (a Voigt function). The Gaussian component of the peak is determined by the overall resolution of the system, dependant on the instrumental broadening and should therefore be constant for all peaks.[24] However, while there is an effective minimum Gaussian value for a system, due mainly to the FWHM of the X-ray emission line in conventional XPS, this can increase depending on the efficiency of the electrostatic lens to focus the full range of electron energies to the same focal point at the entrance to the analyser and the overall resolution of the analyser. Variations in the electron kinetic energy range can result in changes to the acceptance angle in the lens system due to the ability of higher energy electrons to travel greater distances before the electrostatic field compensates for their motion creating a greater spread in the electron energies once they pass through the focal point.

The intrinsic line shape of the photoemission process is Lorentzian in nature and is related to the lifetime of the core hole after electron emission from the atom. The relaxation time of the atom to shield the emission by filling the core hole dictates the lifetime. The core hole lifetime reduces with atomic number and the closer the atomic level is to the nucleus due to the increased number of electrons available to fill the vacated core level.

The width of the Lorentizain component ΔE_L in eV is related to the core hole lifetime by:

$$\Delta E_L = \frac{h}{e\tau}$$

where h is Plank's constant and τ is the core hole lifetime in seconds so that the width is inversely proportional to the lifetime. Therefore, the Lorentzian peak width will be expected to increase with atomic number and for higher binding energy core levels.
In order to put this into context, for the Ag 3*d* peak with a natural line width of ~0.37 eV, this equates to a lifetime of ~1.1 x 10^{-14} s. If the life time were to decrease by 5 x 10^{-15} s to ~6 x 10^{-15} s, this would increase the Lorentzian value to 0.7 eV, effectively doubling the natural line width.

Individual core level assignments are based on the principal quantum number (n), the orbital angular momentum (*l*), the total angular momentum (j) and the spin angular momentum (s). The orbital angular momentum, *l*, breaks each individual quantum shell into one of four subshells, labelled as either an *s, p, d* or *f* orbital taking values for *l* from 0 to 3 respectively. Two energetically equivalent energy states are possible for the electrons in each of these subshells depending on the direction of the electrons spin, being either a spin 'up' or spin 'down' giving a value for s of ± ½ respectively. The *s* subshell, having an orbital angular momentum value of 0 is termed a closed shell, whereas for the other three, the spin of the electrons can have a magnetic interaction with the orbital angular momentum such that the total angular momentum j can have values with different energies, depending on the direction of the spin, with $j = l + s$ creating a doublet peak. The ratio of the intensity of the doublet components also has different values depending on the subshell, with each peak having a relative intensity value of 2j+1. This is summarised in the table below.

Table 2.1 Principal quantum number assignments for the atomic core levels

Subshell (*l*)	Spin (s)	Total angular momentum (j=*l*+s)	Area ratio (2j+1)
s (0)	±½	+½	-
p (1)	±½	1/2 3/2	1 : 2
d (2)	±½	3/2 5/2	2 : 3
f (3)	±½	5/2 7/2	3 : 4

In general, the separation between the doublet peaks decreases with increasing orbital angular momentum for a given n value so *p>d>f*. The separation also increases with atomic number such that for low atomic number elements in some cases the splitting is too small to actually resolve (<0.5 eV) but can increase to tens of electron volts for high atomic number elements. This characteristic separation is another useful factor in the identification of the specific materials present in a sample.

2.3.2. Final State Effects

Final state effects are also detected in XPS spectra and can also provide useful information regarding the state of the sample in terms of both chemical composition and initial sample conditions. While the majority of these are not seen in the studies carried out in this work, they are commented on to highlight some of the subtleties associated with XPS.

Multiplet splitting occurs as a result of the presence of unpaired electrons in the valence band. If after photoemission an unpaired electron remains in a specific orbital and has the same spin as the unpaired electrons in the valence band, energy exchange can take place resulting in an energy variation between the alternate spin states.
Shake up satellites are caused by a change in the nuclear charge ratio as a result of the loss of electrons from individual atoms during photoemission. This can cause the valence band to reorganise itself, potentially leading to the promotion of an a valence electron to an unfilled state, which upon emission would appear in the XPS spectra with a new characteristic energy at the higher binding energy side of the corresponding peak.

Core level asymmetry in metallic samples can be due to a number of factors but the principle cause is due to the presence of electrons in the conduction band. These electrons are virtually free, able to travel between atoms creating conduction paths and as such do not necessarily have fixed energy values like core level electrons, but rather a continuum of values. As a result, upon photoemission they show up as a low kinetic energy tail on the photoemmision peak due to reduced binding energy they experience.[24]

The conduction electrons can also act collectively, such that they contribute to a group oscillation known as bulk or surface plasmons. Photoemitted electrons passing through these oscillations can experience an energy loss characteristic of the mode of the oscillation by exciting the plasmon, showing up on the higher binding energy side of the peak. Higher harmonics of the oscillations will create peaks at regular intervals above the bulk loss feature. Extremely clean surfaces can also show the presence of surface plasmons peaks which can be used as an indication of the effectiveness of in-situ cleaning techniques as the presence of even a small amount of oxide or organic contamination will rapidly suppress these peaks. Energy coupling between the surface and bulk plasmon feature can also produce less intense spectral features.

2.4. Electron attenuation length and film thickness calculations

Calculations of thin film thicknesses using XPS are inherently linked to the surface sensitivity of the technique. This sensitivity depends on the probability of a photoexcited core level electron propagating through the material and escaping into the vacuum where it can be detected in the electron energy analyser. The typical penetration depth of a 1 keV photon beam is on the order of 10 μm into the material meaning that the photoemission process is able to take place up to this depth. However, the escape depth of electrons of this energy is much smaller, approximately 10 nm, with this distance dependant primarily on the inelastic mean free path and more accurately on the effective attenuation length of electrons in the material so that even though free electrons can be created up to 10 μm into the sample, the probability that they will be emitted from the sample is extremely low.

XPS spectra deal for the most part with electrons that emerge from the surface of the material without having experienced any energy loss in collisions or interactions with other atoms and electrons, as electrons emerging after collisions with random kinetic energies contribute to the photoelectron background. The inelastic mean free path (IMFP) is then defined as the average distance that an electron with a given energy will travel between successive inelastic collisions. For a long time, it was assumed that this was sufficient to describe the depth from which electrons of a particular energy were originating and therefore could be used for the calculation of film thicknesses,[25] however it will be shown later that the IMFP overestimated the actual value by up to 10%, but for the moment it is sufficient to describe the emission of electrons in terms of the IMFP and the correction shall be discussed later.

The IMFP is related to the information depth (ID), or distance into the material from which useful information regarding the core level binding energies can be obtained and is described by the equation:

$$ID = 1 - e^{-\frac{x}{\lambda} Cos\theta}$$

where ID is the fraction of the signal coming from a total depth x, λ is the IMFP in nm and θ is the emission angle relative to the sample normal. Typically for XPS we talk about a sampling or information depth of 3λ as this equates roughly to a depth which provides 95% of the detected signal.

The IMFP itself is dependant on a range of parameters and has been modelled by a number of different equations, two of the most notable being the TPP-M2 formula derived by Tanuma, Powell and Penn,[26] and the Gries formula.[27] Both of these have particular benefits in certain situations and ranges of energies of the emitted electron.

The TPP-M2 equation states that:

$$\lambda = \frac{E}{E_p^2\left(\beta \ln(\gamma E_{KE}) - CE^{-1} + DE^{-2}\right)}$$

where

$$E_p = 18.8\left(\frac{N_v \rho}{M}\right)^{1/2} (eV)$$

$$\beta = -0.1 + 0.944\left(E_p^2 + E_g^2\right)^{-1/2} + 0.69\rho^{0.1}$$

$$\gamma = 0.191\rho^{-1/2}$$

$$C = 1.97 - 0.91U$$

$$D = 53.4 - 20.8U$$

$$U = \frac{N_v \rho}{M} = \frac{E_p^2}{829.4}$$

such that E_p is the free electron plasmon energy, N_v is the number of valence electrons per atom or molecule, ρ is the atomic density in g/cm^3, M is the atomic weight, E_g is the bandgap and E is the excitation energy.

The Gries equation makes a few simplifications on this formula such that:

$$\lambda = \frac{k_1\left(\frac{V_a}{Z^*}\right)E}{\log E - k_2}$$

where

$$k_1 = \frac{5.24\times10^{-5} Z^*}{\beta N_v} = \frac{1.51\times10^{-3} Z^{-1/2}}{M_{tot}^2},\ k_2 = -\log\gamma \text{ and } V_a = \frac{M}{\rho}$$

and Z^* is the nominal number of interaction prone electrons in the atom and takes a value of $Z^{1/2}$ where Z is the atomic number.

The TPP-M2 has been found to be more accurate for bulk elemental solids however it is more straightforward to apply the Gries formula in the general case and in the case of compound materials, the formula can be easily modified to account for changes in the composition by allowing

$$Z^{*} = \frac{aZ_a^{\frac{1}{2}} + bZ_b^{\frac{1}{2}} + cZ_c^{\frac{1}{2}} + \ldots\ldots + nZ_n^{\frac{1}{2}}}{a+b+c+\ldots\ldots+n} \quad \text{and} \quad V_a = \frac{aM_a + bM_b + cM_c + \ldots\ldots + nM_n}{a+b+c+\ldots\ldots+n}$$

for each individual material.

In terms of the XPS spectra, this provides us with a method of determining the thickness (t) of a thin film material from the integrated intensities of the peaks corresponding to the overlayer (I_o) and substrate (I_s) peaks such that:

$$\frac{I_s}{I_o} = e^{\frac{-t}{\lambda Cos\theta}}$$

where $I_{(o,s)} = \frac{I_n}{\sigma_n}$ such that I_n is the experimentally calculated intensity for peak (n) and σ_n is the atomic sensitivity factor for the corresponding peak. This gives a value for the thickness t of

$$t = \lambda Cos\theta \ln\left[1 + \frac{I_o / I_o^{\infty}}{I_s / I_s^{\infty}}\right]$$

where I_n^{∞} is the signal of an infinitely thick layer of material n.

This can be further simplified just in terms of the suppression of the substrate signal with increasing overlayer thickness once the IMFP has been determined by:

$$\frac{I_s}{I_s^{\infty}} = e^{\frac{-t}{\lambda Cos\theta}}$$

A plot of $\ln(I_s / I_s^{\infty})$ versus t will then provide a straight line with a slope of $-1/\lambda Cos\theta$ so λ can be expressed as

$$\lambda = -\left[Cos\theta \frac{d}{dt} \ln\left(\frac{I_s}{I_s^{\infty}}\right)\right]^{-1}$$

which remains constant at a constant θ so that once I_s / I_s^{∞} is calculated, t can be predicted. However, the impact of elastic scattering is not taken into account in these calculations. Elastically scattered electrons are electrons that once photoemitted interact with other atoms and electrons but when scattered experience no net energy loss. This will in general mean that the IMFP overestimates the depth distribution of the electrons it is describing.

It is useful at this point to look at the IMFP in terms of the emission depth distribution function (EDDF) *Φ*, still neglecting the contribution of elastic scattering so that the sampling depth can be described as:

$$ID = \frac{\int_0^x \phi(z)dz}{\int_0^\infty \phi(z)dz} = \frac{\int_0^x e^{-z/\lambda}dz}{\int_0^\infty e^{-z/\lambda}dz} = 1 - e^{-x/\lambda}$$

as we had before, where *x* is the electron escape depth, and for a particular emission angle relative to the surface normal *Φ* becomes:

$$\phi(z) = \frac{e^{-x/\lambda Cos\theta}}{\lambda Cos\theta}$$

With the incorporation of elastic scattering, this can no longer be expressed as an exponential function and *λ* has to be replaced by *l*, the effective attenuation length (EAL) of the electrons.

In this case, the measured values of the integrated intensities for I_s and I_s^∞ from the substrate can be expressed by the equations:

$$I_s = k\int_t^\infty \phi(z)dz \quad \text{and} \quad I_s^\infty = k\int_0^\infty \phi(z)dz = k$$

where *k* is a constant relating to the material.

Substituting these values into the equation so as to replace λ allows us to describe an equation for the local EAL (l_L) at a particular thickness of:

$$l_L = -\left[Cos\theta \frac{d}{dt}\ln\left(\int_t^\infty \phi(z)dz\right)\right]^{-1}$$

Now, unlike the IMFP, this value will vary with thickness of the overlayer so it becomes rather inconvenient to use in practice. Therefore, the equation is modified to ascertain a practical value for the EAL (l_P) based around the extrapolation of the calculated value from a normalised film of zero thickness (no overlayer) to a film of thickness *t*.

$$l_p = \frac{1}{Cos\theta}\frac{0-t}{\ln\left(\frac{I_s^\infty}{I_s^\infty}\right) - \ln\left(\frac{I_s}{I_s^\infty}\right)} = \frac{1}{Cos\theta}\frac{t}{\ln I_s^\infty - \ln I_s} = \frac{1}{Cos\theta}\frac{t}{\ln\int_0^\infty \phi(z,\theta)dz - \ln\int_t^\infty \phi(z,\theta)dz}$$

This value for l_P can then be used for thickness calculations in the same way that the IMFP was used by replacing λ with l_P in the equations.

All this is really just providing values for the effective attenuation length based on models designed to fit the data determined for the values from optical density of states measurements over known thickness ranges of materials and as is the case for the IMFP values, the actual determination of the EAL values are much more complex. This involves finding a solution for the kinetic Boltzmann equation[28] with a transport approximation in order to describe the true nature of the EDDF taking into account the impact of elastic scattering. This involves system specific variables like the photoionisation asymmetry parameters, the range of electron emission angles from the sample, the X-ray to sample surface angle, the atomic density, the IMFP and all its associated parameters as stated previously and the differential elastic scattering cross section, for which individual calculations would have to be made which makes the availability of these models so useful. There are also programs available to carry out the various calculations once information regarding material composition, number of valence electrons, emission and analysis angles, the choice of IMFP calculation method (TPP-M2 or Gries) and sample density are provided, like the NIST EAL database.[29]

The error in the thickness calculations by this method are inherently linked to the error in the quality of the fitted data used to calculate the peak intensities and therefore would typically vary from ~ 2-10 % of the actual film thickness depending on the thickness and quality of the film, with variations in surface uniformity and thin film growth mode impacting on the relationship between the ratio of the overlayer to the substrate.

2.5. Thin Film deposition

The ability to deposit high quality thin films is of critical importance to the creation of devices with high-κ metal oxide dielectric layers. Consideration has to be taken of a number of factors in the growth process to ensure good electrical performance in relation to the potential for interfacial layer creation, defect densities, film uniformity, oxide growth rates and potential for high sample throughput in the manufacturing process. There are a number of viable processes available based around chemical vapour deposition whereby the layer grows by undergoing chemical reactions at the surface of the material, or physical vapour deposition methods, whereby the metal oxide being deposited is grown by evaporation of the metal in a background oxygen pressure, the so called reactive evaporation method.

Three different methods have been utilised over the course of this work; thermal deposition, electron beam deposition (e-beam) and atomic layer deposition (ALD).

2.5.1. Physical vapour deposition

Thermal/hot wire evaporation

In this process, probably the most straight forward methods of depositing a thin film, a material is heated by passing a current through a tungsten filament with the material either suspended or contained in a basket formed from the filament, or contained in a tantalum pouch wrapped in a tungsten or tantalum filament.[30] Metals and metal oxides can be evaporated by this process from high purity (typically >99.9% purity) sources creating high purity thin films. Metal oxide films can also be grown by evaporation of high purity metals in an oxygen background pressure so that the metal fully oxidises either before it reaches the surface or as it grows on the surface.

High vacuum depositions are typically carried out in pressures better than 10^{-5} mbar, while for all of the experiments carried out in ultra high vacuum, the pressure was better than $5x10^{-8}$ mbar. Therefore the depositions can be carried out in a surface science chamber allowing for the sequential analysis of the growth process by XPS or synchrotron radiation photoemission. Growth rates of < 0.1nm per minute are achievable by careful control of the filament current allowing for good precision in terms of controlling the film thickness and >1 nm/s growth is easily achievable for thicker film growth. This method was used for the growth of MgO thin films during the course of this work.

Electron Beam

Similar to hot filament evaporation, this deposition method is as a result of thermal evaporation from a source, however, this time the source of thermal energy is from an electron beam directed at the material sample. The electron beam is generated from a tungsten filament as illustrated in figure 2.14 and is directed onto the sample by deflecting magnets to prevent line of site contamination that could potentially be generated by the filament. Accelerating voltages of up to 5 keV are used to give the electron beam kinetic energy. For the studies undertaken in this work, it was typically carried out at vacuum pressures of <1 x 10^{-5} mbar. The localised nature of the electron beam on the material target allows much higher temperatures to be reached than with resistive heating meaning a greater range of materials, with higher melting points can be deposited. In both of these deposition methods, the metal vapours travel in straight lines from the source so the sample has to be placed directly in front of the material source which is another reason for the placement of the tungsten filament away from the source.

Due to the high temperature generated by the electron beam, the crucible holding the source material is generally water cooled to help dissipate the excess heat generated.

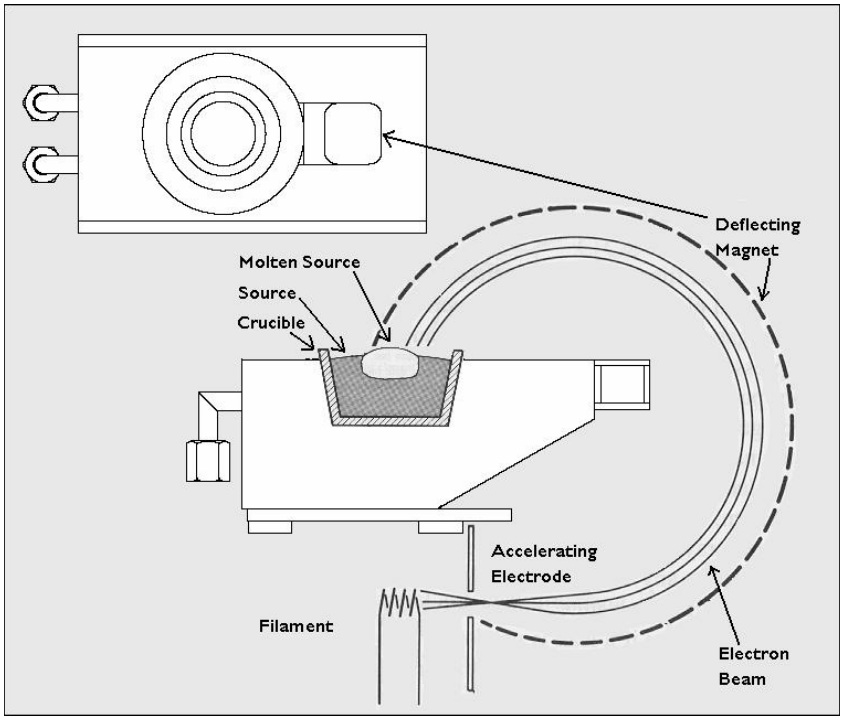

Figure 2.14 Schematic diagram of an e-beam evaporator system

A variation on this method is the micro e-beam evaporator which uses metal wire sources that are placed in the centre of a coiled tungsten filament without making physical contact. The tungsten filament can be at ground potential and a positive voltage is applied to the metal source. This causes electrons to be accelerated towards the tip of the metal creating a localised molten evaporating point allowing for deposition rates of < 0.1 nm per minute by carefully controlling the power generated at the metal tip, shown schematically in figure 2.15.

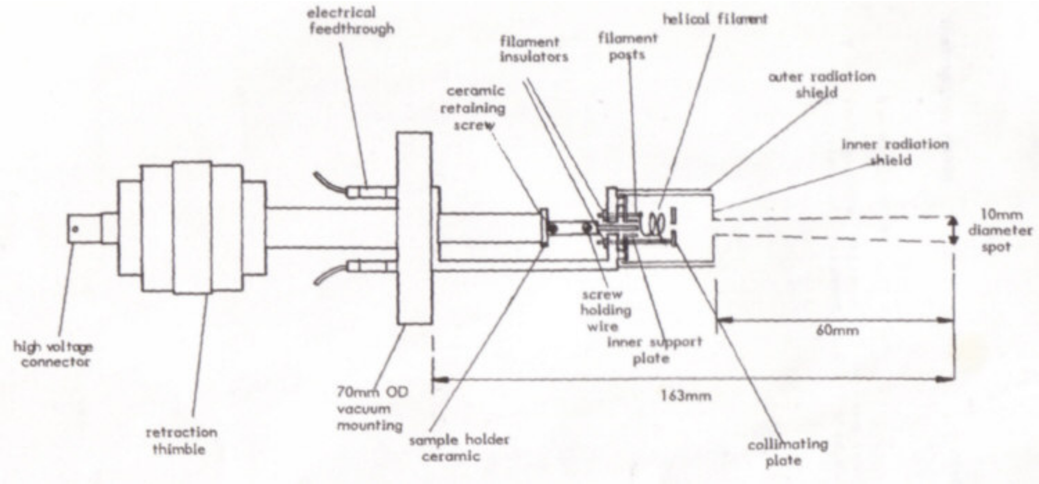

Figure 2.15 Schematic representation of the micro e-beam deposition system

2.5.2. Chemical vapour deposition

Atomic layer deposition (ALD)

Atomic layer deposition is a chemical vapour deposition process distinct from the typical CVD process in that it is a strictly layer by layer growth process with reactions taking place at the sample surface. In the case of metal oxide ALD growth the process consists essentially of a number of cycles of gaseous species which upon interaction with the substrate surface either form a single metallic monolayer reaching saturation once the entire surface is covered or else fully oxidise the surface, again with the oxidation reaching saturation once the metal monolayer is oxidised as schematically illustrate in figure 2.16 representing Al_2O_3 deposition.

Initially, starting with a clean surface (oxide and contaminant free as much as possible) usually hydroxyl terminated, a metal organic precursor is introduced to the ALD reactor, for example tri-methyl aluminium (TMA) $Al(CH_3)_3$ for the growth of Al_2O_3, with the substrate at elevated temperature (200° - 300° C) to increase the reactivity between the surface and the metal precursor. The precursor interacts with the surface hydrogen leaving $Al(CH_3)_2$ bonded to the surface with the release of a methane molecule (CH_4). This process continues until the whole surface is covered with a monolayer of the Al molecule such that no more are able to interact with the surface. At this point the ALD chamber is purged using high purity N_2 to remove all traces of the metal precursor from the reactor. An oxidant cycle then takes place to complete a single monolayer of Al_2O_3, typically H_2O, H_2O_2 or O_3.[31] The general reaction process is a transfer of oxygen to replace the remaining CH_3 molecule bonded to the aluminium with the remaining H again going to the formation of volatile CH_4. This, as well as the remaining oxidant are then purged from the chamber with another cycle of N_2 completing a full ALD cycle.[32]

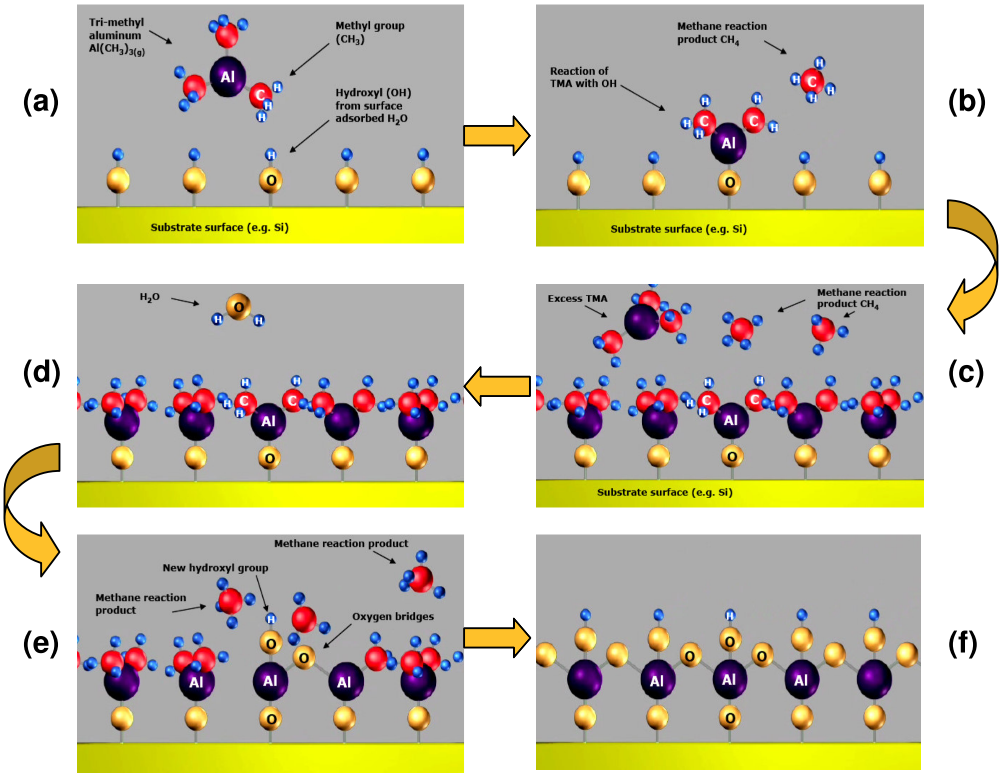

Figure 2.16 Graphic representation of one full ALD cycle starting with (a) a bare substrate, (b) introducing an organo-metallic precursor, (c) saturating the surface with one organo-metallic layer, (d) purging remaining gas and introducing an oxidant, (e) reaction to form a metal oxide and (f) formation of one atomic layer of metal oxide

Due to steric hindrance effects, a full monolayer is not usually formed with a single cycle due to the size of the metal precursor molecule being much larger than the spacing between the surface atoms, so that once a certain number of molecules are present on the surface in close proximity, further interactions are not possible.[33] For this reason typical growth rates are ~0.1 nm per cycle where one monolayer is usually on the order of 0.3 nm, allowing for accurate film thickness control. High surface conformality and uniformity is a characteristic of the ALD process due to inherent surface interactions making it ideal for the deposition of thin films on high aspect ratio structures.

The key criteria for choosing an ALD precursor come down to

(a) high volatility to allow the reaction by-products to be easily removed from the chamber
(b) aggressive surface reactivity to ensure quick cycle times
(c) high purity to reduce the risk of oxide breakdown
(d) minimal self decomposition to ensure that only a monolayer of growth takes place as if the precursor has decomposed before it reaches the surface, it is acting like a normal CVD process and thickness control becomes difficult
(e) relatively inexpensive as a lot of material is used during the growth process that does not contribute to the layer in order to ensure saturation is achieved; non toxic and thermally stable.

Ideally, the reactions at the surface should be exothermic to reduce the risk of interfacial oxidation.

2.6. Atomic Force Microscopy

Atomic force microscopy is a method of imaging the surface of a material with near atomic resolution as well as providing topographical information about the surface. It is more robust than scanning tunnelling microscopy (STM), can easily be operated in air and is suitable for a wide range of materials, including insulators unlike STM, while also providing better resolution and information than many optical based techniques.

When two materials are brought into close proximity, inter-atomic forces are exerted between the two materials. AFM measures the magnitude of these forces, whether they are Van der Waals, electrostatic or magnetic forces, and uses it to determine characteristics of the surface being investigated.[24] The most common mode of operation is measurement of the attractive forces.

Two regimes of operation are possible, contact and non contact and both measure different types of forces. When the tip is in direct contact with a sample, it experiences a repulsive force, whereas when the tip is brought close to the sample without making contact, it will experience an attractive force. The force on the cantilever which holds the tip is related to its deflection via Hooke's law: $F = -kx$, where k is the spring constant of the cantilever and x is the deflection. Values for k can vary from a few tens of N/m down to 0.01 N/m. The type of sample being investigated will determine the type of tip needed with low k values required for soft samples e.g. biological materials, with higher k value tips used for more robust samples.

In the operation of the AFM, the tip is approached to the sample using a stepper motor and finally when in close proximity a piezoelectric motor takes it to its operating position. The sample is then scanned by moving it under the tip using a piezoelectric scanner. As the sample is moved under the tip, the cantilever deforms in response to the interaction forces between the tip and the surface. This is detected by reflecting a laser of the backside of the cantilever arm which is then detected by a four segment photodetector with the position of the laser spot on the detector an indication of the deformation of the tip as indicated in figure 2.17. This coupled with the measurement of the force between the tip and surface allows for an image of the surface to be created.

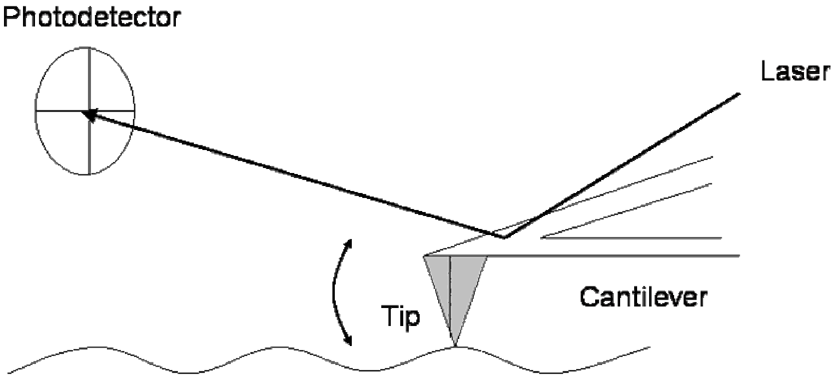

Figure 2.17 Schematic illustration of the operation of the AFM

There are two modes of operation in contact mode; where the tip is in constant contact with the surface and when the tip is oscillated at close to its resonant frequency so that it is just tapping the surface. In the first case, the tip surface can be scanned in two ways, by either keeping the tip position constant and monitoring the deflection in the laser from the tip (constant height mode) or by keeping the deflection from the tip constant, altering the position of the tip relative to the surface as it scans keeping the force between the two constant (constant force mode). The latter of these two is typically used when the initial state and smoothness of the surface is not known as it is not affected by the presence of contamination or rapid changes in the topography of the surface as is the case for constant height mode which can damage the tip. Constant height mode can however provide near atomic resolutions when the sample is known to be atomically clean and flat showing atomic corrugations and steps.

In tapping mode, the frequency of the tip oscillation is kept constant by altering the position of the tip relative to the surface, as with constant force mode, by again monitoring the position of the deflected laser beam. This is even less susceptible to surface contamination, due to less time in contact with the surface, and dramatic changes to topography affecting the scan however if the tip does pick up surface contamination, it can change the resonant frequency of the tip affecting the overall resolution. For softer samples, where physical contact could deform or damage the surface, AFM can be carried out in non contact mode. This again is carried out by oscillating the tip at close to its resonant frequency but instead of modifying the tip position in relation to the repulsive force generated in close proximity to the sample, it takes into account the attractive force, altering the tip position to maintain a constant oscillation frequency. This is the least susceptible mode of operation to surface contamination due to the lack of contact with the surface, however due to the relatively weaker forces involved in the surface interactions, good vibration and acoustic noise isolation is necessary for high quality imaging.

Two different AFM systems during the course of this work; a Veeco Multimode V SPM and a Dimension 3100 SPM equipped with an acoustic and vibration isolation hood and an anti-vibration table to reduce ambient vibrations impacting on the scans. WSxM software was used to plot the spectra and determine surface roughness measurements.[34]

2.7. Atomic Hydrogen cleaning

Molecular gases are typically very reactive and so exposure of oxide surfaces to these, especially atomic hydrogen, under annealing conditions can result in desorption of oxide species from the surfaces at lower temperatures than would be possible with annealing alone. This is especially significant for III-V semiconductor materials as the annealing temperatures needed to remove some of the oxide states for them is typically much higher than the desorption temperature of the group V elements in the material, leading to large levels of defect generation and surface roughening.

In this work, an Oxford Instruments Thermal Gas Cracker (TC-50) was used, which is able to efficiently generate significant amounts of atomic hydrogen at relatively low temperatures (< 1000 °C) and power (~ 50 W) ensuing a low heat load on the UHV system. The operation of the cracker is shown schematically in figure 2.18.

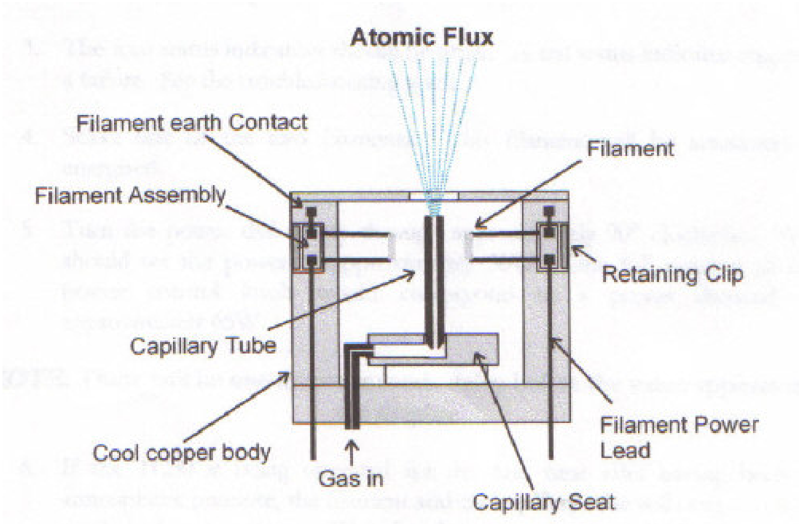

Figure 2.18 Schematic diagram showing the operation of the TC 50 thermal gas cracker system used to produce atomic hydrogen

Hydrogen, equating to a background pressure in the UHV system of 1 x 10^{-7} mbar, is passed through a fine bore capillary tube, connected directly to the gas inlet line. This confines the gas, minimising the gas load while also providing a large surface area and path length for the gas, increasing the efficiency of the cracking. The capillary tube is held at 1 kV so that electrons from a filament at earth potential in close proximity to the tube are accelerated onto it, generating temperatures of > 1000 °C. The emitted electrons can reach a beam current of up to 65 mA, allowing for a total power output of ~ 65W. The power is kept constant throughout by adjusting the temperature of the filament with a feedback loop. Hydrogen molecules hitting the walls of the capillary are thermally dissociated, achieving atomic fractions of ~50%. This atomic flux is then incident on a sample held at elevated temperature (typically 350 -500 °C), for periods of time up to a few hours, which is placed close to the exit aperture of the cracker. The body of the cracker is water cooled to reduce the thermal strain on the UHV system and prevent outgassing.

2.8. References

---

[1] H.R. Hertz, "Ueber einen Einfluss des ultravioletten Lichtes auf die electrische Entladung", Ann. Phys., 267, 983, (1887).

[2] G.J. Stoney, "On the Physical Units of Nature." Philos. Mag. 5, 384, (1881)

[3] J.J. Thomson, Philos. Mag., 44, 293, (1897)

[4] M. Planck, Ann. Phys., 4, 553, (1901)

[5] A. Einstein - On a heuristic viewpoint concerning the production and transformation of light, Ann. Phys., 17, 132, (1905)

[6] Nobel Lectures, Physics 1901-1921, Elsevier Publishing Company, (1967)

[7] P.D. Innes, Proc. Roy. Soc. Ser. A, 79, 442, (1907)

[8] E. Rutherford, “The Scattering of α and β Particles by Matter and the Structure of the Atom.”, Philos. Mag, 21, 669, (1911)

[9] H. G. J. Moseley, M. A., “The High Frequency Spectra of the Elements” Philos. Mag., 1024, (1913)

---

[10] N. Bohr, “On the Constitution of Atoms and Molecules” Philos. Mag. 26, 1, (1913)

[11] L. Meitner, Z. Phys. 17, 54, (1923)

[12] P. Auger, Ann. Phys. (Paris) 6, 183, (1926)

[13] XPS development Thesis R.G. Steinhardt, E.J. Serfass, Ann. Chem. 23, 1585, (1951)

[14] C. Nordling, E. Sokolowski, K. Siegbahn, Arkiv. Fysik., 13, 483, (1958)

[15] S. Hagström, C. Nordling, K. Siegbahn, Z. Phys., 178, 439, (1964)

[16] K. Siegbahn, C. Nordling, A. Fahlman, R. Nordberg, K. Hamrin, J. Hedman, G. Johansson, T. Bergmark, S.-E. Karlsson, I. Lindgren, B. Lindberg, Nova Acta Reg. Soc. Sci. Upsaliensis, 20, 1, (1967)

[17] http://eapclu.iap.tuwien.ac.at/~werner/images/t_exp_pho.gif

[18] D.W.O. Heddle, Electrostatic Lens Systems, Adam Hilger, (1991)

[19] http://eapclu.iap.tuwien.ac.at/~werner/images/t_exp_cha.gif

[20] J. F. Moulder, W. F. Stickle, P. E. Sobol, K. D. Bomben, Handbook of X-ray Photoelectron Spectroscopy Perkin-Elmer Corporation, Physical Electronics Division (1992)

[21] http://srdata.nist.gov/xps/

[22] www.lasurface.com

---

[23] D. Briggs, J. T. Grant. “Surface Analysis by Auger and X-ray Photoelectron Spectroscopy” IM Publications, (2003)

[24] J. C. Vickerman, Surface analysis : the principal techniques, Wiley, (1997)

[25] F.J. Himpsel, F.R. McFeely, A. Taleb-Ibrahimi, J.A. Yarmoff, Phys. Rev B., 38, 6084, (1988)

[26] S. Tanuma, C. J. Powell, D. R. Penn, Surf. Interface Anal., 35, 268, (2003)

[27] S. Tanuma, C. J. Powell, D. R. Penn, Surf. Interface Anal., 25, 25, (1997)

[28] A. Jablonski, C.J. Powell, J. Electron Spectrosc. Relat. Phenom., 100, 137, (1999)

[29] C.J. Powell, A. Jablonski, W.S.M. Werner, W. Smekal, Appl. Surf. Sci., 239, 470, (2005)

[30] J.S. Corneille, J.W. He, D.W. Goodman, Surf. Sci., 306, 269, (1994).

[31] B. Brennan, M. Milojevic, H. C. Kim P. K. Hurley, J. Kim, G. Hughes, R. M. Wallace, Electrochem. Solid-State Lett., 12, H205, (2009)

[32] R. L. Puurunen, Appl. Surf. Sci. 245, 6, (2005)

[33] M. Ylilammi, Thin Solid Films, 279, 124, (1996)

[34] I. Horcas, R. Fernandez, J.M. Gomez-Rodriguez, J. Colchero, J. Gomez-Herrero, A.M. Baro, Rev. Sci. Instrum., 78, 013705, (2007)

3. Characterisation of the native oxides on InGaAs by XPS and synchrotron radiation based photoemission by chemical and thermal modifications of the oxide states

3.1. Introduction

The introduction of high-κ dielectric materials on silicon has allowed for the continued scaling of semiconductor devices[1] in line with the industrial roadmap down to the 45 nm node. However in order to advance further scaling in line with the International Technology Roadmap for Semiconductors (ITRS) it is necessary to look at alternative semiconductor and high-κ material combinations to progress the state of the technology down to the 32 nm node and beyond.[2] With the introduction of high-κ materials, the benefit of using silicon as the basis for the devices is reduced as one of the major advantages of silicon is the relatively facile formation of an extremely high quality SiO_2 interface by thermal processes, with low defect densities and high surface conformality[3]. The integration issues of high-κ materials, apart from the formation of various silicate compounds[4] which have limited κ values, are similar for other semiconductor materials as for silicon. Therefore the possibility for the integration of high mobility semiconductor substrates or layers into devices becomes a viable proposition.[5] This development has the potential to offer an order of magnitude increase in carrier mobility and high transconductance values.[6] One of the major issues with introducing high-κ materials is interface engineering and reduction of interfacial defect states, so it is necessary to develop a suitable passivation technique to keep these defect states to a minimum. [7]

Hydrogen passivation is widely used with silicon based technology to both chemically and electrically passivate the Si surface, where hydrofluoric acid (HF) is used to remove the native oxide and hydrogen terminate the silicon surface[8] reducing the chemical reactivity of the surface preventing reoxidation and electrically passivate the surface defect states which can cause Fermi level pinning, preventing the ability to sweep the Fermi level across the band gap of the Si which is necessary for the realisation of semiconductor devices. However this passivation technique is not a viable option with a lot of other semiconductor materials and especially compound based semiconductors, where different reaction mechanisms take place leading to differential etching rates and surface roughening by removal of certain elements from the substrate.[9] Sulphur passivation has been widely studied on GaAs and InP for many years but even on these substrates there are large variations in the experimental procedures and conditions with little reported apparent agreement on the optimum passivation procedures. Ammonium sulphide based chemicals such as $(NH_4)_2S$ and $(NH_4)_2S_x$ have commonly been used with a wide range of concentrations, passivation times, temperatures and pre-treatments. Results have been reported for passivation times ranging from a few seconds up to 120 minutes and temperature ranges from room temperature to 80 °C. Surface pre-treatments are often widely used, with HF, hydrochloric acid (HCl) and standard organic solvent cleans all being employed. A wide ranging literature survey of parameters varied in the passivation of III-V materials is summarised in the table 3.1 below with references included in the appendix at the end of the chapter.

Table 3.1 Overview of sulphur passivation parameters from literature in terms of time in solution, temperature and sulphur concentration on GaAs, InGaAs and InP

Time (min)	**0.5**	**2**	**5**	**10**	**15**	**20**	**30**	**60**	**90**	**120**
	29	27	1	2	1	16	1	1	1	19
	63		14	11	4	32	6	7		
			15	23	21	42	20	8		
			18	39	22		25			
			40	41	24		34			
			42	70	76		63			
			43							
Temp ℃	**RT**	**30**	**40**	**50**	**60**	**65**	**80**			
	1	1	6	2	1	78	18			
	4	78		42	7		21			
	5				11		24			
	8				14		43			
	10				16					
	14				20					
	18				30					
	23				34					
	25				40					
	39									
	41									
	42									
	63									
S %	**unknown**	**1**	**5**	**6**	**8**	**9**	**10**	**12**	**20**	**22**
	10	3	2	20	34	27	5	42	4	16
	16	18	22	40		29	21		5	32
	23	43	75						19	39
	25								23	
	36								41	
Alt. S	**(NH4)2Sx**	**N2H4-S**	**P2S5**	**S2Cl2**	**H2S**	**NaS**	**SeS**	**ECR**	**Si**	
	1	17	25	26	13	10	9	28	30	
	6			78	28				31	
	7				32				35	
	8				55				37	
	11									
	15									
	24									
	34									
	40									
	78									

Generally speaking, all of these processes show an improvement in device performances and a reduction in defect states relative to devices with untreated substrates.[10] The results therefore highlight that sulphur passivation is an effective procedure at improving the electrical characteristics of devices fabricated on these treated surfaces. However, there is still an underlying lack of understanding as to the most effective treatment, as few systematic comparison studies have been undertaken.[11,12]

Surface and interfacial defects arise from the presence of native oxides, surface contamination and dangling bonds at the semiconductor surface, as well as the presence of Coulomb scattering and surface phonon effects. Electric Spin Resonance (ESR) measurements have shown that the majority of these defects occur at the interface between silicon and high-κ oxides within the first 1 nm,[13] and considering that the active region of typical devices is in this range, it is critical that the interface states are as low as possible.

One of the principal aims of this research is to investigate the effect of ammonium sulphide $(NH_4)_2S$ chemical passivation of $In_{0.53}Ga_{0.47}As$ which is a prime candidate for incorporation into future devices replacing silicon due to its high transconductance and mobility values.[14] While these parameters are not as high as for InAs, $In_{0.53}Ga_{0.47}As$ has been the subject of extensive research due to its use in High Electron Mobility Transistors (HEMT) high power devices[15] and detailed processing protocols exist from this application. It is also a more promising candidate for device applications than GaAs as it has been reported that GaAs and low indium content InGaAs experience significant frequency dispersion preventing true accumulation from taking place which is greatly improved with high indium content InGaAs.[16] As the indium content is increased, the bandgap of the InGaAs is seen to decrease and this has been shown to be primarily associated with a reduction in the conduction band minimum position, effectively increasing the electron affinity value.[17] This has the consequence of moving a defect state present in the top half of the GaAs bandgap into the conduction band of $In_{0.53}Ga_{0.47}As$ rendering it electrically inactive from a device perspective as schematically illustrated in figure 3.1.

This work undertakes a systematic study of the impact of ammonium sulphide based passivation processes on the surface chemical composition and surface topography of $In_{0.53}Ga_{0.47}As$ as both parameters impact on subsequent dielectric growth. XPS measurements give information regarding the level of oxide and ambient contamination remaining on the surface while AFM determines the surface roughness introduced as a result of the processing, however this will be presented primarily in the next chapter.

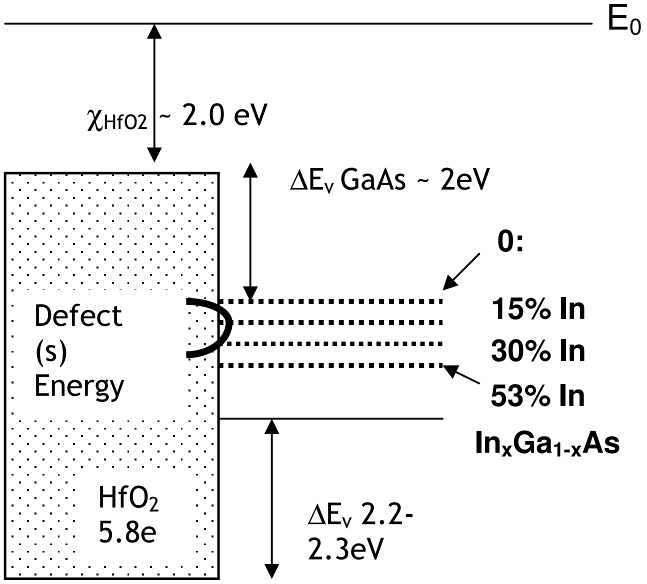

Figure 3.1 Position of defect states in the GaAs bandgap and the position of these states relative to conduction band minimum as a function of indium concentration

In order to fully comprehend what is happening at the surface with $(NH_4)_2S$ treatment, it is first necessary to determine the exact composition of the native oxides present before and after chemical treatment as well as their relative stability, so a systematic study of various surface treatments was carried out. This was coupled with a detailed analysis of the native oxide present on the InGaAs surface before and after thermal annealing. These investigations were undertaken using both conventional XPS and synchrotron radiation based photoemission to provide consistent and repeatable parameters for the peak fitting process. Identification of the various oxidation states present can lead to a better understanding of the effectiveness of the passivation processes investigated. Table 3.2 below details the wide variation in reported binding energy positions of the individual oxidation states of gallium and arsenic, which goes some way to highlighting the difficulty in definitively determining the precise interface chemistry. Again, the references from the table are contained in the appendix at the end of the chapter.

Table 3.2 Peak binding energy separation from bulk peaks from references.

REF	As-As	As_2O_3	As_2O_5	As-S	As-SO	$GaAsO_4$	$Ga(AsO_3)_3$	As-OH	As-H	dimers	As_xO_y
BB *	0.75	3.28	4.44	1.54		5.08				-0.36	1.3, 2.55
5	0.75	2.9			1.7						
6	0.6	3.2	4.5	1.7							
7	0.7			2							
10				4.4							
11	0.7	2.7		1.5							
12	0.7	3.1									
22	0.7			1.44							
23	0.6			1.33							
28		3		1.6							
33	0.88	3.34									
34				-0.7							
39	1	3		2.3							
40	0.24	3		1.5						-0.28, -0.69	
42	0.61			1.1, 1.7						0.4	
44	0.9	3.4	4.9								
45	0.55							3	0.35		
48	0.7	3.2	4.4								2.3
49	0.65	3.63							0.7	-0.6 *	
50	0.63	3.2								-0.42, -0.5	2.8
51	0.5 - 0.7	3.2				4.5		0.9		-0.4	
52	0.6	3.5	4.6							-0.4	
53	0.8	3.2	4.2								2.3
54	0.6										
59											1.7, 2
60		3.2	4.2								
61											
62				1.2							
63	Undisc	Undisc	Undisc								Undisc
67	1	3.9	5								2, 2.9
70	0.6	3.9									2, 2.9
71		3.2	4.2								0.8,
72		4	5.1			5.1	4.8				
77	0.7	3.3	4.5	2.1							

REF	Ga-Ga	Ga_2O_3	Ga_2O/GaO_x	Ga-S	$GaAsO_4$	$GaAs(O_3)_3$	SS	Ga-OH	$In_xGa_yO_z$	GaO_2
BB *		1.1	0.55		2.05				1.6	
6		1.4		0.7						
7				0.55, 1.7						
10			1.5 - 2.5							
11	-0.8	1.4	0.7							
12		1.4								

22			0.85	0.69, 1.72						
23			1.35	0.8						
25		1.9	1.7							
33		1.3								
34				1.8						
39		1.2	0.55	0.75						
42				0.5						
44	-0.6	1.6	1		2.2	1.7				
45							-0.35, 0.35	0.7		
48		1.4	0.7							
49		1.8	1.2							
50		0.85					0.52			
52		1.6					0.3	0.9, 2.2		
53	-0.6	1.6	1					2.5		
60	-0.62	1.6	1					2.5		
62				0.5						
67		2	0.5, 1.2							
69		2								2.9
70	-0.82	1.76	0.5, 1							
71			0.45, 1							
72		1.2			2.1	1.6				
76		1.1	0.55			1.6				
77		1.2		0.7						

REF	In-O	In$_2$O$_3$	In$_x$Ga$_y$O$_z$	In-S	surf	InPO(3,4)	In-In
BB *	0.45	0.8	1.25		-0.65		
20	0.6			0.4			
33		0.9					
47						0.47	
55				0.3			-0.4
56					0.9, 0.58, 0.25		
57		0.25					
58	0.75						
59	0.7-0.8						
65		0.93					
73		0.8				1.5, 1.8	
74		0.7		0.7		1.5	

Because of the complexity of what we are trying to achieve in relation to the identification and consistent curve fitting of the surface oxides on InGaAs, I have had to adopt an approach of cross correlating the results from different surface treatments including annealing, ammonium hydroxide treatment, As decapped samples, ozone oxidation, sulphur passivation and the first cycle in ALD growth because of the reported effects of TMA on the removal of surface oxides. There are no comprehensive investigations in the literature on the identification of the various oxide states of InGaAs, so this broad front approach was used to obtain consistency.

The use of AAnalyzer fitting software for the analysis of the photoemission spectra attained after these thermal and chemical changes to the oxidation states allows for simultaneous fitting of up to 10 spectra at one time, ensuring the maximum correlation of the fitting parameters possible between all the spectra. It systematically applies any variation in the fit parameters seen to develop in one spectra to all the others in the series so that the highest level of consistency possible between them collectively is attained. Confidence in the peak fitting comes from the adoption of this systematic approach in combination with a realistic understanding of what surface chemistry should occur, which has been determined from studies of binary III-V materials such as GaAs and InP.

3.2. Sample preparation and measurement

Samples used in this study were 1 cm x 1 cm pieces cleaved from a single 50 mm diameter wafer which consisted of zinc doped ($4\times10^{17}cm^{-3}$) $In_{0.53}Ga_{0.47}As$ grown by metal organic vapour phase epitaxy (MOVPE) on a heavily doped (Zn ~$4\times10^{18}cm^{-3}$) InP(100) wafer.[18] All samples were initially degreased by dipping in acetone, methanol and isopropanol successively for one in minute each and blown dry in dry nitrogen before being immediately introduced to the next stage in the treatment process.

Ammonium sulphide $(NH_4)_2S$ concentrations of 22%, 10% and 5% in H_2O were used (commercial 22% diluted with deionised water (DIW)) at room temperature (RT ~ 20 °C), 40 °C and 60 °C for periods of 10 and 20 minutes. All samples were then rinsed in flowing DIW for ~10 s following the $(NH_4)_2S$ treatment to remove any residual solution from the surface and then blown dry in N_2. Some samples received a 1:1 HCl to H_2O etch for 10 minutes followed by a 30 second rinse in DIW prior to $(NH_4)_2S$ treatment. Samples were then mounted on a sample stage and introduced to a sample load lock (base pressure of less than 2×10^{-9} mbar) in less than 10 minutes after removal from $(NH_4)_2S$ to minimise both native oxide regrowth and ambient contamination.

XPS analysis was carried using a monochromated Al $K\alpha$ (1486.7 eV) X-ray source with a line width of 0.25 eV and a 125 mm seven channel monchromator at a pass energy of 15 eV in a dedicated analysis chamber at a base pressure of $<2 \times 10^{-10}$ mbar. Spectra were taken of the As 2$p_{3/2}$, Ga 2$p_{3/2}$, In 3$d_{5/2}$, C 1*s*, O 1*s*, S 2*p*, As 3*d*, and Ga 3*d* and In 4*d* regions after loading to UHV and again after a 300 °C in-situ anneal for 30 minutes intended to replicate conditions experienced by the sample under certain deposition conditions. Surface roughness measurements were made using a conventional ex-situ atomic force microscope (Digital Instruments Multimode V) in contact mode with root mean squared (RMS) values determined from software[19] after samples were removed from UHV.

In order to provide a consistent fit for the core level peaks, reference spectra were acquired from an atomically clean $In_{0.53}Ga_{0.47}As$ wafer which had been capped with arsenic, in order to obtain curve fitting parameters. The arsenic cap was removed in situ by annealing the sample to 450 °C for 30 minutes in a liquid nitrogen cooled chamber at pressures $< 10^{-8}$ mbar leaving the surface free from surface contamination with no evidence of carbon or oxygen present within detection limits of XPS. Using the spectra from this sample, Gaussian and Lorentzian bulk peak parameters were determined for the As 2*p*, Ga 2*p* and In 3*d* peaks which were kept constant in all subsequent peak fits.

Reference spectra were also obtained from a sample set containing native oxide, ammonium hydroxide (NH_4OH) etched samples (29% NH_4OH for 3 minutes), as well as the series of samples after various $(NH_4)_2S$ treatments and ozone oxidation to obtain reference spectra. The native oxide samples were also scanned using synchrotron radiation at various photon energies from 69 eV up to 600 eV as well as after sequential annealing in vacuum ranging from 150 °C to 450 °C in periods of 50 °C for 30 minutes and after atomic hydrogen cleaning at a range of substrate temperatures in order to determine fitting parameters for the As 3*d*, In 4*d* and Ga 3*d* peaks as well as looking at the O 1*s*, C 1*s*, In 3*d*, valence band and work function spectra. Native oxides were also scanned using conventional XPS before and after annealing at 300 °C for 30 minutes.

Through modification of the oxide present on the surface by chemical and thermal means, identification of the individual oxide states becomes more obvious, with different oxidation states reacting differently to the varying processes. By initially analysing the as-received $In_{0.53}Ga_{0.47}As$ surface with significant native oxides present the position and peak widths of the largest contributing oxide peaks were determined. Samples were subsequently annealed in vacuum to 300 °C or received a wet chemical treatment in ammonium sulphide or ammonium hydroxide in order to impart changes to the oxides present with the anneal expected to cause thermodynamic changes. After the wet chemical treatment the samples were exposed to one cycle of tri-methyl aluminium (TMA), an organo-metallic precursor used in the ALD process for Al_2O_3 growth and which could be introduced to the sample in-*situ* so that no ambient contamination such as C, O_2 or H_2O could interact with the sample. TMA is known to interact preferentially with certain oxidation states which can give further information regarding the nature of the oxides present on the surface and help in the development of a more accurate peak fit. The cause and nature of these interactions is only alluded to here but shall be discussed in more detail in subsequent chapters.

An $(NH_4)_2S$ treated sample was also exposed to ozone (O_3), a known strong oxidant which was used to significantly oxidise the surface and again provide more information regarding the nature of the oxidation states present.

The fitting procedure was an iterative process whereby all peaks were fitted concurrently with peak widths initially fixed to the values determined from the decapped sample. The peak width of all oxide peaks were allowed to vary as the level of oxide present changed as a result of the various chemical and thermal processes. Both Gaussian and Lorentzian contributions to the lineshape were correlated as well as the peak separation from the bulk component. A Shirley type background was employed for all peaks which was modified to account for the secondary electron cascade background at low kinetic energy in the case of the As 2*p* and Ga 2*p* spectra as well as for certain SRPES spectra where the electrons were emitted with low KE.

The residual (number of counts by which the fit differs from the actual experimental data), was required to be within the noise of the data with fit error being less than 3% of the experimental counts and χ^2, a standard measure of “goodness of fit” via a Pearson’s chi-square test,[20] was required to be less than 10^{-4}. These values are much stricter than usual errors in peak fitting as found in studies by Seah and Brown[21] as well as Conny *et al.*[22]. In addition to using the residuals and the χ^2 measures for fit accuracy, a rigorous analysis of all relevant spectral regions (As 2*p*, As 3*d*, Ga 3*d*, O 1*s*, C 1*s*, In 3*d*, In 4*d*) is performed to ensure a self-consistent analysis. The final criterion for the peak synthesis analysis is that any state identified within the spectral envelope must be explained in terms of the electronegativites of possible bonding arrangements. Initially the spectra were fitted with the minimum number of peaks and additional peaks were only added when it was clear that the spectra could not be fitted without their incorporation after investigating variations in peak widths and positions. Similar to the study carried out by Hinkle *et al.* [23] on the detection of various gallium oxide components in XPS spectra of GaAs with a high level of accuracy, this study tries to investigate the origin of various oxidation states of arsenic and indium as well as those seen for gallium. All peak fitting was carried out using AAnalyser software.[24]

3.3. Oxide modifications by chemical treatments

3.3.1. Oxide free reference surface

The XPS spectra from the As $2p_{3/2}$, Ga $2p_{3/2}$ and In $3d_{5/2}$ core levels of InGaAs after various surface treatments and processing procedures are shown in figure 3.2. Clearly, there are significant variations evident between the different spectra highlighting the complex nature of the binary and ternary oxide phases of the peaks[25] making accurate determination of the various oxidation states difficult.

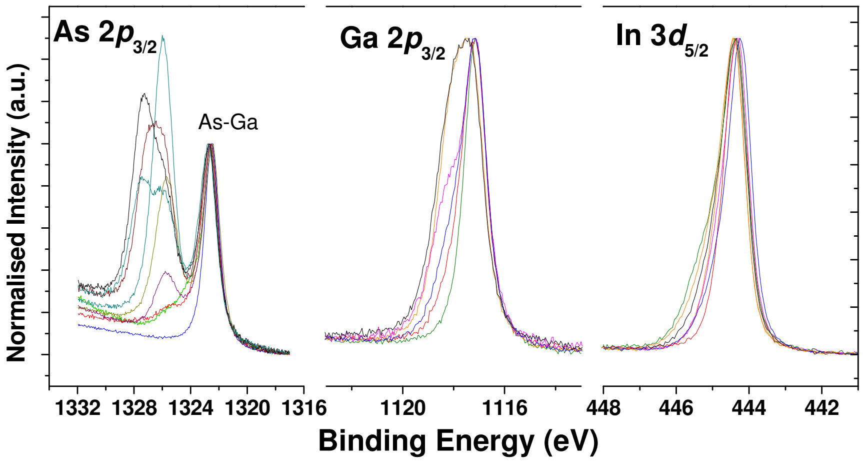

Figure 3.2 Core level spectra from a number of $In_{0.53}Ga_{0.47}As$ samples after various processing conditions and surface treatments highlighting the complex nature of the oxides present

From the arsenic capped sample, it was possible to determine the peak parameters of the oxide free surface once the arsenic cap was removed by annealing in vacuum as shown in figure 3.3 for the peak fitted As 2*p*, Ga 2*p* and In 3*d* spectra.

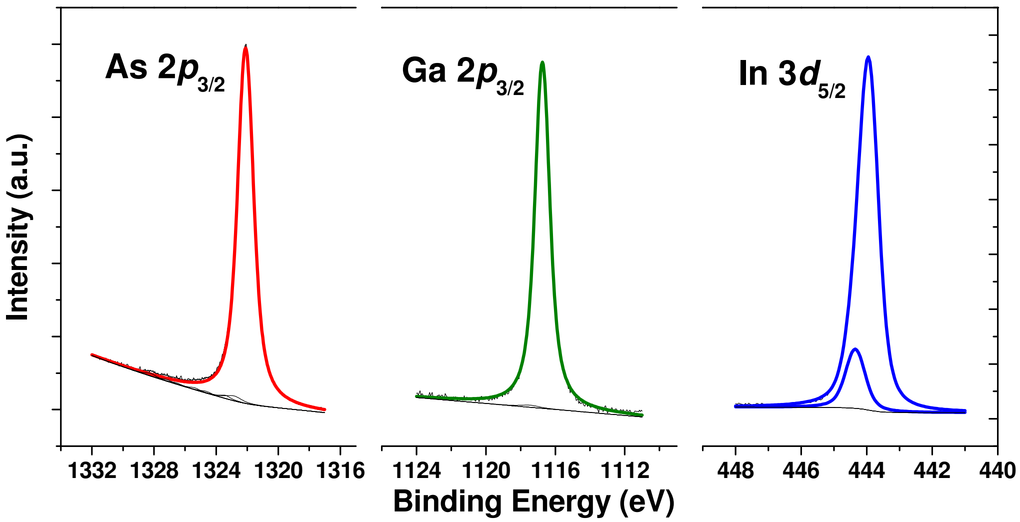

Figure 3.3 Fitted As 2*p*, Ga 2*p* and In 3*d* spectra from a decapped sample with no oxide present providing bulk peak fitting parameters

From these spectra, the Gaussian and Lorentzian peak width values were determined as shown in table 3.3. While the Lorentzian values for the As 2*p* and Ga 2*p* peaks seem quite large, they are in line with values previously reported[26] and attributed to the short core hole life time due to the proximity of the core levels to the nucleus and the potential for atomic configuration rearrangements.

Table 3.3 Gaussian and Lorentzian peak width values from a decapped InGaAs wafer

Peak	Gaussian (eV)	Lorentzian (eV)
As 2*p*	0.705	0.806
Ga 2*p*	0.538	0.73
In 3*d*	0.51	0.319

These peak width values were then used to represent the bulk peak components on all subsequent peak fits where any variation from these values would be indicative of a change in the chemical environment of the element. This is highlighted during the fitting procedure by subtracting the peak fitted data from the raw data so that the residual describes the regions where there are discrepancies between the two. Similar spectra were also attained by hydrogen cracking an InGaAs sample and scanning using synchrotron radiation based photoemission for the As 3*d* and In 4*d* and Ga 3*d* peaks as shown in figure 3.4 where only a small, residual sub monolayer oxygen peak remained on the surface which will be explained in more detail in subsequent sections. These were used to provide the basis for the synchrotron based fits.

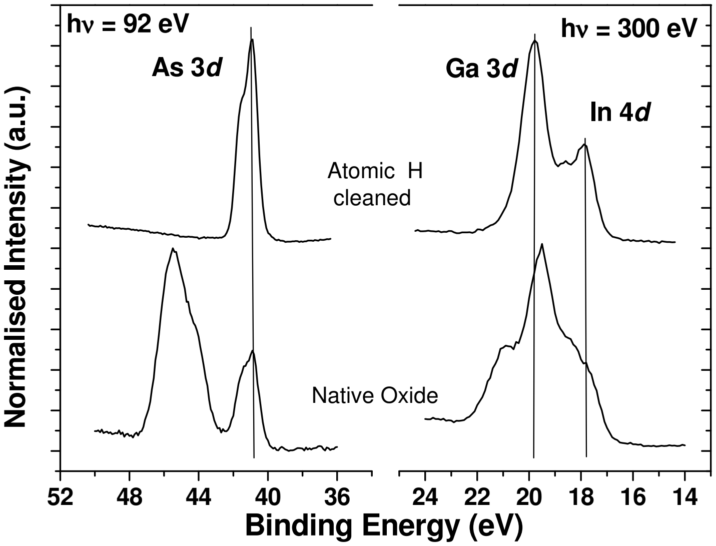

Figure 3.4 As 3*d*, Ga 3*d* and In 4*d* spectra with native oxide and after atomic hydrogen cleaning which significantly reduces the oxides present on the surface, scanned with synchrotron radiation

Using the reference fitting parameters attained from these peaks, it was then possible to deconvolute the InGaAs spectra after various surface treatments and processing conditions. This approach enabled the use of fitting parameters that could consistently fit each spectrum to a high degree of accuracy such that it was not necessary to introduce variations to the parameters unless they could be reliably explained in terms of binding energy shifts and changes in the FWHM of the peaks due to variations in the composition of the oxides.

While the forthcoming spectra are presented individually and are all fitted with the same fitting parameters, it was only by comparing them that the fitting parameters could be developed and all are shown to highlight the changes in the peak shapes and composition of the oxide with each processing step.

3.3.2. Arsenic

3.3.2.1. Native oxide

Investigations of the As $2p_{3/2}$ peak from the native oxide covered InGaAs surface on a sample with no pre-treatments before and after annealing at 300 °C in figure 3.5(a) requires eight component peaks to obtain a consistent fit. These consist of peaks attributed to As_2O_3 (As^{3+} 3.28 eV), As_2O_5 (As^{5+} 4.44 eV), elemental As-As bonds (As^0 0.75 eV), a higher order As oxide attributed to $GaAsO_4$ (5.08 eV), a peak at 1323.75 eV possibly due to As_2O which is 1.3 eV from the bulk As-Ga peak at 1322.46 eV, as well as a lower binding energy peak shifted by -0.35 eV from the bulk labelled As-. This component peak is widely attributed to arsenic surface states at the interface between the oxide and the semiconductor and specifically arsenic dimers. These values are summarised in Table 3.4.

The width of the oxide components were all correlated and were allowed to vary during the fitting process such that initially the Gaussian width was 1.25 eV and after annealing this had reduced to 1.16 eV, consistent with a more uniform chemical environment forming upon annealing. The Lorentzian component however was kept fixed throughout at 0.806 eV as this provided the highest stability and most consistent fits. Upon annealing, the As^{5+} oxidation state is seen to undergo an oxygen transfer to the As^{3+} state with the small As_2O related component present before and after annealing suggesting it is thermally stable.

Table 3.4 Binding energy position of the As 2*p* component peaks

	Peak	**BE (eV)**	**Δ BE (eV)**
	As-Ga	1322.46	-
As^0	**As-As**	1323.21	0.75
dimer	**As-**	1322.1	-0.36
As^{1+}	**As_2O**	1323.76	1.3
As^{2+}	**AsO**	1325.01	2.55
As^{3+}	**As_2O_3**	1325.74	3.28
As^{5+}	**As_2O_5**	1326.9	4.44
	$GaAsO_4$	1327.54	5.08

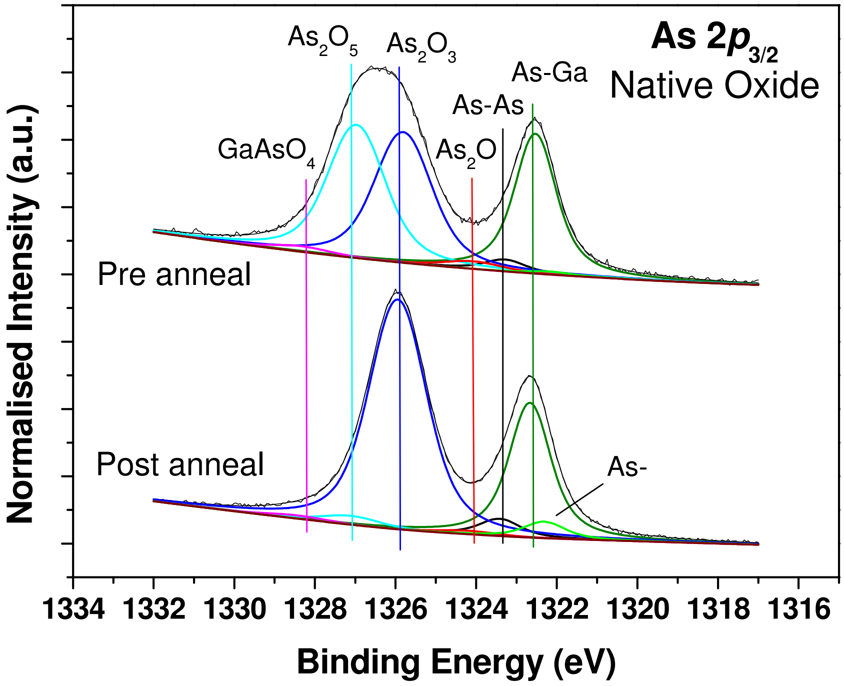

Fig 3.5(a) Curve fitted As 2*p* spectra from a sample with a significant amount of native oxide present before and after annealing at 300 °C

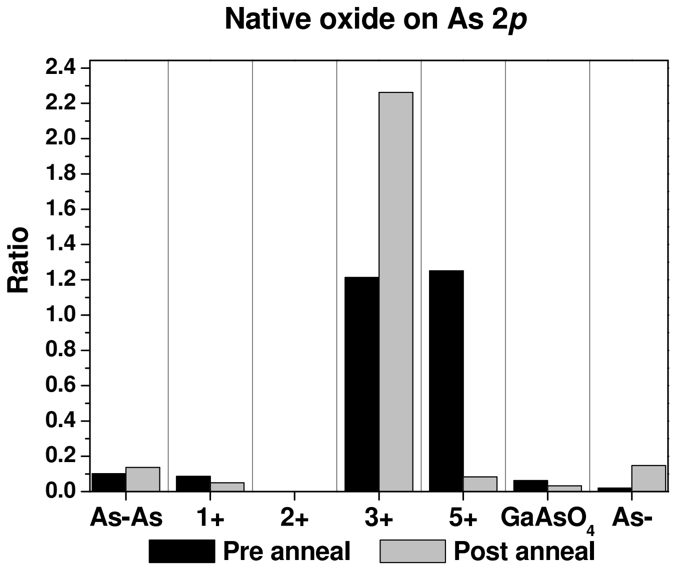

Figure 3.5(b) Ratio of fitted As 2*p* oxide and surface component areas to the area of the bulk component from a native oxide sample before and after annealing at 300 °C

The quantitative analysis of the change in ratio of oxidation states relative to the bulk peak summarised in figure 3.5(b) shows a factor of two increase in the As^{3+} peak and a 12-fold reduction in the intensity of the As^{5+} peak to just above the detection limit. The As- peak is also seen to grow with annealing suggesting that changes to the oxide composition leaves increased levels of arsenic dimers or potentially forming arsenic dangling bonds at the semiconductor surface when the O-As bonds are broken.[27]

Subsequently, two $In_{0.53}Ga_{0.47}As$ samples after degreasing were subjected to wet chemical treatments with one sample receiving an $(NH_4)_2S$ treatment step of 20 minutes in 10 % $(NH_4)_2S$ at room temperature, while the other was etched in NH_4OH. Both were then exposed to one cycle of TMA by ALD to alter the various oxide component peaks due to the impact of the reported "clean up effect" with XPS carried out at each stage. The "clean up", which will be described in more detail in chapter 5, has been shown to target trivalent oxides preferentially[28] with no net oxygen loss taking place within error limits,[29] as a result of oxygen transfer from the native oxide to form Al_2O_3, as shown in the O 1*s* spectra in figure 3.6.

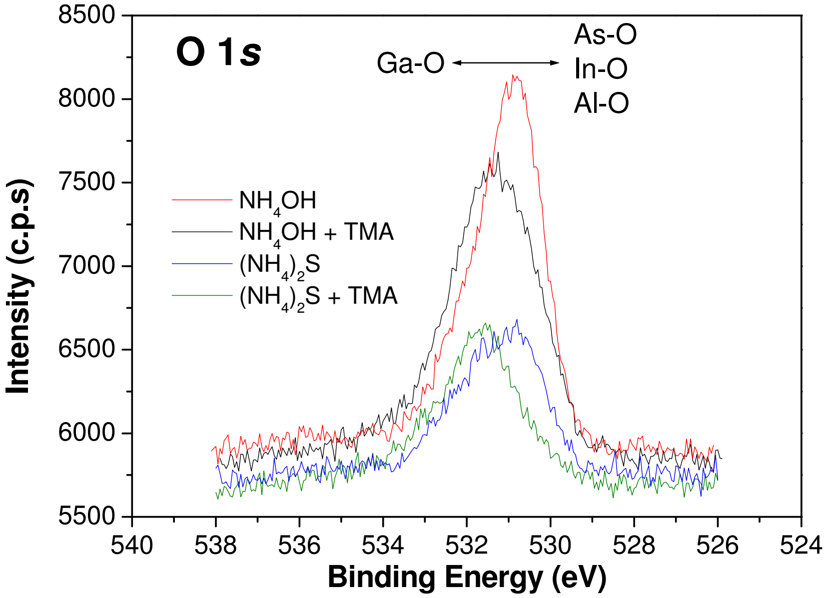

Figure 3.6 O 1*s* spectra before and after TMA exposure on NH_4OH and $(NH_4)_2S$ treated surfaces showing no overall oxygen reduction with TMA, just oxygen bond conversions

Due to the relatively low levels of oxygen present, it is difficult to determine much information regarding the chemical composition from the O 1*s* spectra[30] however, due to the change in shape and binding energy position of the peak it is clear that there is chemical changes taking place in the oxide with the introduction of the TMA.

3.3.2.2. NH_4OH treatment

The curve fitted As 2*p* peak in figure 3.7(a) following NH_4OH treatment this time requires eight component peaks to obtain a consistent fit. Again we see the As_2O_3, As_2O_5 and elemental arsenic (As-As) peaks, as well as a significantly smaller contribution from the $GaAsO_4$ peak. The As^{1+} peak is again present as well as the introduction of another peak labelled As^{2+} at 1325 eV (2.55 eV) shifted from the bulk As-Ga peak. After TMA however, there is a large decrease in As_2O_3 as expected and a relatively smaller decrease in As_2O_5 whereas the As^{1+} and As^{2+} peaks see a slight overall increase. Arsenic-sulphur peaks have been widely reported to appear at a binding energy between that of elemental arsenic and As_2O_3.[28] However, this is the region where any hydroxide or As sub-oxides peaks taking the form of As_2O_x with $x < 3$, would be expected to appear based on Pauling electronegativity values, which leads to difficultly in unambiguously assigning the observed curve fit component peaks . Despite this, the possibility of As sub-oxide formation is rarely proposed as a possible explanation for the origin of spectral features in this binding energy range with only the study by Ishikawa and Ikoma[31] specifically seen to identify the 1+ and 2+ states which they attribute to As_2O and AsO respectively, and others which show the presence of unidentified sub oxides.[32] This increase is hard to interpret if we classify these peaks as being hydroxide related[33] as they would be expected to react readily with TMA and be removed from the surface.

However if we assume that these peaks are due to arsenic oxide species that are not getting consumed during the ALD reaction process it is possible that there is an oxygen bond transfer process from one oxidation state to another taking place causing them to increase in intensity and as such the As^{1+} and As^{2+} are most likely to be representative of As_2O and AsO states. The relative intensities of the individual oxide components with respect to the substrate components peaks are graphically displayed in figure 3.7(b). Again, this highlights the large reduction in As_2O_3 with TMA, the relatively smaller reduction in As_2O_5 and the small increase in elemental arsenic, As^{1+}

and As^{2+} peaks as well as an increase in the As- peak. The actual reaction mechanism will be gone into in more detail in subsequent chapters, with the data again shown principally to highlight the variation in the oxide states taking place.

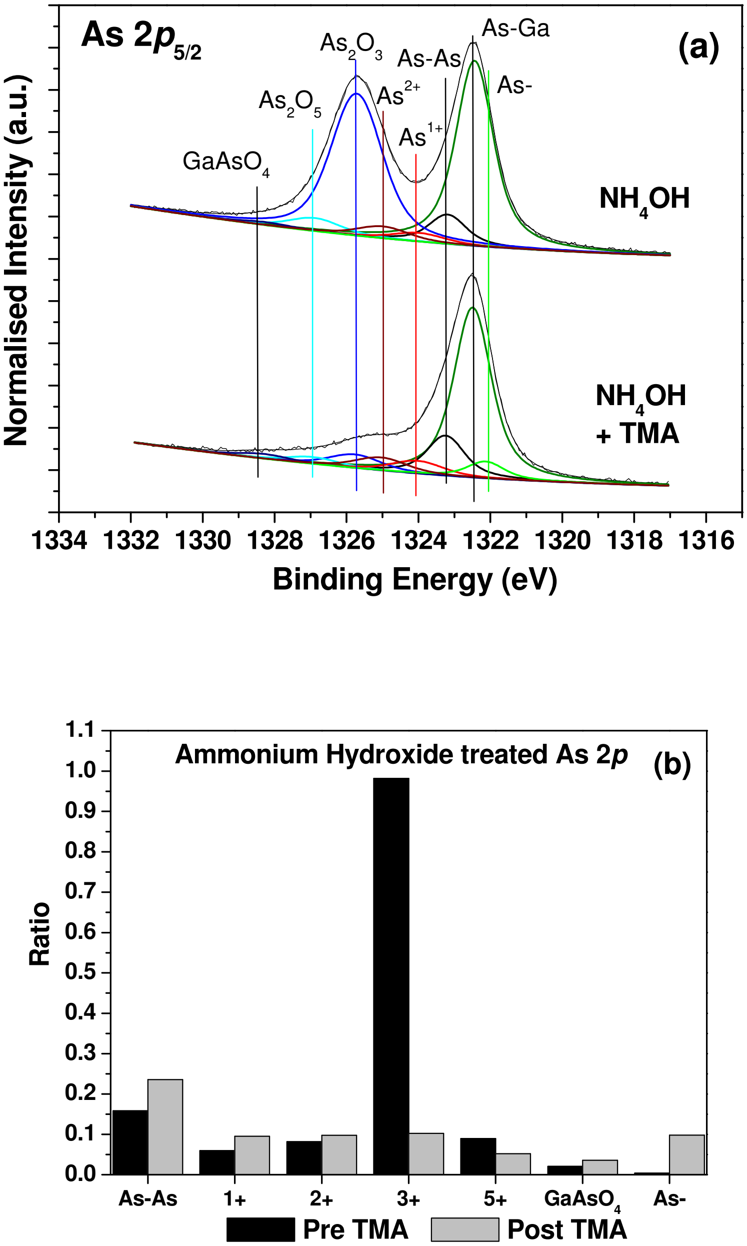

Figure 3.7(a) Curve fitted As 2*p* spectra after NH_4OH treatment and subsequent exposure to one cycle of TMA by ALD and (b) ratio of the corresponding fitted As 2*p* oxide and surface component areas to the bulk peak area

3.3.2.3. $(NH_4)_2S$ passivation

Photoemission spectra for the sample treated in $(NH_4)_2S$ before and after exposure to TMA are observed as shown in figure 3.8(a). As can be deduced from the curved fitted intensity ratio data shown in figure 3.8(b), there is a marked reduction in the intensity of the native oxide component peaks on the surface in comparison to the NH_4OH treated sample, which is attributed to the passivating effect of the sulphur, reducing the level of oxide growth in the time it took to load the samples into the UHV chamber. It is believed that any strong acid or basic solution is effective at removing the native oxides from InGaAs and that any residual oxide is due to oxide regrowth during sample transfer to UHV in ambient conditions.[34]

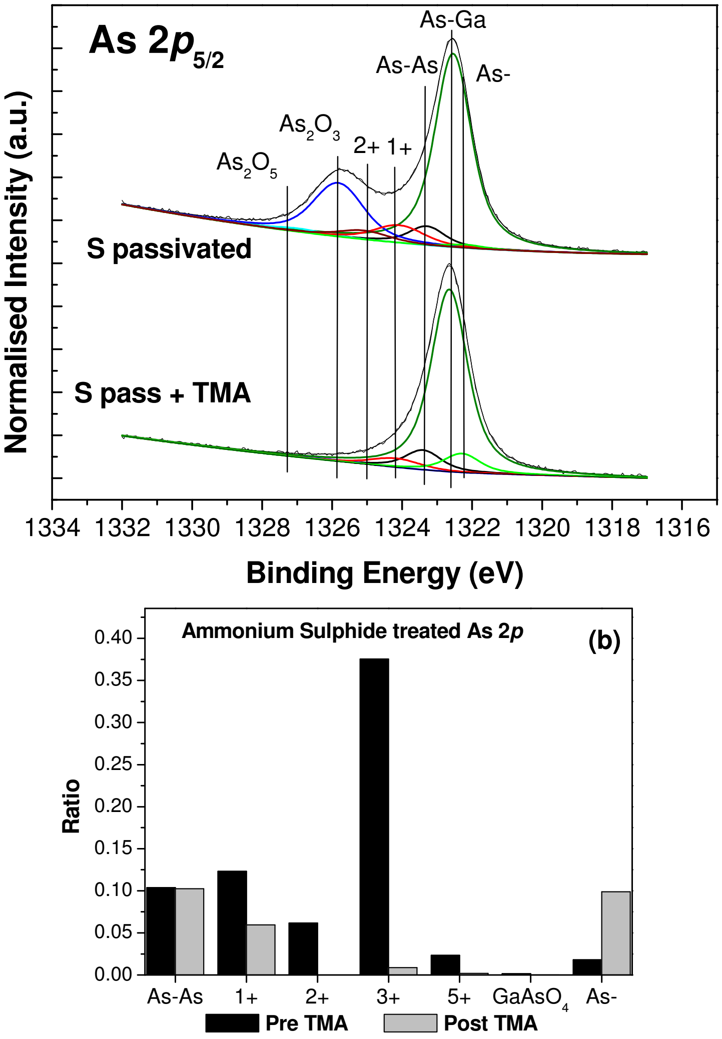

Figure 3.8 (a) Curve fitted As $2p_{3/2}$ spectra after treatment with $(NH_4)_2S$ and subsequent exposure to one cycle of TMA by ALD and (b) ratio of the corresponding fitted As 2*p* oxide and surface component areas to the bulk peak area

Figure 3.9 shows the sulphur passivated sample after exposure to ozone. The O_3 acts as a strong oxidant causing a large increase in the various oxidation states. This allows for an accurate determination of the As^{3+} and As $^{5+}$ oxidation states which, especially in the case of the 5+ state, were not as clearly evident on the as-treated surfaces. Also, with the increase in oxide concentration, the oxide peaks are seen to reduce slightly in width, with the Gaussian value going from 1.17 eV to 1.06 eV after oxidation, consistent with a more uniform chemical composition forming.

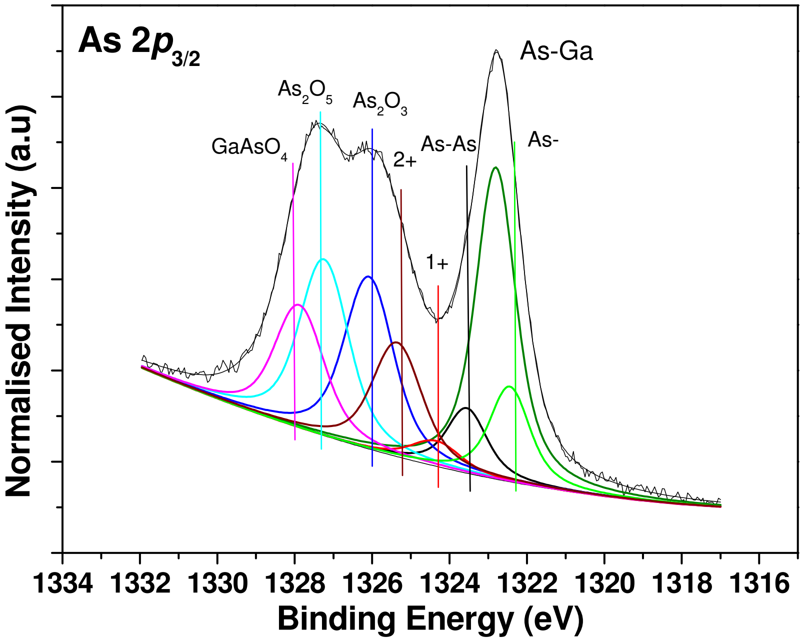

Figure 3.9 Curve fitted As 2*p* spectra after $(NH_4)_2S$ treatment and subsequent exposure to O_3 showing large oxide growth

A sulphur 2*p* component is observed in the spectrum after $(NH_4)_2S$ treatment as shown in figure 3.10 appearing as a shoulder on the Ga 3s peak however it is not possible to fit this peak to any degree of accuracy to determine the bonding environments. Previous studies with GaAs have shown that sulphur bonds are created with both the group III and group V elements prior to annealing of the samples and after annealing the sulphur is only bonded to the gallium with no evidence of As-S bonds remaining.[35]

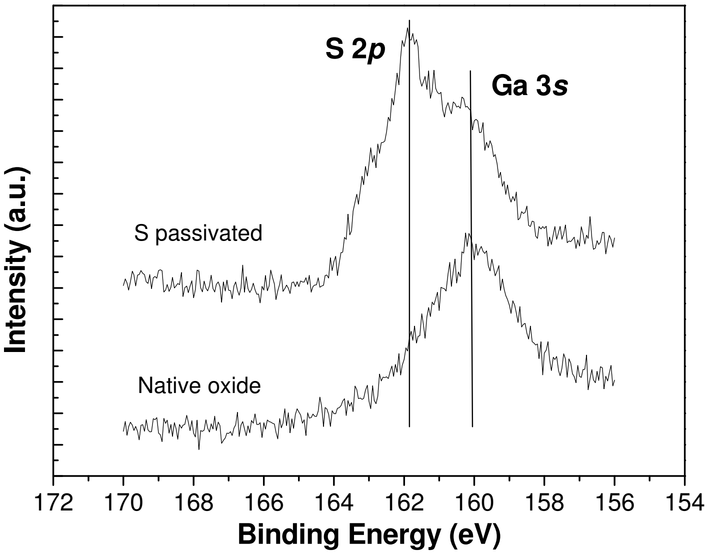

Figure 3.10 S 2*p* spectra before and after $(NH_4)_2S$ treatment

The removal of arsenic oxides by chemical treatments has been well described in literature, [34] and is due to the formation of an arsenic acid as the oxide interacts with the chemicals used by the mechanism:

$$As_2O_5 + H_2O \rightarrow H_3AsO_4$$

and this acid reacts with the substrate to form volatile AsH_3. Elemental arsenic can then be formed through further interactions between the H_3AsO_4 and AsH_3 through the thermodynamically favourable reactions:

$$2AsH_3 + 3H_3AsO_4 \rightarrow 2As + 3HAsO_2 + 6H_2O, E = 1.17 \text{ eV},$$

$$AsH_3 + HAsO_2 \rightarrow 2As + 2H_2O, E = 0.858 \text{ eV}.$$

There is also a lower concentration of elemental arsenic seen on the surface following $(NH_4)_2S$ treatment which is not seen to grow with exposure to TMA unlike on the NH_4OH treated sample. The electronegativity values for As and H are very similar (2.18 and 2.2)[36] so it is possible that any arsenic hydrogen bonds that form are in roughly the same binding energy position as the elemental arsenic peak making them difficult to resolve. This does not explain the increase however as As-H bonds would be expected to be removed following TMA suggesting that the increase is due to elemental arsenic remaining after the decomposition of one or more of the oxidation states. It is possible that the decomposition of the residual oxide by interaction with the TMA and specifically the As_2O_5 state, which is not present after $(NH_4)_2S$ treatment leaves increased levels of residual elemental arsenic behind.

The As^{2+} peak is again present after $(NH_4)_2S$ treatment at a similar level as with NH_4OH, however it is fully removed after treatment with TMA. The lower binding energy As^{1+} peak however is seen to increase in intensity relative to the NH_4OH sample coupled with an increase in the binding energy to ~1.55 eV from the bulk. This is in the range of binding energies reported for this formation of arsenic sulphur bonds.[35] Upon introduction of TMA or when annealed to 300 °C, there is a significant reduction in the As^{1+} peak intensity, and while it is not fully removed, it is seen to shift to the lower binding energy position seen after NH_4OH treatment and on the native oxide. This would again suggest that the peaks at 1323.75 eV (As^{1+}) and 1325 eV (As^{2+}) are due to oxygen bonds, taking the form of As_2O and As_2O_2 and the increase in binding energy of the As^{1+} peak with $(NH_4)_2S$ is due to the formation of As-S bonds.

Post TMA, virtually all of the As^{3+} oxidation state is removed, as well as all traces of the As^{2+} state. Since the TMA reacts preferentially with the As^{3+} state, it is possible that once this most facile reaction is completed, it then moves onto the next most susceptible states, being the As^{2+} and As^{5+} states and finally with the As^{1+} state. For the NH_4OH sample which still showed the presence of As_2O_3 after TMA exposure, due to a possible reaction channel limit of the TMA cycle in terms of its ability to remove all of the oxide, the other oxidation states still remain on the surface.

3.3.3. Gallium oxide modifications

Figure 3.11 displays the curve fitted profiles of the Ga $2p_{3/2}$ peaks from the same samples which again also provide an insight into the stability of the oxides present. The Ga $2p$ spectra from the native oxide was again examined before and after annealing at 300 °C in figure 3.11(a) to determine the relative stability of the gallium oxide states and to get an insight into the thermodynamic changes taking place. There are three oxidation states present with Ga_2O_3 (Ga^{3+}) the largest, Ga_2O (Ga^{1+}) and a significantly smaller peak tentatively ascribed to an indium gallium oxide state (InGaO) at 1.1 eV, 0.55 eV and 1.6 eV from the bulk peak at 1117.06 eV as previously reported.[23] After annealing however, there is a large decrease in the InGaO state and a large increase in both the Ga^{1+} and Ga^{3+} states, with the Ga^{1+} state now dominating suggesting that it is most thermodynamically stable. The level of increase in magnitude of these oxidation states is too significant to be just attributed to oxygen transferring from the $GaAsO_4$ state to form Ga_2O or Ga_2O_3, suggesting that the increase is due to oxygen transferring from either arsenic or indium oxides. There is no evidence of the $GaAsO_4$ related peak as seen in the As 2*p* spectra after exposure to O_3 in figure 3.9 however this will be probed further with increased surface sensitivity using synchrotron radiation later.

The Ga 2*p* spectra from the NH_4OH and $(NH_4)_2S$ treated samples and with subsequent exposure to TMA are shown in figures 3.11 (b) and (c). Again, the same 3 oxide peaks seen on the native oxide sample are present but at a much reduced level, with the Ga^{1+} state this time the most dominant oxide peak suggesting it is either the first oxide to form during sample oxidation or the most stable and difficult to remove by chemical treatment. With TMA, the InGaO peak is virtually all removed and due to the ligand exchange reaction mechanism, the Ga^{3+} peak is also significantly reduced. While also reduced, a significant amount of the Ga^{1+} state remains on both samples.

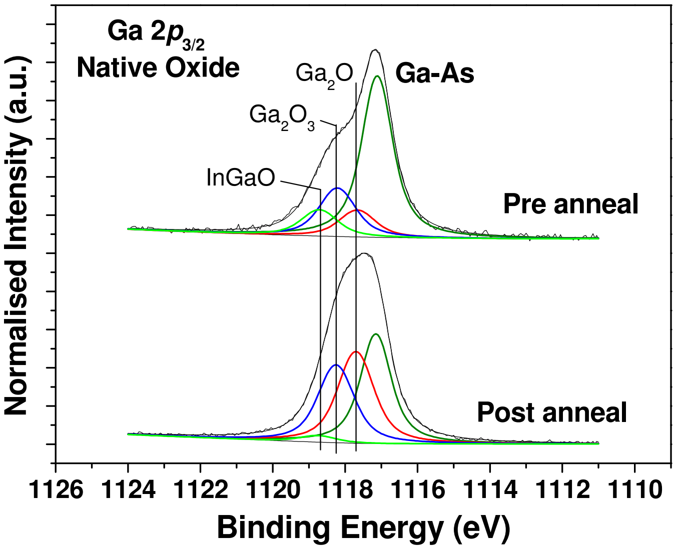

Figure 3.11 (a) Curve fitted Ga 2*p* spectra from a sample with a significant amount of native oxide present before and after annealing at 300 °C

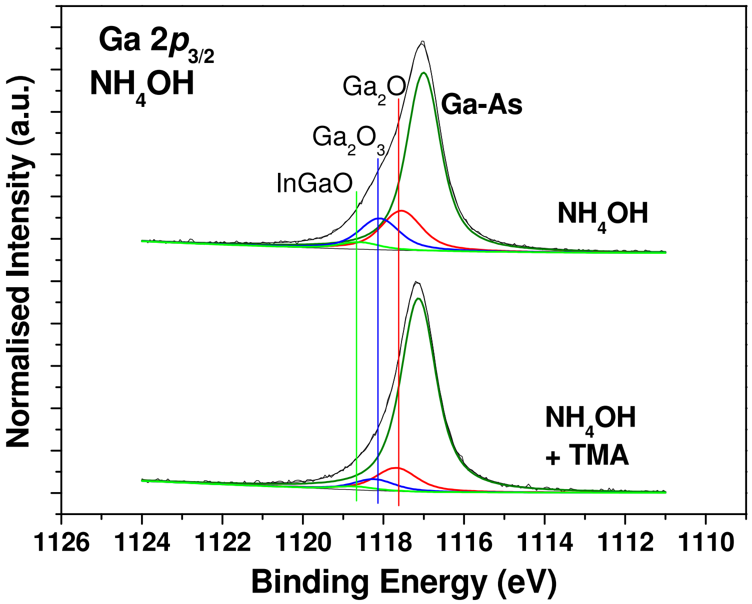

Figure 3.11 (b) Curve fitted Ga 2$p_{3/2}$ spectra after treatment with NH_4OH and subsequent exposure to one cycle of TMA by ALD

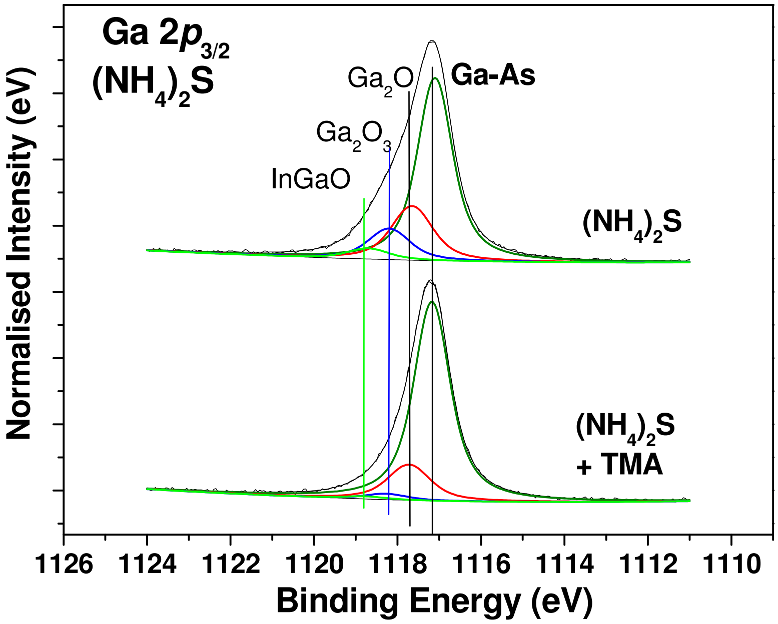

Figure 3.11 (c) Curve fitted As 2$p_{3/2}$ spectra after treatment with $(NH_4)_2S$ and subsequent exposure to one cycle of TMA by ALD

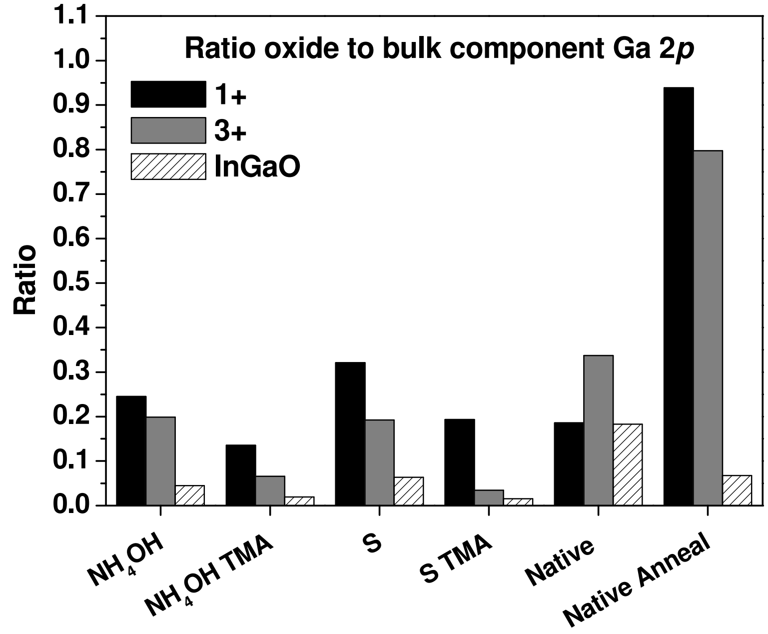

Figure 3.11 (d) Ratio of gallium oxide peak area to bulk peak area with various surface treatments from the fitted Ga 2*p* spectra

The ratio of the various oxide components to the bulk Ga-As peak after the various processing steps is shown in figure 3.11 (d). Again, this highlights a large increase in gallium oxide present upon annealing of the native oxide, specifically the Ga^{1+} and Ga^{3+} states with a reduction in Ga^{4+} again reflecting the relative thermodynamic stabilities of the various states. With TMA exposure however, the oxide level is clearly seen to decrease which confirms there is a reaction taking place, with the TMA reducing the oxide composition as opposed to being as a result of thermodynamic changes due to the processing conditions during exposure to TMA. Another interesting feature is the relative abundance of the Ga^{1+} oxidation state on the $(NH_4)_2S$ treated sample in comparison to NH_4OH. This is possible evidence of the presence of unresolved Ga-S bond formation which would be expected in the binding energy range between the Ga^{1+} and Ga^{3+} peak.[35, 37] Due to the small binding energy separation between the peaks, this would contribute to the Ga^{3+} peak in the fit also and could be the reason that there is a still evidence of a residual Ga^{3+} peak even after TMA exposure. This will be gone into in more detail in chapter 4 when a more rigorous analysis of the $(NH_4)_2S$ passivation process is carried out.

3.3.4. Indium oxide modifications

The In 3*d* spectra from the same samples are shown in figure 3.12 (a-c). Similar to the Ga 2*p* peak, the binding energy separation between the chemically shifted peaks is small making accurate determination of the peaks difficult. Also, in the literature, there is very little definitive information regarding the position of the oxides, as highlighted in table 3.2, so the same iterative process as described for the As 2*p* peak was carried out to develop a consistent fit for the In 3*d* peak. Due to the lower binding energy of the In $3d_{5/2}$ core level at 444.4 eV, the photoemitted electrons have a much higher kinetic energy than those emanating from the As 2*p* and Ga 2*p* core levels. This means that the inelastic mean free path of the electrons from the In 3*d* core level is higher which results in a larger sampling depth. The consequence of this is that a similar thickness of surface In oxide has a smaller contribution to the spectra than that from As and Ga oxides in the As 2*p* and Ga 2*p* core levels, again leading to increased difficulty in the fitting process.

From the decapped oxide free sample in figure 3.3, the In peak has an asymmetric line shape which is usually just seen for metallic elements due the presence of a high density of unfilled states above the Fermi level which can contribute to shake-up like events. For crystalline materials this asymmetry is thought to be caused by vibrations of the atoms around their equilibrium position and as such the emission of an electron from a core level is coupled to this change in position resulting in a Gaussian-type phonon broadening.[38] This could be investigated by increasing the temperature of the sample during scanning as this would be expected to increase the phonon broadening contribution due the increased vibrational energy. The asymmetry manifests itself as a broadening to the higher binding energy side of the peak in the region where oxides are expected to be seen. To counteract this, the line shape from the decapped sample was kept constant throughout the fitting process. Based on this, three chemically shifted peaks were detected after the various treatments and anneals at 0.45 eV, 0.8 ± 0.04 eV and at 1.25 eV from the bulk In peak with Gaussian values of 0.67 eV, as well as the peak at 0.42 eV to compensate for the asymmetry.

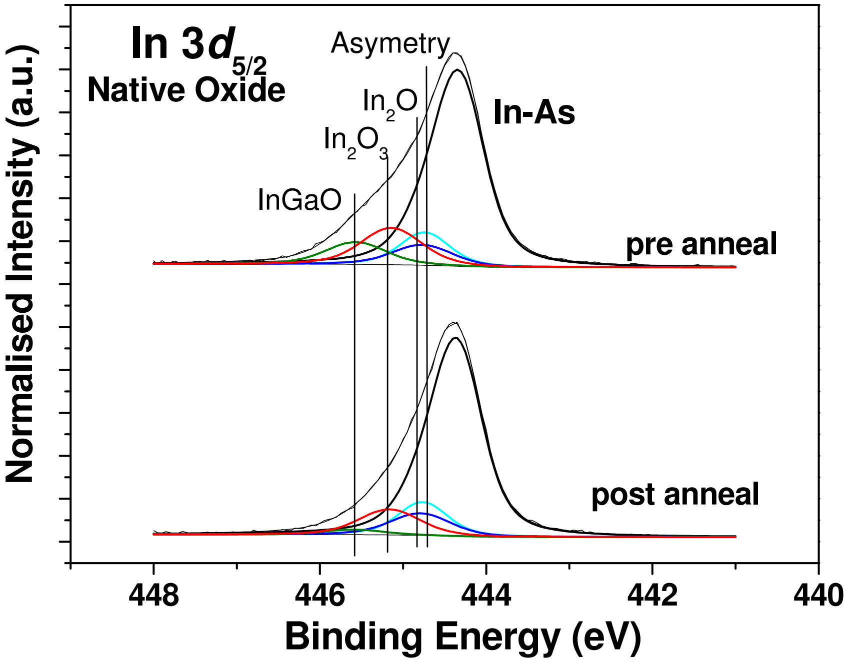

Figure 3.12(a) Curve fitted In 3$d_{5/2}$ spectra after treatment with NH_4OH and subsequent exposure to one cycle of TMA by ALD

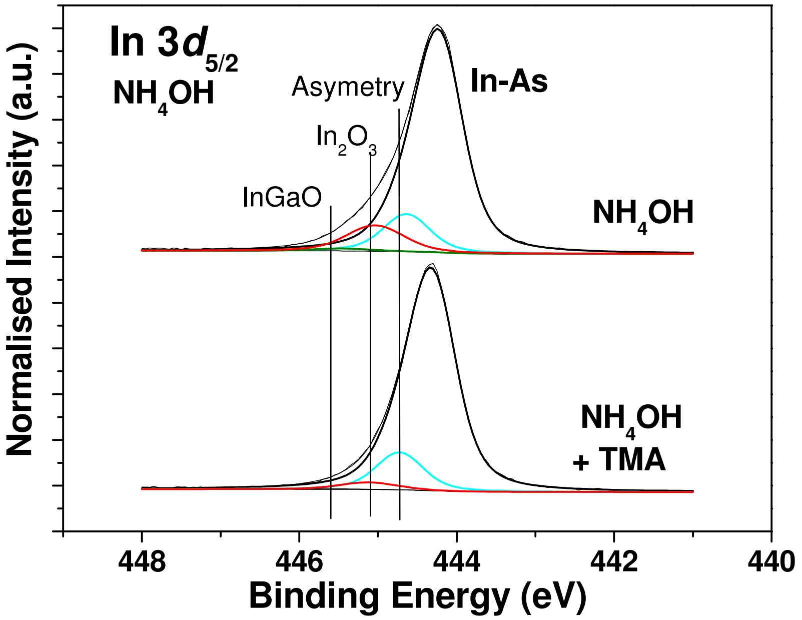

Figure 3.12 (b) Curve fitted In 3$d_{5/2}$ spectra after treatment with NH_4OH and subsequent exposure to one cycle of TMA by ALD

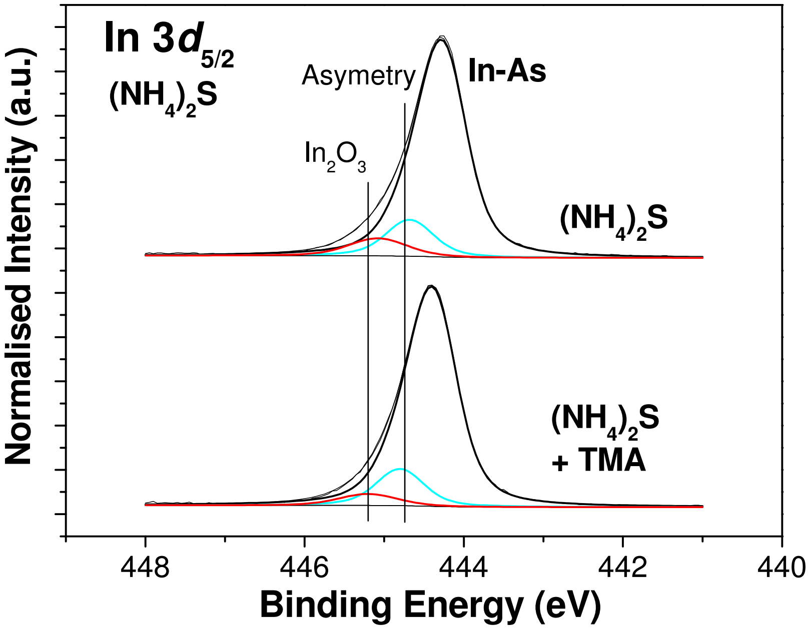

Figure 3.12 (c) Curve fitted In 3$d_{5/2}$ spectra after treatment with $(NH_4)_2S$ and subsequent exposure to one cycle of TMA by ALD

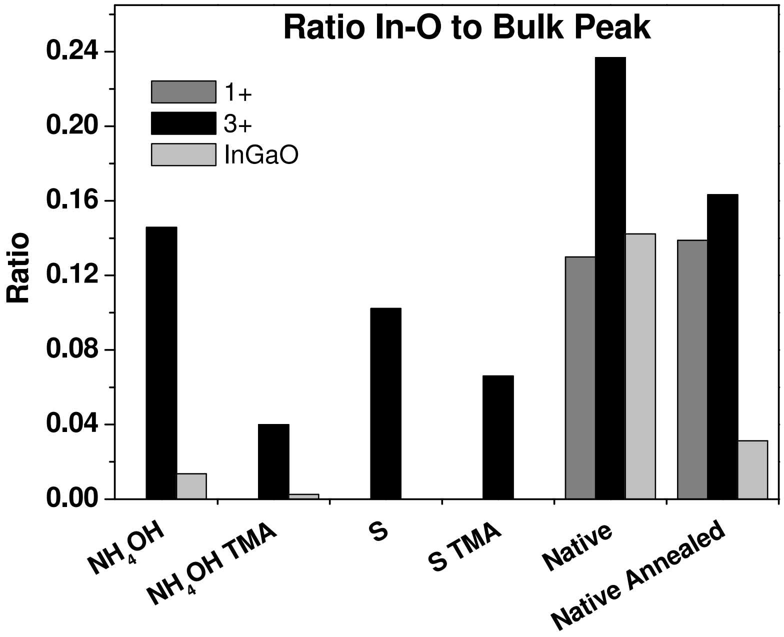

Figure 3.12 (d) Ratio of indium oxide peak to the bulk peak areas with various surface treatments from the fitted In 3*d* spectra

Identification of these peaks is difficult, but it can be speculated that the peak at 0.8 eV from the bulk is due to In_2O_3 due to its relative abundance on all the samples. On the $(NH_4)_2S$ treated sample in figure 3.10 (c), this peak is seen to shift to ~0.07 eV lower binding energy which could be evidence for the formation of In-S bonds, which would be expected to occur at a lower binding energy than In_2O_3 and would subsequently make the peak appear to shift, but due to the relatively small binding energy separations involved, it is extremely difficult to resolve. The higher binding energy peak is only present on the native oxide and the NH_4OH treated sample (although at a much lower level) and is reduced significantly by both annealing and TMA exposure and could be related to the higher binding energy peak seen in Ga peaks suggesting a possible mixed phase oxide state with indium the majority contributor based on the oxide ratios. The assignment of indium sulphur bonds, while expected to occur is not widely reported in literature however a few papers do report their existence on InGaP and InP at ~0.3 eV from the bulk peaks.[39] However due to the presence of the lower binding energy peak in the spectra from the native oxides in figure 3.10 (a), it is likely that in this study at least, this peak is due to an indium sub oxide taking the form In_2O_x where $x < 3$, similar to the Ga_2O peak. This lower binding energy peak also appears to be the most stable state when it is present on the surface with no change detected in the level present upon annealing of the native oxide sample (within error limits).

Figure 3.10 (d) again shows the ratio of the component peaks to that of the bulk peak area after the various treatment steps. It again highlights the reduction of the oxides with annealing and exposure to TMA. The In^{3+} peak on the NH_4OH treated sample is seen to decrease by significantly more than that of the $(NH_4)_2S$ sample, which based on the evidence from the As 2*p* and Ga 2*p* spectra if the trend was to follow, should show the lowest overall value, reinforcing the idea that there could be an In-S peak contributing to this value. The plot also highlights the relative abundance of the three different oxidation states on the native oxide sample and the higher thermal stability of the In^{1+} oxidation state which shows virtually no change upon annealing whereas the higher oxidation state, tentatively labelled InGaO, shows a nearly four fold reduction as well as a less substantial reduction in the In^{3+} state.

We are also able to draw some conclusions about what is happening to the overall oxide composition during annealing. As stated previously, upon annealing the As_2O_5

peak on the native oxide sample decreases with the As_2O_3 peak increasing by a similar amount, which suggests that the arsenic oxides undergo a bond conversion from one form of arsenic oxide to another. However both the Ga^{1+} and Ga^{3+} oxides are seen to increase, whereas there is a large decrease in the indium oxide states suggesting that this reduction takes paces as a result of oxygen bond transfers from indium to gallium. Taking into account the increased inelastic mean free path of the electrons from the In 3*d* peak, the change in the indium oxide concentration is also consistent with the level of increase in the gallium oxides.

In order to definitively ascertain the nature of the individual oxidation states and to determine what is happening to them upon annealing, giving information regarding their relative thermodynamic stabilities, an in-situ annealing study was carried out on a native oxide sample using surface sensitive synchrotron radiation which is described below.

3.4. InGaAs native oxide modification by in-situ annealing and atomic hydrogen cleaning investigated by synchrotron based photoemission

In order to verify and further enhance the reliability of the fit parameters developed in the previous section, specifically in terms of the binding energy position of the oxide peaks and to get an insight into the stability of the various oxidation states, synchrotron radiation spectra were acquired from an $In_{0.53}Ga_{0.47}As$ sample which had been exposed to atmosphere for an extended period of time resulting in the formation of a significant stable native oxide, at a range of photon energies from 37 eV to 600 eV. Scans were also taken after successive anneals in vacuum for 30 minutes at a range of temperatures from room temperature up to 450 °C in steps of 50 °C, followed by an exposure of the sample to atomic hydrogen for 30 minutes at a substrate temperature of 380 °C intended to significantly remove the remaining oxide present. The sample experienced no pre-treatments prior to introduction to UHV.

As 3*d*, In 3*d*, In 4*d* and Ga 3*d*, O 1*s*, C 1*s* core levels, work function and valence band spectra were taken at a range of photon energies to vary the sampling depth of the photoemitted electrons and the photoionisation cross section of the peaks, such that a good fit would only be achieved for the spectra if the same fitting parameters could be used at different photon energies ensuring increased reliability of the fit and a reduced associated error. A number of studies have been carried out to determine the effect of chemical treatments on the native oxide of GaAs and InGaAs with synchrotron radiation, [32, 33, 34, 40, 41] however there has been very few attempts to fully characterise the native oxide itself or to investigate systematically the thermal stability of the individual states.

In order to determine the parameters for a credible curve fit of the As 3*d* spectra, an InGaAs sample was exposed to atomic hydrogen at substrate temperatures ranging from 360 °C to 400 °C for 30 minutes and 60 minutes at a hydrogen base pressure of $1x10^{-7}$ mbar. The profile of the oxide free As 3d peak after 60 minutes exposure at 400 °C is shown in figure 3.13. The atomic hydrogen was generated from an Oxford Instruments TC50 thermal gas cracker source operating at 45W.

The fitted data shows the bulk As-Ga peak at 40.5 eV and also the presence of a state at 40.04 eV or -0.46 eV from the bulk peak, with no trace of arsenic oxide or elemental arsenic. This lower binding energy peak is generally reported as being due to As-As dimmer bond formation at the surface,[42] however it has also been fitted with two peaks at -0.29 eV and -0.69 eV for ultra clean surfaces, due to dimmer formation and possibly As dangling bonds or alternative surface dimer formations respectively.[43] A model has been proposed by Robertson which describes the defect density of the GaAs and InGaAs surface in terms of Ga and As dangling bonds at the conduction and valence band edges[27] which would support the assignment of these peaks. Utilising a doublet ratio of 0.66 throughout, the doublet splitting was determined to be 0.702 eV and the FWHM of the bulk peak was calculated as 0.705 eV with a Gaussian contribution of 0.64 eV and Lorentzian value of 0.065 eV. These values were then used throughout the study for the bulk peak component so that any variations from these parameters would again be indicative of changes in the peak local environment taking place.

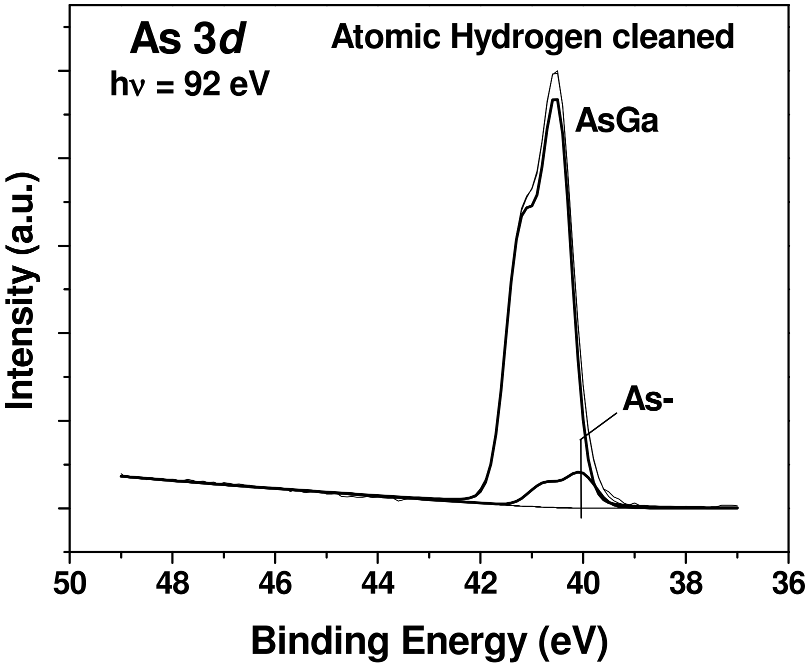

Figure 3.13 Peak fitted spectra of the atomic hydrogen cleaned As 3*d* peak with no evidence of oxide or elemental arsenic present and showing the presence of As dimers at the surface

3.4.1. Annealing

3.4.1.1. Impact on arsenic oxides

The As 3*d* spectra taken during the thermal annealing sequence at a photon of 92 eV energy are shown in figure 3.14. With the spectra normalised to the bulk peak intensity in figure 3.14 (a), the complex nature of the oxide composition is highlighted with clear evidence of variations in binding energy and peak widths of the oxide components in the raw data. Figure 3.14 (b), (c) and (d) show the fitted As 3*d* spectra at various stages in the annealing process, from the native oxide in (b) to the spectrum after annealing this surface at 400 °C in (c), as well as a stacked plot after a number of process steps to highlight the change in fitted spectra in (d).

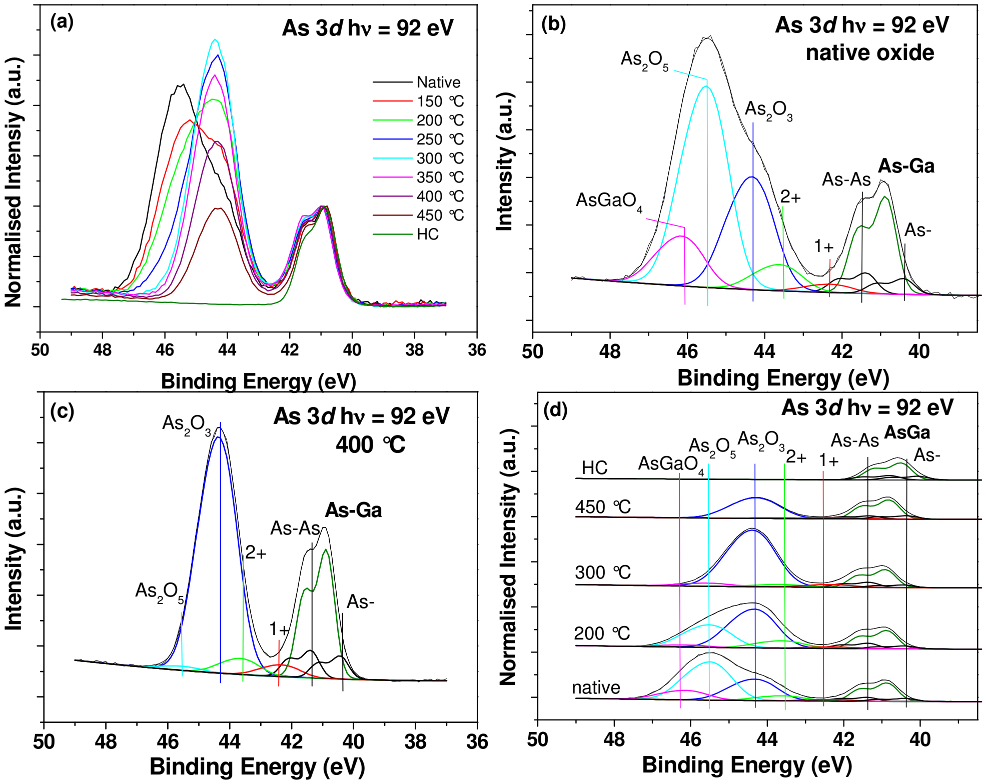

Figure 3.14 As 3d photoemission spectra at hν = 92 eV after successive anneals up to 450 °C and with hydrogen cleaning (a), fitted spectra from the native oxide and after annealing at 400 °C (b, c), and fitted spectra after successive anneals and hydrogen cleaning (d) showing change in oxidation states with increased temperature

Starting with the previously developed parameters in terms of the binding energy separation of the peaks for the As 2*p* spectra of the native oxide in figure 3.5(a), a maximum of eight peaks were needed. The FWHM of the oxide peaks were allowed to vary such that the Gaussian component varied from an initial value of 1.05 eV before annealing to a maximum value of 1.13 eV as the level of oxide reduced. The binding energy shifts for the component peaks from the bulk As-Ga peak are listed in table 3.5 and are consistent with the values determined by XPS for the As 2*p* peaks.

Table 3.5 Relative binding energy peak position of As 3*d* spectral components

Peak	**BE (eV)**
As-As	0.47
As-	-0.52 ± 0.06
As^{1+}	1.23
As^{2+}	2.55
As_2O_3	3.24
As_2O_5	4.44
$GaAsO_4$	5.08

The As- peak at 0.52 eV ± 0.06 eV lower binding energy relative to the bulk peak is again attributed to arsenic dimers or dangling bonds at the surface. The accurate binding energy assignment of the As-As and As- peaks is relatively difficult due to the small binding energy separation of the peaks from the bulk. Also, these values are slightly different to those calculated from the As 2*p* peaks so these two peak positions are assigned tentatively, however they all fall within the range of values previously reported as per table 3.2, possibly reflective of variations in the dimer formations at the surface or the creation of dangling bonds as the oxide reduces. The As^{2+} state was not previously seen on the native oxide sample from the As 2*p* spectra with XPS which could be due to the reduced surface sensitivity associated with XPS and the $GaAsO_4$ is assigned after correlating with the gallium spectra, as will be explained in more detail later.

Figure 3.15 (a) shows the ratio of the As_2O_3 and As_2O_5 peaks to the bulk As peak as well as that of the total oxide ratio from the combined arsenic oxide peaks. As the substrate temperature increases from room temperature, the As_2O_3 peak is seen to increase, concurrent with a decrease in the As_2O_5 peak, suggesting that the increase is due to an oxygen bond transfer from the As^{5+} state to the As^{3+} state up to 300 °C, with the total arsenic oxide ratio staying constant. By 300 °C, the As_2O_5 is virtually all removed and the increase in the 3+ state reaches a maximum.

With further temperature increase above 300 °C, the As^{3+} state is seen to decrease coupled with an increase in the overall arsenic bulk signal from un-normalised spectra (not shown). This suggests that there is a reduction in the oxide thickness as opposed to an oxygen bond transfer to either the indium or gallium which would maintain the overlayer thickness and keep the substrate signal intensity constant above 300 °C. The evaporation of As_2O_3 has previously been reported at an annealing temperature of around 350 °C.[44]

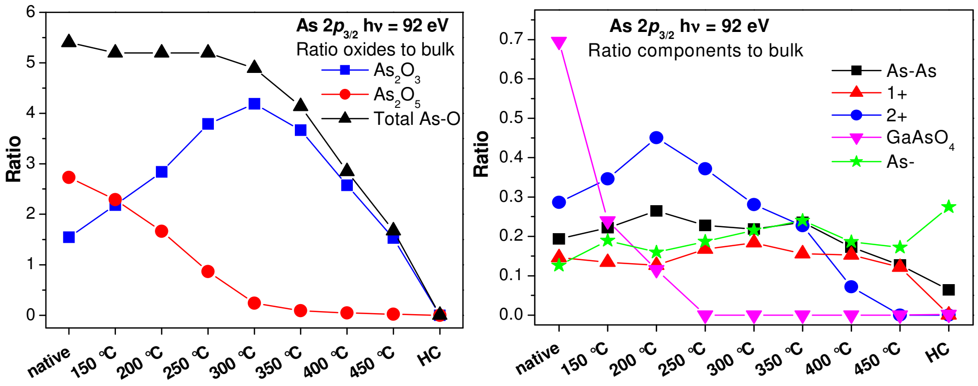

Figure 3.15 (a) Ratio of arsenic oxidation states to the bulk As-Ga peak with increased annealing temperature and (b) ratio of the individual sub-oxide components as a function of thermal anneal.

Figure 3.15 (b) shows the ratio of the remaining spectral components to the substrate peak. The $GaAsO_4$ peak is significantly reduced at 150 °C and is fully removed by 250 °C suggesting that it is the least stable of the oxidation states. The 1+ state shows very little change up to 450 °C whereas the 2+ state is seen to increase up to 200 °C, at which point it begins to decrease again such that by 450 °C it is all removed within detection limits. The elemental arsenic peak is also seen to increase up to 200 °C and steadily decrease up to 450 °C without ever being fully removed. The As- peak intensity is relatively constant throughout until the sample is exposed to atomic hydrogen, at which point we see an increase similar in magnitude to the reduction of the 1+ state. As the 1+ state is suspected to be surface localised, this suggests that when the surface oxide is removed, there is an increase in the formation of As dimers and also potentially As dangling bonds as a result of the surface reconstruction, with the removal of the oxygen.

3.4.1.2. Impact on indium and gallium oxides

In order to fully determine what is happening to the oxidation states, it is necessary to look also at the indium and gallium spectra. Typically with XPS, the In $3d_{5/2}$ and Ga $2p_{3/2}$ peaks are examined, due to the relatively large binding energy separation of the doublet components and also they are the highest binding energy photoemission peaks available using Al or Mg Kα X-ray sources, therefore giving the greatest surface sensitivity. With synchrotron radiation, the ability to tune the photon energy gives enhanced control over the surface sensitivity. The In 4*d* and Ga 3*d* peaks have the benefit that their binding energies are very close together, which although it leaves deconvoluting the spectra slightly more difficult, means their inelastic mean free paths are virtually identical. This means that the determination of the thickness of oxide overlayers is more straight forward. Also, lower binding energy peaks typically have a smaller FWHM as illustrated in figure 3.16 (a) where the In 3*d* and In 4*d* peaks are overlayed, giving greater overall resolution and ability to identify the various oxidation states present. This is due mostly to the SX700 monochromator resolution in terms of an increase in the FWHM of the peaks generated with increasing photon energy, as illustrated in figure 3.16 (b).

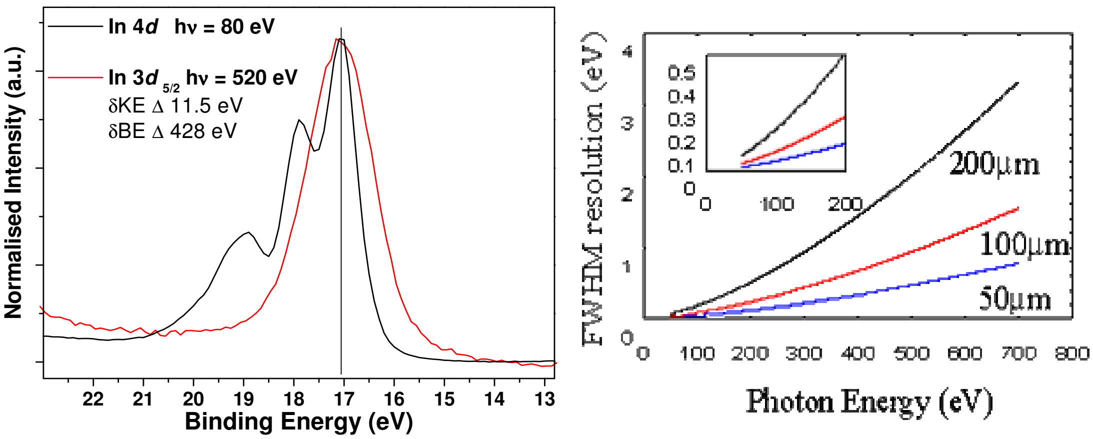

Figure 3.16 (a) Synchrotron photoemission spectra from In 3*d* and In 4*d* core levels highlighting increase in FWHM at increased binding energy and (b) the increase in monochromator resolution with photon energy

However, the photoionisation cross section (PI), which is the probability that an incident photon will create a photoelectron,[45] is different for each core level and varies with photon energy leading to changes in the relative intensities of the peaks. The various PI values taken from Yeh and Lindau [46] are shown in figure 3.17 for the core levels and photon energies investigated.

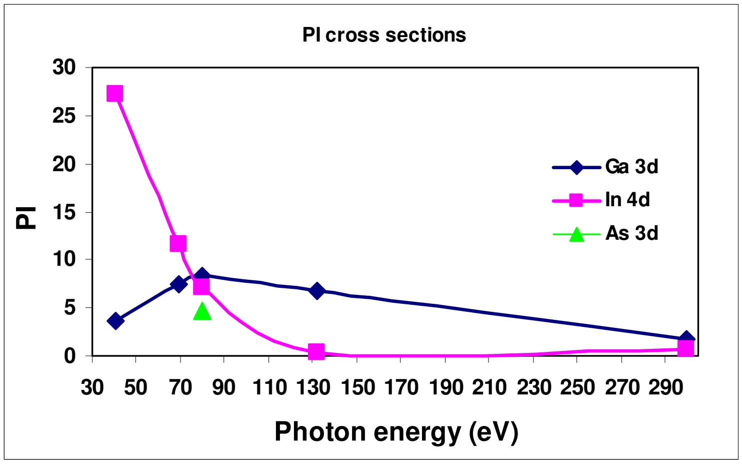

Figure 3.17 Photoionisation cross sections (PI in eV) for the various photon energies investigated from reference [46]

This is illustrated most clearly in the raw data from the In 4*d* and Ga 3*d* peaks in figure 3.18 taken at 69 eV, 80 eV, 130 ev and 300 eV from the native oxide.

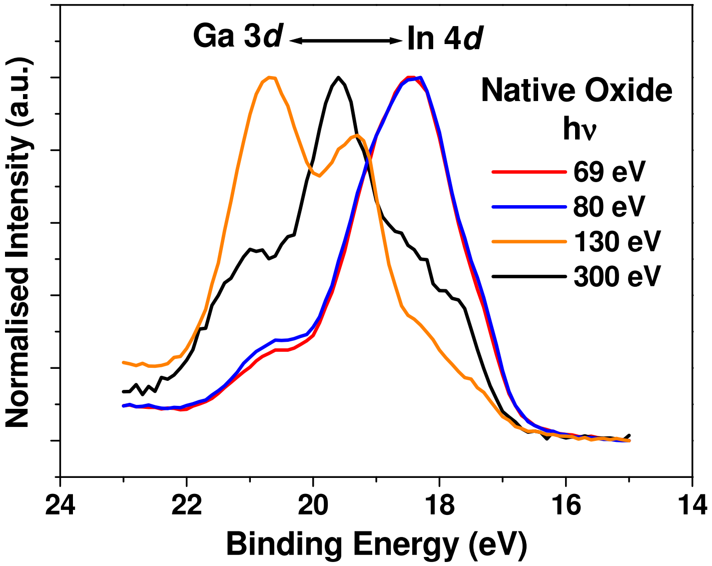

Figure 3.18 In 4*d* and Ga 3*d* spectra from native oxide sample at four different photon energies highlighting changes in the PI cross section

Clearly, at 69 eV and 80 eV, the intensity from the In 4*d* peak is significantly greater than that of the Ga 3*d* peak whereas at 130 eV we see that the Ga 3*d* peaks are significantly more intense and while the In 4*d* peak increases relative to the Ga 3*d* peak at 300 eV, the Ga 3*d* still dominates. All this helps in the deconvolution of the various spectra as it allows for a more accurate identification of the various oxide components by changing their relative intensities without changing the effective attenuation length (EAL) of the photoemitted electrons.

Figure 3.19 (a-d) shows the corresponding spectra at the four different photon energies with 69 eV (a), 80 eV (b), 130 eV (c) and 300 eV (d) after incremental annealing from 150 °C to 450 °C and subsequent exposure to atomic hydrogen. Again these highlight the variation in the peak intensities of the In and Ga peaks with the change in photon energy. It is also clear that the increase in annealing temperature has a significant effect on the composition of the oxides present on the surface with changes in the peak intensities and line shapes evident after the first anneal at 150 °C.

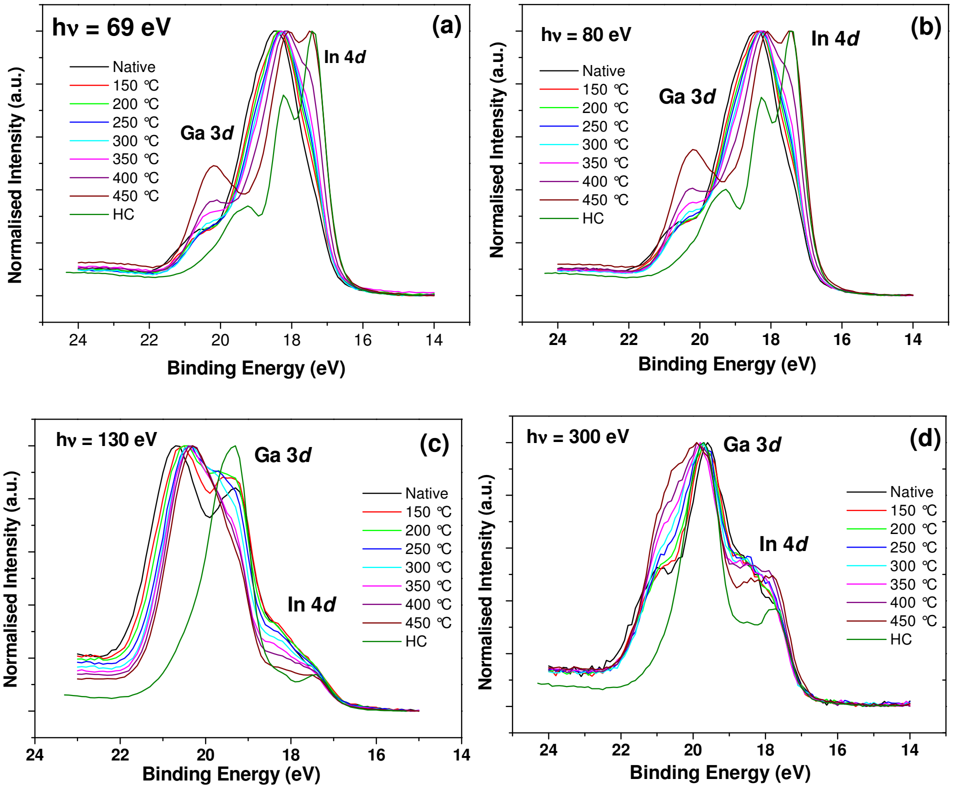

Figure 3.19 Photoemission spectra for the In 4*d* and Ga 3*d* peaks at photon energies of 69 eV (a), 80 eV (b), 130 eV (c) and 300 eV (d) after annealing at temperatures incrementing from 150 °C to 450 °C and after atomic hydrogen cleaning at a substrate temperature of 380 °C

The resultant curve fitted spectra from the native oxides at the four different photon energies are shown in figure 3.20. All binding energies are kept constant throughout such that peak separations are identical at the different photon energies. In all there are 10 components in the spectra which are consistently fitted for each temperature. The indium and gallium bulk peaks are located at ~17.27 eV and 19.09 eV such that the binding energy separation between the two is fixed at 1.82 eV with the spin orbit spitting values also fixed at 0.88 eV and 0.44 eV respectively consistent with reported values[47] (0.84-0.88eV and 0.44-0.46 eV) determined again with the aid of spectra from the hydrogen cleaned surfaces.

There are three peaks attributed to indium oxide, consistent with those seen in the XPS spectra; at 0.448 eV, 0.82 eV and 1.25 eV from the bulk peak, again tentatively assigned as In_2O, In_2O_3 and a mixed phase, $In_xGa_yO_z$ (with x>y initially) respectively. There is also a peak at ~ -0.65 eV from the bulk peak attributed to under coordinated indium at the surface or possibly indium dimers.[48]

The remaining peaks are due to gallium oxides at 0.55 eV, 1.1 eV, 1.6 eV and 2.05 eV from the bulk Ga peak, attributed to Ga_2O, Ga_2O_3, a possible corollary to the high BE oxidation state present in the indium spectra labelled as $In_xGa_yO_z$, and $GaAsO_4$ which was not detected in the XPS spectra, respectively. While the Ga_2O and Ga_2O_3 states are widely reported[23] and the presence of the $GaAsO_4$ is often alluded to, [49, 50] it is hard to find definitive consensus on the oxidation states in the literature, with even the Ga_2O and Ga_2O_3 peak often attributed to the higher binding energy states reported here (table 3.2). In the case of the $In_xGa_yO_z$ peak, we have been unable to ascertain any reported evidence of its existence in the literature. It is worth noting that in the most surface sensitive spectra at 69 and 80eV, there is no evidence of the Ga_2O peak, suggesting that it could form at the interface between the oxide and the substrate although at these energies the photoionisation cross section suppresses the gallium signal relative to that of the indium making accurate deconvolution of the spectra more difficult.

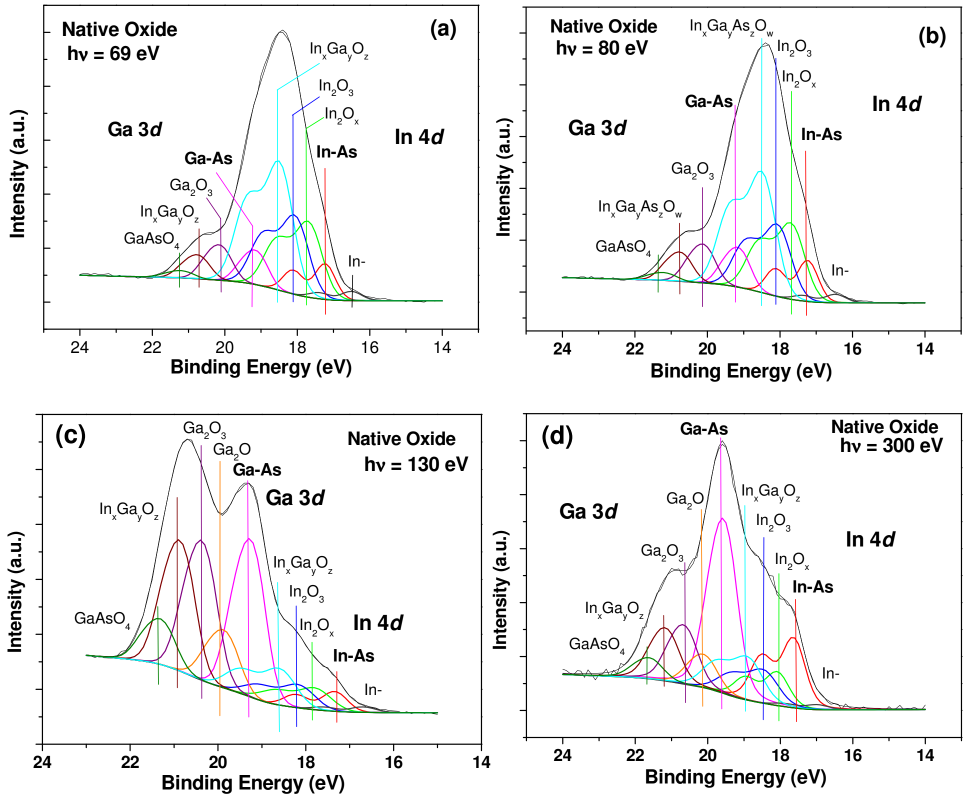

Figure 3.20 Peak fitted photoemission spectra for the In 4*d* and Ga 3*d* peaks at photon energies of 69 eV (a), 80 eV (b), 130 eV (c) and 300 eV (d) from the native oxide.

However, upon annealing, as shown in the curve fitted spectra after the 400 °C anneal in figure 3.21, again for the four different photon energies, a large variation in the oxide composition is observed. As previously reported for the sample scanned using XPS, there is an increase in gallium oxide at the expense of the indium oxide. We can see that the Ga_2O peak is now evident at all photon energies and at quite a significant level in comparison to the other oxidation states, which suggests that it is a relatively stable state of gallium oxide but requires energy or a distinct reaction mechanism to form which is not favoured at room temperature. We can also see that there is no evidence of the $GaAsO_4$ peak at 2.05 eV from the bulk and which as we saw had also been removed from the As 3*d* spectra by 250 °C lending credence to the assignment of this peak as a mixed gallium and arsenic oxide.

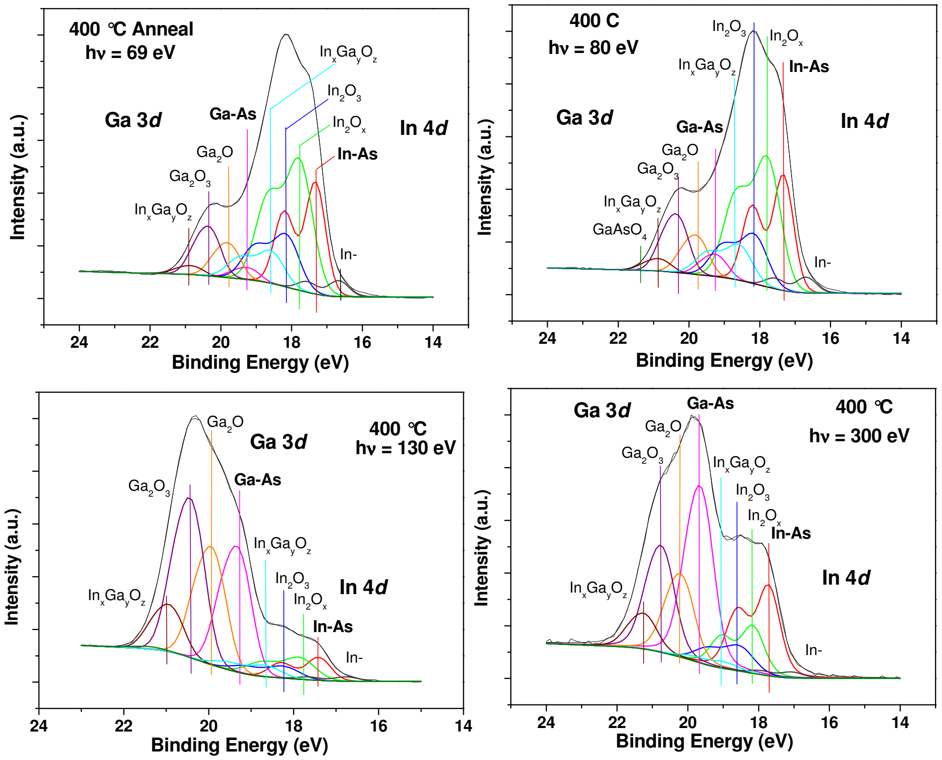

Figure 3.21 Photoemission spectra for the In 4*d* and Ga 3*d* peaks at 69 eV (a), 80 eV (b), 130 eV (c) and 300 eV (d) after annealing at 400 °C for 30 minutes.

If we look more closely at the individual oxidation states and how they change as a function of annealing temperature, we can get an interesting picture regarding their thermal stabilities. To begin with, we will look at the total oxide contribution of the individual peaks in relation to the bulk peak areas to get an overview of what is happening to the level of individual elemental oxides present, as shown in figure 3.22. These plots highlight changes in the relative composition of the oxide layer by tracking the trends determined from the peak fitted data and do not attempt to quantify the actual composition which would be inherently difficult to do to any degree of accuracy based on the errors involved related to the fitting procedure. Also due to the variations in the photoionisation cross sections, this is the most straight forward method of carrying out this analysis as it is independent of the variations in the intensity of the signals while being an accurate reflection of the variations in the combined signals from the oxides.

Again we see the ratio of the oxide to the bulk peak for the four photon energies used to probe the In 4*d* and Ga 3*d* spectra as well as the arsenic oxide ratio, included in figure 3.22(a) as the 69 eV photon energy produces electrons from the In 4*d* and Ga 3*d* core levels with the same KE as electrons from the As 3*d* level at hν = 92 eV of ~50 eV meaning they have virtually the same sampling depth since they are attenuated by the same overlayer. Also included is the ratio of the average of the combined indium and gallium oxide ratios as this provides an added insight into the overall composition of the layer.

Being most surface sensitive, the 69 eV and 80 eV photon energies provide the highest oxide to bulk ratios and hence provide us with the most surface information however, since the higher photon energy plots are less affected by variations in the overlayer oxide thickness, they do help us create a clearer picture of the overall composition.

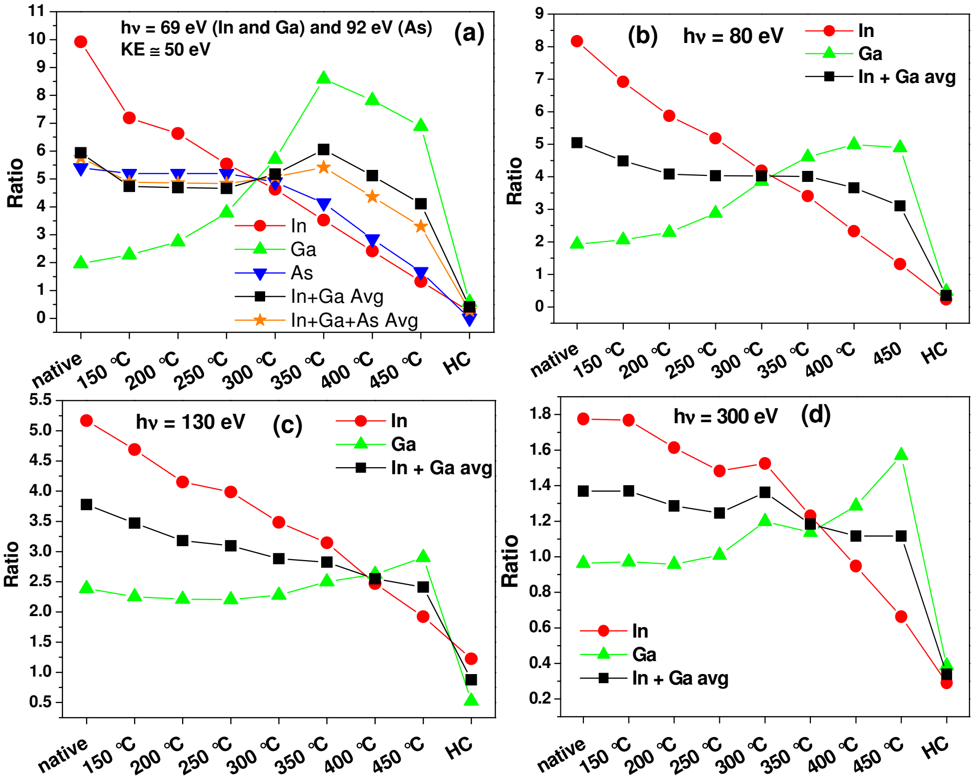

Figure 3.22 Ratio of oxide to bulk peaks from As 3*d* at hν = 92 eV (a) and In 4*d* and Ga 3*d* at hν = 50 eV (a) and for In 4d and Ga 3d at 80 eV (b), 130 eV (c) and 300 eV (d) as a function of annealing temperature and after exposure to atomic hydrogen

In all four plots, we see an increase in the gallium oxide ratio coupled with a decrease in the indium oxide ratio, whereas we see in figure 3.22(a) that the arsenic oxide ratio does not change until it reaches ~250 °C. We also see from this plot that the combined oxide ratios also do not change until we reach this temperature. What this tells us is that up to 250 °C, the increase in gallium oxide is due only to oxygen transfer from indium with no net oxygen loss, apart from a small reduction in indium oxide at low temperature which will be explained by looking at the changes in the individual oxide component ratios later.

Above 250 °C, the arsenic oxide ratio begins to decrease at which point in 3.22 (a) we see an increase in the combined In and Ga oxide ratios. This suggests that there is oxygen transfer to either indium or gallium from the arsenic oxides and since the rate of decrease in the indium oxide does not change and the gallium oxide ratio is seen to accelerate at 300 °C, it is reasonable to conclude that there is oxygen transfer from the arsenic to gallium oxides. By 400 °C, the gallium oxide ratio is also seen to decrease in the 69 eV plot, as well as the combined oxide ratios, which tells us that oxide is being lost from the surface, causing the bulk signals to increase.

Looking at the higher photon energy plots in figures 3.22(c) and (d), which as stated are less sensitive to changes in the oxide thickness, we can see that the combined In and Ga ratio stays relatively constant up to 450 °C until the sample is exposed to atomic hydrogen. This suggests that is it only arsenic oxide that is being removed with increasing annealing temperature and that although the indium oxide continues to decrease with increased annealing temperature, it is only due to an oxygen bond transfer to gallium.

The effect of annealing on the individual indium oxidation states is shown in figure 3.23 again for the four different photon energies used. Initially at 150 °C - 200 °C we see a significant reduction in the $In_xGa_yO_z$ peak. As the temperature increases, the rate of decrease slows but it continues to reduce up to 450 °C at which point it is virtually all removed.

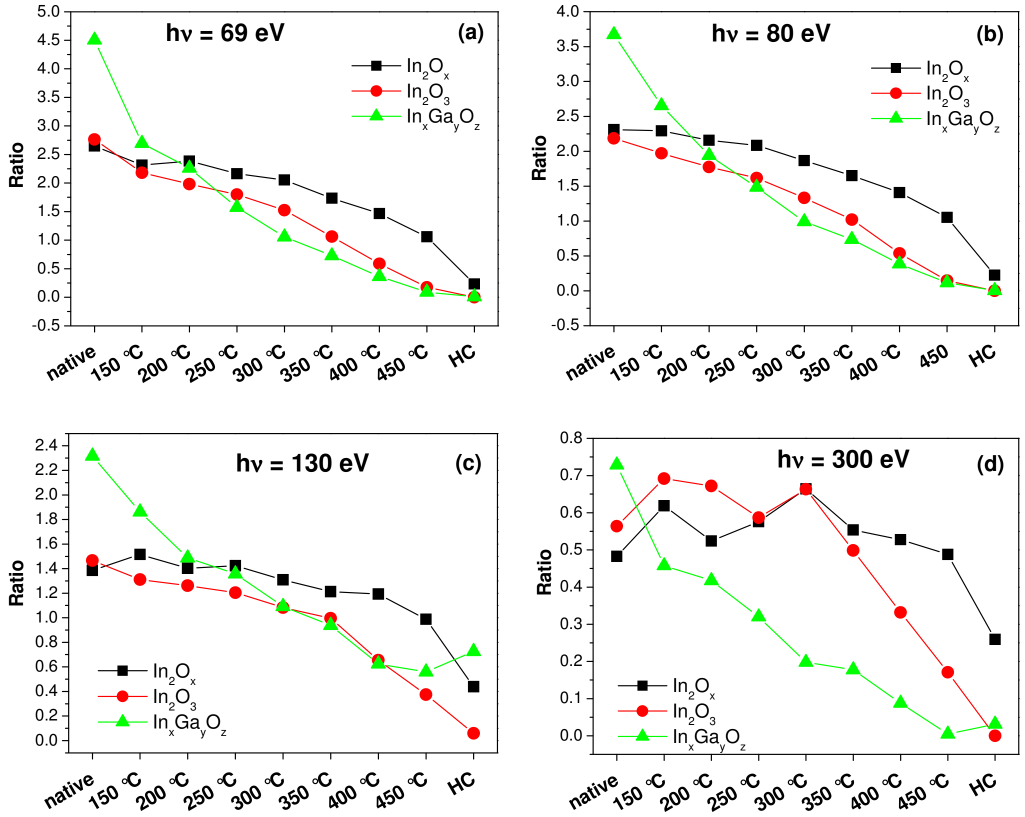

Figure 3.23 Indium oxide components to bulk ratio highlighting changes in oxide composition and thermal stability at various photon energies as a function of annealing temperature

The In_2O_x and In_2O_3 ratios are also seen to decrease as the sample is annealed however the rate of decrease is much slower, especially for the In_2O_x state suggesting that it is the most thermodynamically stable and by 450 °C, there is very little trace of In_2O_3 remaining, whereas there is still an appreciable contribution from the In_2O_x peak. As a result of this, it is concluded that the increase in the total gallium oxide ratio is due predominantly to the reduction of the $In_xGa_yO_z$ peak. The rate of reduction in the In_2O_x and In_2O_3 peak ratios is also seen to increase slightly above 300 °C, which is the point at which the arsenic oxide begins to be removed from the surface and is likely due to the increased contribution from the bulk signal as a result of the reduction in the oxide thickness.

Some observations can also be made about the location of the individual oxide states relative to the substrate by looking at the oxide to bulk ratios. If we compare the initial ratio of the In_2O_x, In_2O_3 and $In_xGa_yO_z$ peak in 3.23(a) and (b) to that in 3.23 (d) we see that there is a relatively larger contribution from the In_2O_x and In_2O_3 components at higher photon energy, suggesting that they are preferentially localised at or near the interface. After exposure to atomic hydrogen there is a significant reduction in the remaining In oxides, however some In_2O_x still remains, again underlining its apparent stability.

The same plots for the gallium oxide peak components are shown in figure 3.24. This time due to the variation in cross section values, the gallium signal is stronger at the higher photon energies relative to the indium signal such that the 130 eV spectra in (c) is likely to provide the highest level of accuracy with regard to the fit and subsequent ratio values.

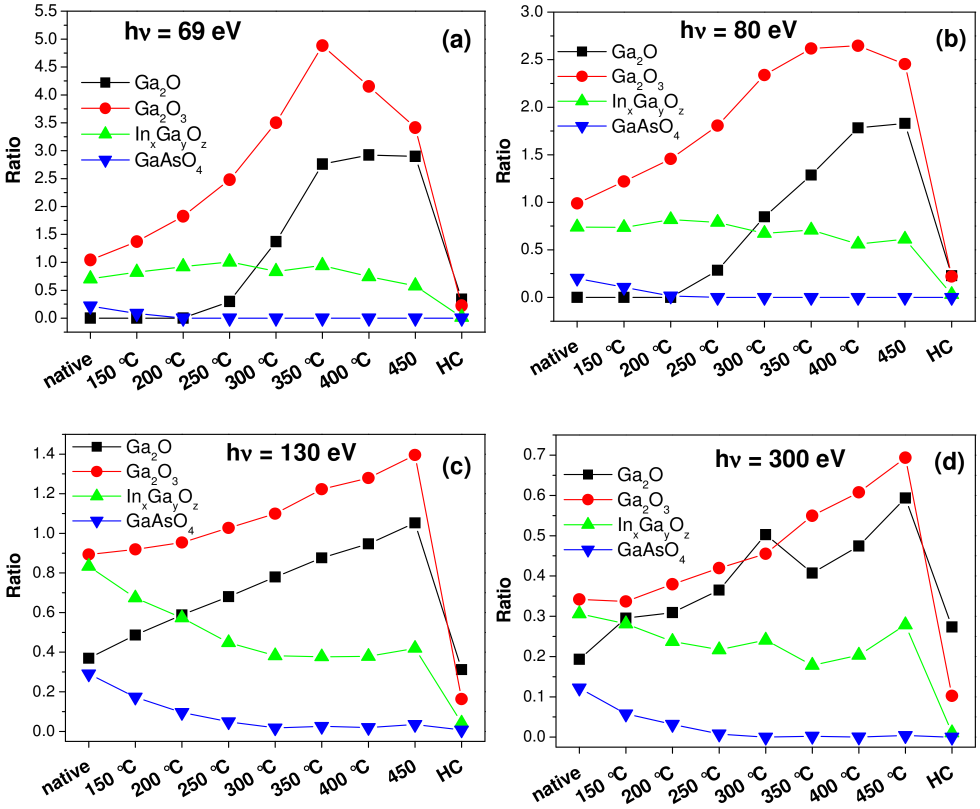

Figure 3.24 Gallium oxide components to bulk ratio highlighting changes in oxide composition and thermodynamic stability at various photon energies as a function of annealing temperature

What is clear from all the plots however is that the increase in the total gallium oxide ratio is due primarily to changes in the Ga_2O and Ga_2O_3 levels present which are seen to increase with the first anneal at 150 °C. From the 130 eV plot in figure 3.24 (c) and 300 eV plot in 3.24 (d) we see that this growth is roughly linear up to the highest annealing temperature and that similar to the indium ratios, the reduction for the low photon energies above 300 °C is likely due to the reduction in the overall oxide thickness as a result of the removal of arsenic oxide. The $GaAsO_4$ ratio is seen to reduce at 150 °C such that there is no trace left within detection limits above 250 °C consistent with the removal of the corresponding peak in the As 3*d* spectra, again suggesting that this is the least stable state.

Based on the relative intensities of the various ratios at different photon energies we are also able to comment on the relative position of the gallium oxides in the layer. At low photon energies initially there is no evidence of Ga_2O however as we move to higher photon energies and increased sampling depth, we begin to see the emergence of the peak suggesting that this state forms preferentially at the interface. It is therefore likely that the In_2O_x, Ga_2O and As^{1+} are located primarily at the interface and provide the bridge to the formation of the other oxide states.

3.4.1.3. Oxide thicknesses

The thickness of the native oxide was calculated from the ratio of the overlayer to the substrate based on the suppression of the substrate signal, taking into account the effective attenuation length of the electrons coming from the sample, as shown in figure 3.25. Initially, we see that the oxide thickness is ~1.3 nm, which equates to roughly 4 monolayers. As the sample is annealed, we see that there is a reduction in the over layer thickness of ~0.15 nm up to 200 °C at which point the thickness stabilises up to 300 °C. As the temperature increases further, we see that there is a dramatic reduction such that the oxide layer has reduced in thickness by over 50% to 0.6 nm or roughly two monolayers by 450 °C.

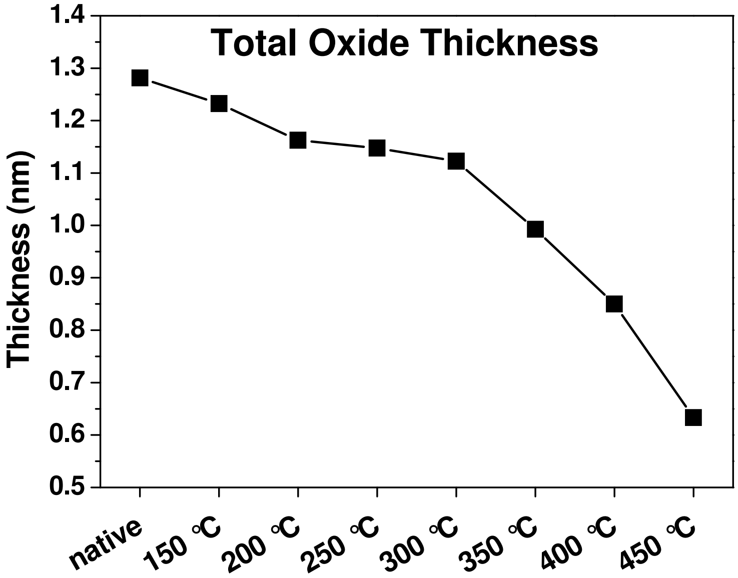

Figure 3.25 Oxide overlayer thickness as a function of annealing temperature based on the attenuation of the substrate peaks

If we look at the breakdown of the thickness contribution of the individual elemental oxides in figure 3.26, we can get an idea of what is causing the reduction. If we take into account that half of the substrate consists of arsenic and the remainder is roughly equal indium and gallium, we can see that initially the combination of indium and gallium oxides has a similar thickness to that of the arsenic oxides, of just greater than 0.6 nm with the indium oxide being twice as thick as the gallium oxide at 0.4 nm. It is worth pointing out that that this oxide is likely to be amorphous, with no distinct definition between the oxides throughout the entire layer. Upon annealing up to 200 °C, we see that there is a reduction in the arsenic and indium oxide thicknesses whereas the gallium oxide thickness increases. However, the combined thickness of the indium and gallium oxides does not change.

This suggests that there is arsenic oxide leaving the surface (being evaporated) which if we correlate to the oxide ratio plots, tells us that it is due to removal of $GaAsO_4$ but with the residual gallium oxide bonds converting to alternate forms of gallium oxide; either Ga_2O or Ga_2O_3. It is therefore reasonable to assume that the reduction in the total thickness of ~1.5Å is the total contribution of the $GaAsO_4$ state, approximating at half a monolayer. The reduction in the indium oxide, again when coupled with the combined indium and gallium oxide thickness, tells us that this is also due to an oxygen bond transfer from the $In_xGa_yO_z$ state to again form gallium oxide.

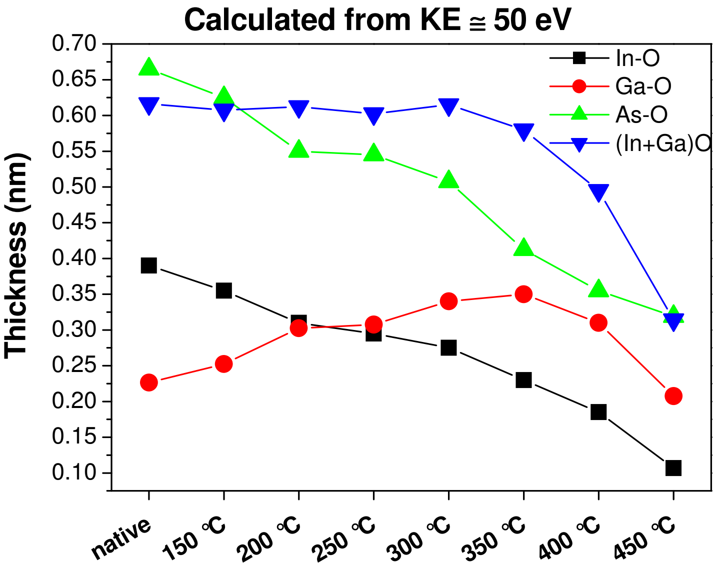

Figure 3.26 Individual oxide component thicknesses contribution to total oxide thickness as a function of annealing temperature highlighting changes in oxide composition with temperature

The thickness is seen to remain stable between 200 °C and 250 °C, with only a minor reduction in the indium oxide but at 300 °C, the point at which the As_2O_3 peak was seen to reach its maximum intensity and the As_2O_5 peak all but removed, we see that there is a reduction in the overall As oxide thickness which continues up to 450°C. What this suggests is that once the As_2O_5 state has finished converting to As_2O_3, the arsenic oxide is no longer stable and begins to evaporate from the surface. The indium oxide continues to decrease to ~1Å at 450 °C and while the gallium oxide is seen to increase, peaking at ~3.5Å at 350 °C, by 450 °C, this has reduced again to ~2Å. Interestingly, the combined gallium and indium thickness is the same as that of the remaining arsenic oxide at 450 °C at roughly 3Å each, or roughly 2 monolayers in total. Since the remaining oxides from the peak fitted data are the As^{1+} peak, In^{1+}, Ga_2O and Ga_2O_3 states, this would add further credence to the idea that the monovalent oxides form the interface between the substrate and the oxide that forms on them, similar to that proposed by Himpsel et al. for the oxidation states of silicon.[51]

3.4.2. Atomic Hydrogen Cleaning

In order to investigate the overall effect of the atomic hydrogen cleaning of the surface after annealing it was necessary to compare it to a sample that was exposed to atomic hydrogen without undergoing prior high temperature annealing. The same scans were taken after exposure to atomic hydrogen at substrate temperatures of 360 °C, 380 °C and 400 °C for periods of time of 30 and 60 minutes, as those during the annealing study, with the same fitting parameters used throughout. From the fitted spectra, the ratio of peaks from the residual oxide to the bulk peak was again calculated in order to determine the changes taking places in the oxide composition, as shown in figure 3.27.

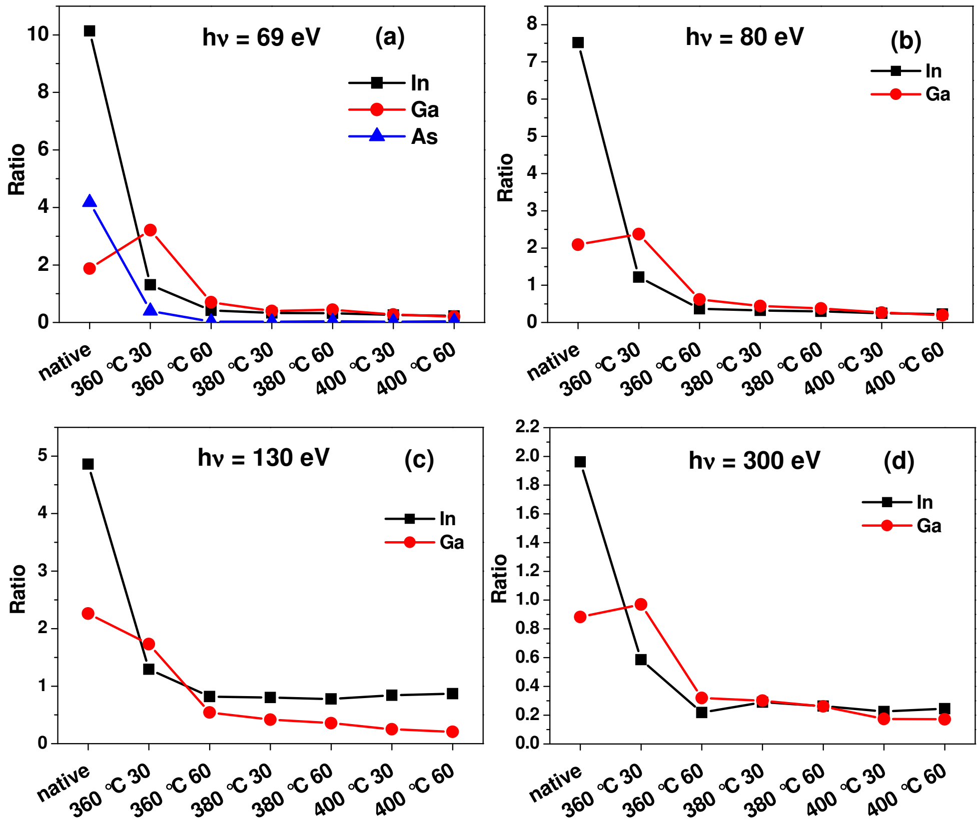

Figure 3.27 Ratio of In, Ga and As oxide to bulk peaks at (a) 69 eV (and 92 eV for As), (b) 80 eV, (c) 130 eV and (d) 300 eV after successive exposures to atomic hydrogen at increasing substrate temperature for 30 and 60 minutes

Again the As 3*d* peak was only taken at a single photon energy of 92 eV, whereas the In 4*d* and Ga 3*d* peak were taken at the same four photon energies as before. We can see that for the first hydrogen clean at 360 °C for 30 minutes, while there is a significant reduction in the level of arsenic oxide present in 3.27 (a), there is still a trace remaining, however with 60 minutes exposure, all of the arsenic oxide has been removed within detection limits.

In terms of the indium and gallium oxides however, this is not the case. After the first exposure, again we see that although there is a significant reduction in the indium oxides, there is an increase in the gallium oxide ratio, suggesting that there is an oxygen transfer from either arsenic or indium and that the atomic hydrogen has not had enough time to fully interact with the oxide. Based on the results with annealing alone, it is fair to say that the increase in gallium oxide is most likely due to oxygen transfer from the indium oxide states as a result of the increased substrate temperature. After 60 minutes exposure however, the level of gallium and indium oxides present are significantly reduced and at a similar level, consistent with that seen after hydrogen exposure on the annealed sample. With increased temperature and exposure time, there is very little change seen in the ratio with a residual indium and gallium oxide signal remaining throughout with calculated thickness values suggesting a thickness of ~ 0.4 nm, however due to the small signal from the oxide, the associated error with this calculation could be on the order of 20%.

Previous studies have shown that is it possible to fully remove the native oxides from the $In_{0.2}Ga_{0.8}As$ surface with atomic hydrogen using substrate temperatures of 390 °C with similar hydrogen flow rates as used here, however this was coupled with a significant indium loss from the surface.[30] It is not clear whether the reported indium loss and the relative stability of the residual oxides in this study is a consequence of the increased indium content in the sample or that slight variations in processing conditions (for example, initially using a lower temperature) have a significant effect on the overall results and would need to be investigated further.

Looking at the ratio of the individual gallium oxide components as a function of atomic hydrogen exposure parameters in figure 3.28, and particularly in 3.28 (c) and (d) which having the largest photoionisation cross section values for the Ga 3*d* peak produce the most accurate peak fit, we are able to determine which oxide states are contributing to the residual oxide.

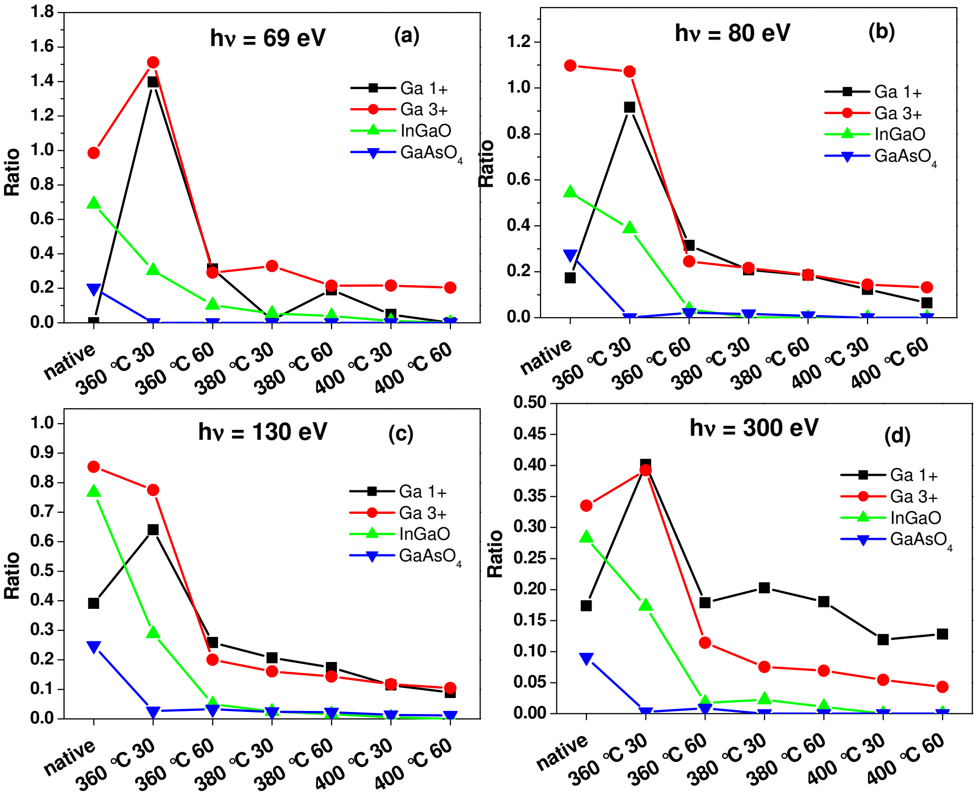

Figure 3.28 Ratio of gallium oxide components to the bulk peak at photon energies of (a) 69 eV, (b) 80 eV, (c) 130 eV and (d) 300 eV after successive exposures to atomic hydrogen at increasing substrate temperature for 30 and 60 minutes

We can see that there is a rapid decrease in the $In_xGa_yO_z$ and $GaAsO_4$ ratios with the first exposure for 30 minutes and also an increase in both the Ga_2O and Ga_2O_3 ratios, similar to the changes seen in the sample upon annealing to 350 °C in figure 3.22. However upon increasing the exposure time to 60 minutes the $GaAsO_4$ state is removed to within detection limits and the $In_xGa_yO_z$ state is also fully removed, which did not occur by annealing alone. There is also a significant decrease in the Ga_2O and Ga_2O_3 states however these are never fully removed. Based on the ratios from the higher photon energy spectra in figures 3.28 (c) and (d), Ga_2O is slightly more abundant throughout, suggesting that it is the most stable state and while both the Ga_2O and Ga_2O_3 ratios are seen to decrease slightly, it is not clear whether increasing the exposure time or the substrate temperature would facilitate the removal of all of the gallium oxide.

In terms of the change in the corresponding indium oxide ratios in figure 3.29, we see that with the first exposure, there is a significant reduction in all three of the oxidation states, and based specifically on the 69 eV and 80 eV photon energy ratios which provide the highest level of accuracy for the In 4*d* peak fit, after 60 minutes exposure at 360 °C, there is no trace of the In_2O_3 or $In_xGa_yO_z$ peaks within detection limits. There is still a residual In_2O peak throughout however, suggesting that again this is the most stable form of the oxide. Increasing the substrate temperature or exposure time has no significant affect on the level of indium oxide remaining, which has a thickness on the order of a monolayer.

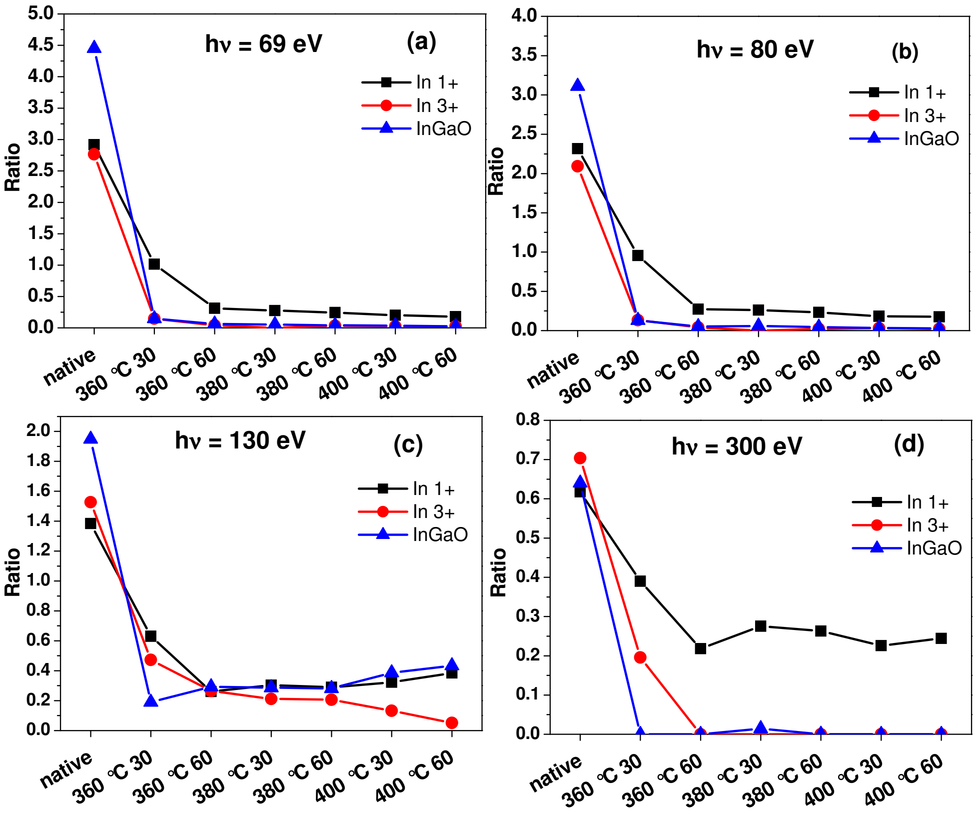

Figure 3.29 Ratio of indium oxide components to the bulk peak at photon energies of (a) 69 eV, (b) 80 eV, (c) 130 eV and (d) 300 eV after successive exposures to atomic hydrogen at increasing substrate temperature for 30 and 60 minutes

Considering there is no evidence of As_2O remaining on the surface and the final thickness of the oxide is estimated at roughly one monolayer, it is reasonable to assume that the surface is left with a group III oxide termination.

3.4.3. Carbon and surface contamination

While all this seems to suggest that it is very difficult to remove the residual gallium and indium surface oxides, which based on the calculated thickness and signal intensities, form the immediate interface with the semiconductor substrate and could have implications for the performance of devices, exposure to atomic hydrogen can play another important role in the preparation of high quality surfaces in terms of removal of surface contamination. The carbon 1*s* spectra from the annealed (and subsequently exposed to atomic hydrogen) sample and the sample only exposed to atomic hydrogen are shown in figure 3.30 and 3.31 respectively, taken at a photon energy of 345 eV. If we look first at spectra from the annealed sample in figure 3.30 (a), with the fitted peak areas shown in 3.30 (b), we can see that there is a significant carbon signal evident throughout the annealing process, with a modest decrease taking place above 200 °C. With annealing at 450 °C and subsequent exposure to atomic hydrogen, there is virtually no change evident in the level of carbon present suggesting that there is a relatively strong interaction taking place between the carbon and the surface preventing its removal. This is also suggested by a 0.2 eV shift of the peak to a lower binding energy with the first anneal.

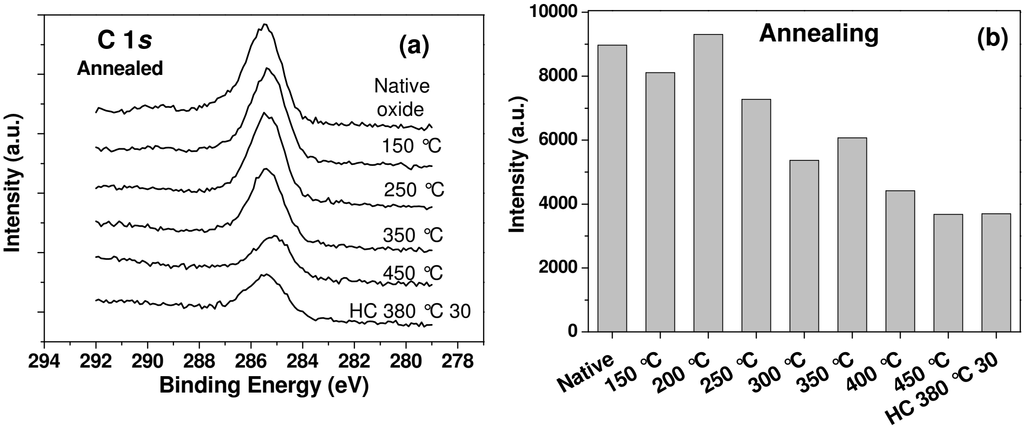

Figure 3.30 (a) Carbon 1*s* spectra from InGaAs sample at a photon energy of 345 eV after successive anneals up to 450 °C and subsequent exposure to atomic hydrogen and (b) a plot of the fitted area of the peaks

When we look at the corresponding spectra in figure 3.31 (a) and (b) with no prior annealing before exposure to atomic hydrogen, we see a significantly different scenario taking place. Prior to exposure, there is a similar level of carbon evident on both samples, however, with the first exposure, the C 1*s* signal is reduced to less than 10 % of it's original value and with the fourth exposure at 380 °C for 60 minutes, there is no evidence of any carbon remaining on the surface within detection limits. This suggests that the carbon is removed before it has a chance to bond with the surface due to the elevated temperature, which could have implications for the level of defect states at the oxide semiconductor interface as well as the growth of subsequent oxides on the semiconductor surface.

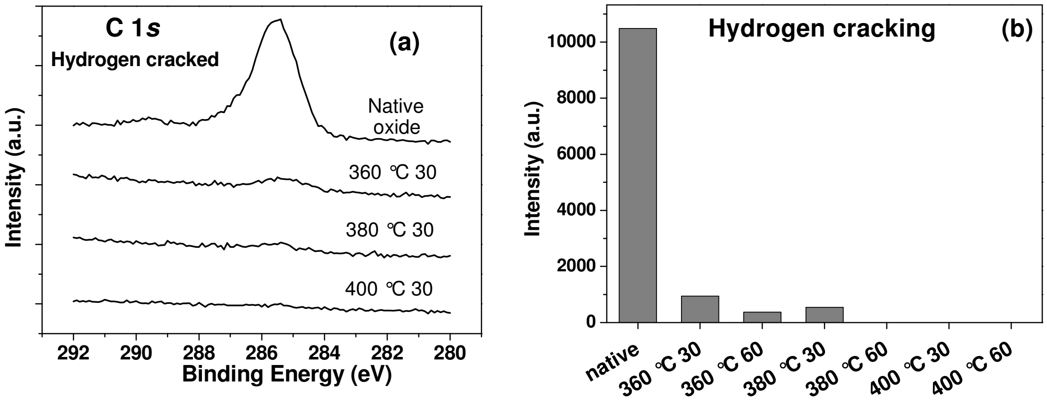

Figure 3.31 Carbon 1*s* spectra from InGaAs sample at a photon energy of 345 eV after exposure to atomic hydrogen with increasing substrate temperature and exposure time and (b) the fitted area of the C 1*s* peaks

A further indication that the surface has become significantly free of oxide and carbon comes from the valance band spectra taken at 130 eV, shown in figure 3.32. The valence band is very sensitive to the presence of oxygen on the surface, more so than any other spectra acquired in this study. If we compare the spectra after annealing to 450 °C to that of the native oxide, there is very little difference evident; however with subsequent exposure to atomic hydrogen, we see the formation of a dramatically different valence band spectra, which compares favourably to the spectra seen from an atomically clean GaAs sample.[32] This spectrum is also consistent with the valence band spectra seen from the hydrogen cleaned sample with no prior annealing.

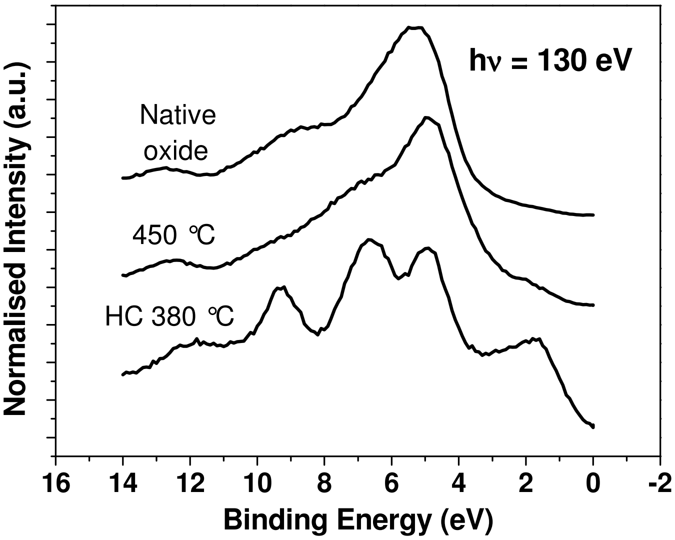

Figure 3.32 Valence band spectra taken at 130 eV from the InGaAs native oxide, after annealing to 450 °C and subsequent exposure to atomic hydrogen

3.5. Conclusions

This chapter has focused on utilising chemical and thermal changes to the native oxide on $In_{0.53}Ga_{0.47}As$ in order to assist in the identification of the various oxide states present and their associated binding energies. Through the use of chemical treatments, the presence of interfacial sulphur bond formation as well as the absence of significant hydroxide contributions to the resultant oxide layers is seen. Using synchrotron based photoemission with its inherent surface sensitivity, in conjunction with sequential thermal annealing of the native oxide, identification of the initial oxide states at the semiconductor oxide interface was possible as well as conclusive determination of the presence of compound oxide states, which have previously been both misasigned and undetected. By monitoring the changes in the spectra as a function of annealing temperature, it was also possible to comment on the relative thermal stability of the various oxide components. The accurate determination of the native oxides remaining on the surface is of utmost importance for the development and manufacture of semiconductor devices, having implications for determination of the level of defect states present. The wide variation in the relative stability of the oxide states suggests that some are more likely to play a significant role in the deterioration of the devices than others. Due to the relatively high thermal stability of the Ga_2O and In_2O oxide states seen in this study, it is possible that they would not impact critically on device performance and would in fact provide a bridge for the formation of other high-κ dielectric oxide materials on the surface, while also reducing the risk of inducing interfacial disruption, with would have significant implications for degradation of charge carrier mobility.

The relatively simple process of leaving the surface terminated in these binary oxides through the use of atomic hydrogen as well as the removal of all spurious contamination to virtually within detection limits is also a significant result, as it was done without the previously reported loss of indium from the surface.

The development of the fitting parameters for the arsenic, gallium and indium peaks means that the determination of surface modifications to the InGaAs surface as a result of further sample processing, for example the growth of alternative high-κ metal oxide dielectric layers on the surface, is much more straight forward with any deviation in the spectra from the fitting parameters indication of interactions at the oxide semiconductor interface.

3.6. References

---

[1] G. D. Wilk, R. M. Wallace, Appl. Phys. Lett. 74, 2854 (1999)

[2] http://www.itrs.net/

[3] H.R. Huff, D.C. Gilmers, High Dielectric constant materials – VSLI MOSFET applications, Springer, 2005

[4] J. J. Chambers, G. N. Parsons, J. Appl. Phys. 90, 918 (2001)

---

[5] A. M. Sonnet, C. L. Hinkle, M. N. Jivani, R. A. Chapman, G. P. Pollack, R. M. Wallace, E. M. Vogel, Appl. Phys. Lett. 93, 122109 (2008)

[6] W. Liu, Fundamentals of III-V Devices, Wiley, (1999)

[7] E. O'Connor, R. D. Long, K. Cherkaoui, K. K. Thomas, F. Chalvet, I. M. Povey, M. E. Pemble, P. K. Hurley, B. Brennan, S. B. Newcomb, G. Hughes, Appl. Phys. Lett. 92, 022902 (2008)

[8] M. Itsumi, SiO_2 in Si microdevices, Springer (2002)

[9] S. Adachiz, D. Kikuchi, J. Electrochem Soc, 147, 4618, (2000)

[10] C-C. Cheng, C-H. Chien, G-L. Luo, C-K. Tseng, H-C. Chiang, C-H. Yang, C-Y. Chang, J. Electrochem. Soc., 155, G56 (2008)

[11] D. Sheela, N. Dasgupta, Semicon. Sci. Tech., 23, 035018 (2008)

[12] E.V. Konenkova, Vacuum, 67, 43, (2002)

[13] A.Y. Kang, P.M. Lenahan, J.F. Conley Jr., R. Solanki, Appl. Phys. Lett. 81, 1128 (2002)

[14] R. Soares, J. Graffeuil, J. Obregon, Applications of GaAs MESFETs, Artech House, (1983)

[15] for example MGF4934AM - SUPER LOW NOISE InGaAs HEMT (4pin flat lead package) - Mitsubishi Electric Semiconductor

[16] É. O'Connor, S. Monaghan, R. D. Long, A. O'Mahony, I. M. Povey, K. Cherkaoui, M. E. Pemble, G. Brammertz, M. Heyns, S. B. Newcomb, V. V. Afanas'ev, P. K. Hurley, Appl. Phys. Letts. 94, 102902 (2009)

---

[17] V.V. Afanas'ev, A. Stesmans, G. Brammertz, A. Delabie, S. Sionke, A. O'Mahony, I.M. Povey, M.E. Pemble, E. O'Connor, P.K. Hurley, S.B. Newcomb, Microelectronic Engineering, 86, 1550, (2009)

[18] http://www.wafertech.co.uk/galliumarsenide.htm

[19] I. Horcas, R. Fernandez, J.M. Gomez-Rodriguez, J. Colchero, J. Gomez-Herrero, A.M. Baro, Rev. Sci. Instrum. 78, 013705 (2007)

[20] H. Chernoff, E.L. Lehmann, Ann. Math. Stat. 25, 579 (1954).

[21] M.P. Seah, M.T. Brown, J. Electron Spectrosc. Relat. Phenom. 95, 71 (1998).

[22] J.M. Conny, C.J. Powell, L. Currie, Surf. Interface Anal. 26, 939 (1998).

[23] C.L. Hinkle, M. Milojevic, B. Brennan, A.M. Sonnet, F.S. Aguirre-Tostado, G. Hughes, E.M. Vogel, R.M. Wallace, Appl. Phys. Lett., 94, 162101, (2009)

[24] AAnalyzer: A. Herrera-Gomez, http://qro.cinvestav.mx/~aanalyzer/

[25] S. Arabasz, E. Bergignat, G. Hollinger, J. Szuber, Vacuum, 80, 888, (2006)

[26] J. Čechal, T. Matlocha, J. Polčák, M. Kolíbal, O. Tomanec, R. Kalousek, P. Dub, T. Šikola, Thin Solid Films, 517, 1928, (2009)

[27] J. Robertson, Appl. Phys. Lett, 94, 152104 (2009)

[28] B. Brennan, M. Milojevic, H. C. Kim, P. K. Hurley, J. Kim, G. Hughes, R. M. Wallace, Electrochem. Solid-State Lett., 12, H205, (2009)

[29] M. Milojevic, C.L. Hinkle, F.S. Aguirre-Tostado, H.C. Kim, E.M. Vogel, J. Kim, R.M. Wallace, Appl. Phys. Lett, 93, 202902, (2008)

---

[30] F. S. Aguirre-Tostado, M. Milojevic, C. L. Hinkle, E. M. Vogel, R. M. Wallace, S. McDonnell, G. J. Hughes, Appl. Phys. Letts., 92, 171906 (2008)

[31] T. Ishikawa, H. Ikoma, Jpn. J. Appl. Phys. 32, L607, (1993)

[32] Zhi Liu, Yun Sun, F. Machuca, P. Pianetta, W.E. Spicer, J. Vac. Sci. Technol., A, v 21, n 1, p 212-18, Jan. 2003

[33] M.V. Lebedev, D. Ensling, R. Hunger, T. Mayer, W. Jaegermann, Appl. Surf. Sci., 229, 226, (2004)

[34] Yun Sun, P. Pianetta, Po-Ta Chen, M. Kobayashi, Y. Nishi, N. Goel, M. Garner, W. Tsai, Appl. Phys. Lett., 93, 194103, (2008)

[35] P. Moriarty, B. Murphy, L. Roberts, A.A. Cafolla, L. Koenders, P. Bailey, G. Hughes, Phys. Rev B, 50, 19,14237, (1994)

[36] Chemix © Arne Standnes: http://home.c2i.net/astandne/

[37] S. Arabasz, E. Bergignat, G. Hollinger, J. Szuber, Appl. Surf. Sci., 252, 7659, (2006)

[38] Phonon broadening 73 P. Unsworth, J. E. Evans, P. Weightman, A. Takahashi, J. A. D. Matthew, Q. C. Herd, Phys. Rev. B, 54, 1, (1996)

[39] S. Sloboshanin, R.K. Gebhardt, J.A. Schaefer, T. Chasse, Surf. Sci, 431, 252, (1999)

[40] M.V. Lebedev, E. Mankel, T. Mayer, W. Jaegermann, J. Phys. Chem. C, 112, 18510, (2008), 61, 62, 63, 65

[41] M. Beerbom, Th. Mayer, W. Jaegermann, D.R. Batchelor, D. Schmeier, Anal. Bioanal.Chem., 374, 650, (2002)

---

[42] M. Larive, G. Jezequel, J. P. Landesman, F. Solal, J. Nagle, B. Lepine, A. Taleb-Ibrahimi, G. Indlekofer, and X. Marcadet, Surf. Sci. 304, 298 (1994).

[43] D. Paget, J.E. Bonnet, V.L. Berkovits, P. Chiaradia, J. Avila, Phys. Rev. B, 53, 4604, (1996)

[44] T. Ishikawa, H. Ikoma, Jpn. J. Appl. Phys. 31, 3981 (1992)

[45] G. Alvarez, H.J. Silverstone, Phys. Rev. A, 40, 3690, (1989)

[46] J.J. Yeh, I. Lindau, Atomic Data and Nuclear Data Tables, 32, 1, (1985)

[47] http://srdata.nist.gov/xps/

[48] V. Chab, L. Pekarek, I. Ulrych, J. Suchy, K.C. Prince, M. Peloi, M. Evans, C. Comicioli, M. Zacchigna, C. Crotti, Surf. Sci., 377, 261, (1997)

[49] G. Hollinger, R. Skheyta-Kabbani, M. Gendry, Phys. Rev. B 49, 11159 (1994)

[50] G. Landgren, R. Ludeke, Y. Jugnet, J. F. Morar, and F. J. Himpsel, J. Vac. Sci. Technol. B 2, 351, (1984)

[51] F.J. Himpsel, F.R. McFeely, A. Taleb-Ibrahimi, J.A. Yarmoff, Phys. Rev B. 38, 6084. (1988)

Appendix

References from table 3.1 and 3.2.

1. D. Sheela, N. Dasgupta, Semicon. Sci. Tech., 23, 035018 (2008)
2. R.S. Besser, C.R. Helms, J. Appl. Phys., 65, 4306, (1989)
3. C-C. Cheng, C-H. Chien, G-L. Luo, C-C. Chang, C-C. Kei, C-H. Yang, C-N Hsiao, T-P. Perng, C-Y. Chang, J. Phys. Conf. Series, 100, 042002 (2008)
4. V.N. Bessolov, M.V. Lebedev, A.F. Ivankov, W. Bauhofer, D.R.T. Zahn, Appl. Surf. Sci., 133, 17, (1998)
5. E.V. Konenkova, Vacuum, 67, 43, (2002)
6. S. Arabasz, E. Bergignat, G. Hollinger, J. Szuber, Vacuum, 80, 888, (2006)
7. H. Sugahara, M. Oshima, H. Oigawa, Y. Shigekawa, Y. Nannichi, J. Appl. Phys., 69, 4349, (1991)
8. M. Katayama, M. Aono, H. Oigawa, Y. Nannichi, H. Sugahara, M. Oshima, Jpn. J. Appl. Phys., Pt. 2 (Letts), 30, L786, (1991)
9. B.A. Kuruvilla, S.V. Ghaisas, A. Datta, S. Banerjee, S.K. Kulkarni, J. Appl. Phys., 73, 4384, (1993)
10. Z.S. Li, X.Y. Hou, W.Z. Cai, W. Wang, X.M. Ding, W. Xun, J. Appl. Phys., 78, 2764, (1995)
11. M.G. Kang, S.H. Sa, H.H. Park, K.S. Suh, J.L. Lee, Mat. Sci. Eng., B46, 65 (1997)
12. M.G. Kang, H.H. Park, K.S. Suh, J.L. Lee, Thin Solid Films, 290, 328, (1996)

13. J.S. Herman, F.L. Terry, Jr., Appl. Phys. Lett., 60, 716, (1992)

14. D. Paget, A.O. Gusev, V.L. Berkovtis, Phys. Rev. B, 53, 4615, (1996)

15. J. Szuber, E. Bergignat, G. Hollinger, A. Polakowska, P. Koscielniak, Vacuum, 67, 53, (2002)

16. X. Yi, L. Hung-Chun, P.D. Ye, IEEE Trans. Electron Devs., 54, 1811, (2007)

17. V.L. Berkovits, V.P. Ulin, M. Losurdo, P. Capezzuto, G. Bruno, J. Electrochem. Soc., 152, 5, G349, (2005)

18. C-C. Cheng, C-H. Chien, G-L. Luo, C-K. Tseng, H-C. Chiang, C-H. Yang, C-Y. Chang, J. Electrochem. Soc., 155, G56 (2008)

19. E. Plis, J.L. Sang, Z. Zhimei, A. Amtout, S. Krishna,. IEEE J. Sel. Top. Quantum Electron., 12, 1269, (2006)

20. L-W. Lai, J-T. Chen, L-R. Lou, C-H. Wu, C-T. Lee, J. Electrochem. Soc., 155, B1270, (2008)

21. M.M. Frank, S.J. Koester, M. Copel, J.A. Ott, V.K. Paruchuri, S. Huiling, R. Loesing, Appl. Phys. Lett., 89, 112905, (2006)

22. P.T. Chen, Y. Sun, E. Kim, P.C. McIntyre, W. Tsai, M. Garner, P. Pianetta, Y. Nishi, C.O. Chui, J. Appl. Phys., 103, 034106, (2008)

23. D. Shahrjerdi, D.I. Garcia-Gutierrez, T. Akyol, S.R. Bank, E. Tutuc, J.C. Lee, S.K. Banerjee, Appl. Phys. Lett., 91, 193503, (2007)

24. C.-I. Kuo, E.Y. Chang, H.-T. Hsu, C.-C. Chen, C.-Y. Chang, Jpn. J. Appl. Phys., 47, 3441, (2008)

25. M.-J. Jeng, H.-T. Wang, L.-B. Chang, Y.-C. Cheng, S.-T. Chou, J. Appl. Phys., 86, 6261, (1999)

26. P. Tomkiewicz, S. Arabasz, B. Adamowicz, M. Miczek, J. Mizsei, D.R.T. Zahn, H. Hasegawa, J. Szuber, Surf. Sci., 603, 498, (2009)

27. Z. Jin, S. Neumann, W. Prost, F.J. Tegude, Phys. Status Solidi A, 201, 1017, (2004)

28. L. Geelhaar, R.A. Bartynski, F. Ren, M. Schnoes, D.N. Buckley, J. Appl. Phys., 80, 3076, (1996)

29. R. Driad, Z.H. Lu, S. Charbonneau, W.R. McKinnon, S. Laframboise, P.J. Poole, S.P. McAlister, Appl. Phys. Lett., 73, 665, (1998)

30. S. Suzuki, S. Kodama, H. Hasegawa,: Solid-State Electron., 38, 1679, (1995)

31. S. Oktyabrsky, V. Tokranov, M. Yakimov, R. Moore, S. Koveshnikov, W. Tsai, F. Zhu, J.C. Lee, Mater. Sci. Eng., B, 135, 272, (2006)

32. E. O'Connor, R.D. Long, K. Cherkaoui, K.K. Thomas, F. Chalvet, I.M. Povey, M.E. Pemble, P.K. Hurley, B. Brennan, G. Hughes, S.B. Newcomb, Appl. Phys. Lett., 92, 022902, (2008)

33. S. Byungha, C. Donghun, J.S. Harris, P.C. McIntyre, Appl. Phys. Lett., 93, 052911, (2008)

34. H.J. Tang, X.L. Wu, K.F. Zhang, Y.F. Li, J.H. Ning, Y. Wang, X. Li, H.M. Gong, Appl. Phys. A, 91, 651, (2008)

35. Y. Sun, E.W. Kiewra, J.P. de Souza, J.J. Bucchignano, K.E. Fogel, D.K. Sadana, G.G. Shahidi, IEEE Electron Device Lett., 30, 5, (2009)

36. N. Goel, P. Majhi, C.O. Chui, W. Tsai, D. Choi, J.S. Harris, Appl. Phys. Lett., 89,163517, (2006)

37. O. InJo, H. Kim, M. Zhang, F. Zhu, S. Park, J. Yum, H. Zhao, D. Garcia, P. Majhi, N. Goel, W. Tsai, C.K. Gaspe, M.B. Santos, J.C. Lee, Appl. Phys. Lett., 92, 202903, (2008)

38. Minghwei Hong, J. Raynien Kwo, Pei-chun Tsai, Yaochung Chang, Mao-Lin Huang, Chih-ping Chen, Tsung-da Lin, Jpn. J. Appl. Phys., 46, 3167, (2007)

39. M. Milojevic, C.L. Hinkle, F.S. Aguirre-Tostado, H.C. Kim, E.M. Vogel, J. Kim, R.M. Wallace, Appl. Phys. Lett., 93, 252905 (2008)

40. D. Paget, J.E. Bonnet, V.L. Berkovits, P. Chiaradia, J. Avila, Phys. Rev. B, 53, 4604, (1996)

41. D. Shahrjerdi, E. Tutuc, S.K. Banerjee, Appl. Phys. Lett., 91, 063501, (2007)

42. P. Moriarty, B. Murphy, L. Roberts, A.A. Cafolla, L. Koenders, P. Bailey, G. Hughes, Phys. Rev B, 50, 14237, (1994)

43. É. O'Connor, S. Monaghan, R.D. Long, A. O'Mahony, I.M. Povey, K. Cherkaoui, M.E. Pemble, G. Brammertz, M. Heyns, S.B. Newcomb, V.V. Afanas'Ev, P.K. Hurley, Appl. Phys. Lett., 94, 102902, (2009)

44. H. Morota, S. Adachi, J. Appl. Phys., 105, 043508, (2009)

45. M.V. Lebedev, E. Mankel, T. Mayer, W. Jaegermann, J. Phys. Chem. C, 112, 18510, (2008)

46. M. Petravic, P.N.K. Deenapanray, B.F. Usher, K.-J. Kim, B. Kim, Phys. Rev. B, 67,195325, (2003)

47. Yun Sun, Zhi Liu, F. Machuca, P. Pianetta, W.E. Spicer, J. Vac. Sci. Technol., A, 21, 219, (2003)

48. F.J. Palomares, M. Alonso, I. Jimenez, J. Avila, J.L. Sacedon, F. Soria, Surf. Sci., 482, 121, (2001)

49. M. Beerbom, Th. Mayer, W. Jaegermann, D.R. Batchelor, D. Schmeier, Anal. Bioanal.Chem., 374, 650, (2002)

50. Zhi Liu, Yun Sun, F. Machuca, P. Pianetta, W.E. Spicer, J. Vac. Sci. Technol., A, 21, 212, (2003)

51. M.V. Lebedev, D. Ensling, R. Hunger, T. Mayer, W. Jaegermann, Appl. Surf. Sci., 229, 226, (2004)

52. M. Beerbom, Th. Mayer, W. Jaegermann, J. Phys. Chem. B, 104, 8503, (2000)

53. D. Ercolani, M. Lazzarino, G. Mori, B. Ressel, L. Sorba, A. Locatelli, S. Cherifi, A. Ballestrazzi, S. Heun, Adv. Funct. Mater., 15, 587, (2005)

54. Yun Sun, P. Pianetta, Po-Ta Chen, M. Kobayashi, Y. Nishi, N. Goel, M. Garner, W. Tsai, Appl. Phys. Lett., 93, 194103, (2008)

55. S. Sloboshanin, R.K. Gebhardt, J.A. Schaefer, T. Chasse, Surf. Sci., 431,252, (1999)

56. V. Chab, L. Pekarek, I. Ulrych, J. Suchy, K.C. Prince, M. Peloi, M. Evans, C. Comicioli, M. Zacchigna, C. Crotti, Surf. Sci., 377, 261, (1997)

57. M.S. Lee, W.C. Choi, E.K. Kim, C.K. Kim, S.K. Min, Thin Solid Films, 279, 1, (1996)

58. M. Burgener, A. Goldmann, Surf. Sci., 540, 89, (2003)

59. D.Y. Petrovykh, J.M. Sullivan, L.J. Whitman, Surf. Interface Anal., 37, 989, (2005)

60. C.C. Surdu-Bob, S.O. Saied, J.L. Sullivan, Appl. Surf. Sci., 183, 126, (2001)

61. P. Unsworth, J. E. Evans, P. Weightman, A. Takahashi, J. A. D. Matthew, Q. C. Herd, Phys. Rev. B, 54, 1, (1996)

62. P. Moriarty, B. Murphy, L. Roberts, A.A. Cafolla, G. Hughes, L. Koenders, P. Bailey, D.A. Woolf, Appl. Phys. Lett, 67, 383, (1995)

63. C-C. Cheng, C-H. Chien, G-L. Luo, C-H. Yang, C-C. Chang, C-Y. Chang, C-C Kei, C-N Hsiao, T-P. Perng, J. Appl. Phys. 103, 074102 (2008)

64. S. Byungha , J. Cagnon, R.D. Long, P.K. Hurley, S. Stemmer, P.C. McIntyre, Electrochemical and Solid-State Letters, 12, G40, (2009)

65. F. S. Aguirre-Tostado, M. Milojevic, C. L. Hinkle, E. M. Vogel, R. M. Wallace, S. McDonnell, G. J. Hughes, Appl. Phys. Letts., 92, 171906 (2008)

66. L. Lamagna, G. Scarel, M. Fanciulli, G. Pavia, J. Vac. Sci. Technol. A, 27, 443, (2009)

67. T. Ishikawa, H. Ikoma, Jpn. J. Appl. Phys. 31, 3981, (1992)

68. T. Ishikawa, H. Ikoma, Jpn. J. Appl. Phys. 32, L607, (1993)

69. C. J. Spindt, D. Liu, K. Miyano, P. L. Meissner, T. T. Chiang, T. Kendelewicz, I. Lindau, and W. E. Spicer, Appl. Phys. Lett. 55, 861, (1989)

70. J. Ivanco, T. Kubota, H. Kobayashi, J. Appl. Phys. 97, 073712, (2005)

71. G. Landgren, R. Ludeke, Y. Jugnet, J. F. Morar, and F. J. Himpsel, J. Vac. Sci. Technol. B 2, 351, (1984)

72. G. Hollinger, R. Skheyta-Kabbani, M. Gendry, Phys. Rev. B 49, 11159, (1994)

73. N. Shibata, H Ikoma, Jpn. J. Appl. Phys., 31, 3976, (1992)

74. I.K. Han, E. K. Kim, J. I. Lee, S. H. Kim, K. N. Kang, Y. Kim, H. Lim, H. L. Park, J. Appl. Phys. 81, 6986, (1997)

75. P. T. Chen, Y. Sun, E. Kim, P. C. McIntyre, W. Tsai, M. Garner, P. Pianetta, Y. Nishi, C. O. Chui, J. Appl. Phys, 103, 034106, (2008)

76. C.L. Hinkle, M. Milojevic, B. Brennan, A.M. Sonnet, F.S. Aguirre-Tostado, G. Hughes, E.M. Vogel, R.M. Wallace, Appl. Phys. Lett., 94, 162101, (2009)

77. S. Arabasz, E. Bergignat, G. Hollinger, J. Szuber, Appl. Surf. Sci., 252, 7659, (2006)

78. D. N. Gnoth, D. Wolfframm, A. Patchett, S. Hohenecker, D. R. T. Zahn, A. Leslie, I. T. McGovern, D. A. Evans, Appl. Surf. Sci., 120, 123/124, (1998)

4. Optimisation of the sulphur passivation process on InGaAs

4.1. Introduction

As stated at the beginning of the last chapter, as the dimensions of the components in semiconductor devices continue to shrink, the impact the surface of the semiconductor has on the device operations becomes more and more pronounced and a number of steps need to be taken in order to prepare the highest quality surface possible in preparation for the deposition of high-κ metal oxide dielectrics. These consist of removal of the native oxide states, surface termination to prevent the regrowth of the native oxides and also preservation of a high level of surface flatness at the nanometre scale, as the introduction of surface roughening can result in mobility degradation and potentially increase the risk of leakage and oxide breakdown due to reduced conformality with the surface. Although other sulphur passivation techniques have been investigated, showing good results in terms of both chemical and electrical passivation, including the use of S_2Cl_2 and H_2S, as referenced in table 3.1, aqueous ammonium sulphide ($(NH_4)_2S$) is widely utilised as it has been shown to be able to fully remove the native oxide from InP, GaAs and InGaAs as well as leave the surfaces passivated,[1,2] and typically involves very straight forward processing procedures. However, there are wide variations in the processing parameters involved and little is known about the roughening effect of $(NH_4)_2S$. This study is a combined XPS and AFM investigation of the optimum time and $(NH_4)_2S$ concentration to obtain an oxide free surface which displays physical flatness on the nanometre scale.[3, 4]

4.2. Experimental

Using the fitting parameters previously determined for InGaAs and understanding the nature of the native oxide from the thermal annealing study, the next step was to investigate the impact of variations in the aqueous $(NH_4)_2S$ processing parameters on the InGaAs surface. This was necessary due to the wide variation reported in the literature as previously described in table 3.1. The sample set investigated involved systematic changes to:

- the time in $(NH_4)_2S$ solution
- the temperature of the solution
- the concentration of $(NH_4)_2S$ in water

- whether a HCl etch was used as a pre-treatment

as described in table 4.1 for samples labelled *b-m*.

Table 4.1 $(NH_4)_2S$ processing parameters for InGaAs samples

#	**Time (mins)**	**Temp (°C)**	**Concentration (% $(NH_4)_2S$)**	**Pretreatment**
(a)	0	RT	0	Native oxide
(b)	20	RT	22	
(c)	10	RT	22	
(d)	20	RT	22	HCl
(e)	10	RT	22	HCl
(f)	20	40	22	
(g)	20	60	22	
(h)	20	RT	10	
(i)	20	40	10	
(j)	20	60	10	
(k)	20	RT	5	
(l)	20	40	5	
(m)	20	60	5	

The parameters investigated were chosen to reflect the various reported procedures in the literature, while at the same time trying not to compromise the samples themselves in terms of potential exposure time to atmosphere prior to being loaded into the UHV analysis chamber. All samples were initially degreased, as described previously and again, a native oxide sample (*a*) was used as a reference. The ultimate assessment of the effectiveness of ammonium sulphide treatments is determined by the electrical characteristics of devices such as metal-oxide-semiconductor structures. This processing involves the deposition of oxide layers onto the passivated surfaces which are subsequently annealed and this could impact on the structure and quality of the semiconductor - oxide interface. As previously seen, annealing the oxide covered surface, even at the relatively low temperature of 150 °C can affect the composition of the native oxide. Therefore, after initial XPS scans post $(NH_4)_2S$ treatment, all samples were annealed to 300 °C for 30 minutes and rescanned to determine the effect this had on the samples. This would also be a sufficient temperature to remove any residual elemental sulphur not involved in the passivation process.

Again, XPS spectra were taken for the As $2p_{3/2}$, Ga $2p_{3/2}$, In $3d_{5/2}$, O 1*s*, As 3*d*, C 1*s* core levels as well as in the In 4*d* and Ga 3*d* region using a monochromated Al Kα X-ray source. AFM measurements were carried out using a Veeco Multimode SPM in contact mode with Silicon Nitride Lever probes.

4.3. Optimisation of $(NH_4)_2S$ parameters

4.3.1. Residual oxide levels by XPS pre/post annealing

Figure 4.1 shows the As $2p_{3/2}$ (a), Ga $2p_{3/2}$ (b), In $3d_{5/2}$ (c), O 1*s* (d) spectra for the samples listed a-m in table 4.1, before and after annealing to 300 °C.

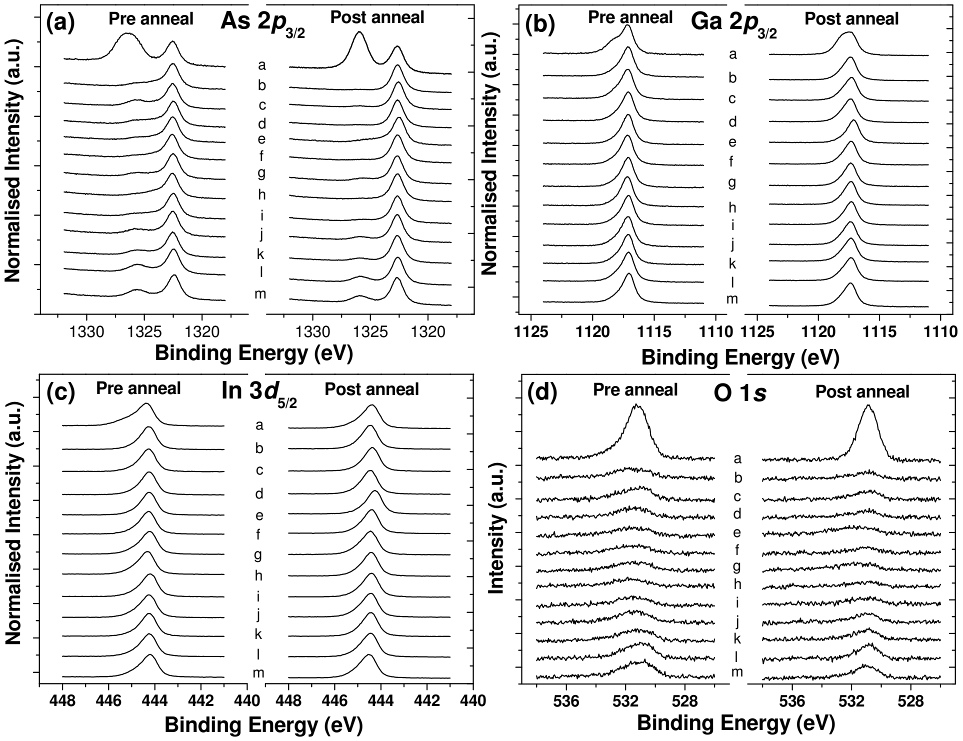

Figure 4.1 XPS spectra of (a) As $2p_{3/2}$, (b) Ga $2p_{3/2}$, (c) In $3d_{5/2}$ and (d) O 1*s* core levels with various $(NH_4)_2S$ treatments, pre and post annealing at 300 °C for 30 minutes

What is clear immediately is that apart from the native oxide sample, which shows a considerable oxide present as seen most clearly in the O 1*s* and As 2*p* plots, there is no obvious significant difference between the various spectra, especially in the case of the Ga 2*p* and In 3*d* spectra where the binding energy separation between the individual oxidation states is very small. Therefore, peak fitting is necessary to determine any variations between the samples and highlights why the accurate determination of fitting parameters is so important.

As a result all spectra were fitted and the ratio of the residual native oxide present to the bulk peak was determined to give an indication of the effectiveness of the ammonium sulphide passivations. It must also be noted again that studies suggest that any strong acid will be effective at removing the native oxide from the surface,[5] so if we are to assume this, we are essentially just testing the effectiveness of the passivation process at preventing reoxidation during the air exposure period prior to loading the samples into the analysis chamber.

In terms of the O 1*s* spectra we can see that there is a significant reduction in the overall signal, to within residual levels after $(NH_4)_2S$ treatment making accurate fitting difficult, however, using fitting parameters in order to determine the over all peak areas without undertaking detailed deconvolutions, we can get an appreciation of the changes in oxide concentration present after treatments and annealing, as shown in figure 4.2.

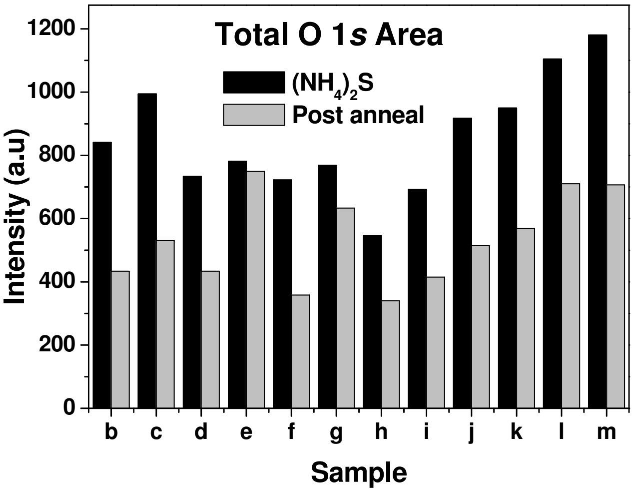

Figure 4.2 Total O1*s* peak areas for the sample investigated before and after annealing at 300 °C

We can see that the lowest level of oxygen present before and after annealing is on sample *h* and that on average there is a ~40% reduction in the overall O 1*s* signal with annealing. In order to get an idea of where this reduction is taking place, if we look at the raw data in figure 4.1 (d), we can see that there does appear to be a slight narrowing of the peaks after annealing with the reduction mainly manifesting itself at the high binding energy side of the peak at ~532 eV. From literature (XPS handbook, NIST database), the possible oxidation states present are reported at 531.7 eV for As-O, 530.8 eV for Ga-O and 530.5 eV for In-O.[6] This would suggest that the principal reduction is due to a loss of arsenic oxides at elevated temperatures, consistent with the annealing study results.

Figure 4.3 shows the fitted core level spectra of the As $2p_{3/2}$ peak from sample *h*, which is representative of the spectra from all of the samples, before and after annealing. When this is compared to the native oxide spectra from figure 3.5 (a), we can see that there is no evidence of the As_2O_5 or $GaAsO_4$ peak after $(NH_4)_2S$ treatment. Peak positions are as reported previously with evidence of As_2O_3, elemental arsenic, As^{1+} and As^{2+}, with the 1+ peak ~1.54 eV from the bulk peak suggesting that there is an As-S contribution.

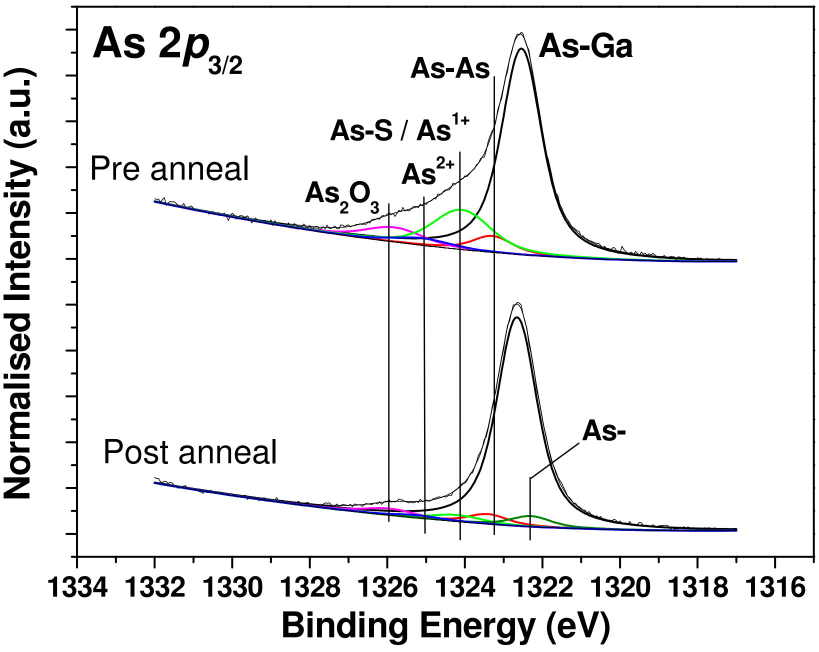

Figure 4.3 Peak fitted As $2p_{3/2}$ spectra pre and post annealing from sample h

When the sample is annealed we see there is a reduction in all of the peaks and the emergence of the lower binding energy peak attributed to the formation of As surface states, primarily As dimers, due to the reduction of the arsenic oxide and possibly sulphur bonds.[7, 8] The As^{1+} peak shift to a lower binding energy ~1.3 eV from the bulk peak, suggesting again that the As-S bonds are being removed upon annealing.

Figure 4.4 shows the S 2*p* spectra taken from sample *h*, again indicative of all the samples, before and after annealing. This allows us to determine if there are any changes taking place in the overall level of sulphur present on the samples as a result of the anneal. Accurate quantification of the level of sulphur present is difficult due to the presence of the Ga 3*s* peak in close proximity to the sulphur peak, making peak fitting difficult, however we can see that there is no apparent change in the overall intensity of the S 2*p* peak after annealing with the increase in the Ga 3*s* peak most likely due to changes in the oxide composition and level of gallium oxide present. This would suggest that with the reduction of the arsenic sulphur component, there is a surface reconstruction taking place with sulphur initially bonded to arsenic transferring to one of the group III elements.[8]

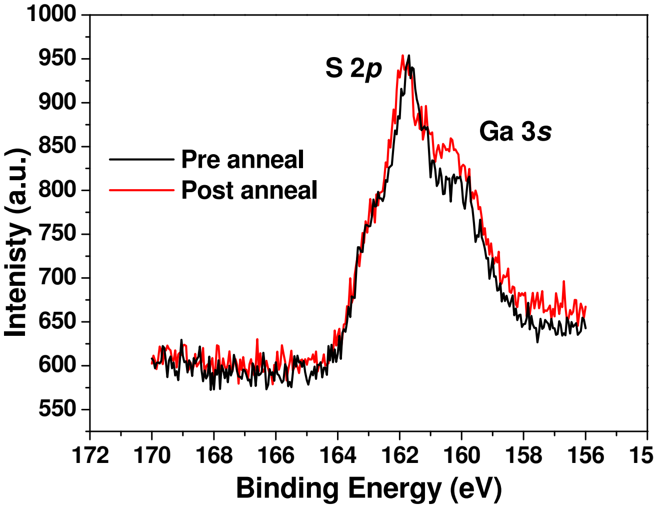

Figure 4.4 S 2*p* and Ga 3*s* spectra from sample h before and after annealing shown no change in the level of sulphur on the surface with annealing

Figures 4.5 (a) and (b) shows the ratio of the arsenic oxide components to the bulk peak before and after annealing respectively. This allows us to compare the passivating quality of the various treatments, assuming all the oxide is removed by the $(NH_4)_2S$ and that all oxide growth is due to reoxidation during sample loading time. The annealing results shown in figure 4.5 (b) highlight the reduction in the oxide states at elevated temperature. While some of these ratios are very small and it could be argued that the results are within experimental error and detection limits of XPS, by using the same fitting parameters for all the samples based on the studies in the previous chapter and monitoring the trends in the data, it is still possible to comment on what is happening to the various oxidation states without commenting on the overall quantity present. These results are also consistent with the changes in the O 1*s* spectra upon annealing showing a reduction and removal of arsenic oxides.

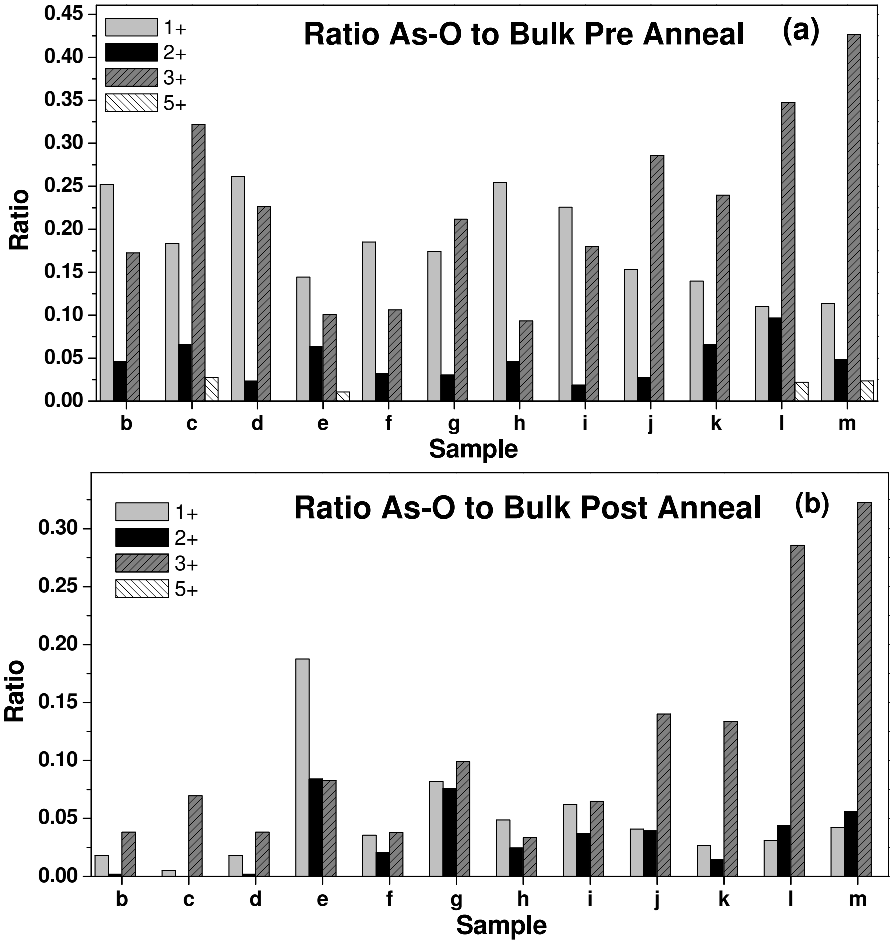

Figure 4.5 Ratio of oxide components to bulk peak (a) pre and (b) post annealing for all treated samples

In order to narrow down the sample set needed to determine the optimal passivation parameters, it was necessary to initially run four samples (*b-e*) which could potentially highlight parameters that were detrimental or unnecessary in the process and could be immediately disregarded. From table 3.1, the most common parameters were 20-22% $(NH_4)_2S$ at room temperature for from 5 up to 30 minutes as well as HCl pre-treatments. Therefore initially using 22% $(NH_4)_2S$, samples were prepared with and without a HCl pre-treatment and for 10 or 20 minutes to determine if the pre-treatment was necessary and what impact time in the solution had on the removal and passivation of the samples.

Focusing first on the samples prior to annealing in figure 4.5 (a) for these four samples, we can see that the only samples where As_2O_5 was present were samples *c* and *e* which were both treated for 10 minutes as well as showing equally large contributions from the As^{2+} state. Sample *c* also showed the largest contribution from As_2O_3. Assuming that the As^{1+} peak involves a large contribution from As-S bonds, (as well as a possible As_2O contribution), these two samples also showed a noticeably smaller As^{1+} value when compared to samples *b* and *d*, which were treated for 20 minutes, suggesting increased As-S bond formation with the increased time. Based on the area ratio, the sulphur levels are on the order of magnitude of one monolayer however, accurate quantitative evaluation is difficult due to the possible presence of an oxide contribution. For this reason it was decided that all further samples would be treated for 20 minutes in order to provide the greatest possibility of forming an effective sulphur passivation layer on the surface.

Upon annealing of the samples in figure 4.5 (b) we can see that there is no significant difference evident between samples *b* and *d*, which were both treated for 20 minutes. This suggests that there was no obvious benefit in utilising a HCl pre-treatment (after also taking into account the data from the In and Ga spectra which will be discussed later) with $(NH_4)_2S$ being just as effective as HCl at removing the native oxides over the time periods investigated. Therefore the remaining samples would be solely investigated to determine the effect of $(NH_4)_2S$ concentration and temperature (*f-m*).
Three $(NH_4)_2S$ concentrations were chosen, again reflecting the variations in parameters reported in literature; 22% (*b, f, g*), 10% (*h-j*) and 5% (*k-m*) $(NH_4)_2S$ in

H_2O, as well as three $(NH_4)_2S$ temperatures; room temperature (*b, h, k*), 40 °C (*f, i, l*) and 60 °C (*g, j, m*).

What is evident immediately from figures 4.5 (a) and (b) is that with 5% $(NH_4)_2S$ concentration, there is a significant amount of As_2O_3 present which does not undergo a significant reduction upon annealing. As_2O_5 is also detected on sample *l* and *m*, which experienced the 40 °C and 60 °C treatments respectively, before annealing. The 5% samples also exhibit the smallest As^{1+} contribution which could be a reflection on a lower level of As-S bond formation and would be expected to allow for increased levels of ambient reoxidation, reflected in the As_2O_3 ratio. Interestingly, with the 3 concentrations the As^{1+} peak is seen to reduce with increasing temperature, possibly suggesting that As-S bonds form preferentially at lower temperatures. While the 5% concentration level overall shows the worst performance, there is no significant difference between the 10% and 22% treated samples at the three temperatures investigated, with the 10% at room temperature sample *h* showing the lowest level of As_2O_3 and a similar As^{1+} peak ratio to that of sample *b*.

To summarise, while there is no significant difference detected in terms of the arsenic oxide present after $(NH_4)_2S$ passivation with or without a HCl pre-treatment, the level of native oxide present was seen to increase with reduced time in $(NH_4)_2S$ solution, with increased $(NH_4)_2S$ temperature and upon reducing the $(NH_4)_2S$ concentration below 10%. Annealing to 300 °C showed a significant reduction in the level of arsenic oxides present on the surface and based on the reduction of the O 1*s* signal, this manifests as arsenic oxide removal from the surface.

The Ga 2*p* spectra and peak ratios before and after annealing are shown in figure 4.6 (a-c). From the fitted spectra in figure 4.6 (a) again for sample *h*, we can see the presence of Ga_2O, Ga_2O_3 and $In_xGa_yO_z$ peaks, with no evidence of $GaAsO_4$. Post annealing we see a slight reduction in the Ga_2O_3 peak, the removal within detection limits of the $In_xGa_yO_z$ peak and an increase in the Ga_2O peak. What must be taken into consideration is the presence of a possible Ga-S bond which is widely reported to appear 0.7 eV from the bulk peak,[9] which would place it between the Ga_2O and Ga_2O_3 peaks making it difficult to resolve. Also the fact that the Ga_2O peak has been shown to increase with annealing, due to oxygen transfer from indium oxides, it is difficult to ascertain if the relative increase is due to the formation of new Ga-S bonds with the reduction of the As^{1+} peak or solely due to an oxide increase.

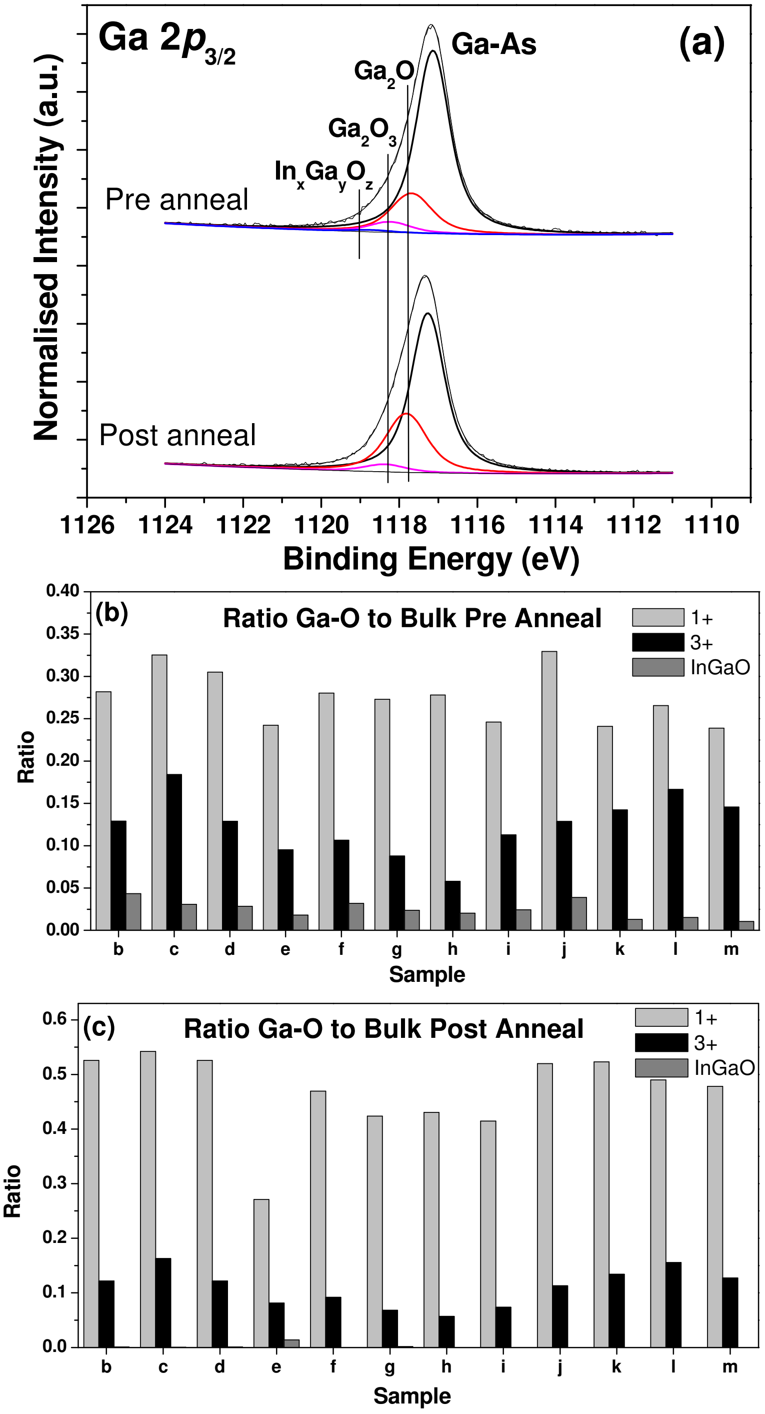

Figure 4.6 (a) Peak fitted Ga 2$p_{3/2}$ spectra pre and post annealing from sample h and ratio of oxide components to bulk peak pre (b) and post (c) annealing for all treated samples

From the oxide ratios before and after annealing in figure 4.6 (b) and (c) we can see that all samples have a roughly similar level of Ga_2O present on the surface after $(NH_4)_2S$ treatment, with the lowest level of Ga_2O_3 seen on sample *h*. Post annealing, we can clearly see an increase in the Ga_2O peak with very little change seen in the Ga_2O_3 peak ratio. The anomalous result for sample *e* post annealing where the Ga_2O state is not seen to increase is likely due to a problem with the anneal and possibly caused by the sample not making prefect contact to the sample holder and hence not reaching the targeted temperature during the anneal. Overall, there are no obvious trends that would suggest which is the optimal process for passivation of the gallium oxides other than on average, the 5% concentration does show an increased presence of Ga_2O and Ga_2O_3 in comparison to the samples treated with 22% and 10% $(NH_4)_2S$. Based on the reduction of the arsenic related feature in the O 1*s* spectra upon annealing and the overall drop in oxygen levels present in figure 4.2, it can therefore be speculated that the oxygen needed to cause the increase the level of Ga-O present must again be coming from the indium oxides.

The fitted In $3d_{5/2}$ spectra again from sample *h* are shown in figure 4.7 (a). The spectra again highlight the asymmetry in the In peak profile which is compensated for with the addition of a peak at 0.42 eV from the bulk peak. Also present are the In^{1+} and In_2O_3 peaks. There is no evidence of the $In_xGa_yO_z$ peak which was seen in the Ga 2*p* spectra, however this could be a result of the reduced surface sensitivity of the In 3*d* peak due to its lower binding energy. However it is also possible that there is only a small indium contribution to the $In_xGa_yO_z$ peak after $(NH_4)_2S$ treatment, which based on the annealing study results, would have been expected to transfer oxygen to gallium creating either Ga_2O or Ga_2O_3. It was not possible in that study to determine if any of the individual indium oxidation states were preferentially causing an increase in an individual gallium state, due to the abundance of oxide present. Here however, the results would suggest that the reduction of the In_2O_3 peak is the major contributor to Ga_2O growth and the reduction of $In_xGa_yO_z$ is the main contributor to Ga_2O_3 growth based on the fact that for $In_xGa_yO_z$ where $x \approx 0$, there is virtually no change in the Ga_2O_3 levels present.

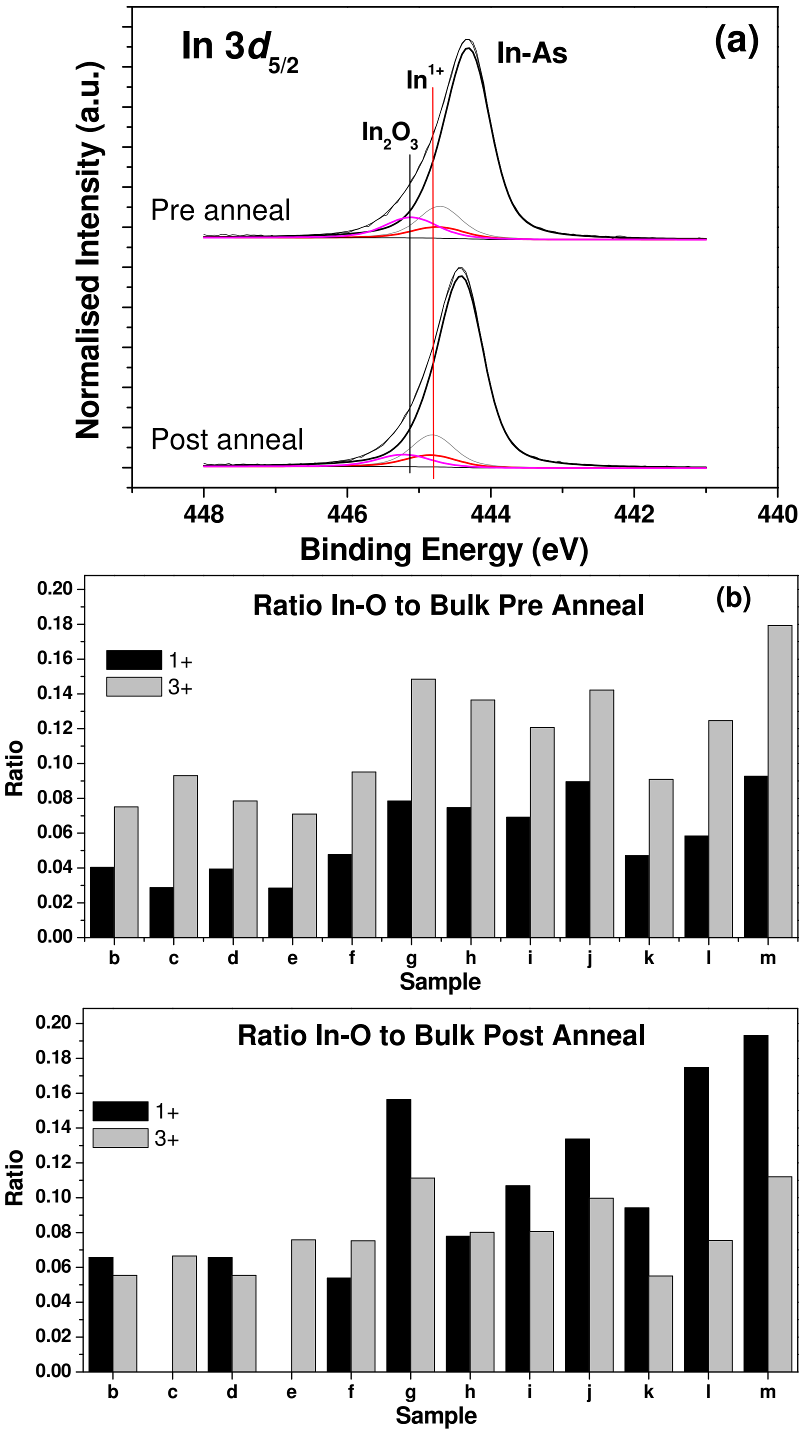

Figure 4.7 (a) Peak fitted In $3d_{5/2}$ spectra pre and post annealing from sample h and ratio of oxide components to bulk peak pre (b) and post (c) annealing for all treated samples

Similar to the Ga 2*p* peak, it is difficult to ascertain if there is an In-S peak present on the surface as a result of the low binding energy separation between the peaks and any In-S bonds would be expected to appear between the 1+ and 3+ peaks. However, based again on the S 2*p* spectra in figure 4.4, which does not show a significant change for all the samples post annealing, and due to the reduction in the As^{1+} peak, it can be speculated that this is further evidence that the sulphur after annealing is preferentially bonded to the group III elements. This could mean a reconstruction of the surface takes place with annealing, leaving the surface group III terminated, consistent with results for sulphur passivation of InP and GaAs.[10, 11]

The ratios of the In 3*d* peak pre and post annealing are shown in figure 4.7 (b) and (c). Similar to that seen for As, we see an increase in the level of oxide present with passivation temperature, which is especially evident on samples k-m with the 5% $(NH_4)_2S$ concentration. Upon annealing of these samples, the In^{1+} peak is seen to grow at the expense of the In^{3+} peak, suggesting that the 1+ peak is more thermally stable than the 3+ peak. However, based on the annealing study results, the oxygen transfer would be expected to cause an increase in gallium oxides preferentially suggesting that the decomposition of the indium contribution in $In_xGa_yO_z$ is the principle mechanism for an increase in gallium oxide to take place.

The increase in the 1+ peak could also be due to the formation of In-S bonds, with sulphur transferring from As-S to an increased In-S state. As-S bonds on GaAs are widely reported to decompose above 200 °C,[12, 13] however there is little reported evidence of bond transformations taking place and it is not clear whether these would manifest itself as a detectable binding energy change in the S 2*p* spectra. Overall, samples *b, c, f , h* and *k* appear to be the best performing in terms of the passivation of the indium oxides and taking into account the information from all the peaks based on XPS results, samples *b, c, f, h* and *i* were the best performing showing the lowest levels of oxide present.

4.3.2. Surface roughness

AFM was carried out on all the samples to determine the effect of the sample processing on the surface roughness. Figure 4.8 shows the AFM images from samples (*h-j*) as well as the root mean squared (RMS) roughness calculations from each of the individual surfaces for 1 x 1 μm and 5 x 5 μm scan areas. Scans were taken after the samples were removed from UHV, and were stored in an evacuated dessicator for a number of days so it is likely that a certain amount of reoxidation took place, however this would be expected to conform to the surface of the substrate and not significantly alter the roughness values. Scans were taken from up to 3 different locations on the surface of the samples in order to give an average value for the surface roughness.

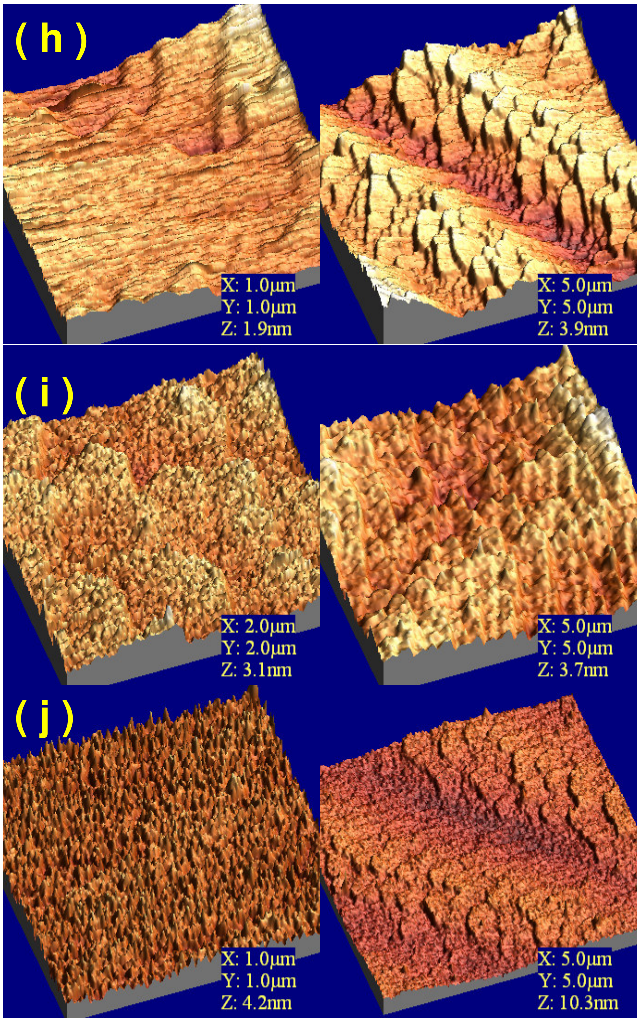

Figure 4.8 AFM images from sample (*h-j*) for the1 x 1 μm and 5 x 5 μm scan areas showing apparent increase in surface roughness with increasing $(NH_4)_2S$ temperature

RMS roughness measurements were calculated by analysing the scans with AFM analysis software[14] for each of the individual samples and shown in table 4.2. In general, the surfaces are extremely flat such that a 1 x 1 μm scan of the samples shows a maximum roughness of 0.45 nm averaged over the total scan area, which is on the order of magnitude of one monolayer and very similar to the value seen on the native oxide sample which underwent no processing suggesting that all of the passivation processes do not aggressively etch the surface. However, the values do seem to suggest that increased concentration and temperature result in slightly rougher surfaces with the lowest overall roughness on the 5% $(NH_4)_2S$ at 40 °C and the largest on the 22% $(NH_4)_2S$ at 60 °C. The variation in roughness values between the 1 x 1 μm and 5 x 5 μm scan areas is possibly due to increased contribution from plane edges with the larger scan area.

Table 4.2 RMS roughness values from AFM measurements of samples

RMS Roughness (nm)		
Sample	**1x1 μm**	**5x5 μm**
a	0.29	0.6
b	0.29	0.5
c	0.24	0.52
d	0.27	0.50
e	0.40	0.73
f	0.38	0.70
g	0.45	0.50
h	0.20	0.61
i	0.33	0.47
j	0.33	0.67
k	0.31	1.16
l	0.14	0.33
m	0.21	0.47

4.3.3. Discussion

Based on these results, there is no conclusive evidence that there are a specific set of parameters that provide the optimal surface chemical passivation, able to prevent reoxidation of the InGaAs surface similar to the performance of H passivation of silicon using hydrofluoric acid. However, taking into account both the XPS and AFM results, sample *h*, treated in 10% $(NH_4)_2S$ for 20 minutes at room temperature with no surface pre treatment other than a standard de-greasing process to remove ambient carbon contamination showed the best combination of results, with one of the lowest RMS roughness values measured, low levels of As, In and Ga oxides as well as the largest As^{1+} contribution pre annealing, suggesting the largest level of sulphur surface bond formation which goes some way to explaining the low oxide levels present.

4.4. Sulphur passivation with H_2S

Alternative sulphur passivations to that of ammonium sulphide have also been investigated as seen from table 3.1, with probably the most interesting being the use of hydrogen sulphide (H_2S) due to ease of processing and incorporation into the manufacture procedures. Previous results on GaAs and InGaAs have shown that H_2S is effective at reducing the defect density at the surface and also increasing photoluminescence yields. [15, 16] Sulphur is used as a dopant in p-type III-V semiconductors and typically with metal oxide vapour phase epitaxy (MOVPE) semiconductor growth, this involves the use of H_2S during the growth process. This makes it quite easy to incorporate a potential sulphur passivation step involving H_2S at the end of the InGaAs growth process, essentially just exposing the sample to a final higher concentration of H_2S than that used for sample doping as the final stage of the MOVPE growth.

In this study, $In_{0.53}Ga_{0.47}As$ lattice-matched epitaxial layers of thickness 2 μm and S doped to $4x10^{17}/cm^3$, were grown in a MOVPE system immediately following growth of a 0.1 μm InP buffer layer (S doped, $2x10^{18}$ /cm^3) on *n*-type InP (100) wafers (S doped, (1–3) x 10^{18} /cm^3). *In situ* passivation of the InGaAs surface was performed in the MOVPE chamber immediately after growth by flowing H_2S over the samples at a flow-rate of 0.1 SCCM (SCCM denotes cubic centimeter per minute at STP), at three different temperatures, 50, 200, or 350 °C, for 90 min in a H_2 carrier gas. These samples were then compared by XPS to a sample treated with ammonium sulphide (22% for 20 minutes at 60 °C similar to sample *g* above), a sample which was not exposed to H_2S after growth and a sample with a significant native oxide present after exposure to atmosphere for an extended period of time. Following MOVPE growth and prior to XPS analysis the samples were stored under nitrogen before being transferred to UHV such that the samples were exposed to atmosphere for less than 5 minutes in total.

XPS spectra from the various treated samples are investigated, initially focusing on the As 3*d* core levels, in order to determine the level of native oxides present after treatments. The samples were then exposed to atmosphere for periods of time, ranging from nominal exposure during sample transfer (1-5 minutes) up to 7 days (or ~10000 minutes) to determine if there are any variations in the effectiveness of the various passivation procedures at inhibiting ambient oxidation. This is further quantified by carrying out a similar exposure study on a commercially grown $In_{0.53}Ga_{0.47}As$ sample that underwent a standard two stage piranha etching procedure (4:1:100 H_2SO_4:H_2O_2:H_2O for 2 minutes followed by 1:3 HCl:H_2O for 30 seconds)[17] to remove the native oxide without passivating the surface and directly comparing it to a $(NH_4)_2S$ treated sample from the same wafer again after periods of exposure to atmosphere ranging from 1 minute to 10000 minutes. While samples were experiencing atmospheric exposure, they were stored in a desiccator at atmospheric pressure to ensure as consistent humidity conditions as possible.

4.4.1. Residual oxide levels by XPS

Curve fitted XPS spectra of the As 3*d* peaks immediately after the different H_2S exposure treatments are shown in figure 4.9 as well as spectra for an unpassivated sample (not exposed to H_2S after MOVPE growth), one subjected to $(NH_4)_2S$ treatment and also a sample with a native oxide present.

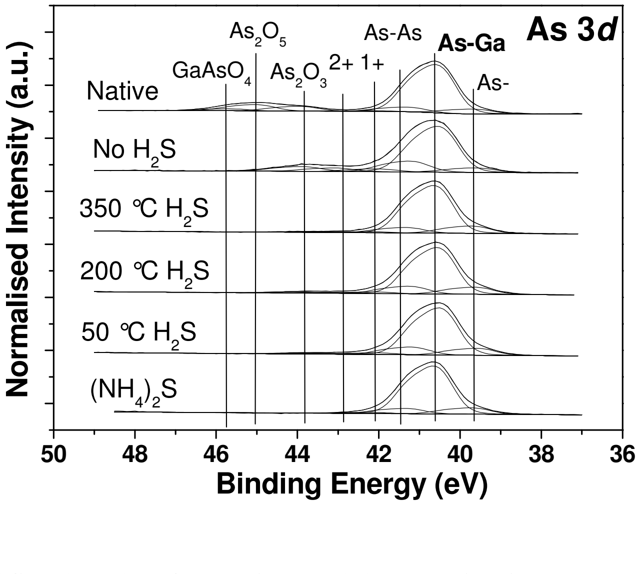

Figure 4.9 As 3*d* fitted peaks after various sulphur passivation processes, from an unpassivated sample and from a sample after extended exposure to atmosphere

What is clearly evident from these spectra is that all the sulphur treatments are effective at preventing or restricting oxide growth on the surface considering the H_2S and $(NH_4)_2S$ samples show very low levels of arsenic oxide on the surface when compared to the native oxide and unpassivated samples. Particularly on the native oxide sample, we again see evidence of $GaAsO_4$, As_2O_5, As_2O_3, elemental arsenic As-As, a lower binding energy peak again likely due to As dimers or under coordinated As at the oxide substrate interface and trace amounts of As^{2+} and As^{1+} with the bulk peak at ~40.5 eV. The binding energy positions and offsets from the bulk peak of the components listed in table 4.3.

Table 4.3 Binding energy position of the As 3*d* component peaks

	Peak	**BE (eV)**	**Δ BE (eV)**
	As-Ga	40.5	-
As^0	**As-As**	41.16	0.66
dimer	**As-**	39.5	-1
As^{1+}	**As_2O**	41.95	1.45
As^{2+}	**AsO**	43	2.5
As^{3+}	**As_2O_3**	43.82	3.32
As^{5+}	**As_2O_5**	44.9	4.4
	$GaAsO_4$	45.55	5.05

Due to the low binding energy of the As 3*d* peak and hence reduced surface sensitivity, accurate peak assignment is difficult, which is the reason for the discrepancy between the values seen here to those in table 3.3, particularly in terms of the elemental arsenic and arsenic dimer related peaks. These peak fitting values however provided the most consistent peak fits for all the spectra and while it is likely that the contribution of the As- dimer peak especially is over estimated as a result, it is likely that any trends that arise for this peak are indicative of changes while not necessarily reflective of the overall quantity present. The binding energy of the oxide components are very similar to that seen previously and are likely to therefore also reflect the quantity and the composition of the oxide present.

In order to clearly show the oxides present on the surface the spectrum from the native oxide sample is shown separately in figure 4.10.

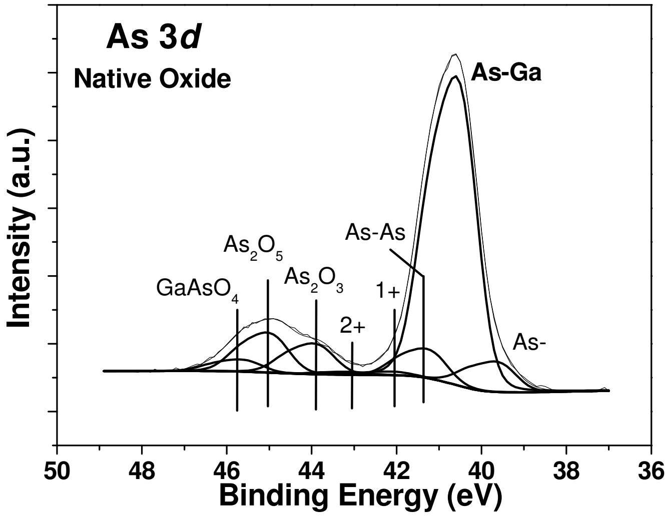

Figure 4.10 Fitted As 3*d* spectra from a native oxide sample after prolonged exposure to atmosphere

The corresponding spectrum from the $(NH_4)_2S$ treated surface is shown in figure 4.11. This time we see no evidence of the $GaAsO_4$, As_2O_5, As_2O_3 or As^{2+} peaks, with just elemental arsenic, the lower BE peak and an As^{1+} peak detected, the latter assumed to be due to a combination of As-S and arsenic oxide bonds based on previous results.

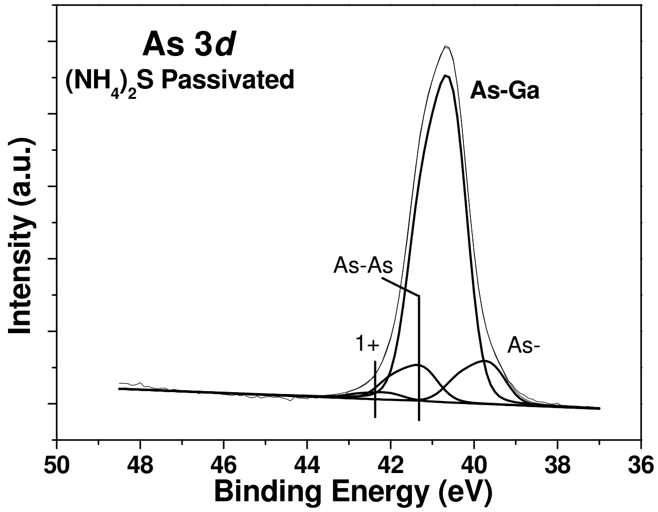

Figure 4.11 Fitted As 3*d* spectra from sample treated with $(NH_4)_2S$ with minimal exposure to atmosphere

By taking the area ratio of all the peak components in these spectra, we are able to compare more clearly the effectiveness of the various passivation procedures and what effect they have on the InGaAs surface in terms of oxidation. From the oxide component ratio in figure 4.12 (a) we see that the $(NH_4)_2S$ treated sample shows the lowest level of oxide present, with only the As^{1+} peak detected, which as stated previously, is most likely due to a combination of As_2O and As-S bond formation. The samples exposed to H_2S show significantly more arsenic oxide present with the As^{2+} and As^{3+} (As_2O_3) peaks detected on all three samples. There are also variations seen between the individual H_2S exposed samples with the 50 °C and the 200 °C samples showing roughly similar levels of oxidation whereas the 350 °C sample shows a similar level of As^{1+} to that of the $(NH_4)_2S$ treated sample and a reduced level of As^{2+} and As^{3+} suggesting it is the most effective of the H_2S treatments in terms of preventing ambient oxidation.

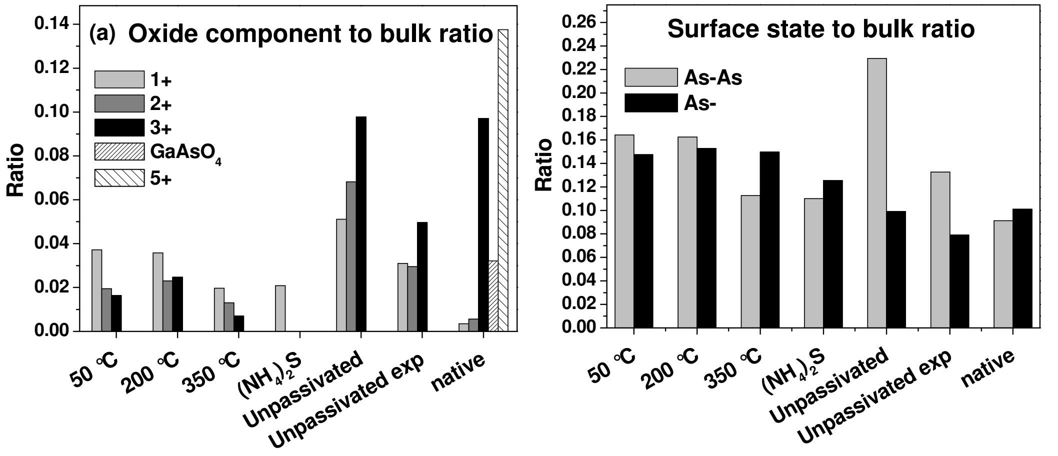

Figure 4.12 (a) Ratio of As 3*d* oxide peak components to the bulk peaks after various sulphur passivation procedures and (b) ratio of As-As and LBE surface component to bulk peak

We also see that the native oxide sample is the only sample with $GaAsO_4$ and As_2O_5 component peaks present, suggesting that these primarily form only after extended periods of time. The level of As_2O_3 on the unpassivated sample is similar to that of the native oxide however there is significantly more As^{2+} and As^{1+} present on the unpassivated sample. This could suggest that the low valency oxides form preferentially at the semiconductor surface with initial exposure and over time these convert into other oxides.[18] Whether that is a consequence of an oxide bond transfer to form Ga and In oxides or through the formation of As_2O_5 and $GaAsO_4$ cannot be determined from this study. The similar levels of As_2O_3 possibly suggest that this is a saturation level for this state and once this level is reached, the oxide primarily begins to form as As_2O_5 which would explain its absence on the H_2S exposed samples.

Looking at the ratio of the As-As and As- dimer peak to the bulk peak in figure 4.12 (b), we can see that there is a consistent level of As- dimers forming on the H_2S passivated surfaces. This reduces for the $(NH_4)_2S$ sample and has its lowest value on the unpassivated and native oxide samples. Again it is worth stressing that the ratio here is a not likely to be an accurate reflection on the level present and it is just the trend in the data that is important. However the level of As- bonds present could also be a reflection on the level of passivation or at least surface termination taking place at the surface. As mentioned previously, Robertson discussed the formation of dimers and possible dangling bonds as a result of oxide growth and reduction,[19] which is essentially what would be taking place as soon as the sulphur passivated samples were exposed to atmosphere. Sulphur would be expected to bond preferentially to any dangling bond states at the semiconductor surface preventing oxidation and with the reduced oxide ratio value on the $(NH_4)_2S$ sample relative to the H_2S samples, this is likely to be correlated to the reduced level of oxidation seen. As oxygen eventually bonds to these surface state, there would also be a significant reduction in this peak as seen on the unpassivated and native oxide samples which show the lowest levels.

In terms of As-As bonds, the largest level is seen on the unpassivated sample and the lowest again seen on the native oxide sample. The 350 °C and $(NH_4)_2S$ samples show the same level while the 50 °C and 200 °C sample shows a ~ 50% increase relative to the other passivated samples. Again, it has been reported that with the oxidation of atomically clean InGaAs surfaces, defect state densities grow as a result of oxide formation, with elemental As forming because oxygen has a higher affinity for Ga than As.[20] From these results, it can be speculated that with further exposure to oxygen the dangling bonds and elemental arsenic will over time convert to oxides which would explain why the lowest level of both As- and As-As bonds are seen on the native oxide sample. The unpassivated sample, not having enough time to reach a saturated oxide level still shows a very significant As-As component whereas the As-states peak, expected to be more receptive to oxygen bond formation than the elemental arsenic is much lower.

Looking at the S 2*s* spectra from the samples in figure 4.13, we see that within detection limits of XPS, sulphur is only present on the $(NH_4)_2S$ and 350 °C H_2S exposed samples with the $(NH_4)_2S$ sample showing a slightly increased level. This is consistent with the relative levels of oxide formation seen on these two samples, which were the two best performing in terms of oxidation prevention with the $(NH_4)_2S$ showing the lowest over all. This suggests that the sulphur is playing an active role in preventing ambient oxidation. However, comparing the arsenic oxide levels on the 50 °C and 200 °C samples, which show no sulphur presence to the unpassivated sample we see that they have a significantly lower oxide level present.

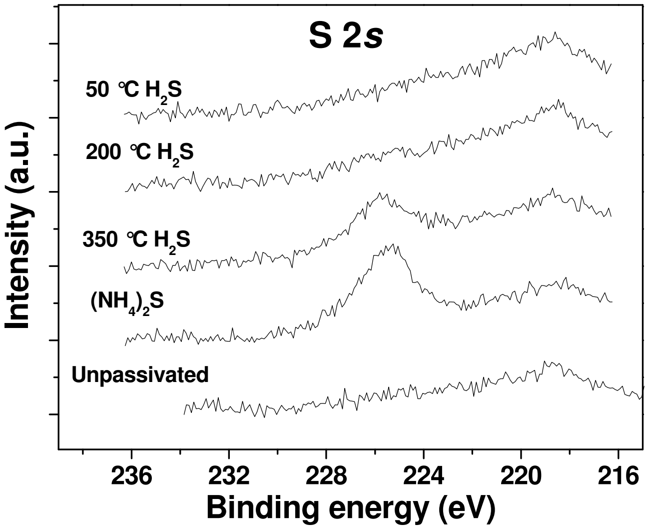

Figure 4.13 Sulphur 2*s* spectra from samples after various sulphur passivation procedures

This would lead to the conclusion that either significantly sub monolayer levels of sulphur (based on the detection limits of XPS) are hindering the oxidation or there is some other passivant preventing it. It has been speculated that hydrogen might be playing a role in this regard,[16] similar to the role it plays with silicon, however it is beyond our capabilities to determine if this is actually the case as hydrogen core levels cannot be detected with XPS.

4.4.2. Passivation effectiveness with ambient exposure

In order to test the effectiveness of the H_2S passivations, the samples were removed from UHV and exposed to atmospheric conditions for periods of 5 minutes, 60 minutes, 24 hours (1440 minutes) and 7 days (10080 minutes) with spectra taken after each successive exposure. Figure 4.14 shows the relevant As 3*d* spectra after the successive exposures for the three H_2S treatment temperatures. Even without curve fitting we can see that the oxide growth rate is significantly lower on the 350 °C H_2S sample.

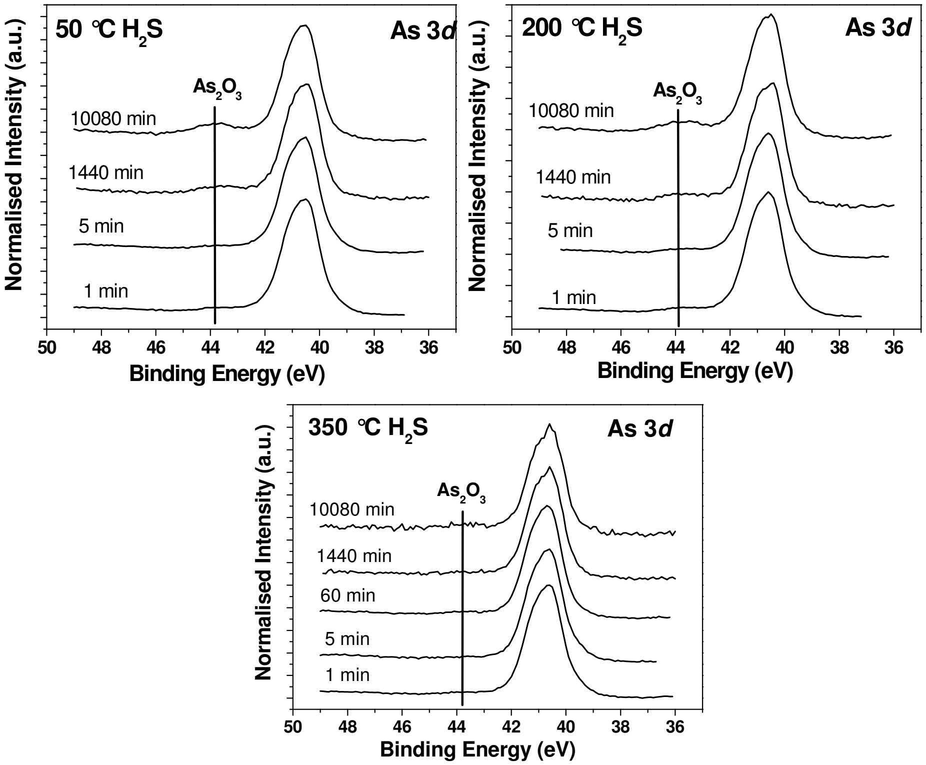

Figure 4.14 As 3*d* spectra after various sulphur passivation procedures followed by exposure to atmosphere for protracted periods from 1 min to 7 days

Upon curve fitting, the ratios of the oxide peaks to the bulk peak were again compared to highlight the changes in the various oxide components, shown in figure 4.15 as a function of time with the time displayed as the log of the exposure time in minutes. On all the samples the As^{1+} peak is initially the most dominant however there is very little change seen over time apart from the 350 °C H_2S sample which is seen to progressively increase with exposure until it reaches the level seen on the 50 °C and

200 °C samples. This could suggest that initially on the 350 °C sample, this state is made up mostly of As-S bonds and with time the formation of As_2O takes place causing it to increase to a level that is already present on the other two samples. An interesting feature of all the spectra is that after 5 minute exposure, there appears to be a reduction in the total arsenic oxide ratio. This can only be explained by a transfer of oxygen from arsenic to either gallium or indium as it unlikely that any oxide could leave the sample without increasing the sample temperature to over 250 °C as seen during the annealing study. With increased exposure, the total oxygen ratio is seen to increase on all samples with the largest increase seen in the As_2O_3 peak.

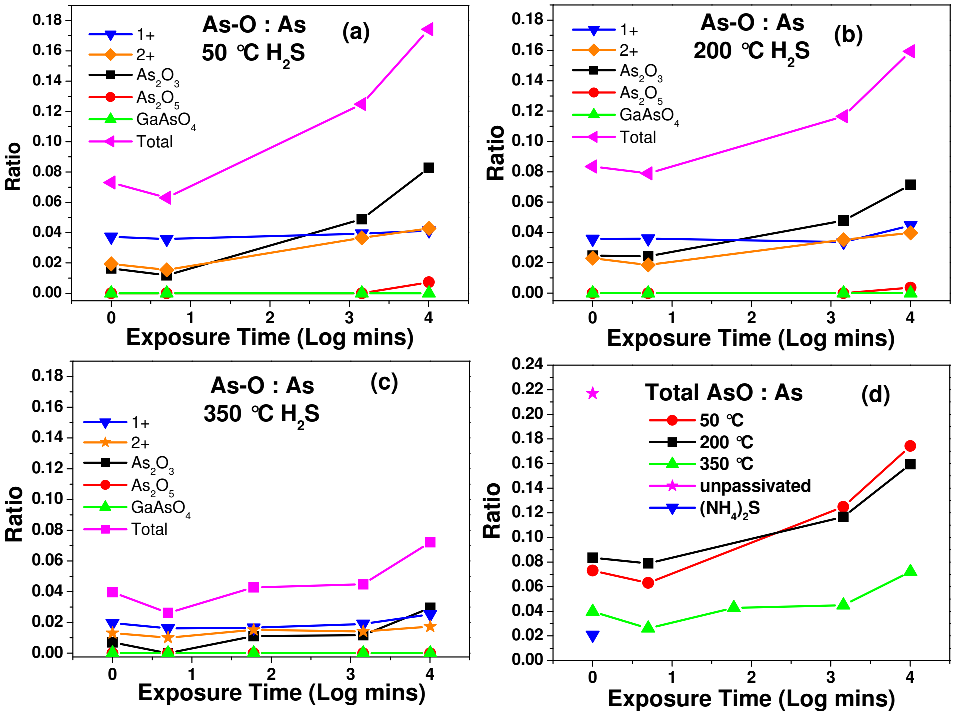

Figure 4.15 Ratio of oxide components from the As 3*d* peaks to that of the corresponding bulk peaks with exposure to atmosphere for protracted periods of time for (a) 50 °C H_2S, (b) 200 °C H_2S and (c) 350 °C H_2S exposure, with (d) showing the total As oxide ratio on all the samples

From figure 4.15 (d), after seven days exposure we can see that no sample has reached the level of oxide present on the unpassivated sample (which experienced minimal exposure). The 50 °C and 200 °C treated samples show an oxide ratio of 70-80% relative to the unpassivated value suggesting that the oxide level has not reached its saturation level even after this prolonged exposure. However the 350 °C sample still only shows a relative ratio of 33% after the final exposure investigated. This further suggests that sulphur plays a key role in the prevention of ambient oxidation. Also, the initial formation and growth of the As^{2+} and As^{1+} peaks further suggests that they form specifically at the InGaAs surface and form the initial building block from which the other oxidation states grow. From figure 4.10 we saw that there was a significant amount of As_2O_5 present on the native oxide sample, however, there is no trace on any of these samples until the final exposure on the 50 °C and 200 °C H_2S samples and even then it makes up only ~5% of the total oxide contribution suggesting that the As_2O_5 state does not grow until the As_2O_3 state reaches a saturation level.

4.5. Effectiveness of $(NH_4)_2S$ versus 2 stage Piranha etch

4.5.1. Removal of oxides and oxidation with ambient exposure – As

To further test the effectiveness of sulphur passivation, two differently prepared MOVPE grown InGaAs wafer supplied by IQE Wafertech were analysed by XPS. One sample was treated with $(NH_4)_2S$ and one etched using the two stage etching procedure mentioned previously. This time the more surface sensitive As 2*p*, Ga 2*p* and In 3*d* peaks were investigated, again after exposure to atmosphere for 1, 10, 100, 1000 and 10000 minutes.

Figure 4.16 shows the As $2p_{3/2}$ spectra with ambient exposure after both 2 stage etching and $(NH_4)_2S$ treatment with the spectra labelled with numbers representing the Log of the exposure time experienced. Spectra of an untreated sample exposed to atmosphere for an extended period of time are included for comparison. Both chemical processes are seen to remove or at least significantly reduce the arsenic oxides present on the surface to within detection limits of XPS. However with exposure we begin to see the growth of the native oxides which are clearly at a much slower rate on the $(NH_4)_2S$ sample. After the final exposure, on the 2 stage etched surface there is a higher oxide concentration present than seen from the native oxide sample.

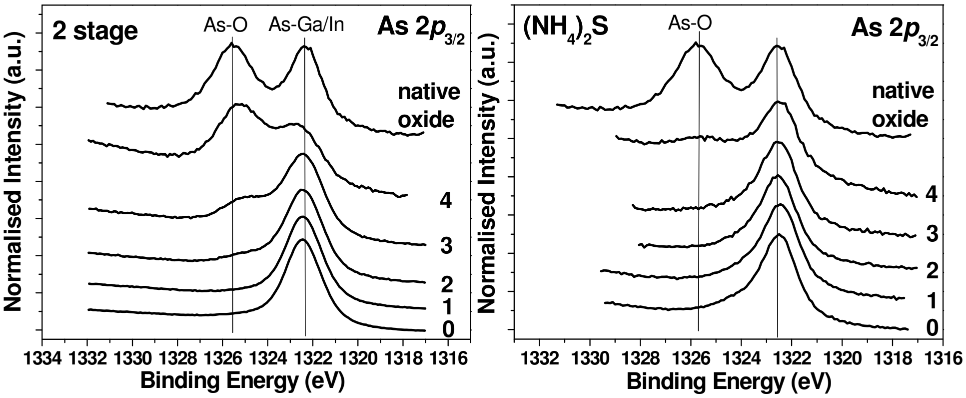

Figure 4.16 Core level spectra from As $2p_{3/2}$ peaks from IQE wafers after a 2 stage etching procedure and treatment with ammonium sulphide followed by exposure to atmosphere for periods up to 10000 minutes

There is also a shoulder evident on the higher binding energy side of the peak immediately after $(NH_4)_2S$ treatment which is not seen in the etched spectra which could be evidence of As-S bond formation. This is seen more clearly in the expanded and overlayed As 2*p* spectra shown in figure 4.17.

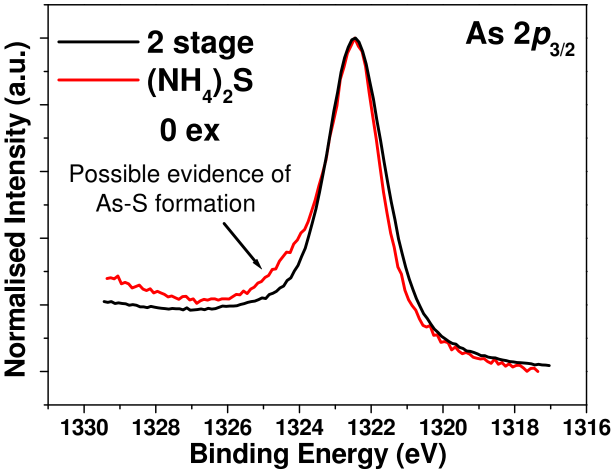

Figure 4.17 Comparison of As $2p_{3/2}$ peaks after initial treatments with minimal exposure to atmosphere

There does however appear to be a slight broadening of the peak to the lower binding energy side on the 2 stage etched sample which could be evidence of an increased level of surface dimer formation or arsenic dangling bonds as a result of the etching procedure.[11, 21]

The curve fitted As $2p_{3/2}$ spectra after treatment and minimal exposure (0 ex) and the final exposure (4 ex) are shown in figure 4.18 using the fitting parameter and peak positions described in table 3.3. After initial etching and passivation, we can see that apart from the As^{1+} peak, the level of oxide present on the surface is very similar, with only As^{2+} present which is virtually at the detection limits of XPS. We can assume that the As^{1+} peak on the $(NH_4)_2S$ sample is due primarily to arsenic sulphur bond formation. There does appear to be an increased amount of elemental arsenic present on the etched surface as well as an increased level of As- bonds when compared to the $(NH_4)_2S$ sample which suggests that as well as forming during oxidation, it is possible that they also form when the oxides are being removed and that the presence of sulphur is effective at preventing their formation.

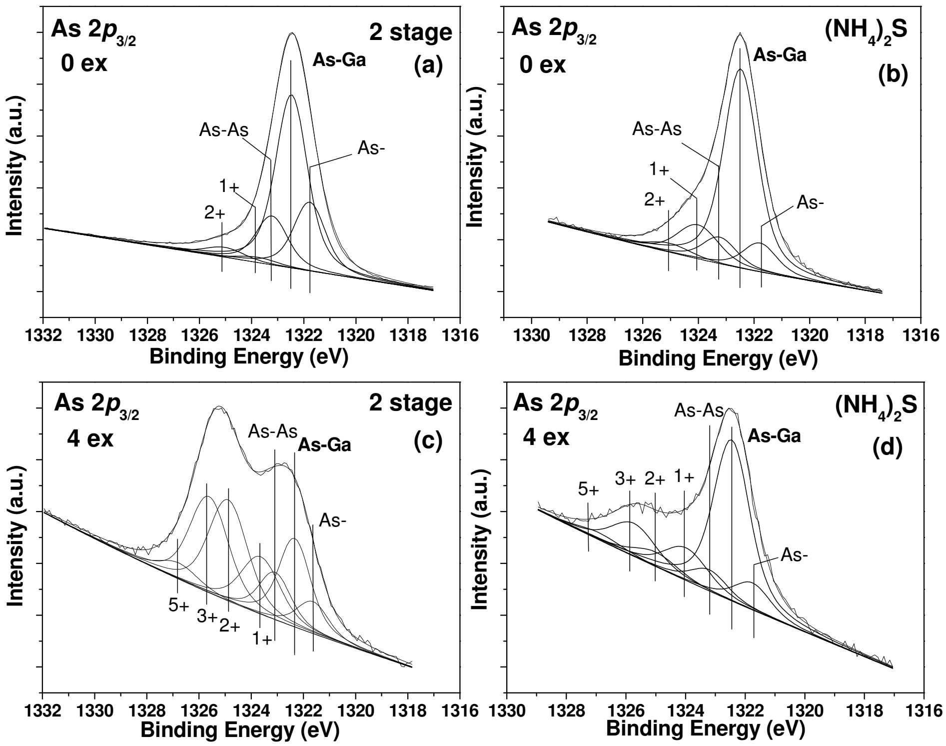

Figure 4.18 Fitted As $2p_{3/2}$ spectra with 2 stage and $(NH_4)_2S$ treatment with (a, b) minimal (0 ex) and (c, d) 10000 minute (4 ex) exposure to atmosphere

When we then look at the spectra after exposure (4 ex) we can see how significant the oxidation is on the 2 stage etched sample in comparison to the $(NH_4)_2S$ sample. While we now see the presence of As_2O_3 and As_2O_5 on both samples, there is obviously more present on the 2 stage etched sample, however the largest variation is seen in terms of the As_2O_3, As^{2+} and As^{1+} peaks. These are seen to increase dramatically on the 2 stage etched sample whereas there is only a small increase in the As^{2+} and As^{1+} peaks and the formation of an As_2O_3 peak at a similar level to the As^{1+} peak on the $(NH_4)_2S$ passivated sample. Again, we still see a larger As-As peak on the two stage etched sample, however the As- peak has reduced relative to the bulk peak consistent with oxygen bonding to a significant number of the surface states that are created during the etching, reducing the over all intensity of the As- peak. There is no evidence of $GaAsO_4$ on either sample in these spectra after exposure to atmosphere, suggesting that it is the least energetically favourable of the oxidation states needing much more exposure time to form.

The ratios of the oxide and surface components to the bulk peaks after each exposure are shown in figure 4.19. The much slower growth rate of the all the oxidation states with $(NH_4)_2S$ again highlights the effect that the sulphur has at hindering the oxidation of the sample. If we look first at figure 4.19 (a), there are some interesting features worth noting. Initially with the $(NH_4)_2S$ sample we see that the ratio of the As^{1+} state is identical to that of the native oxide sample and is at a level consistent with ~1 ML where as the 2 stage etched sample ratio is ~75% lower and approaching the error associated with XPS, and lower than any level previously seen up to this point. Looking first at the native oxide and $(NH_4)_2S$ samples gives us an insight into the formation of the immediate interface between the oxide and the substrate.

From the annealing study, we know that the As^{1+} peak on the native oxide sample is due to As_2O and is located strictly at the semiconductor surface, providing the bridge from which all the other oxide states form. With the introduction of $(NH_4)_2S$ however, it is likely that the vast majority of these As_2O bonds are removed and the surface is left primarily As-S terminated, with only residual As_2O remaining, and based on a similar As^{1+} ratio being seen on both samples it is reasonable to assume that these bonds do saturates at one monolayer.

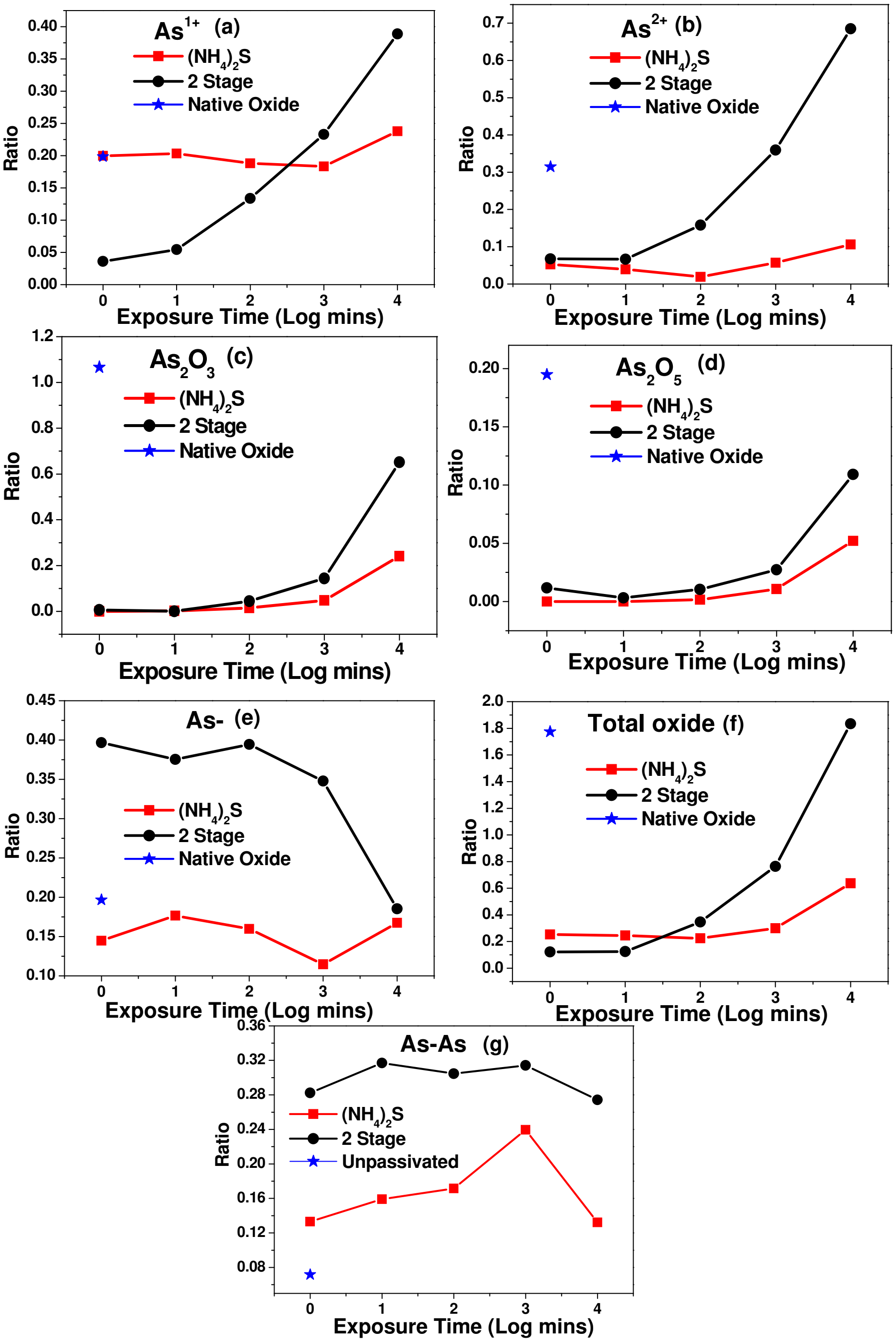

Figure 4.19 Ratio of oxide components to bulk peak from fitted As $2p_{3/2}$ spectra after the two surface treatments and from an unpassivated sample for comparison upon exposure to atmosphere

However on the 2 stage etched sample, we would expect the As^{1+} ratio to also saturate at the same level but it is seen to increase to a level of roughly twice the size with exposure. As stated, we see that there is a significantly lower level immediately after etching than on the native oxide and $(NH_4)_2S$ passivated surface, suggesting that a significant proportion of the As_2O has been removed. As this forms the immediate interface with the InGaAs surface, this would be expected to introduce a significant amount of disorder and surface states as now there is nothing providing a termination to the free bonds created with the removal of the oxygen. This increase in disorder and lack of termination could allow for increased levels of oxygen penetration below the surface layer causing subsurface oxidation which would allow for the increased level of As_2O formation with increased exposure, over and above the one monolayer seen on the other two samples.

Figure 4.19 (e) shows the ratio of the low binding energy (LBE) As- peak to the bulk. As seen in the figure 4.18, this is seen at a similar level on the native oxide and $(NH_4)_2S$ treated surfaces whereas the 2 stage etched samples, which would be the corollary to the unpassivated sample after in house MOVPE growth, shows a considerable amount present on the surface, greater than twice the level seen on the other two samples. While the $(NH_4)_2S$ sample changes very little with exposure and the 2 stage etched sample shows no significant change up to 1000 minutes, with extended exposure there is a dramatic reduction such that a common level is reached on all samples. This would seem to confirm the fact that when the oxide is removed from the surface, arsenic dimers and dangling bonds are formed at the surface. During $(NH_4)_2S$ passivation the sulphur interacts with these immediately as the oxygen is removed so that the As^{1+} peak on the $(NH_4)_2S$ sample remains at a similar level. The 2 stage etched sample relies on oxygen to passivate the created surface states so with increased exposure to atmosphere, there is a greater likelihood that this will take place. The fact that a common level is reached could be due to the fact that these bonds do not necessarily have to form protruding from the surface, potentially pointing in all directions at a disordered surface. A steric hinderance effect could then take place whereby once a monolayer of oxygen or sulphur is formed at the surface, this could reduced the likelihood for the penetration of further oxygen through it to passivate the remaining dangling bonds.

We see in figure 4.19 (b) from the As^{2+} peak that the ratio of the two treated surfaces are initially identical but with exposure there is very little change in the $(NH_4)_2S$

sample whereas above 10 minutes exposure of the 2 stage etched sample, we see a large increase in the As^{2+} signal again to roughly twice that seen on the native oxide sample. If we assume due to its early formation relative to the higher valance oxidation states that it also forms primarily at the surface and provides the initial foundation for the formation of the other oxidation states, the increased ratio relative to the native oxide could again be due to an increase in the number of surface states generated due to the etching process. It is also possible that the As^{2+} state has a lower formation energy than either As_2O_3 or As_2O_5 but is less thermodynamically stable so that while it might grow initially, over time it converts into alternative states.[22]

It is worth bearing in mind again at this point that the X axis is in Log minutes so each data point represents an order of magnitude increase in exposure time. The As_2O_3 and As_2O_5 ratios in figures 4.19 (c) and (d) indicate that there is virtually none detectable on either surface after treatment and there is no growth seen until after 10 minutes of exposure, indicating that As^{2+} and As^{1+} form the initial growth phase.[4] By the final exposure we see that although the ratios on the 2 stage etched sample are much higher than the $(NH_4)_2S$ sample, they are still lower than the values seen for the native oxide sample.

Looking at the total oxide ratios in 4.19 (f) we see that while the $(NH_4)_2S$ sample shows the largest initial ratio, due to the inclusion of As-S bonds, the effect of the passivation is very clear resulting in a much slower oxide growth rate. The 2 stage etched sample is seen to grow to roughly the same level as that of the native oxide which suggests that this could be a saturation limit to the oxide growth. This also could suggest that the As^{2+} state is a transitionary state that eventually will convert to either As_2O_3 or As_2O_5 still leaving the same overall oxide ratio and the prevention of its formation could be the key to preventing increased arsenic oxide formation.

Figure 4.19 (g) shows the ratio of the elemental arsenic peak area to the bulk peak. We can see that after both surface treatments, there is an increased level of As-As formed relative to the native oxide sample, with the $(NH_4)_2S$ sample showing a ~75% increase while the 2 stage etched sample showing a >300% increase, which would suggest that there is more than a monolayer present. The low level on the native oxide sample is likely due to the oxidation of the As-As over time reducing it to a concentration approaching detection limits. This would appear to be confirmed by the $(NH_4)_2S$ sample as while the ratio is seen to increase initially over time, after the final exposure, the ratio is below that seen initially and it can be speculated that this ratio will continue to decrease with time. The 2 stage etched sample however shows little change over time, even after the final exposure where it only returning to its level post etching. This suggests that the increased level present is an artefact of the etching procedure and the formation of the increased disorder at the surface, however to speculate further on this we need to first look at the gallium and indium peaks.

4.5.2. Removal of oxides and oxidation with ambient exposure - Ga

The corresponding spectra from the Ga 2*p* peaks are shown in figure 4.20. We can see on the 2 stage etched sample that by the fourth exposure, a significant broadening of the peak has taking place.

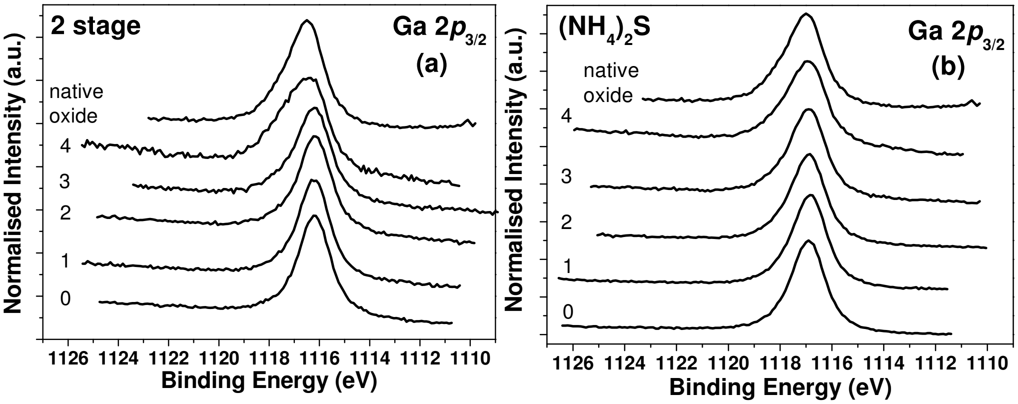

Figure 4.20 Ga $2p_{3/2}$ core level spectra after (a) 2 stage etching and (b) $(NH_4)_2S$ passivation with subsequent exposure to atmosphere for extended periods of time up to 10000 minutes

Due to the reduced binding energy separation between the peaks it is necessary to fit the peaks, again using the parameters developed previously with Gaussian values increased to 0.86 eV for the bulk peak and 1.26 eV for the oxide components, to account for the unmonochromated nature of the X ray source in this study. This leaves accurate deconvolution of the spectra more difficult so the actual determination of the individual peak components has an increased associated error. However, the actual level of total oxide present is still fairly straight forward to determine when comparing the as etched and ambient exposed spectra with the fitted peaks shown in figure 4.21. Initially, on both samples we see the presence of Ga_2O and trace amounts of $In_xGa_yO_z$ with no evidence of Ga_2O_3. [23]

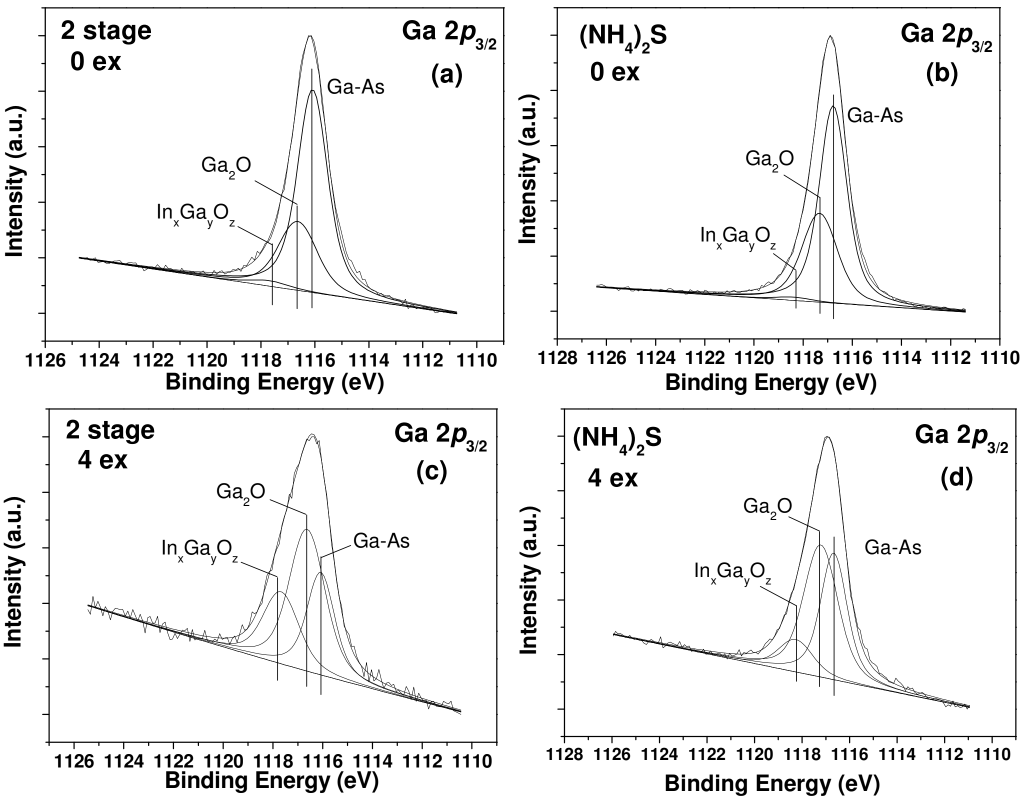

Figure 4.21 Fitted Ga $2p_{3/2}$ spectra with 2 stage (a, c) and $(NH_4)_2S$ (b, d) treatment with minimal (~1 min 0 ex) and 10000 minutes (4 ex) exposure to atmosphere

There is a slightly elevated level of the component peak attributed to Ga_2O present on the $(NH_4)_2S$ passivated sample, likely due to the presence of Ga-S bonds, which are not possible to resolve and are reported to form at 0.7 eV from the bulk peak.[24] With increased exposure on both samples we see the growth of Ga_2O and $In_xGa_yO_z$ and still no evidence of Ga_2O_3 however it is possible that this is a resolution issue. The ratio of the fitted peak components is shown in figure 4.22. As we saw with the annealing study, the thermodynamics of the gallium and indium oxides are very complex, with oxygen bond transfers taking place readily between the two as the substrate temperature is increased and it is possible that this could take place over extended periods of time also as the states try to reach thermodynamic equilibrium. In the figures the three identified oxidation states are plotted in the same graph for comparison purposes and the total oxide ratios are again compared separately.

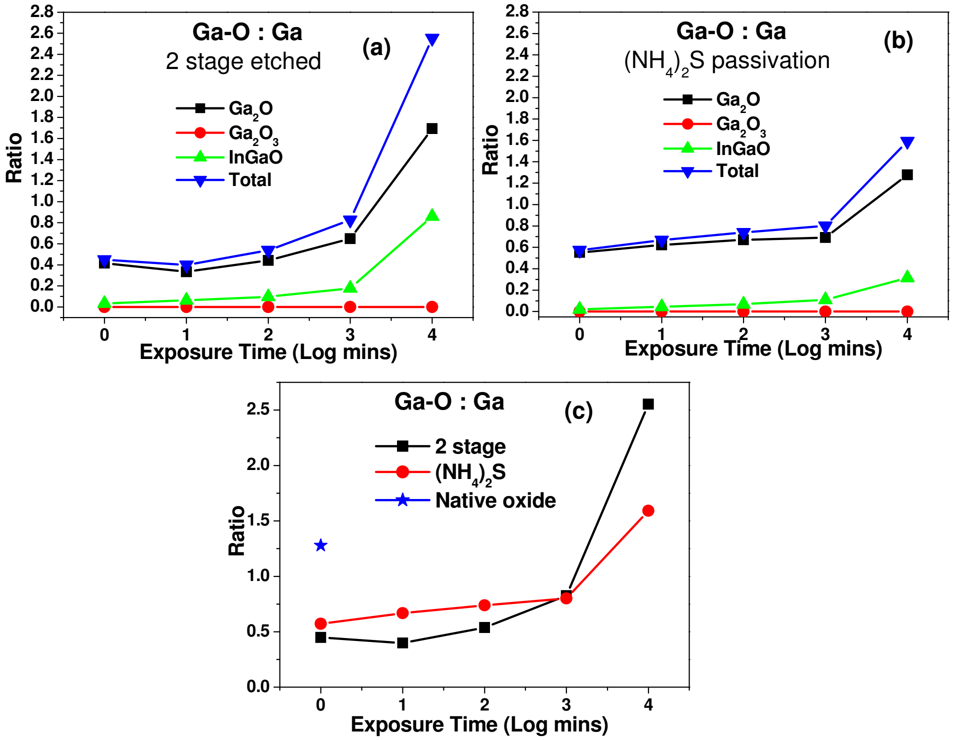

Figure 4.22 Ratio of oxide components to bulk peak from fitted Ga 2$p_{3/2}$ spectra after (a) 2 stage etching and (b) $(NH_4)_2S$ treatments and (c) showing the ratio of the combined oxide peaks

Looking first at the Ga_2O ratios, we see that while the $(NH_4)_2S$ sample shows a greater overall ratio to begin with (due to incorporation of Ga-S bonds in the peak area) the growth rate is much slower and by 1000 minutes or exposure 3 the ratios are very similar even taking into account the presence of Ga-S bonds, and further exposure shows the a greater level of Ga_2O present on the 2 stage etched sample. Whether it is an artefact of the fitting procedure is not fully clear but with the first exposure on the 2 stage etched sample, the Ga_2O ratio is actually seen to decrease, which could be evidence of oxygen conversion to other oxide states.

The $In_xGa_yO_z$ oxide is seen to grow on both samples but again, at a much slower rate on the $(NH_4)_2S$ treated sample, reaching only ~35% of that reached on the two stage etched sample. Looking at the total oxide ratio, the reduced oxide formation with sulphur passivation is again highlighted, however the level of gallium oxide growth on both samples in greater than that seen for the native oxide. The presence of $GaAsO_4$ is not detected on either sample, suggesting that it is the least stable oxidation state, as also seen in chapter 3.4.1, possibly only forming upon the saturation of the other oxidation states.

4.5.3. Removal of oxides and oxidation with ambient exposure – In

The corresponding In $3d_{5/2}$ peaks are shown in figure 4.23. Again however, we are hampered by the relatively small binding energy separation between the peaks and also the reduced surface sensitivity associated with this peak in comparison to the As and Ga 2*p* peaks, reducing the overall oxide contribution in the spectra. As a result of this, there are no obvious changes seen in these spectra with exposure apart from a slight broadening evident after the final exposure on the 2 stage etched sample.

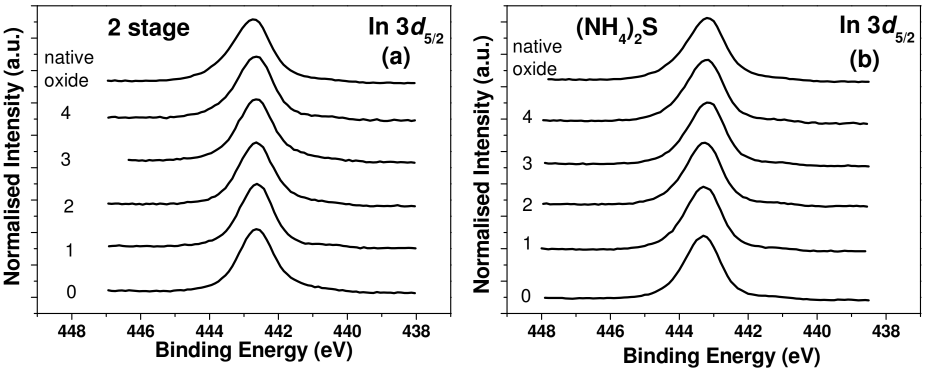

Figure 4.23 In $3d_{5/2}$ core level spectra after (a) 2 stage etching and (b) $(NH_4)_2S$ passivation with subsequent exposure to atmosphere for extended periods of time up to 10000 minutes

In order to try to determine the level of oxide present, the peaks are again fit using previously determined parameters for the oxide binding energy separations from chapter 3.3.4 and the fits after initial surface treatments and the final exposure are shown in figure 4.24. After the initial surface treatments we see the presence of In^{1+}, $In_xGa_yO_z$ and In_2O_3 (In^{3+}) with the latter two at a similar level on both samples. The In^{1+} peak is again seen to be larger on the $(NH_4)_2S$ sample, likely due to the presence of In-S bonds which are difficult to unambiguously resolve. There are two peaks also evident at the lower binding energy side of the peaks labelled X and Y which are difficult to characterise however as they were not seen when these samples were examined with a monochromated XPS source during the sulphur passivation optimisation study, so it can be speculated that these are system specific ghost peaks, although the binding energy separation of ~1.05 eV and 2.1 eV from the bulk peak does seem small for this assignment and would be typical of metallic or surface states.

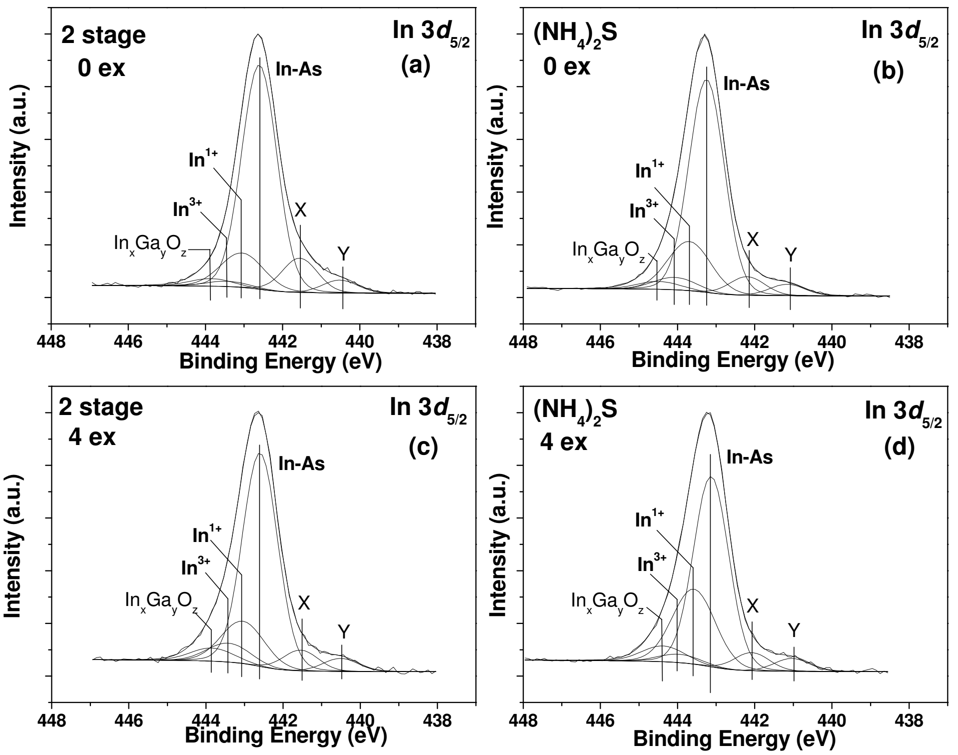

Figure 4.24 Fitted In 3$d_{5/2}$ spectra with 2 stage (a, c) and $(NH_4)_2S$ (b, d) treatment with minimal (~1 min 0 ex) and 10000 minutes (4 ex) exposure to atmosphere

With exposure to atmosphere, we see that there is growth in all of the oxide states however this time, there appears to be more oxide forming on the $(NH_4)_2S$ sample and primarily in the In^{1+} state. If we look at the component ratios in figure 4.25, it is apparent that the changes in the oxidation states are not as well defined as with the gallium and arsenic peaks, with apparently random changes taking place in the ratios and probably exceeding the experimental error. Again due to the small binding energy separation between the peaks, the reduction in surface sensitivity relative to the As 2*p* and Ga 2*p* peaks as well as the increased peak width due to the unmonochromated X-ray source, it is difficult to accurately resolve the peak components unambiguously to tell if these changes are real, however based on the ratio of the total oxide to bulk ratio in 4.25 (d), it is clear that there is more oxide present on the $(NH_4)_2S$ sample throughout the exposure study which could not be solely attributed to the presence of In-S bonds.

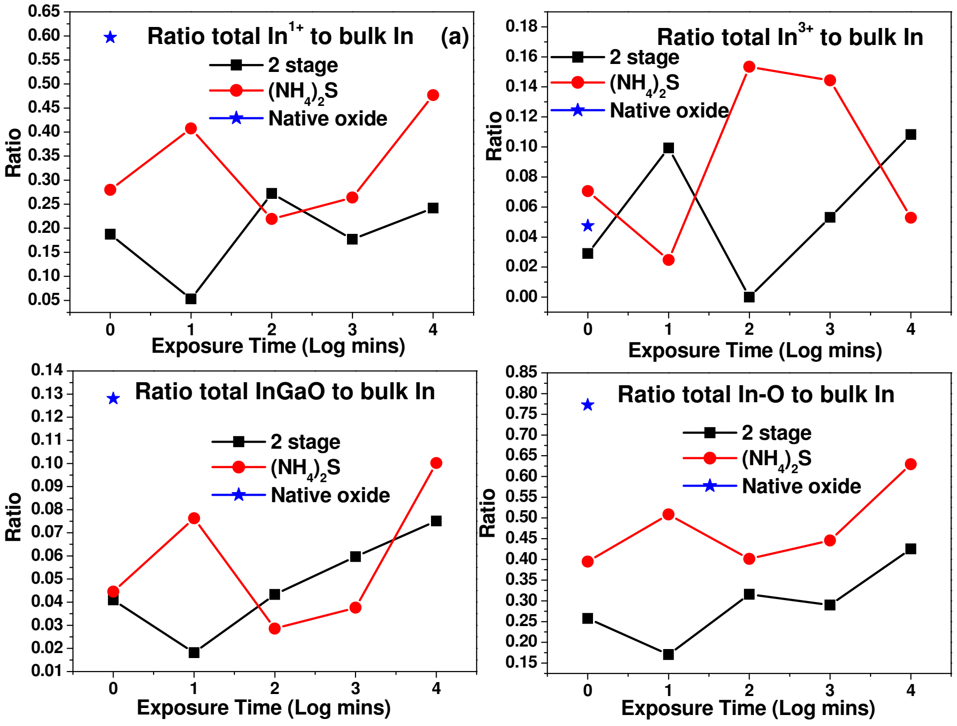

Figure 4.25 Ratio of (a) In^{1+}, (b) In^{3+} and (c) InGaO oxide components to bulk peak and (d) total oxide to bulk peak from fitted In $3d_{5/2}$ spectra after 2 stage etching and $(NH_4)_2S$ treatments

4.6. Discussion and conclusions

Typically ammonium hydroxide (NH_4OH) is used to etch GaAs surfaces,[25] leaving the surface oxide free but unpassivated. It has also been used to etch the InGaAs surface however there is not much literature available to conclusively show that it is effective at removing all of the indium oxides. The two stage etching procedure was primarily designed for use with InP substrates, whereby all the native oxide were seen to be removed, leaving the surface covered with 0.4 monolayers of elemental phosphorous which in turn was terminated with H. This left the surface hydrophobic, preventing certain amounts of ambient oxidation with the elemental phosphorous easily removed by annealing in vacuum to 200 °C.[26] Studies by the same group on GaAs using the same etching procedures, carried out without any exposure to atmosphere, revealed only the presence of elemental arsenic and a gallium sub oxide, and with subsequent annealing to 500 °C, the elemental arsenic and gallium oxide were removed with the generation of surface states.[17] It is possible therefore that the two stage etch leaves the surface primarily terminated in Ga and As, or quite possibly, considering the increased area ratio in figure 4.19 (g), a surface layer of elemental arsenic which could be H terminated. This would have the effect of restricting the growth of the indium oxides and creating an apparent relative increase in the total oxide ratio on the $(NH_4)_2S$ sample due to more In being present at the surface. This elemental arsenic layer would be in addition to that which would form during the reduction or growth of the native oxide creating a thicker layer than seen with $(NH_4)_2S$ making it less likely to fully reoxidise or at least take a longer time to do so. This could also explain the increase in surface states seen with the two stage etched sample relative to the $(NH_4)_2S$ sample due to the increased disruption at the interface between the oxide and the substrate, however a more detailed investigation of the effect of the two stage etch would be necessary and is beyond the scope of this work needing a more comprehensive study.

What this study suggests is that although it may not be possible to generate a totally oxide free surface with aqueous ammonium sulphide passivation, the optimal treatment in terms of terms of prevention of ambient oxidation and surface roughness was found to be 10% $(NH_4)_2S$ for 20 minutes at room temperature. Passivation by H_2S showed that it was possible to sulphur terminate the surface by flowing the gas over the surface after growth and particularly in terms of the sample passivated at 350 °C. By comparing the $(NH_4)_2S$ passivation process to that of a standard two stage etching procedure, it was possible to further highlight the effectiveness of sulphur passivation at preventing ambient oxidation over extended periods of time and also suggested that the passivation process reduces the possibility of defect formation in terms of the generation of increased levels of elemental arsenic and surface states, which could be detrimental to the creation of high quality semiconductor devices on these surfaces. Further studies are needed to compare the effectiveness of these passivation processes to alternative sulphur based passivations which have also been shown to chemically and electrically passivate GaAs and InP surfaces through the generation of group III and sulphur bonding.

4.7. References

---

[1] P. Streubel, H. Peisert, R. Hesse, T. Chasse, R. Szargan, Surf. Interface Anal., 23, 581, (1995)

[2] M. Kang, S. Sa, H. Park, K. Suh, J. Lee, Mat. Sci. Eng. B, 46, 65, (1997)

[3] G. Landgren, R. Ludeke, Y. Jugnet, J. F. Morar, and F. J. Himpsel, J. Vac. Sci. Technol. B 2, 351, (1984)

[4] D. Y. Petrovykh, J. M. Sullivan, L. J. Whitman, Surf. Interface Anal., 37, 989, (2005)

[5] S. Koveshnikov, N. Goel, P. Majhi, H. Wen, M. B. Santos, S. Oktyabrsky, V. Tokranov, R. Kambhampati, R. Moore, F. Zhu, et al., Appl. Phys. Lett., 92, 222904, (2008).

[6] F. S. Aguirre-Tostado, M. Milojevic, C. L. Hinkle, E. M. Vogel, R. M. Wallace, S. McDonnell, G. J. Hughes, Appl. Phys. Lett. 92, 171906, (2008)

[7] M.V. Lebedev, D. Ensling, R. Hunger, T. Mayer, W. Jaegermann, Appl. Surf. Sci, 229, 226, (2004)

[8] P. Moriarty, B. Murphy, L. Roberts, A.A. Cafolla, L. Koenders, P. Bailey, G. Hughes, Phys. Rev B, 50, 14237, (1994)

[9] S. Arabasz, E. Bergignat, G. Hollinger, J. Szuber, Vacuum, 80, 888, (2006)

[10] V. Chab, L. Pekarek, I. Ulrych, J. Suchy, K.C. Prince, M. Peloi, M. Evans, C. Comicioli, M. Zacchigna, C. Crotti, Surf. Sci., 377, 261, (1997)

---

[11] P. Moriarty, B. Murphy, L. Roberts, A.A. Cafolla, G. Hughes, L. Koenders, P. Bailey, D.A. Woolf, Appl. Phys. Lett, 67, 383, (1995)

[12] D. Paget, J.E. Bonnet, V.L. Berkovits, P. Chiaradia, Phys. Rev. B 53, 4604, (1996)

[13] C.J. Spindt, D. Liu, K. Miyano, P.L. Meissner, T.T. Chiang, T. Kendelewicz, I. Lindau, W.E. Spicer, Appl. Phys. Lett. 55, 861, (1989)

[14] I. Horcas, R. Fernandez, J.M. Gomez-Rodriguez, J. Colchero, J. Gomez-Herrero, A.M. Baro, Rev. Sci. Instrum. 78, 013705, (2007)

[15] J. S. Herman, F. L. Terry, Jr. Appl. Phys. Lett. 60, 716, (1992)

[16] E. O'Connor, R. D. Long, K. Cherkaoui, K. K. Thomas, F. Chalvet, I. M. Povey, M. E. Pemble, P. K. Hurley, B. Brennan, S. B. Newcomb, G. Hughes, Appl. Phys. Lett. 92, 022902, (2008)

[17] L. Zhi, S. Yun, F. Machuca, P. Pianetta, W.E. Spicer, R.F.W. Pease, J. Vac. Sci. Technol. A, 21, 212 (2003)

[18] T. Ishikawa, H. Ikoma, Jpn. J. Appl. Phys. 32, L607, (1993)

[19] J. Robertson, Appl. Phys. Lett, 94, 152104, (2009)

[20] C.-C. Cheng, C.-H. Chien, G-L. Luo, C.-K. Tseng, H.-C. Chiang, C.-H. Yang, C.-Y. Chang, J. Electrochem. Soc., 155, G56, (2008)

[21] M. V. Lebedev, E. Mankel, T. Mayer, W. Jaegermann, J. Phys. Chem. C, 112, 18510, (2008)

[22] T. Ishikawa, H. Ikoma, Jpn. J. Appl. Phys. 31, 3981, (1992)

---

[23] C.L. Hinkle, M. Milojevic, B. Brennan, A.M. Sonnet, F.S. Aguirre-Tostado, G. Hughes, E.M. Vogel, R.M. Wallace, Appl. Phys. Lett., 94, 162101, (2009)

[24] S. Arabasz, E. Bergignat, G. Hollinger, and J. Szuber, Appl. Surf. Sci., 252, 7659, (2006).

[25] É. O'Connor, S. Monaghan, R. D. Long, A. O'Mahony, I. M. Povey, K. Cherkaoui, M. E. Pemble, G. Brammertz, M. Heyns, S. B. Newcomb, V. V. Afanas'ev, P. K. Hurley, Appl. Phys. Lett., 94, 102902, (2009)

[26] Y. Sun, Z. Liu, F. Machuca, P. Pianetta, W.E. Spicer, J. Vac. Sci. Technol. A 21, 219, (2003)

5. ‘Half Cycle’ atomic layer deposition study of Al_2O_3 on InGaAs

5.1. Introduction

Having decided on the optimal sulphur passivated surface of 20 minutes in 10% $(NH_4)_2S$ at room temperature following standard degreasing, the next step was to deposit a high-κ dielectric material to investigate the various interactions that take place at the interface between metal oxides and the semiconductor surface.

One particular such study involved the deposition of Al_2O_3 using atomic layer deposition (ALD). Having a dielectric constant of ~10, it is not the seen as the long term solution to the replacement of SiO_2 in semiconductor devices, however the availability of high quality ALD organo-metalic precursors, for example in this study tri-methyl aluminium (TMA or $(CH_3)_3Al$), means it is being widely investigated for its short to medium term benefits.[1, 2]

Typically the oxidant in the ALD process is water,[3] however due to its wetting nature, it is suspected that it can leave residual water in the ALD reactor which can potentially decompose the TMA molecule before it reaches the sample surface and hence introduce contamination which could impact on the quality of the grown oxide layer.[4,5] Therefore, it has been proposed that ozone (O_3) which is well known oxidant, as shown earlier when determining the InGaAs fitting parameters, could be used to replace H_2O in the process.[6] The major benefit of O_3 is that it is gaseous, meaning it can be easily evacuated from the ALD reactor following the oxidation cycle reducing the probability of TMA decomposition and the formation of hydroxyl states in the film.

In order to investigate this, a "half cycle" reaction study was carried out.[7] One full cycle of the ALD process involves the deposition of a metal layer in the first half cycle followed by an oxidation half cycle. Therefore the half cycle study investigates the growth properties after each successive individual metal and oxidation half cycle with analysis by XPS. This is only possible with an in-*situ* ALD and XPS system as it allows the sample to be examined without exposure to atmospheric conditions, preserving the quality of the surface without the introduction of detrimental contamination such as carbon and hydroxyl species.

5.2. Experimental

The samples studied were ~2µm sulphur doped ($4x10^{17}cm^{-3}$) $In_{0.53}Ga_{0.47}As$ grown by metal organic vapour phase epitaxy (MOVPE) on heavily doped (S ~$4x10^{18}cm^{-3}$) InP(100) wafers. 1 cm^2 samples were cleaved from a single 50 mm diameter wafer so that initial conditions were consistent across all samples. Ammonium sulphide passivation (10% $(NH_4)_2S$ for 20 minutes at room temperature as described in the previous chapter) with prior degreasing was carried out immediately before loading the samples to UHV, with a maximum of 5 minutes ambient exposure. The TMA was delivered to an integrated dual chamber ALD reactor with a substrate temperature of 300°C and a base pressure of ~700 mTorr through heated lines and valves.[8] Prior to the deposition process, the ALD reactor was baked at 300 °C for 24 hours and seasoned with 300 cycles of TMA to remove the possibility of spurious H_2O remaining in the reactor. High purity H_2 (99.999%) was used as the purging gas and ozone from an O_3 generator delivering an O_3 concentration of ≥ 350 g/m^3 at the generator, which is located 25 m from the ALD reactor. XPS spectra from the As 2*p*, Ga 2*p*, In 3*d*, O 1*s*, C 1*s*, In 4*d* and Ga 3*d*, Al 2*p* and S 2*p* regions were taken after each half cycle up to three full cycles and finally after a 1 nm film was grown (such that one cycle ≈ 0.1 nm and 10 cycles ≈ 1 nm). Each full cycle consisted of:

0.1 s TMA/N_2 + 4 s N_2 + 0.1 s O_3 or H_2O + 4 s N_2.

5.3. Results

5.3.1. ALD with H_2O oxidation

The curve fitted XPS spectra from the As $2p_{3/2}$ peaks after successive half cycles with H_2O oxidation are shown in figure 5.1. For the As 2*p* in figure 5.1(a) after $(NH_4)_2S$, we again see the bulk As-Ga peak at 1322.61 eV, a small residual As_2O_3 (1325.89 eV) and elemental As peak (1323.36 eV) with trace amounts of As_2O_5 (1327.05 eV) and the 2+ peak (1325.16 eV) and a lower binding energy peak attributed to surface dimers (1322.25 eV). There is no evidence of any $GaAsO_4$ within detection limits of the XPS.[9]

As per the sulphur passivation study, we see a peak at ~1.54 eV from the bulk peak consistent with the formation of As-S bonds.[10,11] With the first TMA cycle, the As_2O_3

peak is reduced to within detection limits with all traces of 2+ and As_2O_5 also removed. A small residual 1+ peak remains, possibly due to surface bonded As_2O as it is possible that the As-S bonds are removed due to the elevated substrate temperature in the reactor. The elemental arsenic peak also remains as well as a small increase in the LBE peak, possibly due to the decomposition of the oxide leaving As dangling bonds at the surface. With successive cycles, there is no evidence of arsenic oxide growth suggesting that the H_2O only reacts with the deposited Al layer at the surface.[12] A small 1+ peak is seen to remain, but this does not appear to grow throughout the deposition process suggesting it is stable. It is possible that this provides the initial bonding site for the Al creating AlO_x (with $x<3$) with the first cycle and is backed up by the annealing study of the InGaAs native oxide in chapter 3.4 which suggested that the As^{1+} state was localised at the semiconductor oxide interface.

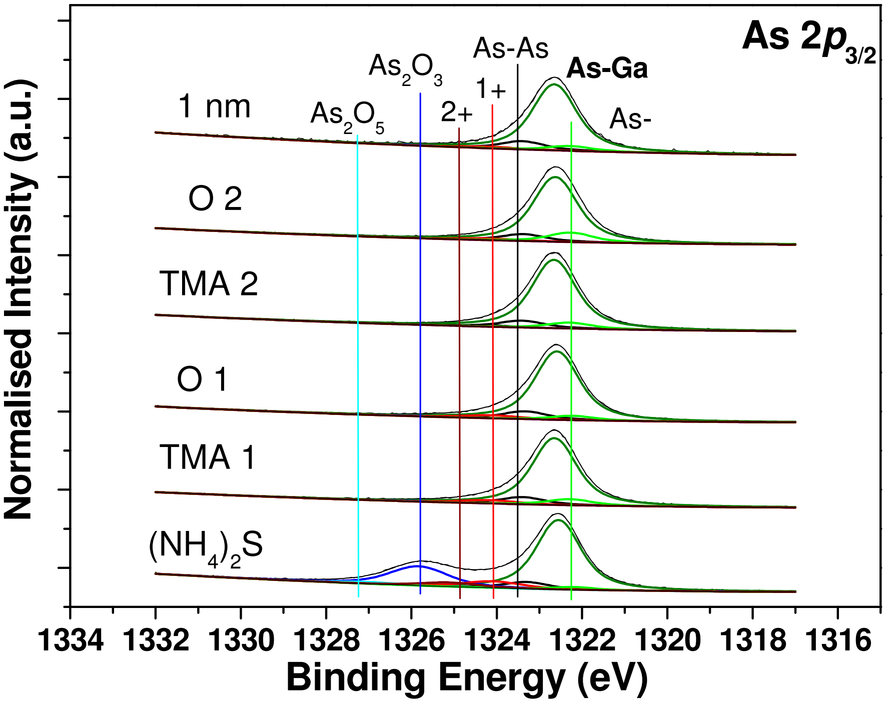

Figure 5.1 Fitted As 2*p* spectra after successive ALD 'half cycles' during the Al_2O_3 deposition with H_2O oxidation

Typically for ALD growth on Si, the sample is prepared by etching the surface with HF, leaving the surface hydrogen terminated, which is useful as hydrogen is generally the key to instigating the TMA reaction with the surface.[13] It is possible that the surface of the InGaAs after $(NH_4)_2S$ and subsequent transfer to UHV contains hydroxyl species, which are not easily detected with XPS, which would facilitate the reaction of the TMA with the surface such that Al_2O_3 would be formed in a single cycle to create the desired stochiometry of:

$$2Al(CH_3)_3 + 3H_2O \rightarrow Al_2O_3 + 6CH_4$$

where the TMA reacts with water species to create Al_2O_3 and volatile CH_4 through the two stage reaction[14,15]

$$Al - OH + Al(CH_3)_3 \rightarrow Al - O - Al(CH_3)_2 + CH_4$$

and

$$Al - CH_3 + H_2O \rightarrow Al - OH + CH_4$$

This would initially leave the surface ethyl terminated and with further interaction with water would leave the surface hydroxyl terminated again producing volatile CH_4.

The reduction of the As_2O_3 peak seen as the so called “clean up”, effect, is due to a ligand exchange mechanism between the trivalent As_2O_3 and Al_2O_3 whereby the Al^{3+} in the $Al(CH_3)_3$ precursor preferentially reacts with the 3+ oxidation states and presumably forms volatile reaction products such as $As(CH_3)_3$.[17] There are no significant changes evident throughout the remaining half cycles such that with the final spectra after 1 nm of Al_2O_3 growth we see virtually the same spectra as after the first TMA cycle.

The corresponding Ga $2p_{3/2}$ spectra are shown in figure 5.2. Initially after $(NH_4)_2S$ passivation we see the presence of Ga_2O (1117.75 eV), Ga_2O_3 (1118.3 eV) and a trace amount of $GaAsO_4$ (1118.8 eV) with the bulk peak at 1117.2 eV.[9,16,17] After the first TMA half cycle, there is no sign of the $GaAsO_4$ peak, which is probably removed due to the increased substrate temperature in the ALD reactor. There is a small reduction in the Ga_2O peak and the Ga_2O_3 peak has also been reduced to within detection limits, again due to the ligand exchange mechanism with Al^{3+} in $Al(CH_3)_3$.

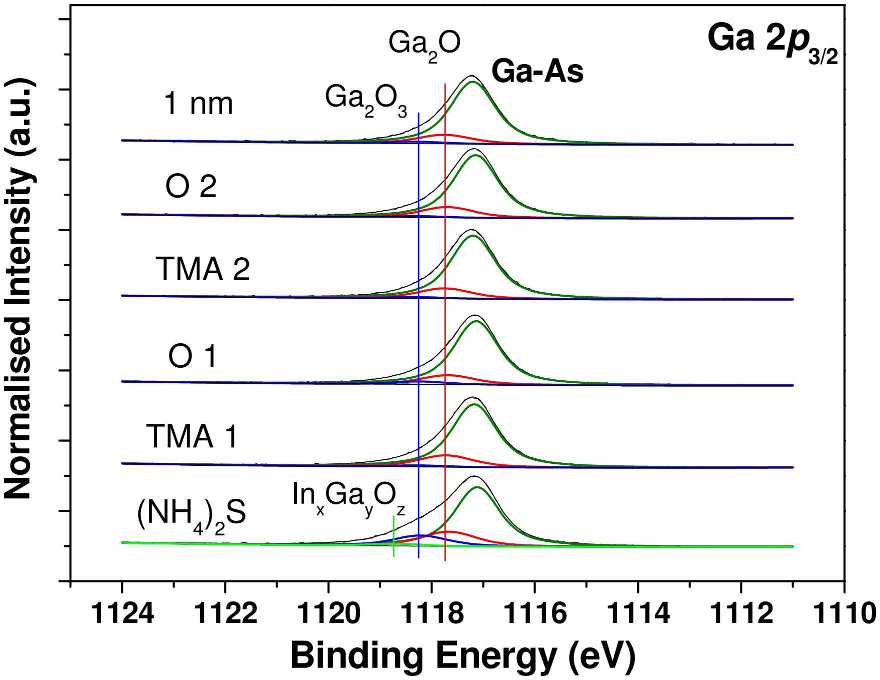

Figure 5.2 Fitted Ga 2*p* spectra after successive ALD 'half cycles' during the Al_2O_3 deposition with H_2O oxidation

With subsequent cycles, only the Ga_2O oxide state remains and at a relatively constant level throughout. Again, this is possibly due to Ga_2O providing the interface between the Al_2O_3 and the substrate. It is also possible that there is a contribution from Ga-S bonds incorporated in this peak, which as shown in table 1 are reported to be ~0.7 eV from the bulk peak[18,19] however they are difficult to resolve here.

For the In 3*d* $_{5/2}$ spectra in figure 5.3 there are a few interesting features. Again we see the characteristic asymmetry in the In 3*d* peak that we saw earlier. Initially after $(NH_4)_2S$ passivation, there is no evidence of the In^{1+} peak which we had seen from earlier after $(NH_4)_2S$ treatments. There is also no evidence of the $In_xGa_yO_z$ peak which was detected in the Ga 2*p* spectra, however this is likely due to the reduced surface sensitivity of the In 3*d* peak and clearly from the Ga 2*p* spectra, this oxide would be present at a very low level. The absence of the In^{1+} peak however could be due to a slightly reduced transfer time loading to UHV after removal from the $(NH_4)_2S$ preventing it from forming. There is evidence of the In^{3+} peak at 445.2 eV[20] with the bulk peak at 444.38 eV however, and with the first TMA cycle, this is seen to reduce but is not fully removed like the As^{3+} and Ga^{3+} peaks.

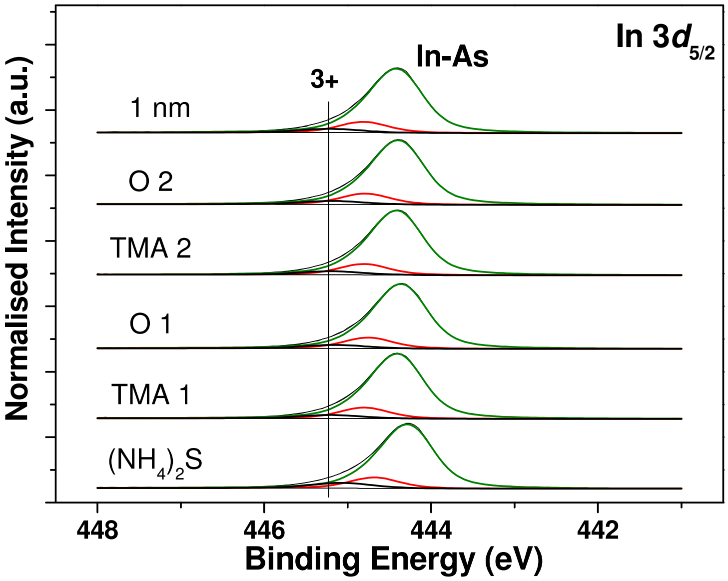

Figure 5.3 Fitted In 3*d* spectra after successive ALD ‘half cycles’ during the Al_2O_3 deposition with H_2O oxidation

This might suggest the presence of a significant level of In-S bonding as the ligand exchange mechanism would be expected to target this oxidation state preferentially converting the oxide to Al_2O_3. There is very little information regarding the exact binding energy position of potential In-S bonding or what form it would take so the possibility is that it has a similar binding energy to that of In_2O_3 which might explain these anomalies. It has also been reposted that sulphur bonds form preferentially with the group III elements[20] suggesting that they are more stable which increases the probability of them remaining on the surface. It is also possible that this is due to the formation of In-OH bonds, however again, there is very little reliable information available regarding their relative peak positions. With subsequent half cycles, there is no change evident in the spectra.

5.3.2. ALD with O_3 oxidation

Figure 5.4 shows the corresponding As 2*p* spectra, replacing H_2O with O_3 as the oxidant. The As 2*p* spectra initially shows perfect reproducibility of the $(NH_4)_2S$

passivation and after first TMA half cycle. However, with the first ozone cycle, dramatic changes are evident.

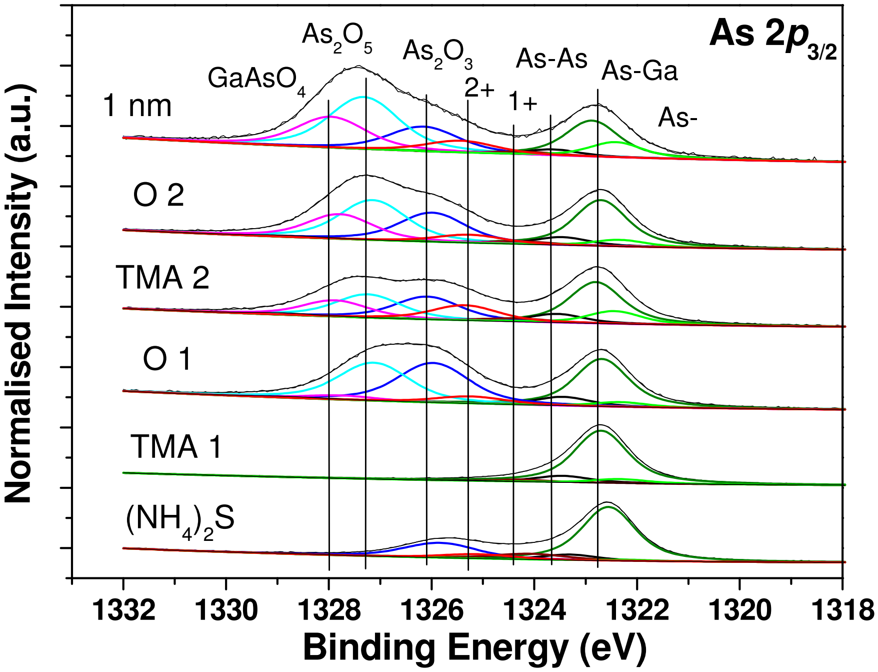

Figure 5.4 Fitted As 2*p* spectra after successive ALD 'half cycles' during the Al_2O_3 deposition with O_3 oxidation

An interfacial oxide similar in appearance to that of the native oxide prior to $(NH_4)_2S$ treatment is seen, with the emergence of As_2O_3 and As_2O_5 at significant level, as well as evidence of a $GaAsO_4$ (5.08 eV from the bulk peak) and the As^{2+} peak. The As^{1+} peak however remains at a consistent level and with subsequent cycles is not seen to vary which again suggests that it only resides at the interface between the substrate and the other oxide states. With the second TMA cycle, there is a reduction in the As_2O_3 and As_2O_5 peaks of ~35% however a significant amount does still remain suggesting that there is a reaction channel limit during a given TMA cycle over which the clean up effect can take place. Given that the As_2O_3 and As_2O_5 peaks are seen to reduce by a similar amount, and since this reduction goes towards the formation of Al_2O_3, there are two residual oxygen bonding sites left over from the decomposition of the As_2O_5 which cause an increase in the $GaAsO_4$ and As^{2+} peaks. There is also an increase seen in the As- peak.

With subsequent cycles, the As_2O_5 and $GaAsO_4$ peaks are seen to increase while the As_2O_3 peak stays relative constant, only returning to the level seen after the first ozone cycle. This is the most conclusive evidence that a ligand exchange mechanism is causing the clean up effect. The As^{3+} ions in As_2O_3 react with the tri-valent Al atoms in the precursor to form Al_2O_3. Because the As in As_2O_5 is in a 5+ oxidation state, this ligand exchange mechanism is less favourable, so this oxide state continues to grow while the 3+ state is suppressed. The LBE peak is also seen to grow throughout as the cycle of oxidation and reduction of the substrate causes increased disruption possibly leaving increased levels of As dimers or potentially low levels of dangling bonds.

The Ga $2p_{3/2}$ spectra are shown in figure 5.5. Again we see the same peak conditions after $(NH_4)_2S$ treatment and the first TMA cycle as were seen an on the previous sample, with only Ga_2O remaining on the surface.

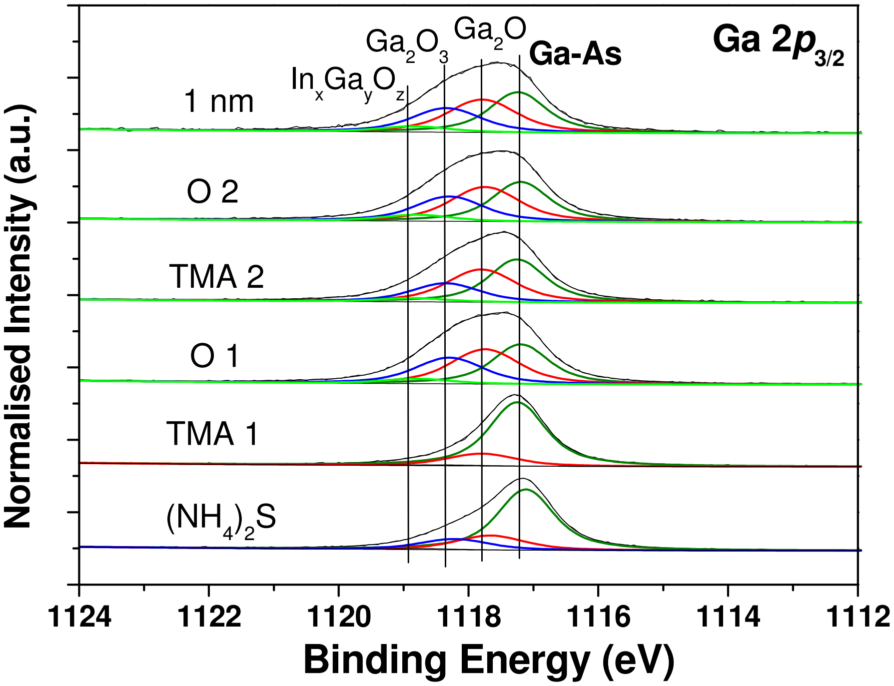

Figure 5.5 Fitted Ga $2p$ spectra after successive ALD 'half cycles' during the Al_2O_3 deposition with O_3 oxidation

With the first ozone cycle, we see a large increase in the Ga_2O and Ga_2O_3 peaks as well as the emergence of an $In_xGa_yO_z$ peak, however there is no evidence of the $GaAsO_4$ peak 2.05 eV from the bulk, corresponding to the peak seen in the As 2*p* spectra. With subsequent TMA and ozone cycles, there is no significant change in the amount of oxide present again suggesting that the trivalent Al_2O_3 is able to control the level of tri- and lower valency oxide states, without fully removing them due to a reaction channel limit.

The In 3$d_{5/2}$ spectra in figure 5.6 again highlight the repeatability of the $(NH_4)_2S$ passivation and clean up with the first TMA cycle, with only In_2O_3 present within detection limits, possibly including an In-S contribution. With the first O_3 cycle, we see the emergence of an In^{1+} peak at 444.83 eV and an $In_xGa_yO_z$ peak at 445.63 eV, which remain throughout the remaining half cycles and are still seen after 1 nm of Al_2O_3 growth. The oxides do not appear to grow after the first full cycle, suggesting that either the ligand exchange mechanism is effective at reducing any further growth or the Al_2O_3 acts as a barrier preventing any further interfacial oxidation.

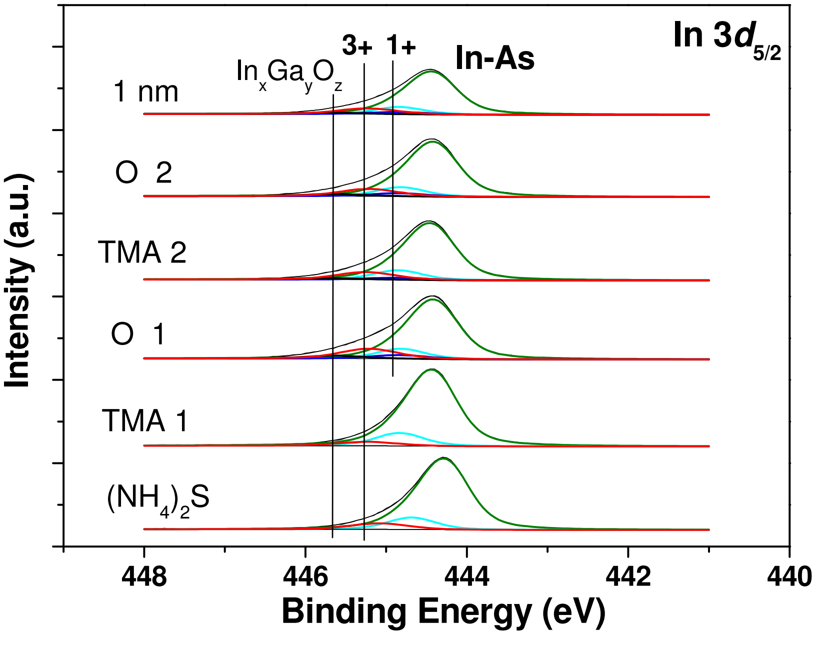

Figure 5.6. Fitted In 3*d* spectra after successive ALD ‘half cycles’ during the Al_2O_3 deposition with O_3 oxidation

5.3.3. Comparison

To highlight the variation between the two oxidation methods, the corresponding spectra after one cycle of H_2O and O_3 are presented in figure 5.7, showing in more detail the increased interfacial oxidation with O_3.

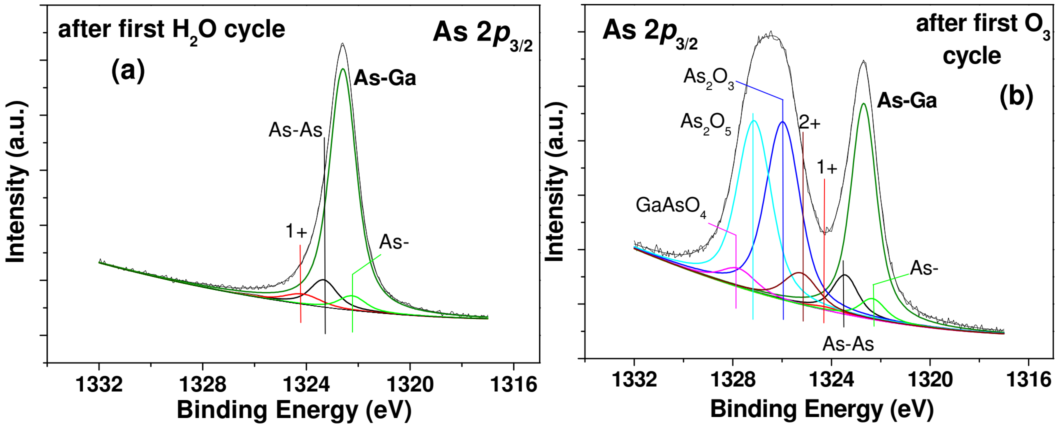

Figure 5.7 Fitted As 2*p* peak with one cycle of (a) H_2O and (b) O_3

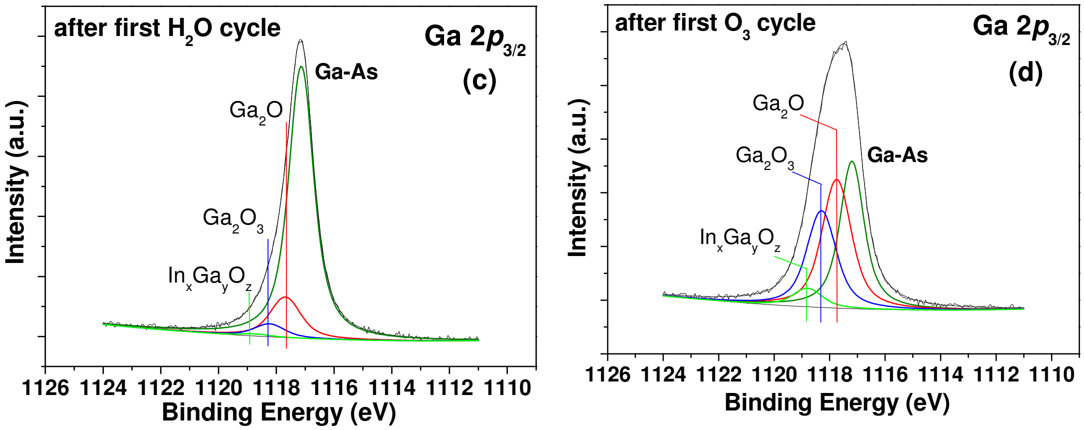

Figure 5.7 Fitted Ga 2*p* peak with one cycle of (c) H_2O and (d) O_3

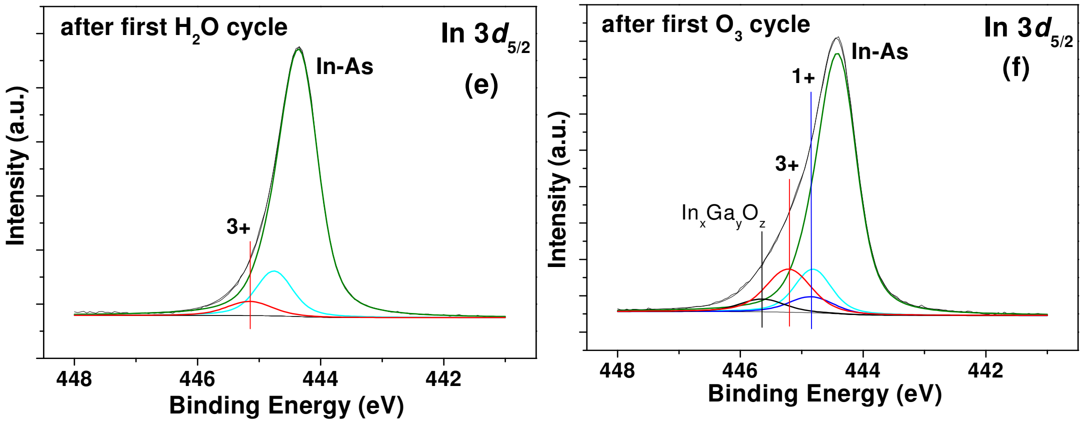

Figure 5.7 Fitted In 3*d* peak after one cycle of (e) H_2O and (f) O_3

Taking the ratio of the area of the oxide peak components to that of the corresponding substrate peaks, we can get a clear idea of the level of oxide growth taking place and at what stage in the deposition process. Figure 5.8 shows the ratio of the total oxide contribution to that of the bulk for the As 2*p*, Ga 2*p* and In 3*d* peaks while figure 5.9 shows the ratio of the contributing oxide components to the bulk peaks. Comparing the total ratios highlights the large difference between the O_3 and H_2O oxidations. The large variation between the indium and both Ga and As ratios after oxidation with O_3 can be attributed to the variations in the relative kinetic energies of the photoemitted electrons with the more surface sensitive Ga and As peaks giving a larger surface localised oxide signal. It is also clear that the most significant amount of interfacial oxidation occurs with the first cycle of O_3 with no overall change seen in the Ga or In ratios after this cycle.

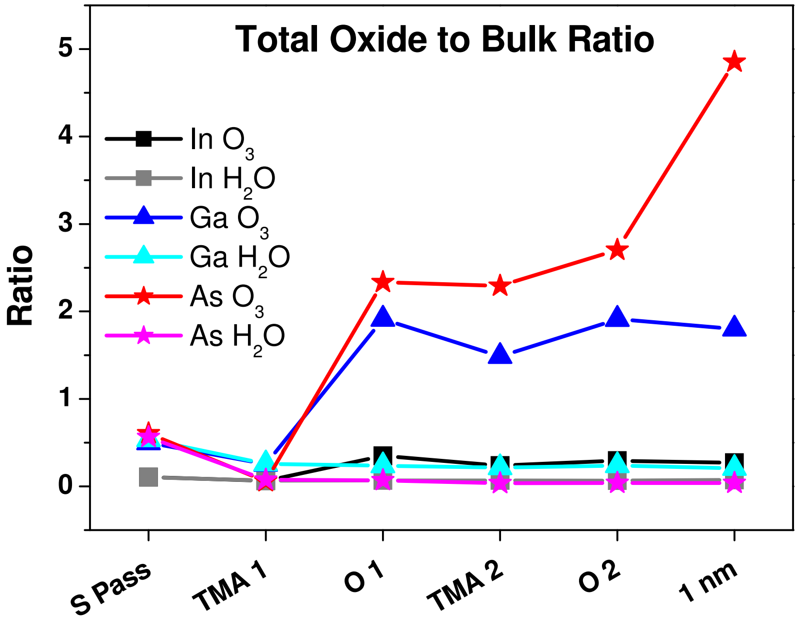

Figure 5.8 Ratio of oxide components to bulk peak areas from fitted data after successive half cycles of the ALD process

The As ratio does increase however and looking at the figure 5.9, we see that this is as a result of an increase in As_2O_5 and $GaAsO_4$ specifically, and the only oxides present with a valency higher than that of Al_2O_3, reaffirming the concept of a ligand exchange reduction mechanism taking place.

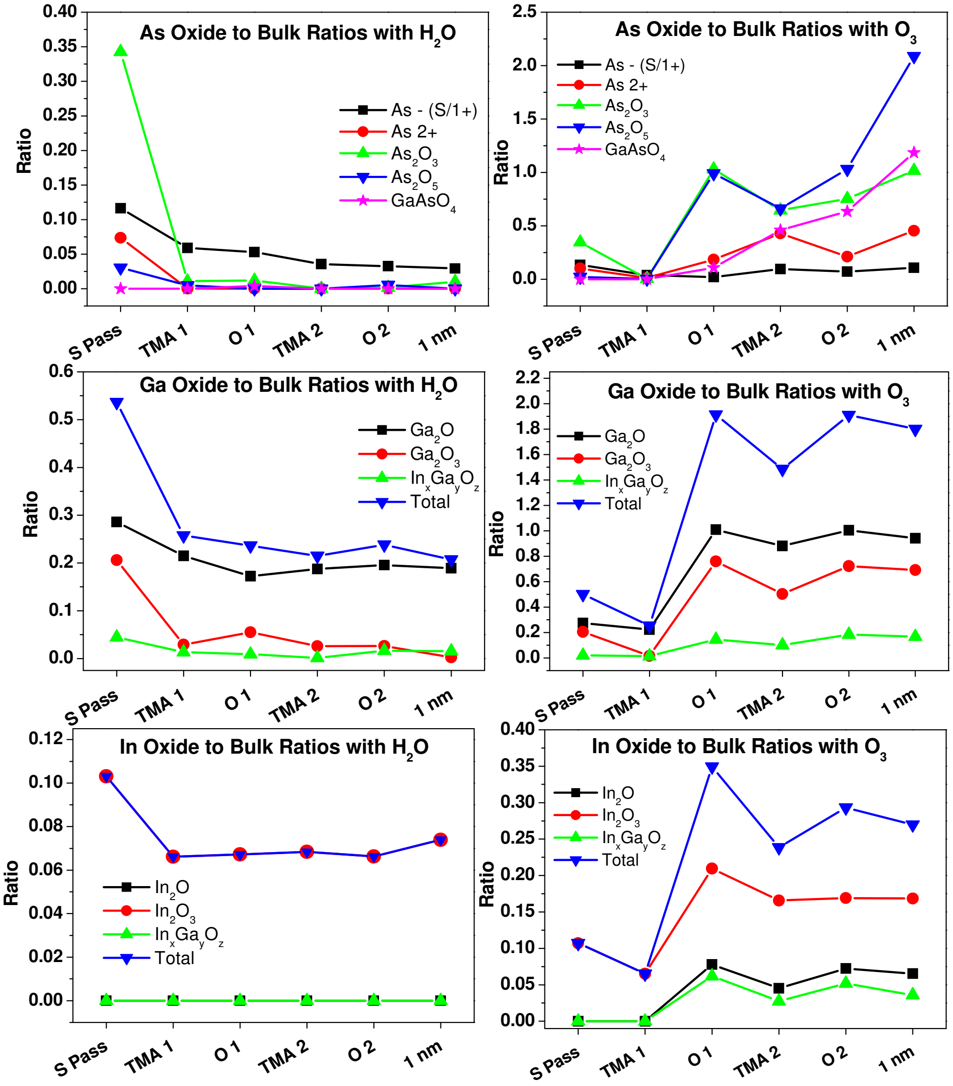

Figure 5.9 Ratio of oxide component peaks to bulk peak areas after successive half cycles

5.3.4. Interfacial oxide thickness

The initial large increase with the first ozone cycle is likely due to the fact that the first TMA cycle does not form a complete monolayer, limited as it is by steric hindrance and the availability of bonding sites. This would leave regions of the substrate exposed to the subsequent oxidation cycle allowing for a facile pathway for interfacial oxidation. Upon the second cycle of TMA, it is likely that a complete monolayer of Al_2O_3 is formed, which can act as a barrier to further oxidation. The increase in the As_2O_5 and $GaAsO_4$ could possibly be due to the creation of atomic oxygen at the Al_2O_3 surface during the oxidation of Al. This atomic oxygen could easily propagate through the Al_2O_3 layer, potentially forming increased levels of arsenic oxide at the interface.[21]

Rough thickness calculations of the interfacial oxide, based upon the attenuation of the substrate peaks, assuming that the Al_2O_3 overlayer attenuates the native oxide and the substrate equally and each half cycle forms ~0.1 nm of Al_2O_3, were carried out to determine the level of interfacial oxide growth with O_3, as shown in figure 5.10. Using the 3 main peaks investigated, the same final thickness was reached of ~ 0.8 nm. TEM studies of the ALD of oxide layers using O_3 have claimed that the use of O_3 does not cause any interfacial oxidation,[22,23] however it is unclear how well resolved an interfacial oxide of this thickness would be in these images and whether there would be a significant enough density difference between the oxide and the substrate to highlight its presence.

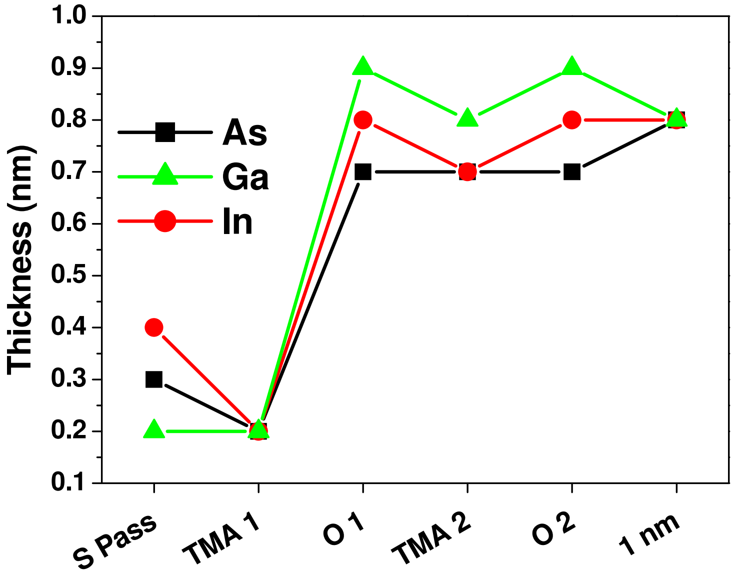

Figure 5.10 Thickness calculations of the individual elemental oxide contributions to the interfacial oxide based on the attenuation of the substrate peak

Interestingly for the As peak, even though we see a relatively large increase in the As_2O_5 ratio in figure 5.9 with the other As oxide components staying relatively constant, this does not translate into a significant change in the over all thickness with only a relatively nominal increase of 0.1 nm seen. It could be speculated that the As_2O_5 is therefore forming preferentially at the oxide Al_2O_3 interface which would result in a larger overall signal. Angular resolved XPS analysis would be able to confirm this. It is worth bearing in mind however that there is a relatively large error associated with thickness calculations on this scale (probably 10 % of the actual value) so a variation of 0.1 nm is fairly speculative.

It also appears that there is slightly more indium oxide present after $(NH_4)_2S$ treatment which has been previously reported for alternative chemical treatments[24] however these measurements also include the contribution of any potential sulphur or OH bonding and this could be a sign of increased levels of In-S bond formation relative to both As and Ga. It would appear that the oxide thickness essentially reaches a saturation point after the initial O_3 cycle with very little growth with subsequent depositions. It is therefore reasonable to assume that the Al_2O_3 acts as a barrier to oxygen diffusion to the substrate. It could therefore be speculated that changes in the interfacial oxide composition after the formation of one monolayer of Al_2O_3 could be due to thermal effects induced by the elevated substrate temperature in the ALD reactor.

5.3.5. Residual sulphur levels

The sulphur 2*p* peaks for the various half cycles are shown in figure 5.11. Due to the presence of the Ga 3*s* peak in close proximity as well as an As 3*p* loss feature causing the apparent increase in the background at the low binding energy side of the spectra, it is difficult to accurately deconvolve the spectra with a high degree of accuracy. What is clear however for both H_2O and O_3 oxidised samples, is that sulphur remains throughout the deposition process at a relatively constant level. Taking this into account and assuming that the As^{1+} peak immediately after $(NH_4)_2S$ passivation is likely to be due primarily to As-S bonding with a small contribution from a possible As_2O state, with the introduction of TMA, the As^{1+} peak is seen to significantly reduce, due most likely to a reduction in As-S bonding leaving only residual As_2O. However, with no apparent reduction in sulphur seen from the S 2*p* peak, this suggests that the sulphur is transferring to the group III elements.[21]

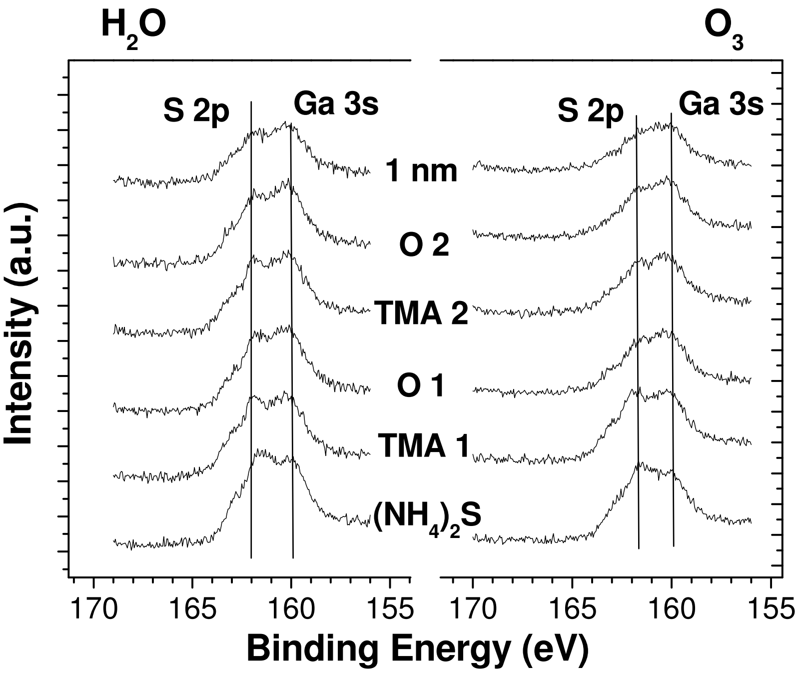

Figure 5.11 S 2*p* and Ga 3*s* spectra showing presence of sulphur on the surface throughout the deposition process

The loss in definition of the two peaks from the ozone oxidised peaks is likely due to the increasing presence of gallium oxide as the deposition progresses, which having binding energies 0.5-1.6 eV from the Ga 3*s* peak.

5.3.6. Al_2O_3 growth

Variations are seen however in the Al 2*p* spectra with H_2O and O_3 as displayed in figure 5.12 (a) and (b) with 5.12 (a) showing the peak fitted spectra after successive half cycles and 12 (b) showing the peak areas as a function of ALD cycle. With the first cycle of TMA, we see the formation of a peak at ~74.9 eV, consistent with the reported binding energy for Al_2O_3, with the same peak area for both samples highlighted in figure 5.12 (b). This suggests that the TMA is reacting with the oxides on the surface to form fully oxidised Al_2O_3. With the introduction of the first oxidation cycle, there is no change in the peak binding energy positions, suggesting that the aluminium is fully oxidised before the oxidation cycle.[25]

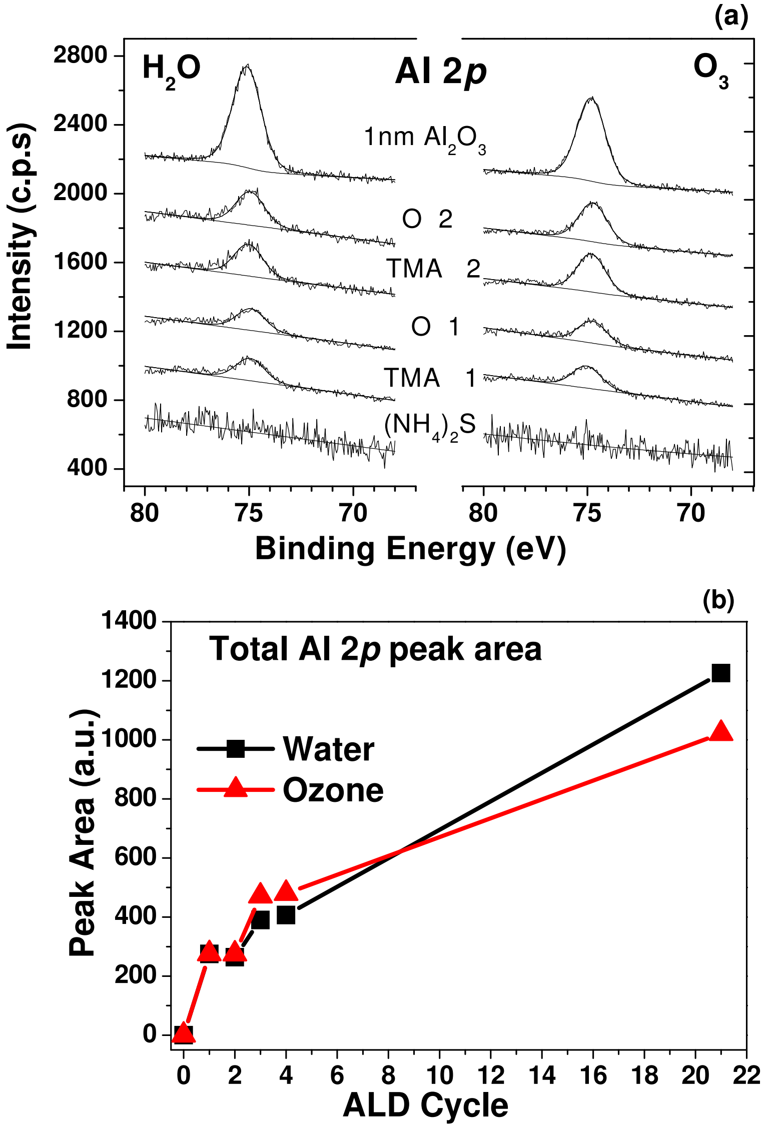

Figure 5.12 (a) Al 2*p* spectra showing growth of Al_2O_3 following the first cycle of TMA and (b) area of fitted Al 2*p* peaks as a function of ALD cycle highlighting a variation in growth rate with H_2O and O_3

With the second TMA cycle however, we see an increased level of Al_2O_3 on the O_3 oxidised sample relative to that of the H_2O oxidised sample. This is likely due to increased bonding sites available for the TMA as a result of the increased interfacial oxidation with O_3 and possibly suggesting a rougher surface resulting in a greater surface area for the TMA to interact with. Again, the binding energy of the peaks suggests that the layer on both samples is fully oxidised Al_2O_3 so no change is evident following the second oxidation cycle.

With subsequent half cycles up to nominal 1 nm growth with 10 full cycles, we see from figure 5.12(b) specifically, that while the growth rate of the Al 2*p* peak with H_2O is extremely linear suggesting true ALD growth with the same layer thickness growing with each cycle, with O_3 although we see an initial increased growth rate with the second full cycle, by the final deposition the Al 2*p* peak area is >15 % lower than the corresponding peak with H_2O. This suggests that the water might be playing a key role in the deposition process. Since the TMA molecule are more likely to react with hydrogen to form Al and a volatile CH_4 molecule, the H_2O could be leaving the surface with a degree of H termination, not readily detected with XPS, whereas the O_3 process leaves the surface oxygen terminated creating a more difficult reaction pathway for the TMA to react with the surface. This slower growth rate for films grown with O_3 has previously been reported for HfO_2 and Al_2O_3 on Si.[26] This can also be explained in terms of steric hindrance as it has been proposed that due to the release of CH_4 with H terminated surfaces, there is also more space available on the surface for the TMA to adsorb during the cycle while with O termination, CH_3 remains on the surface after the initial interactions and prevents further TMA adsorbtion in that cycle reducing the growth rate per cycle.

5.3.7. Carbon and contamination

In order to investigate the reason why O_3 was initially proposed as a candidate for ALD oxidation, we need to look at the carbon data. The peak area of the fitted C 1*s* peaks after successive half cycles is shown in figure 5.13. The level of carbon present initially on the surface is on the order of one monolayer or less, so there is a very small XPS signal, making accurate determination of the peak areas difficult. The initial discrepancy between the two samples after $(NH_4)_2S$ treatment is probably due to sample variation, however with the first TMA cycle we see that there is a similar level of carbon present on both samples. With the first oxidation cycle, we see that there is a large reduction in the signal from the O_3 oxidised sample whereas there is virtually no change with H_2O oxidation. This is likely due to the reactive O_3 interacting with the surface carbon, creating volatile C-O or CO_2 molecules which desorb from the surface.

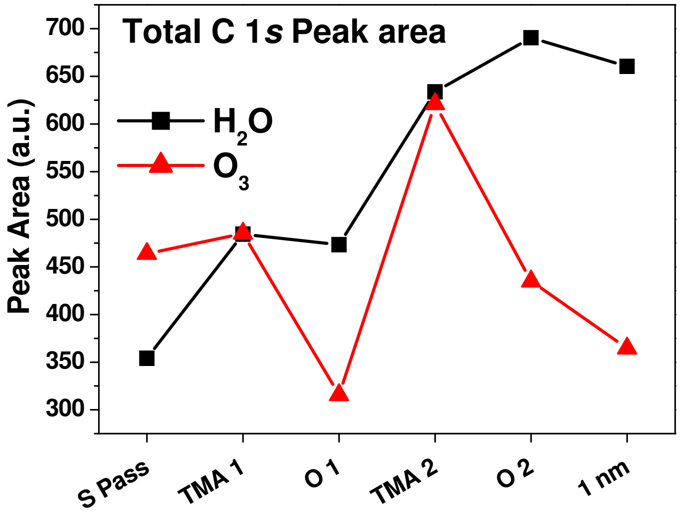

Figure 5.13 C 1*s* peak area as a function of ALD cycle to determine the level of carbon incorporation in the Al_2O_3 layer with H_2O and O_3 oxidation

With the second TMA cycle, we see that the carbon signal increases to the same level on both samples. This could be explained by residual H_2O remaining in the reactor and gas lines with H_2O oxidation due to its wetting nature, decomposing TMA before it reached the sample surface. However, it is not as obvious how this would happen with O_3 oxidation as it is expected to be easily evacuated from the reactor reducing the probability of TMA decomposition. It is possible that this is evidence for the proposed CH_3 termination of the surface as a result of TMA interaction with O as opposed to H termination after the oxide half cycle, which would result in an increased carbon signal coming from the CH_3.

With subsequent half cycles, we see a further increase in the carbon signal with H_2O oxidation and a significant reduction with O_3. This is again possibly due to the reactive nature of the O_3 removing the carbon or CH_3 present on the surface after the TMA cycle such that after 10 full cycles, the carbon signal with O_3 oxidation is roughly half that seen with H_2O.

5.4. Discussion and conclusions

The increase in interfacial oxide is consistent with previous studies of HfO_2 deposition on Si by ALD using O_3 which showed an increase in SiO_2 with the first ozone oxidation cycle.[28] Such substantial oxidation resulting in the formation of higher oxidation states would be expected to have a negative impact on III-V transistor device characteristics as the native oxides have poor insulating properties. In contrast, recent studies suggest using an unidentified "organometallic" zirconium containing precursor in conjunction with ozone[24,25] as a promising approach for gate dielectrics on $In_{0.53}Ga_{0.47}As$. Minimal interfacial layer formation is reported with only weak Fermi level pinning for this material system. Although the reports lack sufficient detail to explain the detailed surface reactions employed, we speculate that a precursor specific reaction must be present to control excess, deleterious oxidation in that work.

In summary, this study highlights the differences in interface chemistry associated with using ozone instead of water as the oxidant in the ALD growth of Al_2O_3.[27] The results clearly show that the excess interfacial oxidation of the InGaAs surface initiated by the use of ozone means that the clean up effect observed using TMA and H_2O as the oxidant cannot completely remove the interfacial oxides. This would be expected to negate the benefit of using ozone to prevent potential alternative reaction channels of TMA due to residual H_2O remaining in the ALD reactor and incorporation of O-H bonds and carbon in the high-κ films after the H_2O pulse.

5.5. References

---

[1] G.D. Wilk, R.M. Wallace, J.M. Anthony, J. Appl. Phys., 89, 5243, (2001)

[2] P.D. Ye, G.D. Wilk, B. Yang, J. Kwo, H.-J. Gossmann, M. Hong, K.K. Ng, J. Bude, Appl. Phys. Lett., 84, 434, (2004)

[3] R. L. Puurunen, J. Appl. Phys., 97, 121301, (2005).

[4] C. Cheng, E. A. Fitzgerald, Appl. Phys. Lett., 93, 031902, (2008).

[5] T. Watanabe, H. H. Funke, R. Torres, M. W. Raynor, J. Vininski, and V. H. Houlding, J. Cryst. Growth, 248, 67, (2003)

[6] Y. Wang, M. Dai, M.-T. Ho, L.S. Wielunski, Y.J. Chabal, Appl. Phys. Lett., 90, 022906, (2007)

[7] M. Milojevic, C.L. Hinkle, F.S. Aguirre-Tostado, H.C. Kim, E.M. Vogel, J. Kim, R.M. Wallace, Appl. Phys. Lett., 93, 252905, (2008)

[8] Picosun Oy.: http://www.picosun.com

[9] T. Ishikawa, H. Ikoma, Jpn. J. Appl. Phys. 31, 3981, (1992)

[10] S. Arabasz, E. Bergignat, G. Hollinger, and J. Szuber, Appl. Surf. Sci., 252, 7659, (2006).

[11] F. S. Aguirre-Tostado, M. Milojevic, K. J. Choi, H. C. Kim, C. L. Hinkle, E. M. Vogel, J. Kim, T. Yang, Y. Xuan, P. D. Ye, and R. M. Wallace, Appl. Phys. Lett., 93, 061907, (2008).

[12] M. Milojevic, C.L. Hinkle, F.S. Aguirre-Tostado, H.C. Kim, E.M. Vogel, J. Kim, R.M. Wallace, Appl. Phys. Lett, 93, 202902, (2008)

---

[13] R. L. Puurunen, Appl. Surf. Sci. 245, 6, (2005).

[14] A. C. Dillon, A. W. Ott, J. D. Way, S. M. George, Surf. Sci., 322, 230, (1995).

[15] R. L. Puurunen, A. Root, S. Haukka, E. I. Iiskola, M. Lindblad, A.O. I. Krause, J. Phys. Chem. B 104, 6599, (2000).

[16] C.L. Hinkle, M. Milojevic, B. Brennan, A.M. Sonnet, F.S. Aguirre-Tostado, G. Hughes, E.M. Vogel, R.M. Wallace, Appl. Phys. Lett., 94, 162101, (2009)

[17] T. Ishikawa, H. Ikoma, Jpn. J. Appl. Phys. 32, L607, (1993)

[18] P. Moriarty, B. Murphy, L. Roberts, A.A. Cafolla, L. Koenders, P. Bailey, G. Hughes, Phys. Rev B, 50, 14237, (1994)

[19] S. Arabasz, E. Bergignat, G. Hollinger, J. Szuber, Vacuum, 80, 888, (2006)

[20] B. Shin, D. Choi, J.S. Harris, P.C. McIntyre, Appl. Phys. Lett. 93, 052911, (2008)

[21] R. Xu, Z.J. Yan, S. Chen, Y.L. Fan, X.M. Ding, Z.M. Jiang, Z.S. Li, Surf. Sci., 581, 236, (2005)

[22] N. Goel, D. Heh, S. Koveshnikov, I. Ok, S. Oktyabrsky, V. Tokranov, R. Kambhampati, M. Yakimov, Y. Sun, P. Pianetta, et al., Tech. Dig. - Int. Electron Devices Meet., 363, (2008)

[23] S. Koveshnikov, N. Goel, P. Majhi, H. Wen, M. B. Santos, S. Oktyabrsky, V. Tokranov, R. Kambhampati, R. Moore, F. Zhu, et al., Appl. Phys. Lett., 92, 222904, (2008)

[24] S. Byungha , J. Cagnon, R.D. Long, P.K. Hurley, S. Stemmer, P.C. McIntyre, Electrochemical and Solid-State Letters, 12, G40, (2009)

---

[25] J. F. Moulder, W. F. Stickle, P. E. Sobol, K. D. Bomben, Handbook of X-ray Photoelectron Spectroscopy Perkin-Elmer Corporation, Physical Electronics Division, (1992)

[26] Y. Wang, M. Dai, M.-T. Ho, L. S. Wielunski, and Y. J. Chabal, Appl. Phys. Lett. 90, 022906, (2007)

[27] B. Brennan, M. Milojevic, H. C. Kim P. K. Hurley, J. Kim, G. Hughes, R. M. Wallace, Electrochem. Solid-State Lett., 12, H205, (2009)

6. Surface preparation and high-κ HfO_2 deposition on InP substrates

6.1. Introduction

Indium phosphide, due to its high electron mobility is under investigation for introduction into future n channel devices.[1] Having a direct bandgap, unlike silicon, it is widely used in optoelectronic devices,[2, 3] so there has already been quite a lot of research carried out on InP in comparison to InGaAs. Another reason for this is the relative cost of materials involved with InGaAs typically much more expensive to produce than InP, GaAs or InAs with InGaAs actually grown on these substrate materials to form lattice overlayers with different In content. The $In_{0.53}Ga_{0.47}As$ substrates used in the previous chapters were actually grown by metal oxide vapour phase epitaxy (MOVPE) lattice matched to InP substrates. The extra processing needed to grow $In_{0.53}Ga_{0.47}As$ makes InP a cost effective alternative for high speed n channel devices and also a cost effective material to investigate the interaction of high-κ metal oxide layers with indium based semiconductors which, having the same lattice constant, negates the impact of variations in surface strain between the semiconductor substrates when comparing results.

Similar to InGaAs, there is no effective native oxide on InP of sufficient insulating quality to provide good FET device performance characteristics without readily breaking down and generating large leakage currents.[4] Therefore the growth of a high-κ dielectric on the InP surface is a significant prerequisite for the formation of efficient devices. The engineering of a high quality interface between the high-κ and the InP substrate is a key goal in order to reduce the defect density at the interface and prevent large leakage currents and Fermi level pinning.[5]

The surface preparation of InP has been investigated extensively due to its application in photodetectors and photodiode arrays where order of magnitude improvements in device performance have been demonstrated with passivation of the interface states with sulphur.[6] Most surface treatments for InP are based on either a ‘piranha’ etch[7] or ammonium sulphide $(NH_4)_2S$ / polysulphide $(NH_4)_2S_x$ treatment.[8, 9] The piranha etch consists of sulphuric acid and hydrogen peroxide diluted in water which was developed initially for the surface treatment of GaAs.[10] Studies by Spicer et al have investigated modified piranha etches for InP consisting of a two stage etching process with the first stage designed to a remove the native oxide and form a less stable chemical oxide on the surface and the second stage used to then remove the residual oxide, leaving the surface oxide free and terminated with a quarter monolayer of hydrophobic phosphorous.[7] Upon annealing at 330 °C, the excess phosphorous at the surface is desorbed leaving an atomically clean surface. Ammonium sulphide treatments of InP have been studied extensively and have been shown to both remove the native oxide and to terminate the surface in a monolayer of sulphur bonded to the surface.[11]

Immediately after this passivation process, the surface has been reported to consist of both indium and phosphorous sulphur bonds which upon annealing over 200 °C, convert into predominantly In-S bonds, which are extremely stable up to 460 °C.[12] This is approaching the decomposition temperature of InP and hence the upper temperature limit available for InP processing. This relatively low decomposition temperature makes chemical treatment of InP an attractive technique for removing the native oxides compared to high temperature annealing as in the case of silicon[13] and hydrogen cracking for GaAs,[14] which as reported in chapter 3.4.2 requires high temperature annealing to instigate the full removal of the indium oxide bonds and has also been seen to deplete indium from InGaAs substrates.[15]

The aim of this study was to compare the effectiveness of ammonium sulphide passivation and two stage etching on n and p type InP surfaces in order to determine if there are any significant differences in terms of photoemission results. The effectiveness of the $(NH_4)_2S$ treatment at preventing ambient oxidation was also tested by exposing a treated sample to atmosphere for extended periods of time and plotting the change in the oxide intensity as a function of exposure time similar to previous studies.[16] Having gained an insight into the chemical composition and the ambient stability of the treated surface, the next step was to deposit ultra thin high-κ dielectric layers to determine whether the surface chemistry had any effect on the thin film growth.

Hafnium dioxide, having a dielectric constant of ~25, is seen as one of the prime candidates for inclusion in next generation semiconductor devices.[17] With a sufficiently high κ value to scale beyond the 32 nm node in the industrial roadmap[18] and a band gap of 5.8 eV the growth of HfO_2 layers on III-V semiconductor substrates is an increasingly important area of research. Hafnium silicate layers, which have a dielectric constant intermediate between HfO_2 and SiO_2 are already being included in current high end MOSFET devices in order to lower the leakage currents. [19, 20] In this chapter, the growth of HfO_2 on InP substrates will be investigated to determine the interaction and chemical characteristics of the layers formed.

6.2. Experimental

Sulphur passivation was carried out the on 1 cm x 1 cm n and p type InP samples, using 22% $(NH_4)_2S$ at 60 °C for 20 minutes, followed by a rinse in de-ionised (DI) water for roughly 10 seconds to remove any residual solution and finally blown dry with dry nitrogen. The samples were then mounted to a sample holder or sample heater capable of reaching 700 °C and loaded to UHV within 2 minutes of removal from ammonium sulphide. Similarly, 2 stage etched samples were first dipped in 4:1:100 of H_2SO_4(96%): H_2O_2(30%):H_2O for 2 minutes followed by 1:3 HCl(36%) : H_2O for 30 seconds and subsequently rinsed in DI water and blown dry in N_2 before mounting and transfer to UHV in the same period of time.

HfO_2 thin films were grown by a number of different deposition methods, namely micro e-beam, conventional e-Beam and ALD to determine if there were any differences in interface chemistry. Both the chemical composition and the surface roughness of the grown films were investigated by XPS and AFM respectively. Electrical measurements were also carried out on these samples after metallisation, however as I was not directly involved in the analysis, the results are not presented here. During micro e-beam growth, the power output was maintained at ~1.65 W in order to generate a consistent hafnium metal deposition rate, in a background pressure of oxygen of 5×10^{-7} mbar. During ALD growth, the substrate temperature was maintained at 250 °C throughout the deposition process with the organo-metallic $Hf[N(CH_3)_2]_4$ hafnium precursor the first cycle in the deposition with H_2O acting as the oxidant in the process with cycle times of 0.1 seconds per pulse.

XPS was carried out during in-situ sequential deposition by micro e-beam and after ex situ e-beam and ALD using an unmonochromated Al Kα dual anode X-ray source at a pass energy of 20 eV and at a base pressure of $< 2 \times 10^{-9}$ mbar. AFM images were taken using a vibration isolated Digital Instruments Dimension 3100 system operated in non contact tapping-mode in ambient conditions using an Olympus OMCL-AC160TS tip.

6.3. $(NH_4)_2S$ passivation and 2 stage etching

6.3.1. XPS and residual oxide levels

The XPS spectra from the In $3d_{5/2}$ and P $2p$ core levels after $(NH_4)_2S$ and 2 stage etching and subsequent anneals at 200 °C and 330 °C respectively are shown in figure 6.1. The spectra from an untreated sample are also shown to indicate the changes in the level of native oxide present as a result of the surface treatments. After both surface treatments, there is no evidence of phosphorous oxide remaining on the surface from the P $2p$ spectra within detection limits of the XPS. There is also no evidence of any phosphorous sulphur bonds forming after $(NH_4)_2S$ treatment consistent with other studies.[16, 21] Due to the relatively low binding energy of the peak, it is possible that residual amounts of both phosphorous oxide and P-S bonds are present on the surface on the order of a fraction of a monolayer which could be below XPS detection limits, however this is unlikely. After annealing to 200 °C, there is no apparent change seen in the spectra.

The In $3d$ peaks, with a much smaller binding energy separation between the bulk and oxide peaks are much more difficult to deconvolve than the P $2p$ spectra. The nature of the native oxide is not well known and the binding energies are reported as being anywhere from 0.4 to 1.3 eV from the bulk peak, which is likely to include a range of different oxidation states (table 3.2). This coupled with the incorporation of In-S bonding with $(NH_4)_2S$ treatment,[11] which is likely to show up as a peak with a similar binding energy to that of low coordinated oxide states, makes the fitting process even more difficult. However, we can gain some information by just looking at the peak shape from the normalised spectra after the various surface treatments.

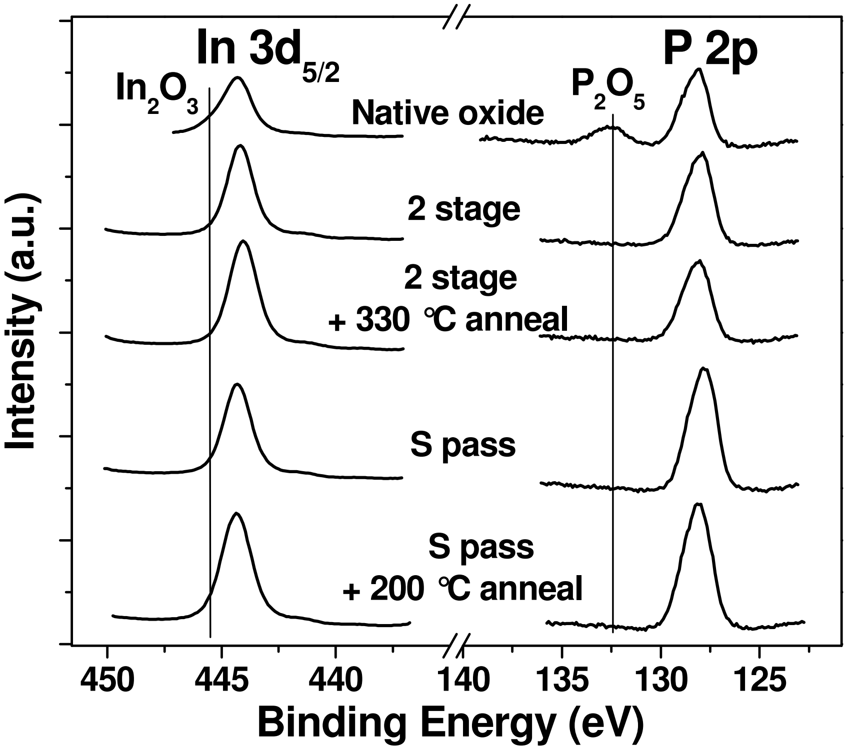

Figure 6.1 In 3*d* and P 2*p* XPS spectra from a native oxide on InP, after 2 stage etching, ammonium sulphide passivation and subsequent annealing

Figure 6.2 (a) shows the In $3d_{5/2}$ spectra from the native oxide and after the two surface treatments. We can see that there is a significant reduction in the peak width after surface treatment leaving a symmetric peak shape, consistent with the removal of a significant amount of indium oxide, seen as the shoulder at the HBE side of the native oxide spectra. The peak shapes after both treatments line up extremely closely, suggesting that if not all of the oxide is removed, a similar level is achieved with both processes. There is also likely to be an In-S signal contributing to the $(NH_4)_2S$ treated sample. After annealing the samples, shown in figure 6.2 (b), a broadening of the peak at the HBE side is observed, suggesting that there is either indium oxide growth at elevated temperature or transfer of sulphur bonds from phosphorous, however considering a similar change is seen on both samples, an increase in the oxide seems most likely. This would suggest that there is either reconstruction of indium oxide present on the surface after treatment to form an oxide with a higher electronegativity (containing more oxygen per molecule) or a residual amount of phosphorous oxide is present on the surface below detection limits after treatment and with annealing, some of this transfers to form increased levels of indium oxide. However, the level of change in the spectra would be consistent with sub monolayer changes in the composition of any oxide present.

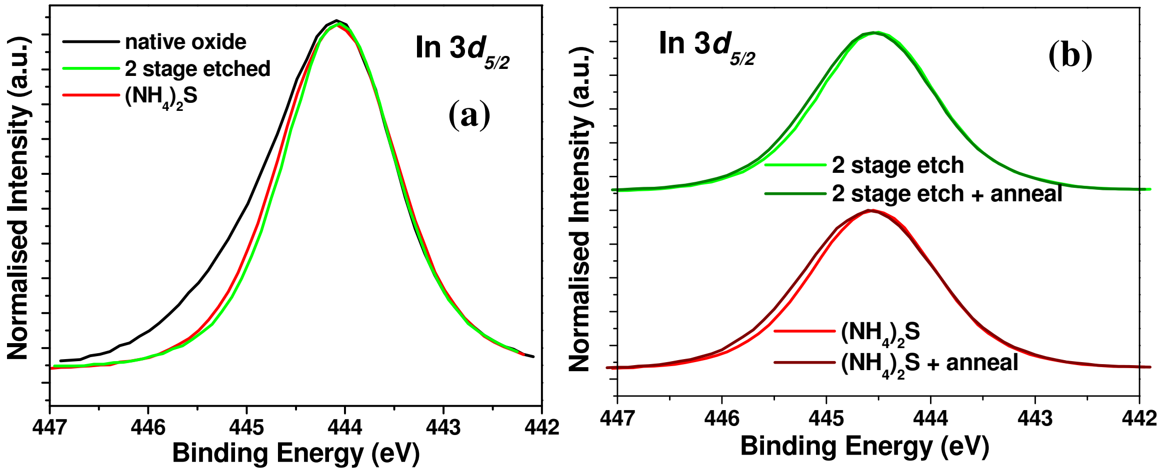

Figure 6.2 (a) In 3*d* spectra from an InP sample with a significant native oxide present as well as after 2 stage etching and $(NH_4)_2S$ treatment, with (b) showing the effect of annealing the treated substrates, causing a small increase in indium oxide

Looking at the survey spectra in figure 6.3 from (a) the $(NH_4)_2S$ treated sample, (b) the native oxide and (c) a sample with ~4 nm of HfO_2, we can get an idea of the change in the amount of oxide present after the chemical treatments. If we consider first the intensity of the O 1*s* component from (c) with 4 nm of oxide present, we can see that the native oxide is considerably smaller than this in (b) and based on the relative intensities, is on the order of 1 nm thick. The spectrum after $(NH_4)_2S$ treatment (with the spectra after two stage etching essentially the same apart from a small sulphur signal) shows that the O 1*s* signal is reduced even further to roughly 30% of that from the native oxide, which would put a thickness of roughly 1 monolayer (0.3 – 0.4 nm) on the native oxide.

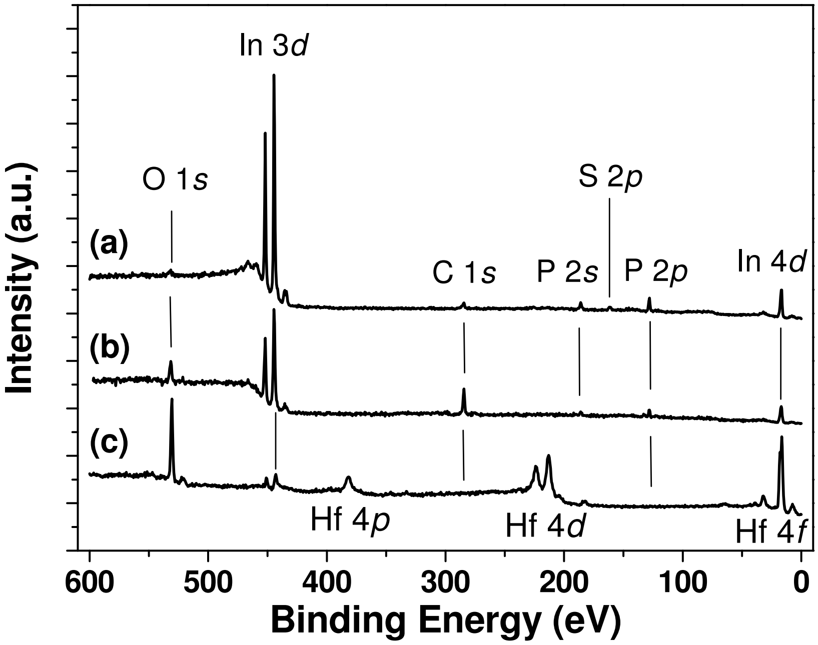

Figure 6.3 XPS survey scans from (a) $(NH_4)_2S$ passivated InP, (b) native oxide on InP and (c) after ~ 4 nm deposition of HfO_2 on InP

The increased intensity of the In 3*d* peak is another good indicator that the overlayer on the surface has been reduced, however the reduction in the C 1*s* signal seen after $(NH_4)_2S$ treatment relative to the native oxide sample will also contribute to this also although due to the low level present, to a much lesser extent. These spectra also highlight the significantly lower ionisation cross section of the P 2*p* peak (0.016) relative to that of the In 3*d* peak (0.31), considering they are present in the same ratio in the sample, resulting in a much lower relative intensity.

The oxygen 1*s* spectra from the $(NH_4)_2S$ and 2 stage etched samples in figure 6.4 (a), as well as the peak area of the components from the fitted data in 6.4 (b), provides us with more information regarding the changes in the oxide composition with treatment and subsequent annealing. With both samples we can see that there is a reduction in the peak at the HBE side upon annealing, which is consistent with the reported binding energy position for phosphorous oxides (532.2 – 534 eV) whereas the lower binding energy component, is likely to be composed of some form of indium oxide based on reported binding energy position for In_2O_3 of 530.5 eV.[22] The higher binding energy component in the spectra could also indicate the presence of water or hydroxide related features at ~533 eV which could form following atmospheric exposure prior to loading and these species would also be expected to be reduced or removed at elevated temperatures.

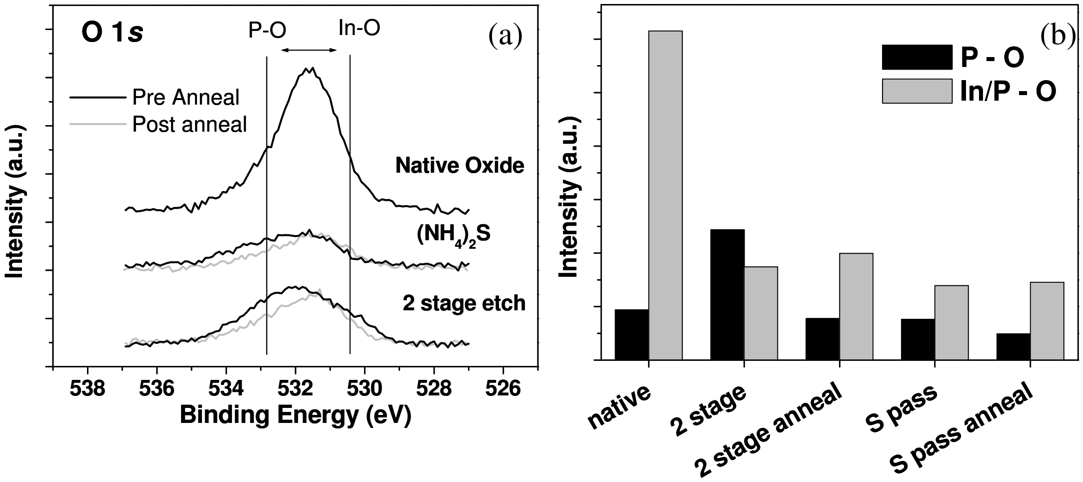

Figure 6.4 (a) O 1*s* spectra from native oxide on InP, after $(NH_4)_2S$ passivation and 2 stage etching with subsequent anneals and (b) fitted area of the peak components from the corresponding spectra

There is a lower level of oxide present on the $(NH_4)_2S$ treated surface relative to the two stage etched sample, suggesting that if both techniques are effective at removing all the native oxides present as reported, then the $(NH_4)_2S$ is more effective at preventing ambient re-oxidation. Since the lower binding energy peak is at a significantly higher energy than that reported for In_2O_3, it is likely to represent an indium phosphorous oxide state. If we assume that the higher binding energy component is purely phosphorous oxide related, from figure 6.4 (b) we can compare the relative changes in the oxides present. With both treated samples there is a small increase in the lower binding energy In/P-O peak upon annealing, consistent with the change seen in the In 3*d* spectra in figure 6.2, whereas there is large decrease in the phosphorous oxide component, especially on the two stage etched sample which had the largest oxide level present after treatment. The increased phosphorous oxide level on the 2 stage etched sample is possibly due to the reported phosphorous termination of the InP surface after the etching process which would oxidise once exposed to atmosphere. The subsequent reduction in the phosphorous oxide upon annealing is much greater than the increase seen in the indium oxide which suggests that while some of the oxygen initially in P-O bonds could be transferring to form indium containing oxides, the predominant reduction is as a result of phosphorous oxide leaving the surface at elevated temperature. Based on these results, with increased annealing time or temperature it is possible that this phosphorous oxide component could be fully removed.

If we compare the treated spectra to that of the native oxide, we can see that there is a significantly larger signal from the lower binding energy InP-O region with evidence of the phosphorous oxide still present at a level similar to that seen after $(NH_4)_2S$ treatment and upon annealing the two stage etched sample. It is possible that this level of phosphorous oxide is intrinsic to all the samples and to the formation of further oxide on the surface. With the level present less than a monolayer, it could be forming at the interface between the substrate and the rest of the native oxide. What these results highlight is that it is not possible to passivate the surfaces to such an extent to prevent a certain amount of native oxide forming in the period of time it took to load the samples after treatment into UHV (< 3 mins) and that in situ annealing was not successful at fully removing this reformed oxide, so further work is needed to fully realise the creation of an atomic clean InP surface after ambient chemical treatments, whether this entails further in situ annealing or exposing the surface to atomic hydrogen.[23, 24]

6.3.2. Surface Roughness

In order to determine the effect of the surface treatment on the surface roughness of the samples, AFM measurements were taken on the InP native oxide and $(NH_4)_2S$ treated surface. A 1μm x1μm reference scan on the native oxide shown in figure 6.5 (a) gave a root mean squared roughness of 0.2 nm. When the sample was etched in $(NH_4)_2S$ and scanned within 15 minutes of removal from UHV post XPS, as shown in figure 6.5 (b) and (c), the sample roughness increased to 0.4nm with an average height of 1.4nm. The bright protrusions in the image which are typically 50 nm in diameter and 3-5 nm in height are randomly distributed across the surface. This random distribution can be seen clearest in the 5µm x 5µm scan in figure 6.5 (b). These clusters are thought to relate to the sulphur treatment and could be as a result of the aggregation of excess sulphur following the treatment. AFM studies of $(NH_4)_2S$ passivated InGaAs, not presented here, also revealed the presence of similar surface clusters which were found to aggregate when the sample was annealed at 200 °C supporting the idea that they could be sulphur related.

When the RMS roughness for this surface is calculated without including the larger clusters, it gives a value of 0.3 nm, which suggests that there is no obvious roughening taking place as a result of the passivation process.

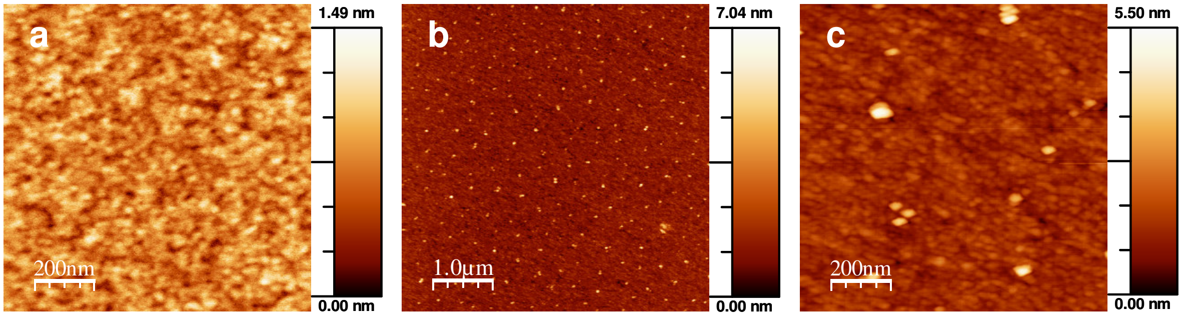

Figure 6.5 AFM images of (a) 1µm x1µm native oxide on InP, (b) 5µm x5µm of $(NH_4)_2S$ passivated InP and (c) 1µm x1µm scans of the same sample

Similar spectra from a 2 stage etched sample are shown in figure 6.6. The sample had been exposed to atmosphere for a number of hours before scanning so it is likely that a significant native oxide layer had reformed, however this native oxide would be expected to conform to the roughness of the surface, preserving any roughness induced after the etching process. Again, we see an extremely flat surface with an RMS of 0.2 nm. This suggests that both surface preparation methods do not negatively impact on the roughness of the surface. There is also no evidence of the large features seen on the $(NH_4)_2S$ treated surface which suggests that they are sulphur related.

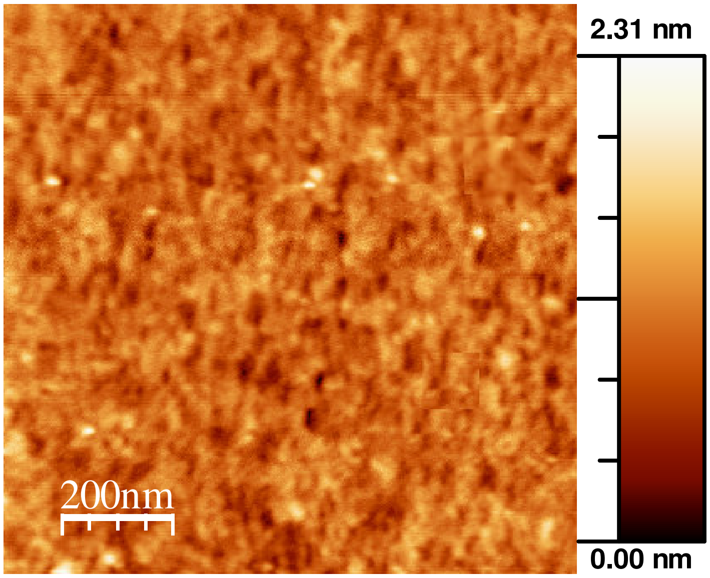

Figure 6.6 1µm x1µm AFM image of 2 stage etched InP surface

6.3.3. Passivation effectiveness by exposure to ambient conditions

In order to test the effectiveness of the ammonium sulphide passivation on InP, a sample was exposed to atmosphere for extended periods of time, up to seven days with XPS spectra taken at regular intervals to monitor the level of oxide growth. It was also compared to the spectra from a sample with a significant native oxide present after prolonged exposure to atmosphere. Figure 6.7 shows the P 2*p* spectra after $(NH_4)_2S$ treatment and successive exposures compared to a native oxide covered surface. It is evident that there is significantly less oxide present after 7 days exposure than that seen on the untreated sample suggesting that the treatment is successful at inhibiting native oxide regrowth over an extended time scale with the oxide level not reaching saturation. There is no evidence of phosphorous oxide within detection limits up to 1440 mins (24 hours) exposure, which even considering the bulk sensitivity of the P 2*p* peak, suggests that the $(NH_4)_2S$ is having a considerable effect at preventing the formation of phosphorous oxide. This could be due to the fact that the surface is reported to be In-S bond terminated with the surface layer containing no phosphorous.[21]

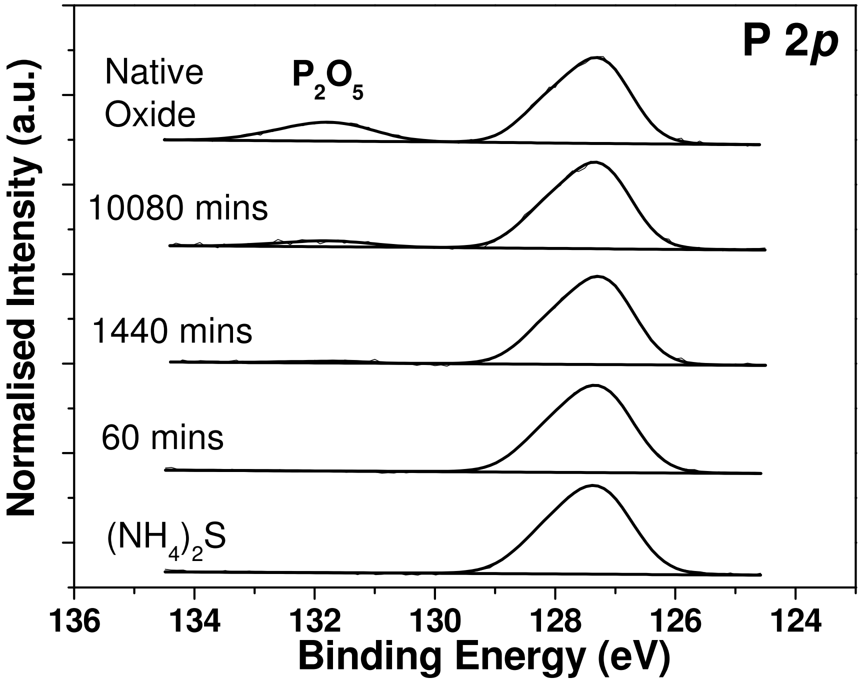

Figure 6.7 P 2*p* spectra after $(NH_4)_2S$ passivation and subsequent exposure to atmosphere for periods up to seven days

As discussed when investigating the sulphur passivation of InGaAs in chapter 4, accurate fitting of the In 3*d* spectra is difficult due to the relatively small binding energy separation between the oxide and bulk peaks, and also due to the presence of a series of lower binding energy component peaks relative to the bulk which are intrinsic to the line shape. However, it is possible to fit the spectra to a reasonable approximation with four peaks, as shown in figure 6.8, with the bulk peak at ~444.3 eV, an oxide peak fixed at 0.8 eV from the bulk and two LBE peaks labelled X and Y, shifted by 1.1 and 2.6 eV respectively.

This oxide position is consistent with a number of studies[1] however there is debate as to its exact composition. As mentioned earlier, the native oxide is likely to be made up of a number of different oxidation states throughout an amorphous oxide layer so in this study the peak position is fixed in order to give a representation of the level of oxide present, without making any claims on the actual nature and composition of the oxide.

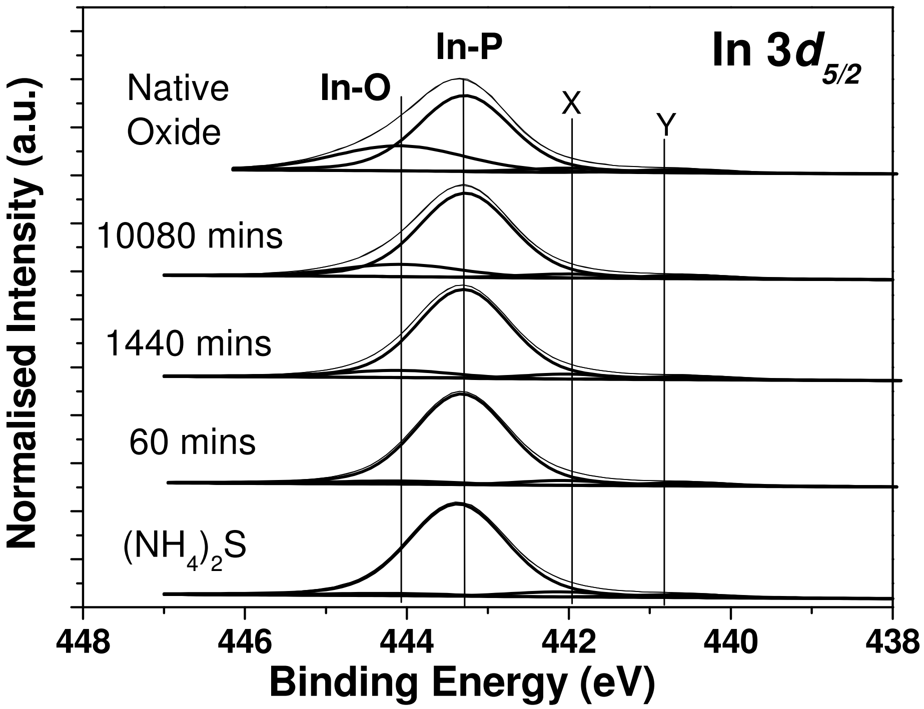

Figure 6.8 Indium 3*d* spectra after $(NH_4)_2S$ passivation and subsequent exposure to atmosphere for periods up to seven days

The Gaussian and Lorentzian components of the bulk peak width were 1.14 eV and 0.36 eV respectively and were also kept constant throughout the fitting process with the oxide peak Lorentzian value correlated to that of the bulk peak, and the Guassian allowed to vary. The fitted spectra after $(NH_4)_2S$ and 7 days exposure in figure 6.9 show more clearly the change in the level of oxide present. With minimal exposure, there appears to be only a residual trace in the indium oxide/sulphide region, which based on similar measurements from InGaAs samples is likely due to the presence of roughly 1ML of indium sulphur bonds and a possible indium sub oxide, reported for InP at ~0.46 eV from bulk,[7] likely to take the form In_2O.

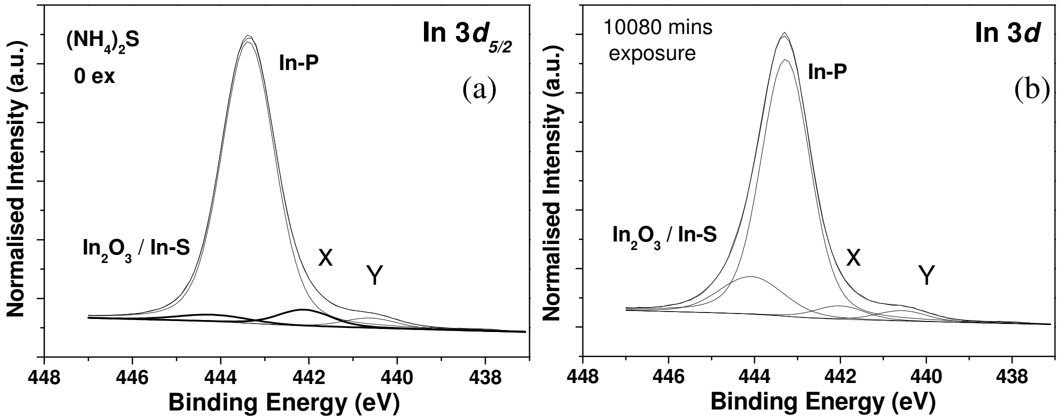

Figure 6.9 In 3d spectra immediately after (a) $(NH_4)_2S$ passivation and (b) after 7 days exposure to atmosphere highlighting the level of oxidation occurring with time

This only provides information regarding changes in the indium oxide present, as opposed to providing any information on the overall quantity of oxide, due to the uncertainty in the oxide peak positions and the contribution of any indium sulphur peaks. However, by taking the ratio of the integrated intensity of the fitted oxide peak to that of the bulk peak, we are able to plot the trend of the change in the level of native oxide on the surface as a function of exposure time, as shown in figure 6.10.

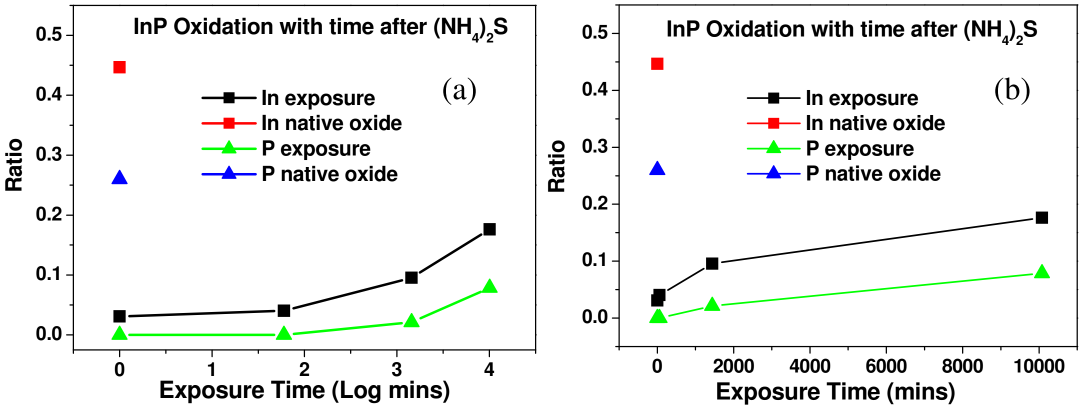

Figure 6.10 Ratio of indium and phosphorous oxide to the bulk peak components from the fitted spectra as a function of time in (a) log minutes to highlight to slow initial oxide growth rate and in (b) minutes to show the relative saturation of the growth

It is worth noting that this does not provide the ratio of the atomic concentrations which would require normalisation of the peaks using atomic sensitivity factors calibrated for the XPS system which were not available for this study, and hence why we see a large variation between the values for the two elements. After 7 days exposure to atmosphere, we see that the level of oxidation is still significantly less than half of the level seen from the native oxide sample. The variation in the indium and phosphorous oxide ratios is likely to be due to the difference in binding energy between the In 3*d* and P 2*p* peaks as opposed to variations in the composition and we do see that there is a similar growth rates in both oxides ratios with increased exposure time. It is worth pointing out that the exposure time is in log minutes, so although there appears to be a significant growth rate, the linear plot shown in figure 6.10(b) shows that the oxide regrowth rate is very slow suggesting that the $(NH_4)_2S$ treatment is effective at suppressing the reoxidation of the surface.

6.3.4. Discussion

In a previous exposure study carried out by Peisert et al.,[16] conducted over a shorter exposure times than investigated here but with a similar initial level of oxide detected, it was found that there was an initial rapid increase in the indium oxide present after $(NH_4)_2S$ treatment, however by 25 minutes, the rate of increase had significantly decreased consistent with these results. They also showed that this growth rate was considerably slower than that seen on a chemically etched surface without sulphur present, similar to what we saw with InGaAs treatments. From these results it could be suggested that there are phases of oxide growth which have different growth rates dependant on the type of oxide forming. Again, similar to observations on InGaAs, an initial surface localised oxide would be the first to form, which is likely to saturate at a monolayer, forming a route to subsequent oxide formation. The presence of sulphur at the surface could stifle this initial oxide formation and making it more difficult for the other oxidation states to grow as a result. Having shown the ability to produce relatively oxide free surfaces by chemical treatments, the next step was to investigate the growth and interface characteristics of HfO_2 thin films on the chemically treated InP surfaces to determine if the treatments were effective at preventing interfacial oxidation during the deposition process.

6.4. In-situ micro e-beam deposition of HfO_2 on InP

6.4.1. HfO_2 growth and thickness calculations

The first deposition method investigated was micro e-beam deposition. This method differs from conventional e-beam deposition primarily in that it involves the evaporation of metal in an oxygen atmosphere as opposed to evaporating the metal oxide directly. The major benefit of this system is that the depositions can be carried out in-situ with the XPS so spectra can be taken during the course of the oxide depositionss to monitor changes in the layer and interface as the HfO_2 grows. N and p type substrates were used after $(NH_4)_2S$ and two stage surface treatment with depositions taking place on substrates at room temperature (RT) and 200 °C.

The In 4*d* and Hf 4*f* spectra from 3 different samples taken at sequential stages during the growth process are shown in figure 6.11, representative of all samples investigated which are listed in table 6.1. Due to the In 4*d* peak having a similar binding energy to that of the Hf 4*f* peak, we are able to monitor the suppression of the In 4*d* peak as the Hf 4*f* peak increases during the course of the HfO_2 deposition. The overlap of the peaks does leave accurate peak fitting difficult so in order to compensate for the loss in resolving power, the separation between the In 3*d* and In 4*d* was kept fixed at 427.6 eV. The In 4*d* peak parameters were also fixed at the values attained from the scan pre HfO_2 deposition, with Gaussian and Lorentzian values of 1.51 and 0.1 eV respectively, a spin-orbit splitting of 0.7 eV and the peak ratio fixed at 0.66. The spin-orbit splitting on the Hf 4*f* peak was kept constant at 1.69 eV with a peak ratio of 0.75, the Lorentzian was fixed at 0.1 eV which provided the most consistent peak fit. The Gaussian value and peak position was allowed to vary to allow for identification of any changes in the chemical composition.

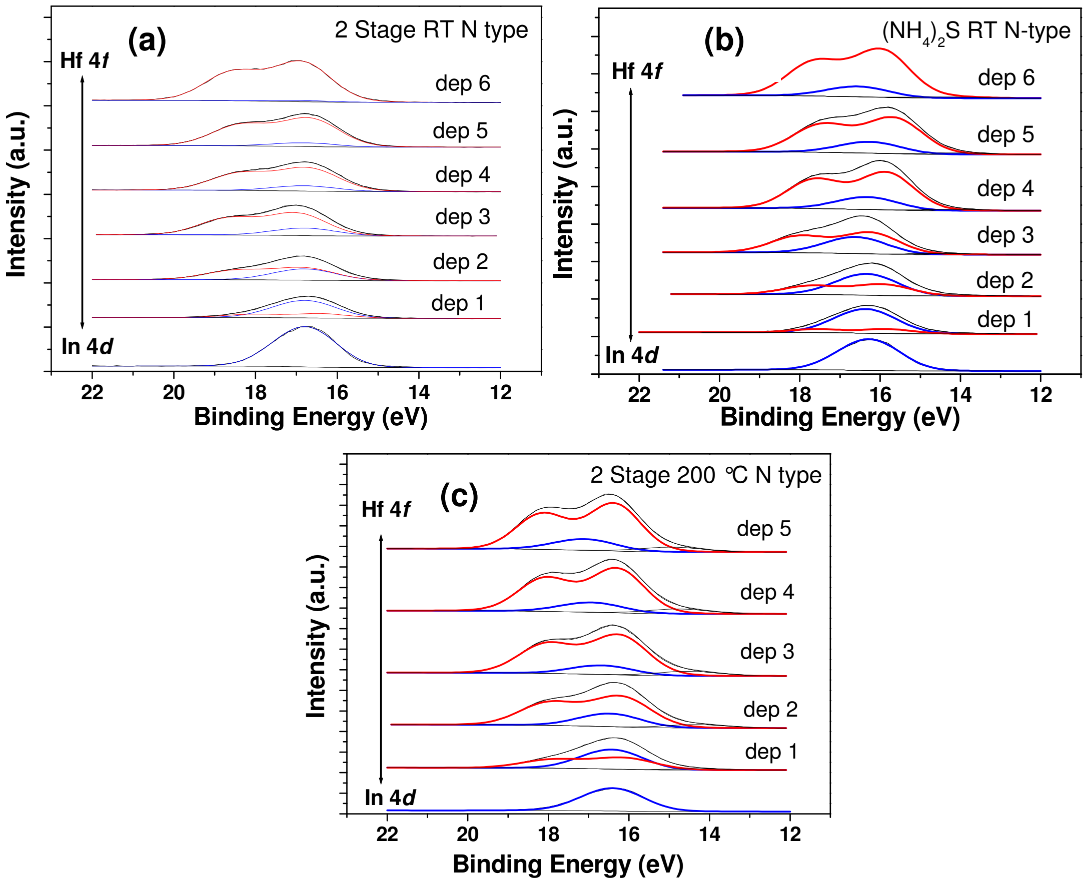

Figure 6.11 Fitted In 4*d* and Hf 4*f* spectra after sequential deposition of HfO_2 at room temperature on (a) 2 stage etched (b) $(NH_4)_2S$ passivated InP and (c) 2 stage etched at 200 °C InP

From the first depositions, we see that the Hf 4*f* peak positions are consistent with hafnium oxide formation at ~16.4 eV with no evidence of a metallic hafnium peak (~14.5 eV) on any of the samples.[25] During the course of the deposition, the Gaussian width of the Hf 4*f* peaks decrease by up to 20%, as highlighted in table 6.1, (where SP represents the $(NH_4)_2S$ passivated samples and 2S the two stage etched). The FWHM reduces to a fairly consistent value across all the samples of ~1.6 eV. This suggests that as the film thickness increases, a more homogeneous chemical environment develops. The fact that the peak width is similar at the initial stages of growth across all the samples, even when deposited at elevated temperatures, suggests that there is a specific chemical environment at the interface which differs from that of the bulk which could be evidence of the formation of HfO_x, where $x<2$ in the early stages of deposition, as previously reported by Xu et al.[26] The variations seen initially are likely due to differences in thickness after the first deposition, with the final values all within experimental error of each other.

Table 6.1 Hf 4*f* Gaussian peak widths for N and P substrates

Sample	**initial (eV)**	**final (eV)**
SP 200°C N	1.87	1.5
2S 200°C N	1.91	1.55
SP RT N	1.97	1.56
SP RT P	1.69	1.6
2S RT N	1.79	1.6
2S RT P	1.837	1.6

The thickness of the hafnium oxide layer during the course of the depositions was determined from the suppression of the In 3*d* peak as the overlayer increased. Figure 6.12 shows the In 3*d* spectra from the 2 stage etched p-type sample as depositions were carried out at room temperate.

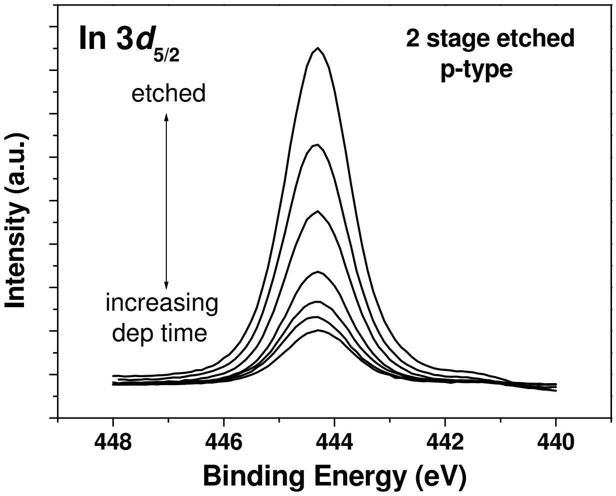

Figure 6.12 Indium $3d_{5/2}$ spectra during sequential deposition of HfO_2 showing suppression of the peak with increasing overlayer thickness

Using the fitted peak areas and an effective attenuation length of 1.42 nm, the thickness of the various oxide layers were determined using values attained from the EAL database[27] based on the Gries thickness calculation model. The calculated film thicknesses were then plotted against deposition time as shown in figure 6.13.

The deposition rate of the hafnium is controlled by the current applied to the e-beam filament, which in turn affects the power supplied to the hafnium metal. However this is dependant on the position of the hafnium metal relative to the filament and as such, as the deposition progresses and hafnium is evaporated, this can potentially result in fluctuations in the deposition rate. This is compensated for by manually adjusting the position of the metal wire in order to keep the power constant but it does introduce an element of uncertainty and error to the deposition rate. Even taking this into account, trends are seen to develop which suggests that there are different deposition rates for the films deposited at RT and at 200 °C.

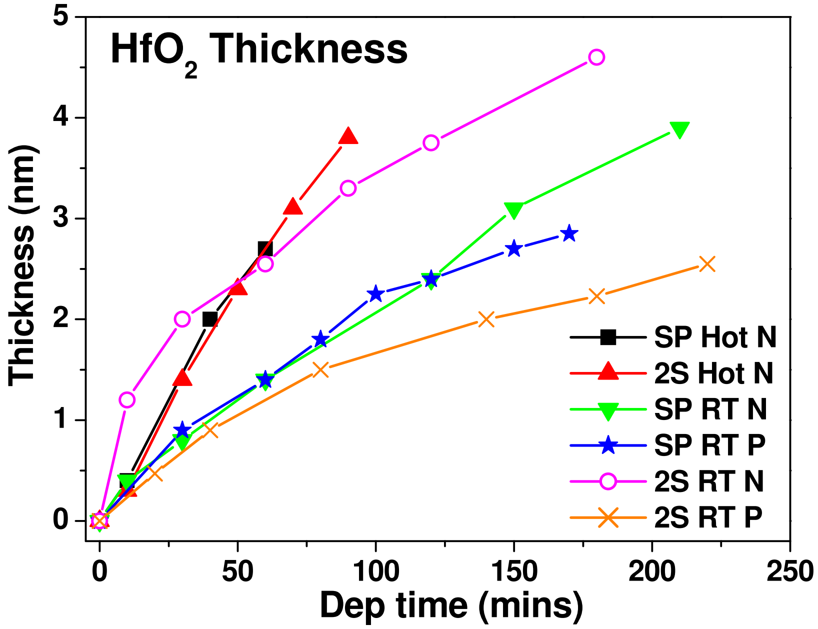

Figure 6.13 Calculated HfO_2 film thicknesses as a function of deposition time on room temperature and 200 °C substrates showing different growth rates

Films of final thickness between ~2.5 and 4 nm were grown with typically 5 to 6 sequential depositions taking place during the growth process. (Reaching the same final thickness on the samples was difficult without having prior knowledge of the deposition rate as it meant the final thickness was based on comparisons of the suppression of the substrate peaks which was just roughly estimated by comparing survey spectra during the course of the depositions.) While the 2 stage etched RT n-type sample shows the largest initial growth, we see that very quickly it develops the same growth rate as the other RT deposited samples of 0.015 ± 0.004 nm/min. After this, a relatively consistent growth rate develops on the 2 stage etched and $(NH_4)_2S$ treated surfaces, and that there is nothing to suggest any variation in growth rate with doping content of the substrate or the initial surface chemistry of the substrates. However, by increasing the substrate temperature to 200 °C during deposition, the growth rate increases to 0.045 ± 0.001 nm/min. There are a couple of possibilities as to what could cause this change in growth rate. It is possible that the increase in substrate temperature increases the sticking coefficient of the surface making it much more likely for the HfO_2 to react with and bond to the surface. Another explanation would be that the increase in temperature allows the formation of a more uniform HfO_2 film which would suppress the substrate signal more rapidly than if the layer was growing as islands at lower temperature and hence give an apparent faster growth rate.

Looking at the carbon 1*s* spectra in figure 6.14 would suggest that the latter of these two possibilities is the case. As the films are grown in situ, there should be no change in the level of carbon present on the surfaces throughout the deposition process. Typically carbon is surface localised due to contamination, either not removed during the etching and passivation processes or forming in the time taken to transfer the samples to UHV after surface treatment. As a result of this surface localisation and low levels present, it is attenuated much more readily than the substrate signal upon the deposition of an overlayer. On the room temperature deposited samples, we see a significant C 1*s* signal throughout the deposition process, which changes very little with successive depositions. With depositions at 200 °C however, we see a rapid suppression of the C 1*s* signal from the first deposition onwards. This suggests that on the RT deposited samples, there are regions of the surface left exposed allowing for the photoemission of electrons from the carbon layer without attenuation as a result of HfO_2 growth in a Volmer-Weber island formation[28] (as opposed to Stranski-Krastanov formation), as there is no apparent initial layer forming before the onset of island formation based on the lack of C 1*s* attenuation. While it is also possible that the 200 °C grown oxide forms islands during growth, the results suggest that there is at least an initial uniform thin film growth before the potential onset of island formation. Also, based on the linearity of the growth rate at elevated temperature in figure 6.13, this would be expected to be a few nanometres thick as the onset of island formation would be expected to change the apparent growth rate of the oxide layer.

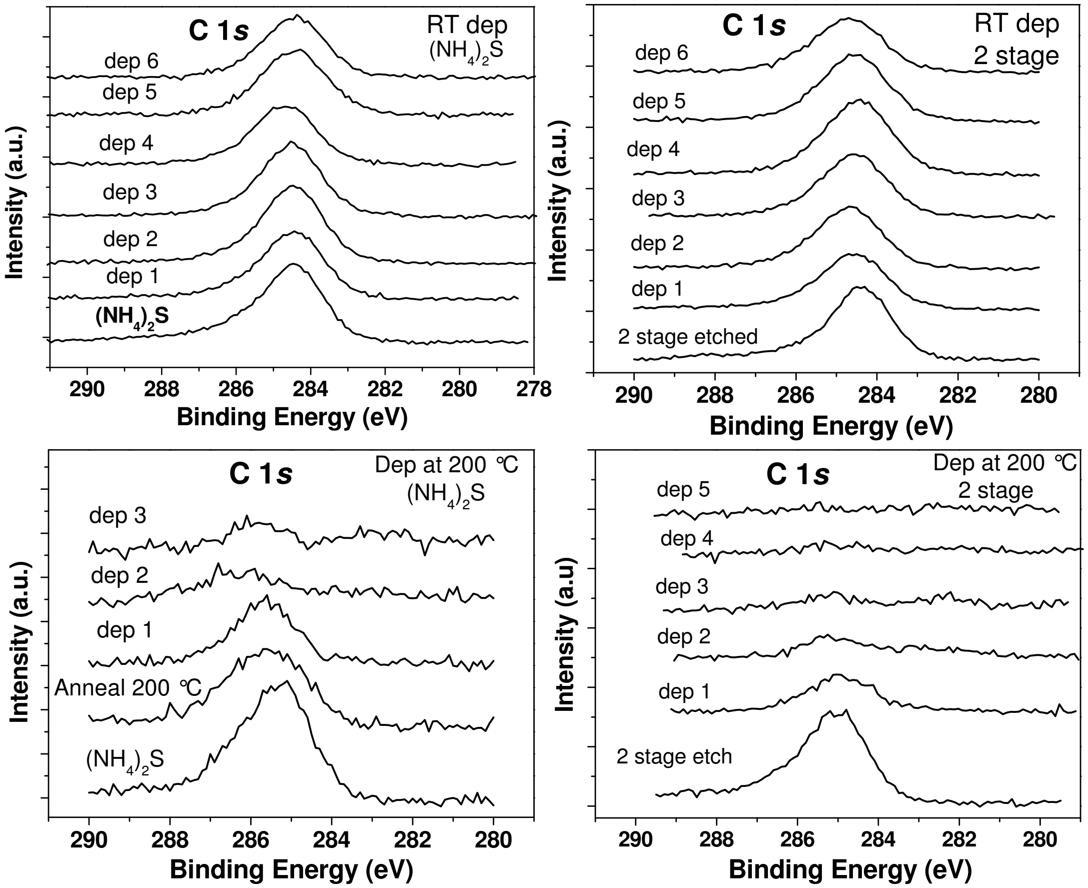

Figure 6.14 Carbon 1*s* spectra during the sequential deposition of HfO_2 showing the suppression of the carbon signal with elevated temperature deposition

Plotting the Hf 4*f* peak position from the fitted spectra against the thickness of the layer reveals more information in relation to the chemical nature of the layer during the deposition process, as shown in figure 6.15. As previously mentioned, all peaks were referenced to the In 3*d* peak at 444.3 eV due to the suppression of the C 1*s* peak during the course of the depositions in the 200 °C depositions, making it unfeasible to use as a reference. As a result you would expect to see a small variation in the binding energy separation between the peaks as the thin films grown on n and p type samples due to the different doping which impacts on the Fermi level position. There is no obvious trend seen based on doping type, however, what is common across all the samples is an increase in the binding energy of the Hf 4*f* peak by ~0.4 - 0.7 eV as the thickness of the oxide layer increases which is seen to remain constant once it reaches a maximum value. It is fair to say that there is a large margin for error in these calculations, due to the uncertainty in the Hf 4*f* fit as a result of the In 4*d* peak overlap and the difficulty in deconvolving the In 3*d* spectra, however the fact that the trend is seen on all of the samples suggests that it is not just due to differential charging of the oxide relative to the substrate or inconsistencies in the fits.

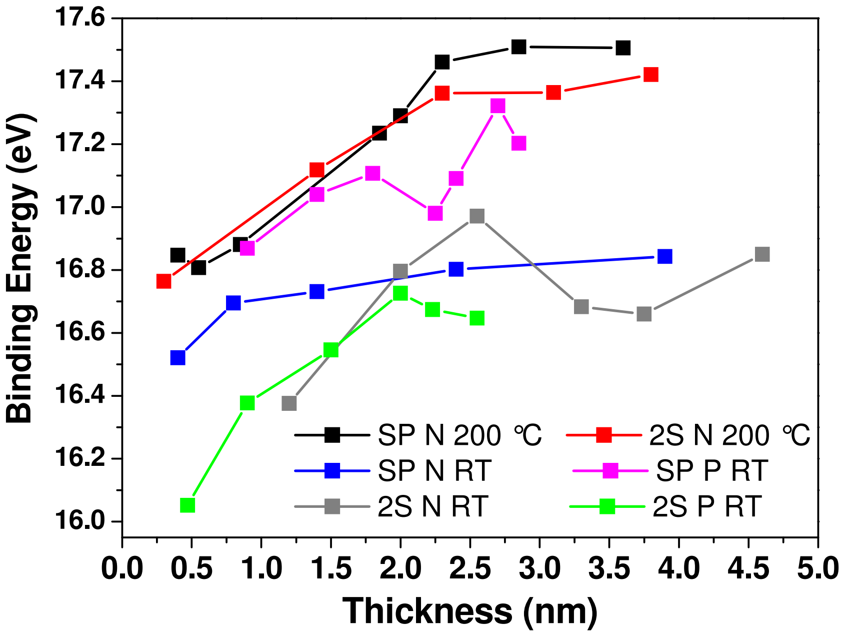

Figure 6.15 Binding energy of the Hf 4*f* peaks as a function of film thickness

This change in binding energy is consistent with the reduction of the Gaussian width as the film thickness increases creating a more uniform, stochiometric oxide. It is also consistent with the formation of a sub stochiometric HfO_x layer forming initially at the interface and as the film thickness increases, the BE of the bulk like HfO_2 begins to dominate, shifting the peak to a higher binding energy.[29]

Looking at the stochiometry of the grown films in table 6.2, calculated from the ratio of the O 1*s* and Hf 4*f* fitted spectra using the relative sensitivity factors of 0.66 and 2.050 for the O and Hf peaks respectively, we can see that the films all appear to be oxygen rich, however this very much depends on the validity of the sensitivity factors.

Table 6.2 HfO_2 stochiometry values after micro e-beam deposition

Sample	**HfO_2 Stochiometry**
SP 200°C N	2.76
2S 200°C N	2.57
SP RT N	2.39
SP RT P	2.12
2S RT N	2.66
2S RT P	2.25

In this context consistent ratios are more important than precise values and if the two anomalously low ratios of 2.12 and 2.25 are excluded, the other four values are within margin of error comparable. The oxygen rich nature of the films could suggest that the HfO_2 is forming at the surface of the InP as the reaction at the surface between the deposited hafnium and the molecular oxygen which could provide the excess oxygen for incorporation into the film.[26]

The HfO_2 layers deposited at 200 °C were subsequently annealed for 30 minutes at 300 °C, 400 °C and 500 °C to determine the stability of the HfO_2 films at these temperatures and whether this would have any effect on the composition of the layers. No changes were evident in terms of the binding energy, stochiometry or FWHM of the films suggesting that the limiting factor in the annealing temperature range for HfO_2 on InP is restricted by the decomposition temperature of the substrate.

6.4.2. Interfacial oxidation

In order to determine whether the HfO_2 deposition was having any effect on the level of interfacial oxide present, the In 3*d* spectra were also fitted throughout as shown in figure 6.16 (a), which shows the spectra from the 2 stage etched p-type sample at each step in the deposition process and is representative of the full sample set. The P 2*p* spectra are also shown in 6.16 (b) and there was no evidence of phosphorous oxide growth throughout, however, due to the bulk sensitivity, rapid suppression when deposited at 200 °C and relatively low ionisation cross section, it is difficult to say unambiguously if this is the case and it is possible that an oxide component could be present below the detection limits of the XPS. So although the In 3*d* spectra are much more difficult to deconvolute, they were investigated preferentially to determine the level of native oxide present.

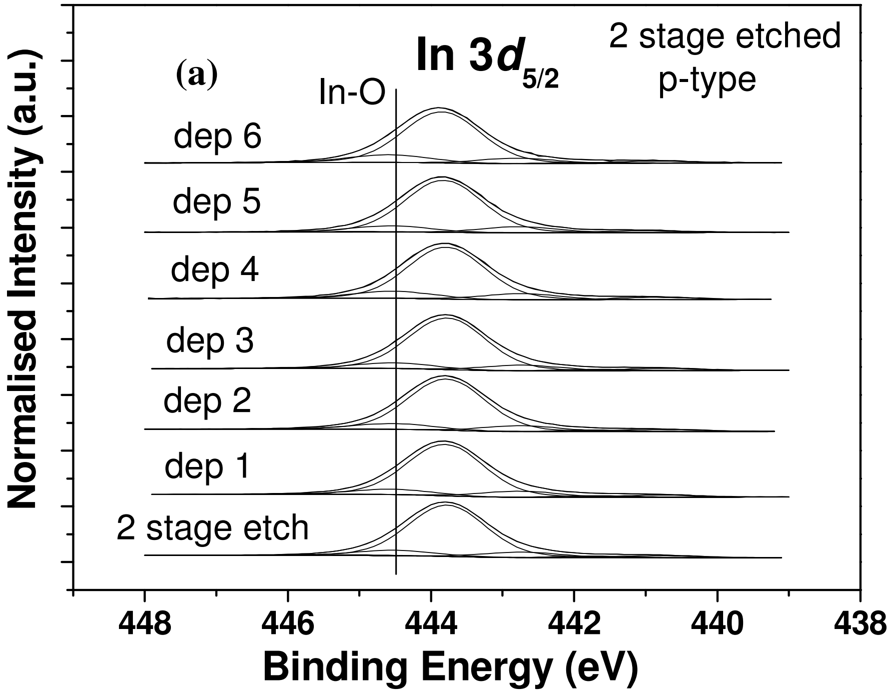

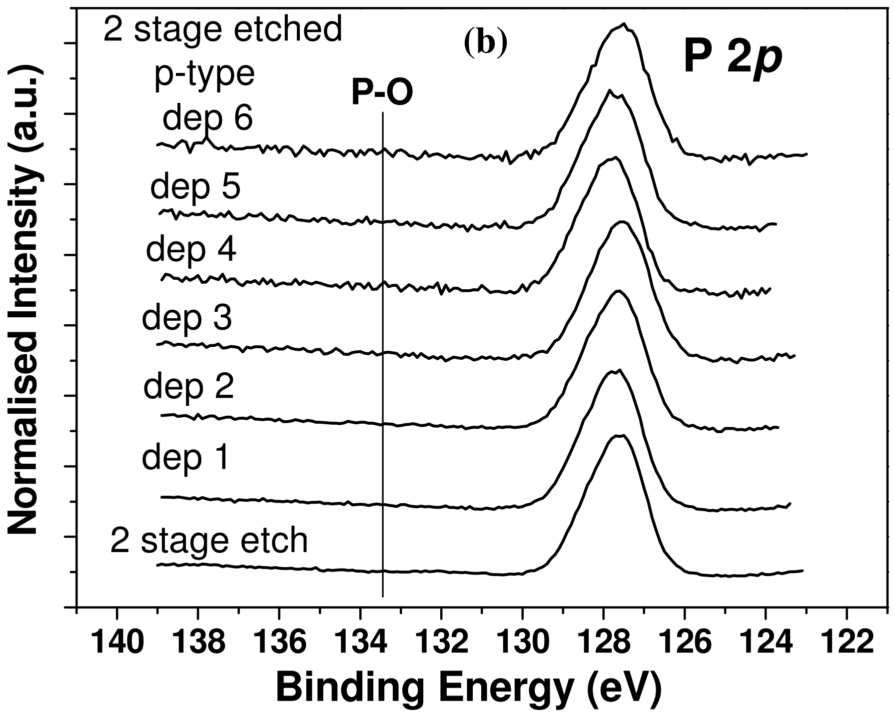

figure 6.16 (a) Fitted indium 3*d* spectra from the 2 stage etched p type InP sample after sequential deposition of HfO_2 at room temperature and (b) the corresponding P 2*p* spectra showing very low levels of interfacial oxidation with depositions

The indium oxide peaks were again fixed 0.8 eV from the bulk so, while the actual quantity of oxide present might not be accurately represented, the overall trend in the level of oxide present should be a good representation of changes and as such the calculated In-O to In ratio is shown in figure 6.17 as a function of overlayer thickness. The level of interfacial oxidation is very small across all the samples, this analysis shows a greater level of interfacial oxide is present as a result of the depositions carried out at elevated temperature, whereas the ratio with room temperature depositions seems to stay relatively constant even though there are likely to be regions exposed to the oxygen in the chamber for much longer than during depositions at 200 °C as a result of island formation. This could be due to oxygen transfer from phosphorous to indium at elevated temperatures or it could suggest that the increase in temperature makes the surface more reactive and susceptible to oxide growth which could explain the increased tendency to form more uniform HfO_2 layers. Further in-situ studies with oxygen exposure at various substrate temperatures would help to identify the origin of this oxide increase.

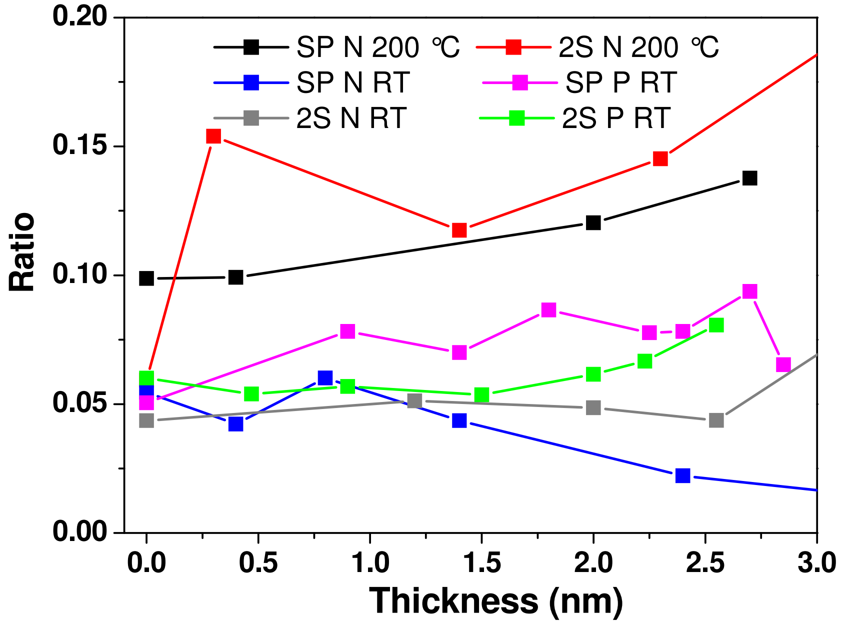

Figure 6.17 Ratio of indium oxide to bulk indium peak as a function of HfO_2 thickness to determine the growth of interfacial oxidation occurring

Due to the presence of a hafnium oxide component in the O 1*s* spectra it was not possible to compare the changes in the native oxide composition from this spectra, as carried prior to HfO_2 deposition in figure 6.4, in order to determine changes in the native oxide present as the Hf-O component has a similar binding energy to the In-O component.

6.4.3. Surface roughness and growth mode

AFM measurements were taken from the two stage etched and $(NH_4)_2S$ passivated samples post HfO_2 deposition at 200 °C and subsequent annealing to 500°C. Figure 6.18 shows a 1 µm x 1 µm scan of the 2 stage etched sample and shows clear evidence of island formation, roughly 50 nm in diameter and range from 2 nm to 15 nm in height producing an RMS roughness of 3.2 nm. This is not strictly consistent with XPS results which suggested the formation of a uniform thin film at elevated temperature, so it is possible that this is evidence of a Stranski-Krastanov growth mode where the initial stages of the HfO_2 growth was as a uniform film and above a critical thickness we see the onset of island formation.

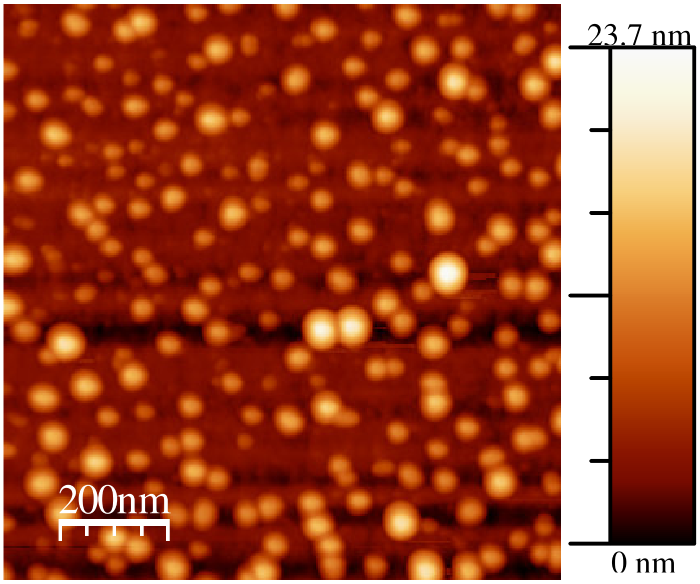

Figure 6.18 1 µm x 1 µm AFM spectra of HfO_2 by micro e-beam on 2 stage etched InP at 200 °C after annealing to 500°C showing evidence of island formation

A similar AFM image from a 1µm x1µm region on the $(NH_4)_2S$ passivated surface after HfO_2 deposition and annealing to 500 °C is shown in figure 6.19. The topography of the film is consistent with the coalescence of HfO_2 islands at elevated temperatures, having an RMS roughness of 0.6 nm (not taking into account the remaining island features). Features which approximate to randomly distributed pits, roughly 50 nm in diameter and 3-3.5 nm deep (which is consistent with the calculated thickness of the film from XPS measurements), are seen in the scans, with cluster features seen to reside in these pits. These pits and islands are thought to correspond to the clusters seen after $(NH_4)_2S$ passivation in figure 6.5. It is possible that these features inhibit HfO_2 growth and hence lead to the pits in the deposited film. There are also two other distinct type of islands seen on the surface. In the 1 µm x1 µm scan in 6.19 (a), we see an island, ~14 nm in height and 100 nm in diameter similar in dimension to those seen on the 2 stage etched sample. These are seen as the smaller peaks in the 5 µm x 5 µm scan in figure 6.19 (b).

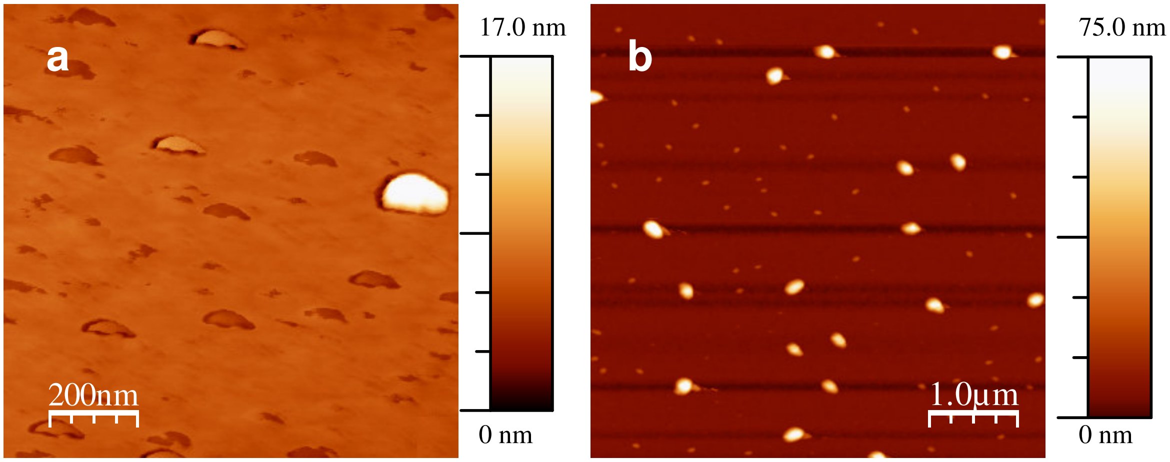

Fig 6.19 (a) 1μm x 1μm and (b) 5μm x 5μm AFM spectra of HfO_2 by micro e-beam on $(NH_4)_2S$ passivated InP after annealing to 500°C in vacuum

The larger island features are 50-80 nm in height and ~ 200 nm in diameter. It is possible that these are due to the coalescence of a number of smaller islands, as a result of the increased surface temperature, to form the larger features. It is not clear whether it is a specific feature of the $(NH_4)_2S$ treated surface that promotes formation of a relatively uniform layer and the coalescence of the islands on the surface, or whether similar film growth properties would be seen on the 2 stage etched surface with variations in the processing parameters so further investigation is needed in this regard.

6.5. Alternative deposition processes

6.5.1. E-beam and ALD

HfO_2 layers were also deposited by conventional e-beam as well as by ALD to a nominal thickness of 3 nm in a single deposition. The substrate temperature was maintained at 200 °C during the e-beam depositions and 250 °C during the ALD growth. The samples again underwent either a 2 stage etch or $(NH_4)_2S$ passivation prior to deposition. Unlike the micro e-beam deposited samples however, these depositions were carried out ex-situ. Post deposition the samples were stored under nitrogen for a number of days prior to XPS analysis in order to minimise exposure to ambient atmospheric conditions. During the transfer to the nitrogen environment and loading to UHV, the samples were exposed to atmosphere for less than 10 minutes. Hf 4*f* and O 1*s* spectra from the deposited films by the three deposition methods are shown in figure 6.20 and are representative of the full sample set for each method.

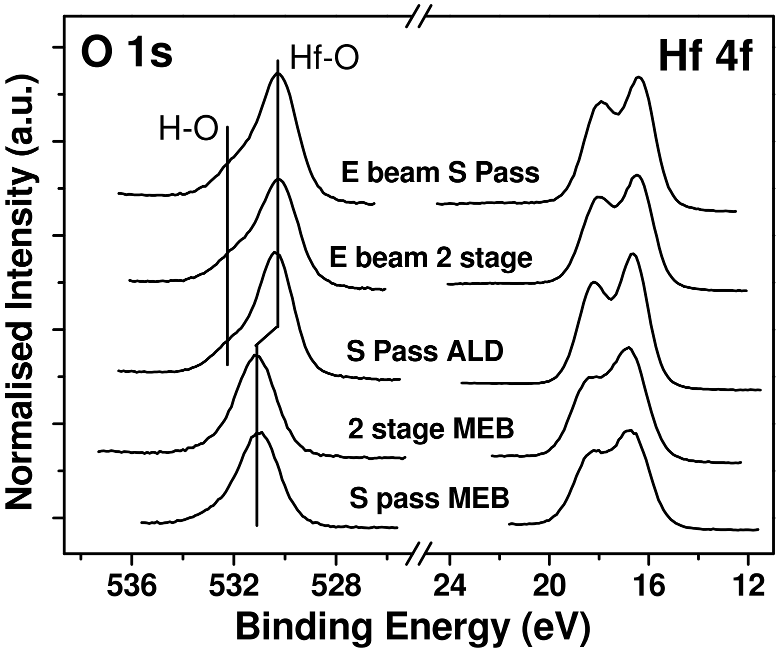

Figure 6.20 Hf 4*f* and O 1*s* spectra after various HfO_2 depositions by ex-situ e-beam, ALD and in-situ micro e-beam

The presence of two components in the O 1*s* spectra from the e-beam and ALD grown samples is evidence of hydroxide species forming on the surface, with the hydroxide corresponding to the shoulder at the higher binding energy side of the peaks. This is as a result of exposure of the samples to atmosphere which could potentially degrade the quality and performance of the films. This suggests that in-situ deposition methods are more favourable for the formation of high quality layers. However, the discrepancy in the binding energy position of the Hf-O component in the O 1*s* spectra is not understood and suggests the formation of oxygen rich layers by micro e-beam.

Due to the thickness of the overlayer and the possibility of surface charging taking place during XPS scanning, it was not possible to accurately identify peak shifts in the individual Hf 4*f* spectra which would reveal changes in the chemical composition of the

HfO_2, however, measuring the BE separation between the Hf component in the O 1*s* peak and Hf 4*f* fitted peaks can provide us with similar information and these values are listed in table 6.3 for the various deposition methods used.

Table 6.3 Binding energy separation between the O 1*s* and Hf 4*f* to highlight changes in chemical composition

Deposition	ΔBE O 1*s* – Hf 4*f*
Micro E-Beam	514.3 ± 0.1 eV
E-Beam	513.8 ± 0.2 eV
ALD	513.75 ± 0.05 eV

As can be seen, there is a reasonably large variation between the in-situ and ex-situ deposition methods again suggesting variations in the chemical composition of the grown oxide layers. There is good correlation between the ALD and the e-beam, both ex situ measurements which shows it is possible to grow chemically similar HfO_2 layers by different deposition methods with the binding energy separation of 513.8 eV being reported for fully stochiometric HfO_2 layers.[25] Based on the improved resolution seen between the spin orbit split components of the Hf 4*f* peaks, it is reasonable to say that the composition of the HfO_2 films grown by e-beam and ALD create a more chemically uniform layer than those grown by micro e-beam. This loss of definition is likely due to variations in the oxygen content throughout the layer, due to excess oxygen incorporated during the growth process.

6.5.2. Stochiometry

One way to investigate the variation in oxygen content is to look at the relative stochiometry of the various films by comparing the area of the fitted Hf 4*f* peaks and the hafnium component in the O 1*s* spectra. The stochiometry is derived using relative sensitivity factors[22] which are ideally determined for each individual XPS system so it is possible that there is a significant error involved in these results, however by using the same values throughout we can still compare the variation between the samples and the deposition methods, with the average values presented in table 6.4.

Table 6.4 Stochiometry values of the HfO_2 films grown by different deposition methods

Sample	**HfO_2 Stochiometry**
Micro E-Beam	2.46
E-Beam	2.21
ALD	1.83

What they suggest is that the micro e-beam samples are significantly more oxygen rich than the films growth by the other two deposition methods, consistent with the increase seen in O 1*s* binding energy. The e-beam samples were also grown in an oxygen atmosphere, although from a HfO_2 source, but this could be the reason for the increased oxygen content relative to the ALD samples due to possible dissociation of atomic oxygen at the interface.

6.5.3. Interfacial oxidation

Due to the presence of the overlayer, the signal from the substrate is considerably suppressed, resulting in poor resolution for the P 2*p* peaks from the e-beam and ALD samples, as shown in figure 6.21 (a). This leaves accurate determination of the level of phosphorous oxide difficult; however there is evidence of variations in the level of phosphorous oxide forming with the various deposition methods.

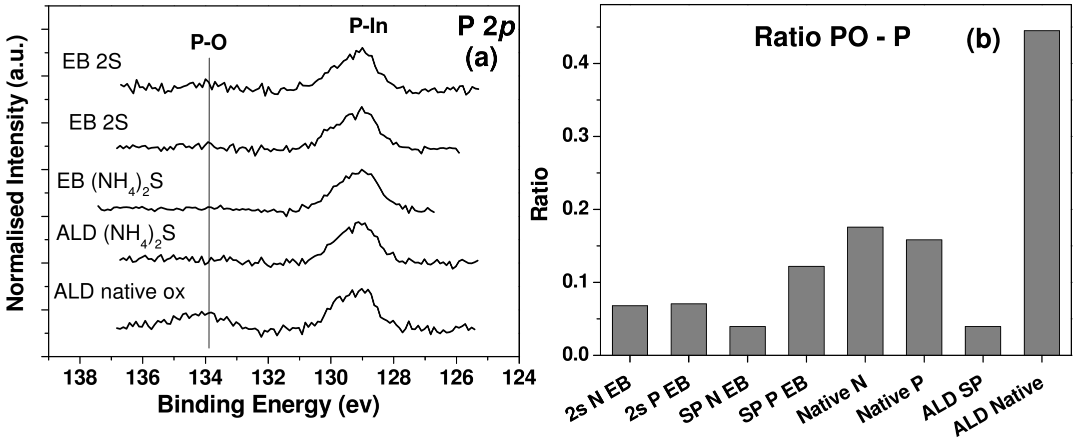

Figure 6.21 (a) Phosphorous 2*p* spectra after HfO_2 deposition on various 2 stage etched and $(NH_4)_2S$ passivated InP substrates by e-beam and ALD and (b) ratio of phosphorous oxide to the bulk peak component from the fitted spectra

The ratio of the calculated oxide to bulk ratio is also shown in figure 6.21 (b) but due to the large signal to noise ratio and relative bulk sensitivity of the P 2*p* peak resulting in a small overall contribution from the interfacial oxide, there is a large margin for error involved with these fits. It is clear however that after all of the deposition methods, there is evidence of phosphorous oxide, which was not seen with micro e-beam growth. It is not possible to tell whether this is as a result of the deposition process or a slightly longer ambient exposure time in comparison to the in-situ depositions.

Due to the poor resolution of the P 2*p* peaks, the In 3*d* peak is again examined as shown in figure 6.22. The lowest oxide ratio is seen on the $(NH_4)_2S$ passivated ALD grown sample as well as the 2 stage etched p type e-beam grown sample, however there is no obvious trends seen between the samples and no apparent benefit in terms of prevention of oxide growth seen with $(NH_4)_2S$ passivation. Again there are no differences observed between n and p type samples. The reported clean up effect during ALD depositions of HfO_2 on GaAs[30] is not in evidence here as it has not been able to remove the indium oxide present on the surface. It is possible that since the clean up effect is due primarily to ligand exchange mechanisms, the coordination of the oxides on InP may not be susceptible to the reactions taking place. It is worth bearing in mind that there is likely to be an In-S contribution (and from the half cycle study on InGaAs, a possible In_2O contribution) to the oxide peak after $(NH_4)_2S$ treatment, which will increase the overall ratio seen from these samples, however as this is likely to be restricted to 1 ML, it is likely to only contribute a small fraction to the measured ratios.

It is not possible to say conclusively whether the level of oxide present on the e-beam grown samples is formed as a result of the deposition process or forms post surface treatment and prior to introduction to vacuum and as such further work is needed to conclusively determine the effect of the various deposition processes in terms of interfacial oxidation.

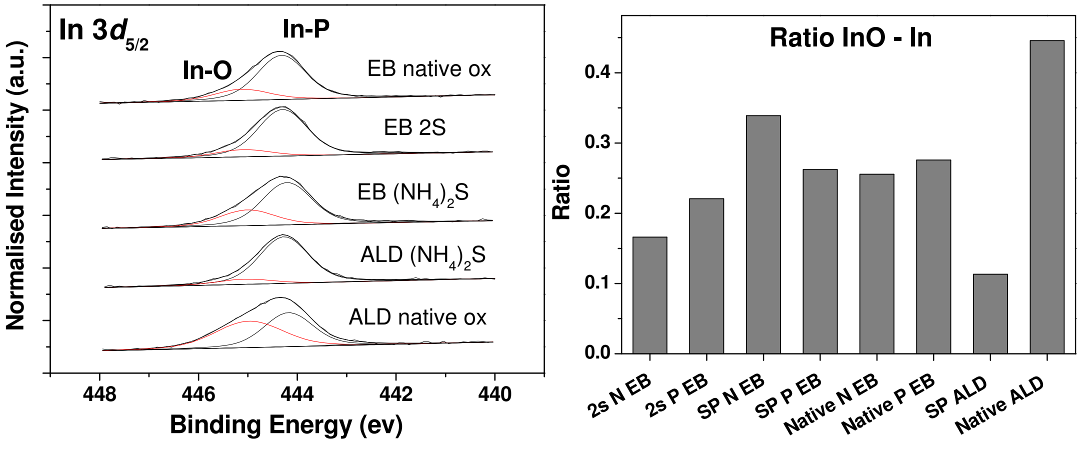

Figure 6.22 (a) Fitted In 3*d* spectra after HfO_2 deposition on various 2 stage etched and $(NH_4)_2S$ passivated InP substrates by e-beam and ALD and (b) ratio of indium oxide to the bulk peak component from the fitted spectra

6.6. Conclusions

The removal of the native oxides on InP has been demonstrated by treatment with both $(NH_4)_2S$ and 2 stage etching, with only a small residual oxide remaining. Assuming that both methods are fully effective at removing all of the native oxides present, neither is successful at preventing ambient re-oxidation in the time it takes to load the samples to UHV after removal of the samples from the chemical solutions. However, of the two processes, the lowest level of native oxide was seen on the $(NH_4)_2S$ treated sample. Ambient oxidation of the $(NH_4)_2S$ treated sample, for periods of time up to 7 days showed significantly lower levels of the native oxides present when compared to the sample prior to passivation, showing that the process is effective at stifling the re-oxidation of the sample. Due to the relatively small binding energy separation of the indium oxide peaks and the low binding energy of the phosphorous 2*p* peak and hence low surface sensitivity, accurate identification of the individual oxide states is not possible, unlike those identified for InGaAs.

HfO_2 deposition was carried out by a number of different deposition methods again on $(NH_4)_2S$ passivated and 2 stage etched InP substrates, with in-situ micro e-beam growth highlighting different growth characteristics of the HfO_2 films at different substrate temperatures. At a substrate temperature of 200 °C, the HfO_2 formed relatively uniform films, based on the suppression of the substrate and carbon signals with increasing deposition time. At room temperature however, the suppression of the substrate progressed much slower and the carbon signal was seen relatively strongly throughout suggesting non uniform film formation and island growth. Films grown ex-situ by conventional e-beam and ALD were shown to create chemically similar layers based on the binding energy position of the peaks, however the for both e-beam deposition methods, the films were seen to be oxygen rich, suggesting oxygen incorporation into the films during the growth process. Both ex-situ procedures showed the presence of the possible hydroxyl related feature in the O 1*s* XPS spectra which was not seen during in-situ deposition.

6.7. References

---

[1] H. Zhao, D. Shahrjerdi, F. Zhu, H.-S. Kim, OK Injo, M. Zhang, J.H. Yum, S.K. Banerjee, J.C. Lee, Electrochem. Solid-State Lett., 11, H233, (2008)

[2] F. J. Leonberger, P. F. Moulton, Appl. Phys. Lett. 35, 712, (1979)

[3] M.A. Itzler, M. Entwistle, M. Owens, X. Jiang, K. Patel, K. Slomkowski, T. Koch, S. Rangwala, P. F. Zalud, Y. Yu, J. Tower, J. Ferraro, Proc. of SPIE, 7320, (2009)

[4] J.F. Wager, K.M. Geib, C.W. Wilmsen, L.L. Kazmerski, J. Vacuum Sci. Tech. B, 1, 778, (1983)

[5] O.L. Krivanek, Z. Liliental, J.F. Wager, R.G. Gan, S.M. Goodnick, C.W. Wilmsen, J. Vacuum Sci. Tech. B, 3, 1081, (1985)

---

[6] I.K. Han, J. Her, Y.T. Byun, S. Lee, D.H. Woo, J.I. Lee, S.H. Kim, K.N. Kang, H.L. Park, Jpn. J. Appl. Phys., 33, 6454, (1994)

[7] Yun Sun, Zhi Liu, F. Machuca, P. Pianetta, W.E. Spicer, J. Vac. Sci. Technol., A, 21, 219, (2003)

[8] W.M. Lau, S. Jin, X.-W. Wu, S. Ingrey, J. Vacuum Sci. Tech. B, 8, 848, (1990)

[9] M.-K. Lee, J.-J. Huang, C.-F. Yen, J. Electrocheml Soc., 154,G117, (2007)

[10] Zhi Liu, Yun Sun, F. Machuca, P. Pianetta, W.E. Spicer, J. Vac. Sci. Technol., A, 21, 212, (2003)

[11] I.K. Han, E.K. Kim, J.I. Lee, S.H. Kim, K.N. Kang, Y. Kim, H. Lim, H.L. Park, J. Appl. Phys. 81, 6986, (1997)

[12] G. W. Anderson, M. C. Hanf, P. R. Norton, Z. H. Lu, M. J. Graham, Appl. Phys. Lett. 65, 171, (1994)

[13] F.J. Himpsel, F.R. McFeely, A. Taleb-Ibrahimi, J.A. Yarmoff, Phys. Rev. B, 38, 6084, (1988)

[14] M. Yamada, Y. Ide, K. Tone, Jpn. J. Appl. Phys., 31, L1157, (1992)

[15] F. S. Aguirre-Tostado, M. Milojevic, C. L. Hinkle, E. M. Vogel, R. M. Wallace, S. McDonnell, G. J. Hughes, Appl. Phys. Letts., 92, 171906, (2008)

[16] H. Peisert, P. Streubel, T. Chassé, R. Szargan, Fresenius J. Anal. Chem., 358, 201, (1997)

---

[17] G. D. Wilk, R. M. Wallace, Appl. Phys. Lett. 74, 2854, (1999)

[18] http://www.itrs.net/

[19] M.A. Quevedo-Lopez, S.A. Krishnan, D. Kirsch, C.H.J. Li, J.H. Sim, C. Huffman, J.J. Peterson, B.H. Lee, G. Pant, B.E. Gnade, M.J. Kim, R.M. Wallace, D. Guo, H. Bu, T.P. Ma, International Electron Devices Meeting 2005 (IEEE Cat. No.05CH37703C), 4, (2005)

[20] K. Kuhn, C. Kenyon, A. Kornfeld, M. Liu, A. Maheshwari, W.-K. Shih, S. Sivakumar, G. Taylor, P. VanDerVoorn, K. Zawadzki, Intel Technology Journal, 12, 93, (2008)

[21] G.J. Hughes, P. Ryan, P. Quinn, A.A. Cafolla, Vacuum, 57, 131, (2000)

[22] J. F. Moulder, W. F. Stickle, P. E. Sobol, K. D. Bomben, Handbook of X-ray Photoelectron Spectroscopy, Perkin-Elmer Corporation, (1992)

[23] J.T. Wolan, G.B. Hoflund, J. Vac. Sci. Tech. A,16, 2546, (1998)

[24] M. A. Hafez, H. E. Elsayed-Ali, J. Appl. Phys., 91, 1256, (2002)

[25] K. Cherkaoui, S. Monaghan, M. A. Negara, M. Modreanu, P. K. Hurley, D. O'Connell, S. McDonnell, G. Hughes, S. Wright, R. C. Barklie, P. Bailey, T. C. Q. Noakes, J. Appl. Phys., 104, 064113, (2008)

[26] R. Xu, Z. J. Yan, S. Chen, Y. L. Fan, X. M. Ding, Z. M. Jiang, and Z. S. Li, Surf. Sci., 581, 236, (2005)

[27] C.J. Powell, A. Jablonski, W.S.M. Werner, W. Smekal, Appl. Surf. Sci., 239, 470, (2005)

---

[28] L. B. Freund, S. Suresh, Thin film materials : stress, defect formation and surface evolution, Cambridge University Press, (2003)

[29] S. McDonnell, B. Brennan, G. Hughes, Appl. Phys. Letts., 95, 072903, (2009)

[30] C. L. Hinkle, A. M. Sonnet, E. M. Vogel, S. McDonnell, G. J. Hughes, M. Milojevic, B. Lee, F. S. Aguirre-Tostado, K. J. Choi, H. C. Kim, J. Kim, R. M. Wallace, Appl. Phys. Lett., 92, 071901, (2008)

7. Photoemission studies of the initial interface formation of ultrathin MgO dielectric layers on the Si(111) surface

7.1. Introduction

MgO has been proposed as a high dielectric constant material (high-κ) for integration into advanced transistor fabrication.[1] Many of the candidate high-κ dielectric materials which have been investigated result in poor interfacial electronic properties and the growth of interfacial silicon oxides during post deposition annealing treatments.[2] Magnesium oxide, while having a dielectric constant (9.8) which is just over twice that of silicon dioxide, has the attribute of being chemically very stable. This should reduce the chemical reactivity at the silicon and III-V semiconductor surfaces seen with alternative high-κ oxides and so could prevent the interfacial oxidation of InP which was seen in the previous chapter during the e-beam deposition of HfO_2 if it was used as an intermediate buffer layer between the semiconductor and the HfO_2 layer. Bulk MgO has a bandgap of between 7.3 eV and 7.83 eV [1,3] which has the potential to ensure band offsets of sufficient magnitude to minimise leakage currents. Yan *et al.*[1] have recently reported that MgO films deposited on silicon substrates by sputter depositing magnesium metal in an oxygen partial pressure reveal sharp interfaces with interface state densities comparable with the SiO_2/Si system. Gallium nitride metal oxide semiconductor field effect transistor devices have been fabricated using an 80 nm MgO dielectric layer which exhibited high breakdown field strength.[4] The dielectric properties of MgO layers deposited on GaAs[5,6] and InP[7] have also been reported. MgO has recently been epitaxially grown on SiC surfaces as a potential gate dielectric material and has displayed low gate leakage and high breakdown fields.[8,9] The objective of this experiment was to deposit a high-κ metal oxide onto an ultrathin SiO_x layer grown on the Si(111) surface. This approach was adopted in an attempt to preserve the electrical quality of the Si/SiO_2 interface while benefiting from the higher κ value of the dielectric overlayer [10] as the absence of an interfacial silicon oxide layer can detrimentally impact on the carrier mobility in the silicon substrate.[11] The lower heat of formation of MgO (-601 kJ/mol) in relation to that of SiO_2 (-859 kJ/mol) would suggest that the deposition of the dielectric might promote the formation of an abrupt interface without chemical interaction. Both soft x-ray synchrotron radiation based photoemission and conventional x-ray photoelectron spectroscopy have been used to characterise the formation of the MgO interface with the pre-oxidised silicon surface by depositing magnesium in an oxygen partial pressure. High resolution core level photoemission experiments have investigated the evolution of the Si/MgO interface and monitored the change in interfacial oxide thickness. The thermal stability of the deposited layers up to 1000 °C has also been investigated.

7.2. Experimental

The soft x-ray photoemission experiments were carried out on the SGM1 beamline at the Astrid synchrotron in the University of Aarhus in an ultrahigh vacuum (UHV) system consisting of a preparation chamber ($5x10^{10}$ mbar) and an analysis chamber ($2x10^{10}$ mbar) allowing sample transfer under UHV conditions. The SCIENTA SES-200 electron energy analyser collects photoelectrons over a solid angle of 8° centred at 40° from the direction of the incoming photons. The SGM monochromator and the SCIENTA analyser were set up such that the combined instrumental resolution was 70 meV for the Si 2*p* acquired with 130 eV photons. All photoemission scans were taken at normal emission to the sample surface. The x-ray photoelectron spectroscopy (XPS) analysis of the samples was carried out in a VG Microtech electron spectrometer at base pressures in the preparation and analysis chambers of $2x10^{9}$ mbar and $1x10^{10}$ mbar, respectively. The photoelectrons were exited with a Mg Kα (hν =1253.6 eV) x-ray source and an electron energy analyzer operating at a 20 eV pass energy yielded an overall resolution of 1.2 eV. Prior to dielectric deposition, an ultra thin SiO_2 film was grown on atomically clean boron doped p-type Si(111) of resistivity 1-3 mΩ cm (2-5 x 10^{19} cm^{-3}) which had been cleaned by flash annealing to 1050 °C several times in ultra high vacuum. The oxide was grown in a partial pressure of 5 x 10^{-7} mbar oxygen at 500 °C for 30 minutes which resulted in a self limiting oxide similar to that reported by Morgen *et al.*[12] The magnesium metal was evaporated onto room temperature substrates from a resistively heated tantalum pouch which contained high purity magnesium chips in a stepwise incremental fashion in an oxygen partial pressure of 5 x 10^{-7} mbar with photoemission spectra taken after each step in the growth process, in a procedure similar to that described by Xu *et al.*.[5] Stoichiometric MgO films were grown under similar conditions by Corneille *et al.*[13] on a metal surface at room temperature. Workfunction measurements were acquired by biasing the sample with a battery voltage of 9 V and measuring the low energy cutoff. Atomic force microscopy (AFM) images were taken using a Digital

Instruments Dimension 3100 system operated in non contact tapping-mode in ambient conditions using an Olympus OMCL-AC160TS tip.

7.3. Results

7.3.1. SiO_2 fitting and growth during MgO depositions

Figure 7.1 shows the photoemission spectra acquired at 130 eV photon energy of the thermally grown oxide and following sequential MgO depositions.

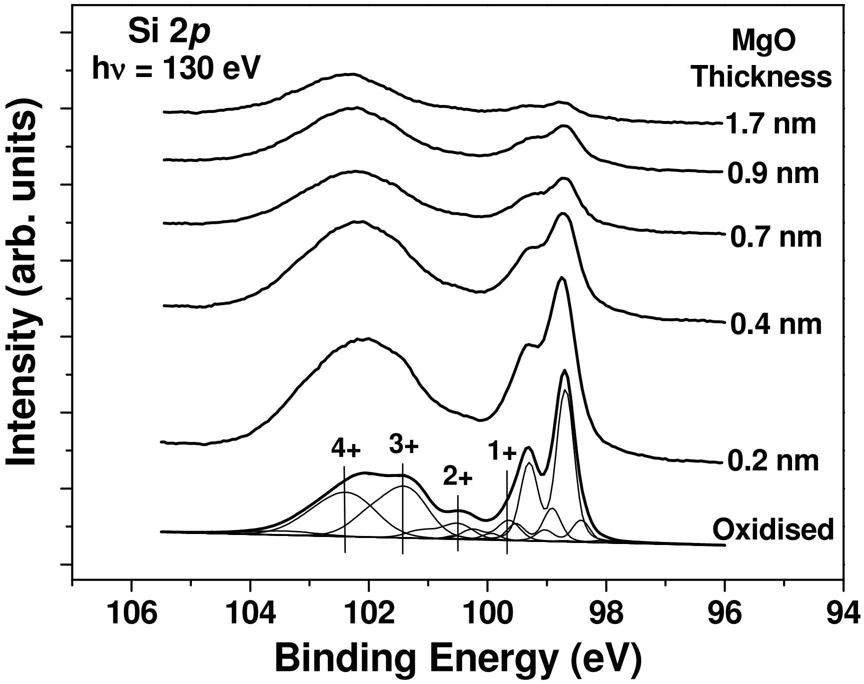

Figure 7.1 Core level photoemission spectra of the ultra thin thermal oxidation and the subsequent MgO depositions showing an increase in the intensity of the interfacial oxide as the substrate peak is attenuated.

The peak profile of the thermal oxide is similar to that previously reported[12] and shows clear evidence of the presence of the four separate oxidation states which are resolved by curve fitting in agreement with previous studies.[14] Using parameters for the Si/SiO_2 system taken from Himpsel *et al.* [15] for a photon energy of 130 eV, the thickness of the self limiting oxide was calculated from the relative intensities of the substrate and oxide features in the Si 2*p* spectrum and found to be approximately 0.3

nm, which effectively means that it is one monolayer thick as previously reported by Miyata *et al.*.[16] As the MgO depositions proceed, the substrate-oxide intensity ratio is seen to change indicating that the interfacial oxide is increasing in thickness. Nominal MgO thicknesses were calculated from the attenuation in the intensity of the Si 2*p* core level feature assuming uniform coverage. The deposition of MgO on top of the ultrathin interfacial oxide layer would not alter the ratio of Si-O to Si integrated intensities, since both signals should be equally attenuated by the MgO overlayer.[17] The MgO has therefore catalysed the oxidation at the interface between the silicon substrate and the chemically stable ultrathin thermally grown oxide.

These interactions are more clearly observed in the curve fitted spectra in figure 7.2 of a native oxide on silicon and following the deposition of 1.7 nm of MgO on the ultrathin thermal oxide.

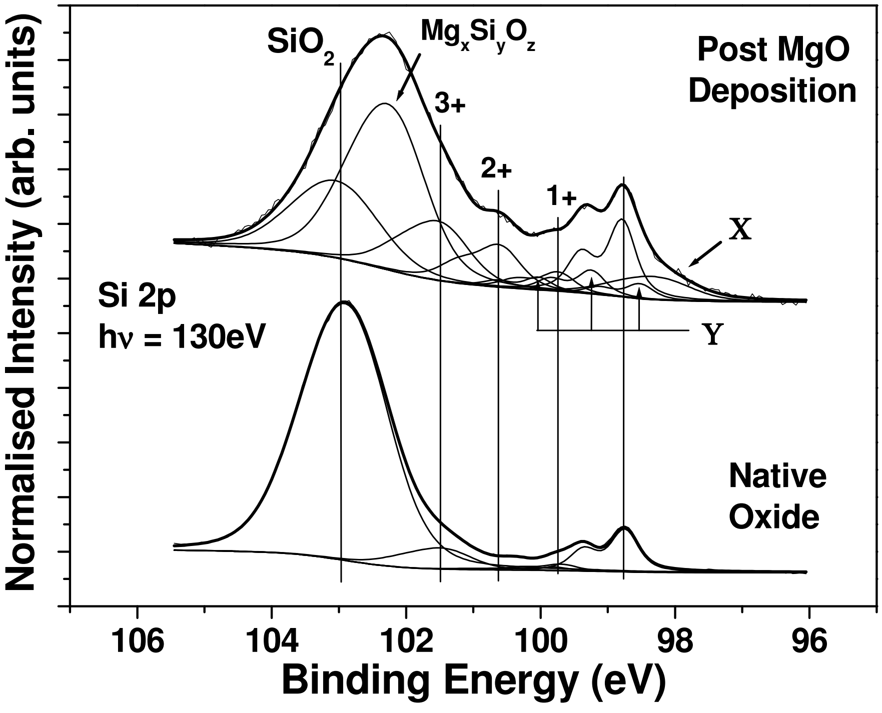

Figure 7.2 Curve fitted Si 2*p* core level photoemission spectra for a native SiO_2 oxide and the highest MgO coverage from figure 7.1 acquired at 130 eV photon energy.

All peaks were fitted using a Shirley background with fixed Gaussian and Lorentzian components and all peak positions remaining correlated to the bulk Si peak such that only the peak intensities were allowed to vary. A peak doublet splitting of 0.61 eV was used, determined from the most bulk sensitive photon energy spectra at 260 eV as well as a branching ratio of 0.5. The native oxide peak profile can be curve fitted with parameters similar to those previously reported with chemical shifts of 0.95 eV, 1.82 eV, 2.7eV and 3.57 eV for the four oxidation states of silicon,[15] however in order to achieve the best peak fit to the profile of the MgO covered silicon surface, it was necessary to include a series of peaks (labelled Y) between the bulk Si and suboxide peaks which have been variously attributed to up-dimers atoms in the Si surface and sub surface layers [14], dangling bonds of adatoms and rest atoms,[18] asymmetric phonon broadening of surface states,[19] unbound silicon atoms in the oxide[20] and strain induced defects at the oxide silicon interface.[21] The position of the lower binding energy silicon component at 0.6 eV below the bulk Si 2*p* peak (labelled X) is similar to that observed for surface states on atomically clean, unpassivated, silicon[22,23] and so could indicate the presence of silicon atoms at the interface without a full complement of 4 silicon neighbours.[20]

These results indicate that the interfacial oxide which contains Si, O and Mg atoms grows by incorporating silicon atoms from the substrate leaving a thin disordered region at the interface which would be expected to have a detrimental impact on the carrier mobility in the substrate.[24] Other groups have shown that the growth of certain metal[25,26] and metal oxide[25,27] layers, 5-8 monolayers thick on atomically clean Si can result in island formation with patches of the clean surface remaining uncovered which could explain the observation of the low binding energy silicon component peak. This would also be expected to impact on the carrier mobility in the substrate. We do not believe that this is happening in our experiments, as the MgO is deposited onto a thermally stable monolayer oxide and the photoemission study of the attenuation of the substrate signals is consistent with this layer increasing in thickness rather than coalescing into islands.

The degraded mobility at the high-κ dielectric silicon interface has been widely observed with both coupling of carriers to surface soft-optical phonons[28] and remote-Coulomb scattering[29] being proposed as possible explanations of this degradation.

Both of these mechanisms are reported to have a reduced impact on mobility degradation, as the thickness of the SiO_2 interlayer is increased, however, this negatively impacts on the minimum equivalent oxide thickness (EOT) which can be realised. The observation of atomic disruption at the Si/SiO_x interface seen in our work would be reduced as the thickness of the thermally grown interfacial oxide is increased, as this layer would act like a barrier layer between the high-κ metal oxide and the silicon substrate.

7.3.2. MgO growth and characterisation

The fitted spectrum of the MgO covered silicon in figure 7.2 also shows a peak shifted by 3.4 eV to higher binding energy from the bulk Si peak, between the Si^{3+} (+2.8 eV) and Si^{4+} (+4.2 eV) oxidation states of the bulk SiO_2 peak which is similar to that reported for the chemical shift of silicon bonded in a hafnium silicate environment [21] which having a very similar electronegativity value to magnesium should give a similar peak shift. This suggests that the interfacial oxide in this case has an $Mg_xSi_yO_z$ magnesium silicate composition. It is important that the thickness of this interfacial oxide layer is controlled as otherwise it will have a detrimental effect on the EOT of the dielectric stack. In order to establish the ultimate thickness of the interfacial layer, Si 2*p* spectra were also acquired at three additional photon energies, 160 eV, 200 eV and 260 eV with different sampling depths which consistently showed that the growth of the interfacial oxide saturates at a thickness of approximately 0.7 nm, which is similar to that previously reported.[1] This thickness is limited by the extent to which additional silicon is incorporated into the interfacial layer from the substrate.

While the dielectric constant of this interfacial magnesium silicate layer would be expected to be greater than that of an equivalently thick SiO_2 layer, it would be difficult to compensate for the disrupted nature of the Si/SiO_2 interface and subsequent mobility degradation in terms of device performance. The Mg 2*p* peak profiles in figure 7.3 show no evidence of either magnesium silicide formation or the presence of metallic Mg.[30] An analysis of the full width at half maximum (FWHM) of the Mg 2*p* peak as a function of coverage (inset in figure 7.3) shows a significant decrease as the film thickness grows which is consistent with a more homogenous chemical environment developing as a function of film growth.

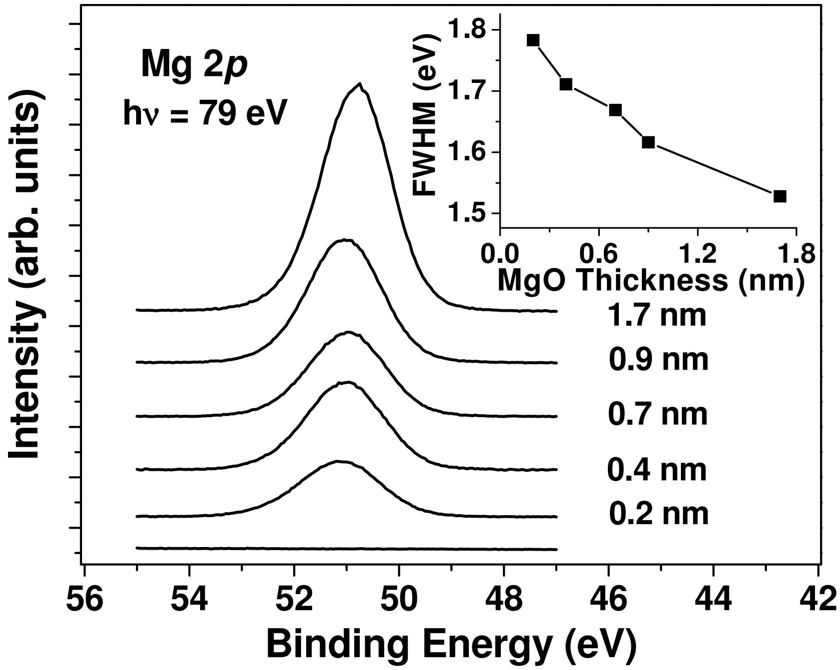

Figure 7.3 Photoemission spectra of the Mg 2*p* core level as a function of film thickness and the inset plots the FWHM of the peak for the coverages investigated.

7.3.3. Growth mode

When the temperature of the substrate was increased to 200 °C during MgO deposition, the initial Mg FWHM was lower than reported here, but the final value was comparable. This suggests that the deposition at elevated temperatures leads to the formation of a more homogeneous chemical environment in the deposited layer in the early stages of film growth.

The changes evident from the workfunction measurements in figure 7.4 shows that two low energy cutoffs are detected for the initial depositions. Photoemission is a local probe of the surface potential and in the presence of a non-uniform layer can reflect the presence of more than one secondary electron threshold.[31] As the deposition progresses, there is the suppression of the oxidised silicon substrate workfunction in parallel with the increasing dominance of the MgO related workfunction which reaches the bulk value of 2.8 eV on the final coverage investigated. This suggests that the MgO deposition in the early stages does not form a continuous layer and that the oxidised silicon surface is still uncovered between islands of MgO. A subsequent study in which MgO was deposited on a silicon surface at elevated temperature displayed a single workfunction cutoff, suggesting a more uniform surface coverage consistent with a reduced tendency of the deposited layer to form islands.

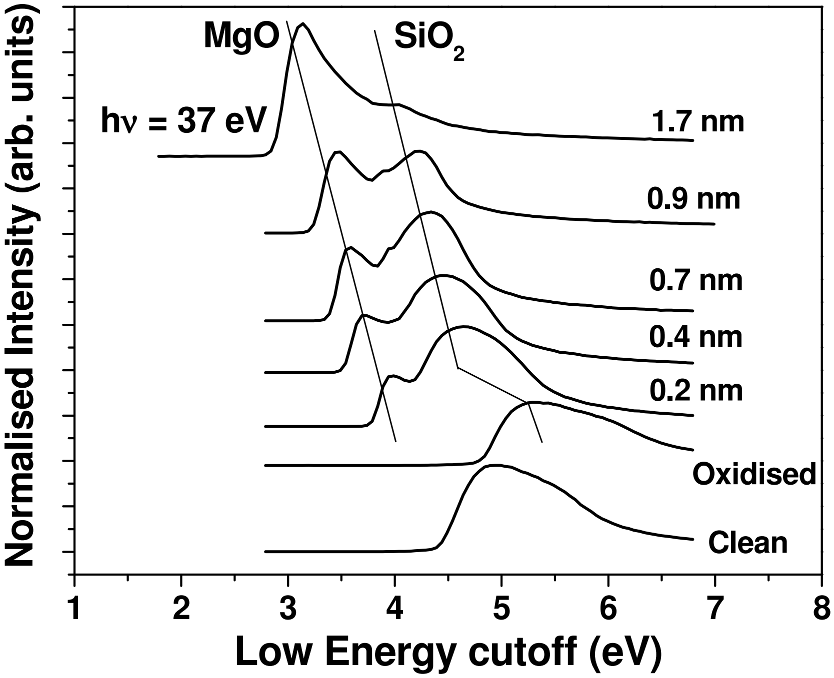

Figure 7.4 Plot of the low energy cutoff as a function of coverage clearly showing the presence of two workfunction reflecting the non-uniform nature of the early MgO film growth.

The 2 µm x 2 µm AFM image in figure 7.5 acquired in air shows the presence of two distinct island types. The smaller islands have an average diameter of 30 nm and a height of 4 nm while the larger features have an average diameter of 200 nm and are ~25nm in height. Previous AFM studies of air exposed MgO single crystal surfaces reported the observation of surface protrusions similar in dimension to the larger islands in the above image and were attributed to the formation of magnesium hydroxide or carbide related features on the surface due to the tendency of MgO to interact with ambient contaminants.[32] The smaller islands are attributed to the initial growth of a nonuniform layer consistent with the results of the workfunction study.

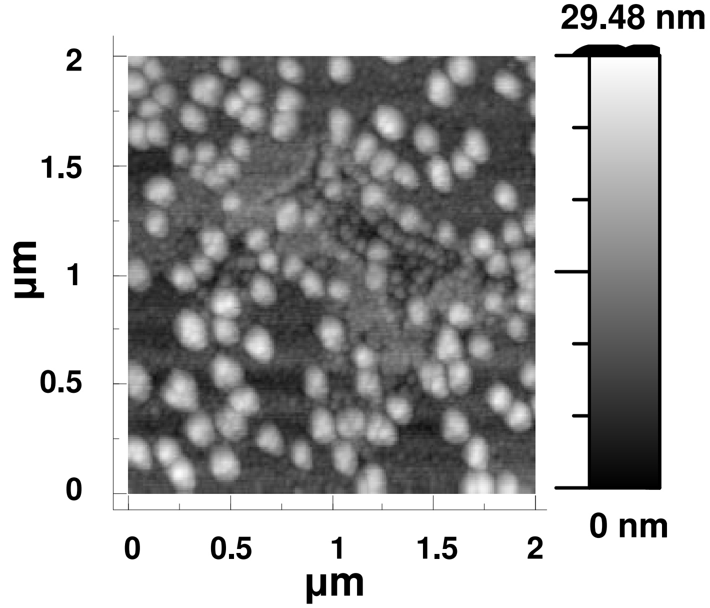

Figure 7.5 2 µm x 2 µm AFM image showing MgO island growth when deposited at room temperature. The small islands are attributed to the intrinsic thin film growth mechanism while the larger features are evidence of $Mg(OH)_2$ growth upon exposure to atmosphere.

7.3.4. Electronic Structure

The valence band spectrum of the pre-oxidised silicon surface shown in figure 7.6 indicates that the valence band offset between the ultra thin silicon oxide and the silicon substrate is 4.3 eV in agreement with previous measurements.[33] With the deposition of MgO, the valence band offset reduces by 0.4 eV to 3.9 eV which remains unchanged as the thickness of the overlayer increases.

MgO has a small positive electron affinity of 0.85 eV. As stated earlier, for the thickest film studied, the workfunction derived from the final thickness in figure 7.4 was 2.8eV. When this is used in conjunction with the energy position of the valence band maximum it is possible to determine that the ionization potential for this film is 7.4 eV. If it is assumed that the electron affinity value of 0.85 eV is correct, the bandgap of this film is given by the ionization potential minus the electron affinity which comes out as 6.55 eV which is smaller than that reported for a bulk MgO layer.[1] The calculated conduction band offset is then 1.55 eV which is sufficiently high to inhibit charge carrier transport.

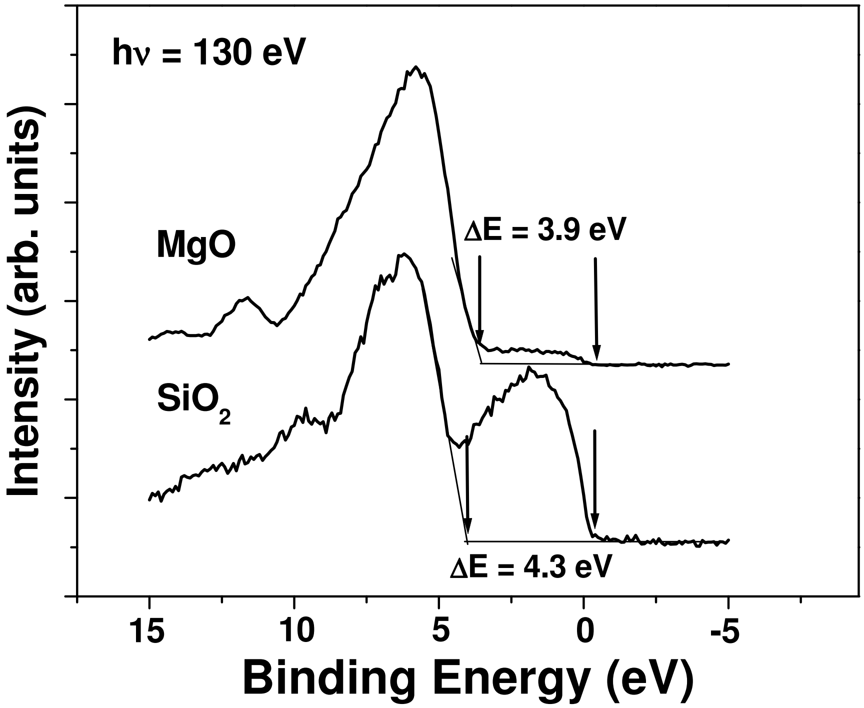

Figure 7.6 Valence band spectra acquired at 130 eV showing the change in the valence band offset resulting from the MgO deposition.

7.3.5. MgO Thermal Stability

XPS spectra for the thermal annealing studies shown in figure 7.7 indicate that the film is stable up to 600 °C. It is interesting to note that the interfacial oxide component on the Si 2*p* spectrum following room temperature deposition of the MgO, clearly visible using 130 eV photons, is just detectable by XPS analysis. Above a 600 °C anneal temperature, the MgO begins to dissociate by desorption of the magnesium and the oxygen reacting with the silicon substrate to form a surface oxide layer. There is no evidence of silicide formation which is observed in the thermal decomposition of ultrathin HfO_2 on silicon. As the dissociation of bulk MgO occurs at much higher temperatures, this dissociation at 600 °C must involve a reduction reaction between the silicon and the MgO. The curve fitted oxygen 1*s* core level spectra show the relative magnitudes of the MgO and the SiO_2 components as a function of annealing with the intensity of the SiO_2 component peak maximised at the 900 °C anneal. For the final 1000 °C anneal, the silicon dioxide and magnesium oxide have virtually all been desorbed from the surface. This thermal study puts an upper limit on the annealing temperature to which these films can be subjected prior to decomposition, however the presence of a capping layer preventing the Mg desorption could allow this limit to be increased.

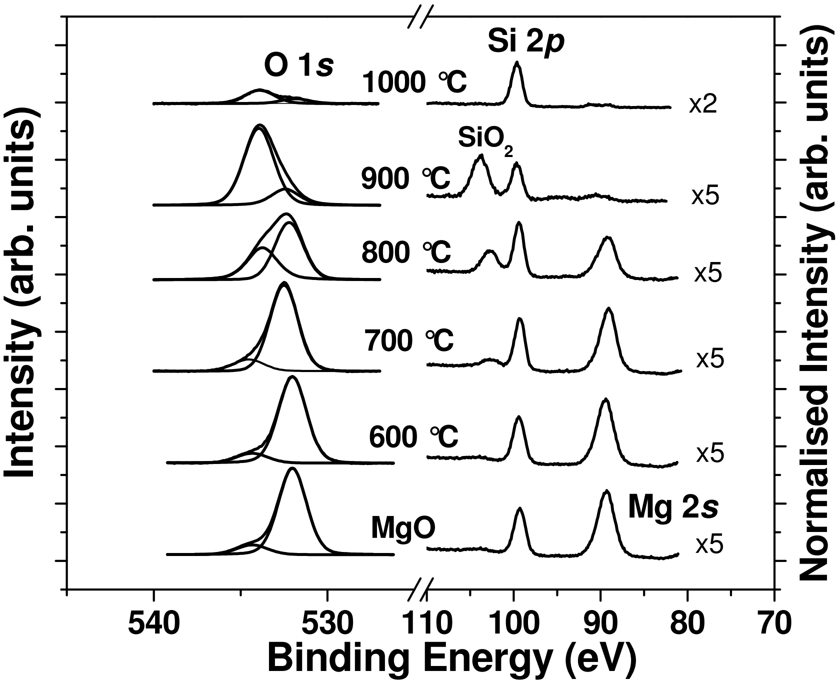

Figure 7.7 Core level XPS spectra of the thermal annealing of a thin MgO film on Si(111) illustrating the decomposition of MgO and the oxidation of the silicon surface as the temperature is increased up to 1000 °C.

7.4. Conclusion

Both soft x-ray synchrotron radiation based photoemission and conventional x-ray photoelectron spectroscopy have been used to characterise the evolution of interface formation between ultrathin MgO layers and the pre-oxidised Si(111) surface. Despite the chemical stability of the thin thermally grown silicon oxide layer, the MgO deposition leads to an increase in the thickness of the interfacial oxide which saturates at a thickness of 0.7 nm. The induced disorder at the Si/SiO_2 interface would be expected to increase carrier scattering mechanisms and hence be a contributing factor to the observed degradation in mobility at high-κ silicon interfaces. Thicker buffer oxides which could be grown to prevent the interface disruption, thereby preserving the high quality Si/SiO_2 interface, would have a self defeating effect in terms of the primary objective of reducing the EOT of the dielectric stack. The valence band and the conduction band offsets between MgO and silicon are found to be 3.9 eV and 1.55 eV, respectively. Thermal annealing studies of deposited MgO films show that dissociation begins to occur above 600 °C with the desorption of Mg and the oxidation of the silicon substrate.

7.5. References

---

[1] L. Yan, C. M. Lopez, R.P. Shrestha, E.A. Irene, A.A. Suvorova, M. Saunders, Appl. Phys. Lett., 88, 142901, (2006)

[2] J-P. Locquet, C. Marchiori, M. Sousa, J. Fompeyrine, J.W. Seo, J. Appl. Phys., 100, 051610, (2006)

[3] Y. Lu, J.C. Le Breton, P. Turban, B. Lepine, P. Schieffer, G. Jezequel, Appl. Phys. Lett., 88, 042108, (2006)

[4] Y. Irokawa,Y. Nakano, M. Ishiko, T. Kachi, J. Kim, F. Ren, B.P. Gila, A.H. Onstine, C.R. Abernathy, S.J. Pearton, C.-C. Pan, G.-T. Chen, J.-I Chyi, Phys. Stat. Sol. C, 7, 2668, (2005)

[5] F. Xu, H. Pan, W. Zhang, G. Wang, Z. Li, P. Xu, J. Electron. Spectrosc. Relat. Phenom., 144, 385, (2005)

[6] J. C. Le Breton, S. Le Gall, G. Jézéquel, B. Lépine, P. Schieffer, P. Turban, Appl. Phys. Lett., 91, 172112, (2007)

[7] T.W. Kim, Y.S. You, Appl. Surf. Sci., 180, 162, (2001)

---

[8] T.L. Goodrich, Z. Cai, M.D. Losego, J.-P. Maria, K.S. Ziemer, J. Vac. Sci. Technol. B, 25(3), 1033, (2007)

[9] A. Posadas, F.J. Walker, C.H. Ahn, T.L. Goodrich, Z. Cai, K.S. Ziemer, Appl. Phys. Lett., 92, 233511, (2008)

[10] M.C. Zeman, C.C. Fulton, G. Lucovsky, R.J. Nemanich, W.-C. Wang, J. Appl. Phys., 99, 023519, (2006)

[11] G. Bersuker, J. Barnett, N. Moumen, B. Foran, C.D. Young, P. Lysaght, J. Peterson, B.H. Lee, P.M. Zeitzoff, H.R. Huff, Jpn. J. Appl. Phys., 43, 7899, (2004)

[12] P. Morgen, A. Bahari, U. Robenhagen, J.F. Andersen, J.-K. Hansen, K. Pedersen, M.G. Rao, Z.S. Li, J. Vac. Sci. Technol. A, 23(1), 201, (2005)

[13] J.S. Corneille, J.W. He, D.W. Goodman, Surf. Sci., 306, 269, (1994)

[14] H.W. Yeom, R.I.G. Uhrberg, Jpn. J. Appl. Phys., 39, 4460, (2000)

[15] F.J. Himpsel, F.R. McFeely, A. Taleb-Ibrahimi, J.A. Yarmoff, Phys. Rev. B, 38, 6084, (1988)

[16] N. Miyata, M. Ichikawa, T. Nabatame, T. Horikawa, A. Toriumi, Jpn. J. App. Phys., 42, L138, (2003)

[17] R.G. Vitchev, J.J. Pireaux, T. Conard, H. Bender, J. Wolstenholme, Chr. Defranoux, Appl. Surf. Sci., 235, 21, (2004)

[18] C.J. Karlsson, E. Landemark, Y.-C. Chao, R.I.G. Uhrberg, Phys. Rev. B, 50, 5767, (1994)

[19] C.J. Karlsson, F. Owman, E. Landemark, Y.-C. Chao, P. Mårtensson, R.I.G. Uhrberg, Phys. Rev. Lett., 72, 4145, (1994)

---

[20] C.R. Fluchter, D. Weier, M. Schurmann, U. Berges, S. Doring, C. Westphal, Surf. Sci., 602, 2623, (2008)

[21] S. Toyoda, J. Okabayashi, H. Kumigashira, M. Oshima, K. Ono, M. Niwa, K.

[22] J. Roche, P. Ryan, G. Hughes, Surf. Sci., 465, 115, (2000)

[23] H.W. Yeom, H. Hamamatsu, T. Ohta, R.I.G. Uhrberg, Phys. Rev. B, 59, R10413, (1999)

[24] S. McDonnell, B. Brennan, G. Hughes, Appl. Phys. Lett., 95, 072903, (2009)

[25] Patricia A. Baeza, K. Pedersen, J. Rafaelsen, T.G. Pedersen, P. Morgen, Z. Li, Surf. Sci., 600, 610, (2006)

[26] B.S. Semak, T. Jensen, L.B. Tækker, P. Morgen, S. Tougaard, Surf. Sci., 498, 11, (2002)

[27] T.-W. Pi, C.-P. Ouyang, J.-F. Wen, L.-C. Tien, J. Hwang, C.-P. Cheng, G.K. Wertheim, Surf. Sci., 514, 327, (2002)

[28] G. Ferrari, J.R. Watling, S. Roy, J.R. Barker, A. Asenov, J. Non-Cryst. Solids, 353, 630, (2007)

[29] S. Barraud, O. Bonno, M. Casse, J. Appl. Phys., 104, 073725, (2008)

[30] I.J. Malik, J. Hrbek, M.-L. Shek, J. Vac. Sci. Technol., A10, 2367, (1992)

[31] W. Ranke, Phys. Rev. B, 27, 7807, (1983)

[32] P. Liu, T. Kendelewicz, G.E. Brown Jr., G.A. Parks, Surf. Sci., 412, 287, (1998)

[33] J.W. Keister, J.E. Rowe, J.J. Kolodziej, H. Niimi, T.E. Madey, G. Lucovsky, J. Vac. Sci. Technol. B, 17, 1831, (1999)

8. Conclusions

The principal aims of this work were to investigate various surface preparation methods for semiconductor substrates in terms of the removal of the native oxides and surface contamination, preservation of surface uniformity and the potential for chemical passivation as well as the growth and characterisation of thin film, high-κ metal oxides on the treated surfaces. These studies gave a particular insight into some of the problems that exist which need to be addressed to fully realise high speed semiconductor devices using high mobility III-V substrates.

Through the use of rigorous peak fitting of photoelectron core level spectra with tightly held constraints on the peak parameters, it was possible to determine the various oxidation states of InGaAs, InP and Si. This approach was then consistently applied to study the impact of thermal annealing, exposure to atomic hydrogen, various chemical treatments and subsequent exposure to atmospheric conditions on the native oxides present on these surfaces. It was also used to investigate interface formation between these semiconductor surfaces and deposited ultrathin high-κ metal oxide thin films. This allowed for the identification of previously unresolved oxidation states, the determination of oxygen bond transfer from indium to gallium oxides on InGaAs as a result of increased substrate temperature and an insight in the relative thermal stability of the various oxidation states. A procedure was also identified utilising atomic hydrogen which left the InGaAs surface with a small residual, thermally stable oxide while also removing all carbon from the surface, which could not be removed by annealing alone and could potentially act as a suitable surface for the subsequent deposition of high-κ dielectric materials.

In order to reduce the detrimental impact of native oxides on potential semiconductor device performance, sulphur passivation using the commonly available aqueous ammonium sulphide was investigated as a method to both remove and prevent the native oxides from forming on the semiconductor surfaces. While other sulphur passivation techniques and treatments have been investigated, the straight forward processing involved with aqueous ammonium sulphide means it is widely used in order to reduce interfacial oxidation and defect states, however the reported processing parameters used vary greatly. A series of InGaAs samples were prepared which underwent different sulphur passivations by systematically changing the parameters involved in the process such that the optimal processing parameters were determined to be 10% $(NH_4)_2S$ in water at room temperature for 20 minutes. This provided the greatest level of chemical passivation combined with good surface uniformity, determined through combined XPS and AFM measurements. The performance of the passivation process is ultimately determined by electrical measurements where the extent of electrical passivation is determined through calculation of the level of defect states present in the band gap which contribute to Fermi level pinning. While not presented in this work, concurrent measurements were taken from $In_{0.53}Ga_{0.47}As$/ Al_2O_3/ TaN metal-oxide-semiconductor (MOS) structures to determine the optimal passivation parameters in terms of the electrical passivation. The results of this study supported the findings presented here, with the best results again seen using 10% $(NH_4)_2S$ at room temperature for 20 minutes.

The effectiveness of the passivation process at preventing ambient oxidation of both InGaAs and InP substrates was tested by comparing the reoxidation of both substrate materials after treatment with a standard two stage wet chemical etch and by passivation using either $(NH_4)_2S$ or hydrogen sulphide (H_2S). The level of native oxide present was calculated from core level XPS spectra after successive exposures to atmosphere for extended periods of time. The growth rate of the native oxides was seen to be significantly slower on the sulphur treated surfaces, due to the formation of predominantly group III sulphur bonds at the surface which prevented the interaction of oxygen with the substrate, thus confirming the benefits associated with sulphur treatments in terms of chemical passivation.

Aluminium oxide layers were subsequently grown on the optimally sulphur passivated InGaAs surface by atomic layer deposition using tri-methyl aluminium (TMA) as the metal precursor and either H_2O or O_3 as the oxidant, with XPS carried out after each successive “half cycle” in the growth process. The principal aim of the investigation was to determine whether the use of O_3 as the oxidant could generate higher quality oxide films than using H_2O due to the reduced potential for carbon incorporation into the films due to decomposition of the TMA precursor. While the results did show a lower level of carbon present in the Al_2O_3 layers as a result of the O_3 oxidation, this was offset by a significant amount of interfacial oxidation of the substrate which would negate any potential benefits that the O_3 would have in terms of carbon reduction. The results also highlighted the ligand exchange mechanism involved in the "clean up" effect where-by the tri-valent TMA molecules preferentially converted the tri-valent native oxide species into Al_2O_3 reducing the native oxide at the interface.

Al_2O_3 was principally investigated due to its well known growth properties by ALD, however it has a relatively low κ value of 12 which is not sufficient to fully realise semiconductor devices beyond the 32 nm node, so the growth of HfO_2 thin films was also investigated. These were grown on indium phosphide substrates, which essentially act as good template to the $In_{0.53}Ga_{0.47}As$ surface due to the lattice matched nature of these two semiconductors. InP also exhibits a much higher electron mobility than Si in its own right and due to its direct bandgap, it is also a very important material in the development of high speed optoelectronic devices. The HfO_2 layers were grown by two different e-beam methods; micro e-beam where the films were grown and scanned by XPS in-situ without exposure of the samples to atmosphere, and conventional e-beam where the HfO_2 films were grown in a separate vacuum chamber and subsequently exposed to atmosphere prior to loading to UHV for XPS analysis. The in-situ samples showed no evidence of interfacial oxide growth during the deposition process; however the samples that experienced exposure to atmosphere showed evidence of an interfacial oxide and it was not possible to determine whether this formed during the growth process or as a result of the atmospheric exposure.

In order to overcome this potential interfacial oxidation, it was proposed that a stable intermediate barrier layer could be formed between the semiconductor substrate and the high-κ oxide which could prevent this oxidation from taking place. Magnesium oxide (MgO) is known to be chemically very stable and so was investigated as a potential candidate for this role. MgO depositions were carried out on an ultra thin thermally grown SiO_2 layer on Si in order to determine the growth characteristics of the MgO and it was envisaged that the information gained from these studies could be transferred to aid characterisation of MgO growth on III-V substrates. The MgO layers were seen to be thermally stable up to 600°C, significantly higher than the decomposition temperature of both InP and InGaAs which is the ultimate thermal processing limit for these substrates. However, the deposition of the MgO did cause an increase in the interfacial oxide thickness through the formation of magnesium silicate, leaving a disordered region at the interface between the substrate and the oxide, which could potentially degrade electron mobility at the high-κ silicon interface. Further studies are needed to determine the effect of the growth of MgO layers on III-V substrates to determine whether this interfacial disruption is just a characteristic of deposition on silicon and silicon dioxide or whether a similar effect is seen with InGaAs and InP substrates.